Orthotropic Modelling of the Skeletal System

Diogo Miguel Geraldes

Department of Civil and Environmental Engineering,

Imperial College of Science, Technology and Medicine

November 2012

Declaration

I hereby declare that the research presented in this thesis is entirely my own work, undertaken under the supervision of Dr. Andrew Phillips in the Structural Biomechanics Group, Department of Civil Engineering, Imperial College London between October 2008 and November 2012. Full references are given where other sources are quoted. This thesis is submitted for the degree of Doctor of Philosophy of Imperial College London and has not been submitted for any other degree or professional qualification.

Diogo Miguel Geraldes

November 2012

Acknowledgements

The work undertaken in this thesis would not have been possible without the help and guidance of Dr. Andrew Phillips, my PhD supervisor. Thank you for believing that I could contribute to the field of Biomechanics, for the invaluable ideas and discussions which were crucial in the progress of the research here presented, and for the opportunities to share my findings around the world. I am extremely grateful to my PhD colleague and friend Luca Modenese for providing data from his musculo-skeletal model, and his comments and company throughout my journey. I would also like to thank the rest of the Structural Biomechanics group at Imperial College (Susannah Clarke and Alice Younge) as well as soon to be Dr. André Pereira for the precious feedback provided during the many stages of my PhD; Dr. Doube at the Royal Veterinary College and Dr. Abel at Charing Cross Hospital for their help with CT and micro CT analysis; the Blast Group at Imperial College (Dr. Masouros and Mr. Bonner) for the femur specimens used in this study; and the Biomechanics Group at Imperial College for the helpful suggestions given along the way.

The past four years have been the best years of my life. Therefore, I would like to thank all my friends and family in London, Lisboa and around the world, too many to name, for the smiles you put on my face and the joy and happiness that you have always surrounded me with.

Gloria, I will be forever thankful for the time you spent reading my thesis, for your calming presence, for making me complete and, above all, for showing me what Love is.

Finally, and most importantly, I would not be writing these lines without the company, care and love of my sister, Lara, and parents, Ana Luísa and António. I will never forget your valuable advice, the belief you have always put in me, the chances you have given me to improve myself and your support throughout my life. All of which have made me the person I am today. I hope this thesis makes you proud.

Muito Obrigado.

Diogo Miguel Geraldes

“There is grandeur in this view of life, with its several powers, having been originally breathed into a few forms or into one; and that, whilst this planet has gone cycling on according to the fixed law of gravity, from so simple a beginning endless forms most beautiful and most wonderful have been, and are being, evolved.”

Charles Darwin, ‘On the Origin of Species’, 1859

Abstract

The femur's shape, geometry and internal structure are the result of bone's functional adaptation to resist the mechanical environment arising from different daily activities. Many studies have attempted to explain how this adaptation occurs by embedding bone remodelling algorithms in finite element (FE) models. However, simplifications have been introduced to the representation of bone's material symmetry and mechanical environment. Trabecular adaptation to the shear stresses that arise from multiple load cases has also been overlooked. This thesis proposes a novel iterative 3D adaptation algorithm to predict the femur's material properties distribution and directionality of its internal structures at a continuum level. Bone was modelled as a strain-driven adaptive continuum with local orthotropic symmetry and optimised Young's and shear moduli. The algorithm was applied to the Multiple Load Case 3D Femur Model, a FE model of a whole femur, with muscles and ligaments spanning between the hip and knee joints included explicitly. Several artificial structures were included to allow for more physiological modelling of the femur's mechanical behaviour. Multiple load cases representing different instances of daily activities were considered. The model's positioning and applied inter-segmental loading were extracted from a validated musculo-skeletal model. The mechanical envelope produced by the FE model was matched up with published studies and the model's suitability as a platform for the prediction of bone adaptation was confirmed. The resulting material properties distributions were compared against CT data of a human femur specimen and published studies. Furthermore, the predicted directionality of the femur's internal structures was validated by comparison with micro CT data of the proximal and distal regions of the same specimen. It was concluded that the proposed model can reliably produce the observed optimised structures in the femur. It is recommended that multiple activities and different instances of each load case should be considered when attempting to model bone's adaptation. The final result of this work is a physiological orthotropic heterogeneous model of the femur. This method has the potential to be an invaluable tool in achieving a more thorough understanding of bone's structural material properties, improving the knowledge we have of its mechanical behaviour.

Contents

List of Figures

List of Tables

Chapter 1

Introduction

The shape and structure of the femur have been analysed, since the first biomechanical studies of the human skeleton and shown to be adapted to its functions during the daily living activities it is subjected to. Ageing population suffer from significant progressive biomechanical bone complications: osteoarthritis can lead to the need to replace hip and knee joints in order to improve patients' life quality; osteoporosis weakens the bone, increasing the risk of femoral fractures with an extremely high mortality rate. Both conditions cause significant burdens in countries' healthcare systems and efficient solutions are required in order to improve their treatment. The progression of such degenerative diseases can only be understood with an improved knowledge of bone's structural and mechanical behaviour in healthy and affected subjects. The femur's geometry, the available data in literature, and the many studies and measurements of its material properties, make it an ideal subject in the attempt to understand the process of bone adaptation, growth and healing.

Bone adaptation algorithms have been used in many areas of Biomechanics that focus on bone's morphogenesis and reaction to altered loading conditions such as the behaviour of bone-implant interfaces, fracture initiation and healing. In order to simplify the analysis and reduce computational times, bone is usually assumed to have isotropic material properties. This assumption is insufficient in predicting the directionality and orientation of bone's microstructure, key factors in modelling its interface with implants or fracture mechanics, as well as providing a better understanding of bone's mechanical behaviour. Orthotropic material properties for bone have been measured experimentally and the orthotropic assumption has been shown to be the closest approximation to bone's anisotropy, short of full anisotropic modelling. It is required to produce a physiological continuum model of femur's material properties distribution and structure orientation in order to understand its biomechanical behaviour. Consequently, an iterative strain-driven orthotropic 3D bone adaptation algorithm with material orientations aligned with the principal stresses was developed. Finite element (FE) studies in biomechanics have incorporated remodelling algorithms in order to study bone's mechanical properties, behaviour and adaptation to changing mechanical environments. In order to model such process, the driving stimulus of bone adaptation needs to be appropriate and, most importantly, a physiologically meaningful representation of what is observed *in vivo*). Therefore, the FE model of the bone studied is required to be as close to the physiological state as possible. This involves careful selection of its constitutive representation, mesh, geometry and the loading and boundary conditions applied.

This thesis describes a novel method of achieving a physiological orthotropic heterogeneous model of the femur by incorporating a bone adaptation algorithm with FE modelling of the femur spanning the hip and knee joints. A fully balanced loading configuration with all muscle and ligament forces applied along their attachment sites, as well as physiologically relevant boundary conditions that do not constrain the femur in non-physiological ways, were also considered. The validation and public release of the orthotropic heterogeneous models obtained from this approach can contribute to structure and directionality dependent research areas such as fracture mechanics and implant design improvement. These models can also contribute to the understanding of the mechanics underlying bone adaptation and the influence of certain activities in bone formation. They can improve the information regarding recommendations for the effect of certain physical activities in the prevention of osteoporosis and femoral fractures. The aim of this thesis is to describe the creation, development and validation of this method of achieving a physiological orthotropic heterogeneous model of the femur.

Chapter 1 is divided in 6 Sections. Section 1.1 outlines the historical progression of the study of functional adaptation in the femur. Section 1.2 describes the development of bone adaptation theories and some of the evidence that supports them. Section 1.3 explores the reasons behind the focus of these studies on the femur and the importance of understanding its structural properties. Section 1.4 analyses different remodelling algorithms and discusses their limitations. Section 1.5 describes the evolution of FE models in order to achieve more physiologically significant results. Lastly, Section 1.6 presents the aims and objectives of this thesis.

1.1 Functional Adaptation in the Femur

Bone's biomechanical properties have been the subject of research since the Renaissance saw the first multi-disciplinary collaborations of anatomists, clinicians, engineers and scientists in order to achieve a better understanding of the human skeleton's functions and pathologies.

Galilei made the first published comment on the mechanical function and shape of bone in one of his dialogues, when he stated that bone dimensions were not linearly proportional to the animal's size (Galilei 1638) after his observations of the long bones across different species (Figure 1.1).

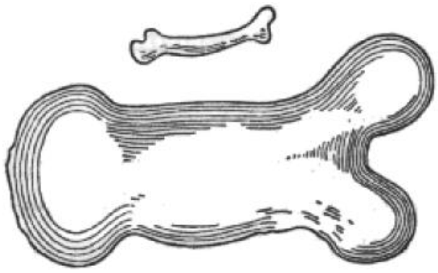

Figure 1.1 - Galilei's drawings of a long bone and its corresponding proportional equivalent for an animal three times larger in size (Galilei 1638).

In 1803 an anatomical atlas by the physician Loder included some of the first drawings of the internal architecture of long bones, in particular of the femur (Loder 1803). Bourgery and Jacob improved upon the structural representation of the lower limb bones in the anatomical treaty published in 1832 (Bourgery and Jacob 1832).

Frederick Ward compared the geometry of the proximal femur to that of a street lamp (Figure 1.2) and suggested that both the shape of the femoral shaft and the alignment of the internal trabeculae resisted the stresses that arise from human body weight (Ward 1838). The clinician also considered the angles of the femoral neck and shaft to provide the widest range of flexion and ideal moment arms for the application of muscle forces at the greater trochanter, whilst maintaining structural strength, stability in pelvic motion and anatomical space for the thigh muscles (Ward 1838). In addition, Ward observed two main compressive and tensile trabecular groups (Figure 1.2, a and b, respectively), and a triangular area, the *trigonum internum femoris* or Ward's triangle as it is more commonly known (Figure 1.2, g), comprised of thin and loosely arranged trabeculae in the proximal femur.

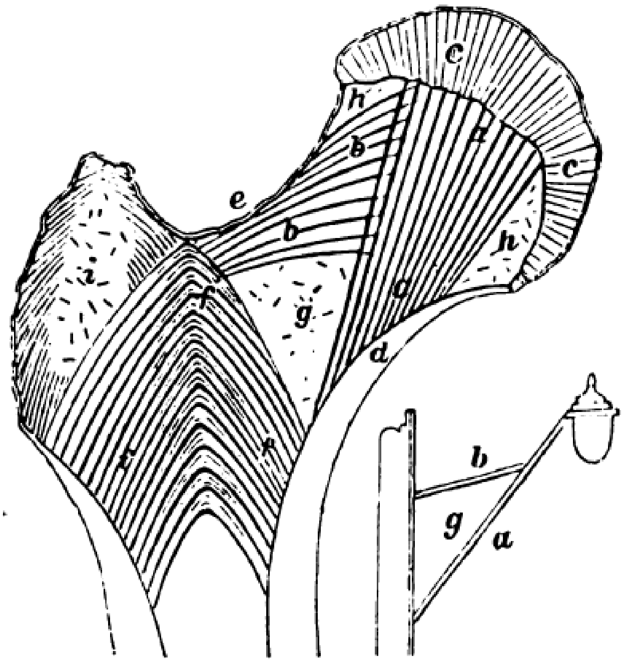

Figure 1.2 - Comparison of the geometry of the proximal femur with that of a street lamp (Ward 1838). The compressive (a) and tensile (b) groups are highlighted, as well as the Ward's triangle region (g).

George Humphry published in 1858 two key observations on trabecular bone structure in the femur: that the trabeculae are perpendicular to the articular surface of the femoral head, and that the two main trabecular groups intersect at 90° (Humphry 1856).

The structural engineer Karl Culmann studied the drawings of the arching trabecular patterns found in different bones of the lower limb by the anatomist von Meyer (von Meyer 1867). He noticed the coincidence of the structures documented (Figure 1.3), with the maximum internal stress lines of cantilevered beams undergoing analogous loading conditions (Skedros and Brand 2011). Special attention was drawn to the proximal femur, where the trabeculae seemed to be aligned with the principal stress trajectories of a similarly shaped Fairbairn crane (Culmann 1865) (Figure 1.4).

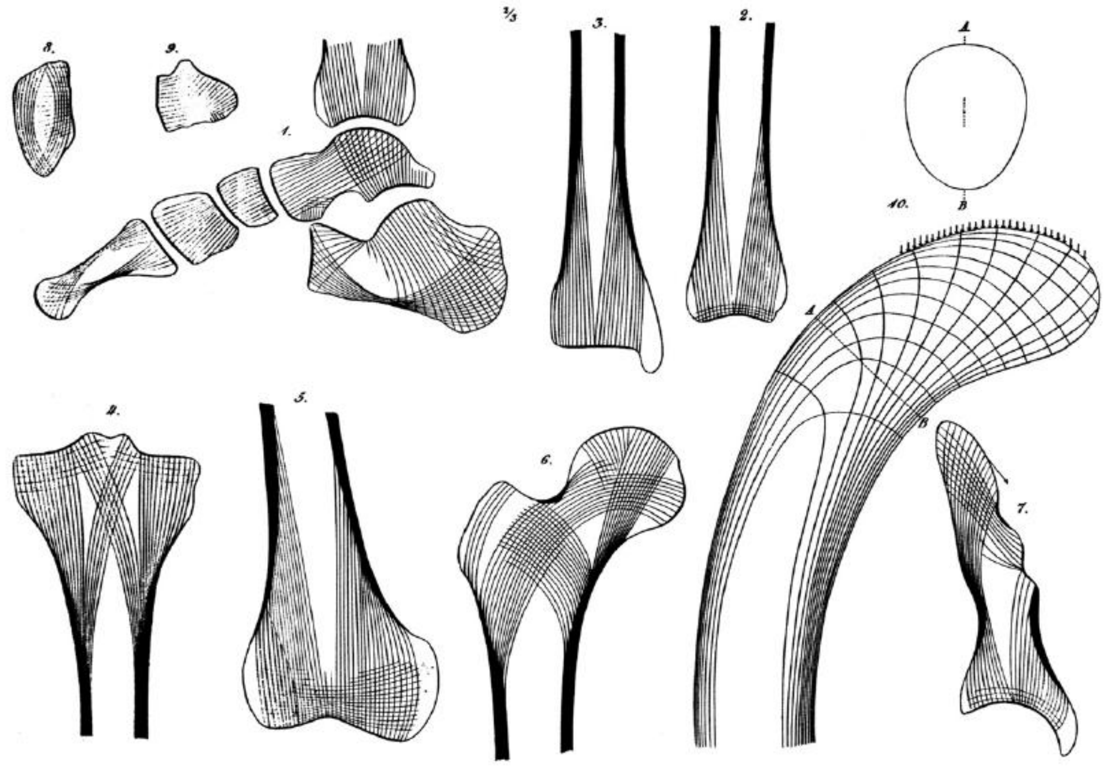

Figure 1.3 - Drawings of the alignment of trabeculae for different lower limb bones (Skedros and Baucom 2007), taken from von Meyer.

During his career as an orthopaedic surgeon, Julius Wolff noticed that traumatic and congenital changes to the geometry and function of bones resulted in changes in their internal architecture (Wolff 1892). He related Culmann's and von Meyer's findings through his observations to formulate the hypothesis commonly known as *Wolff's Law*:

"Every change in the form and function of the bones, or of their function alone, is followed by certain definite changes in their internal architecture, and equally definite secondary alterations of their external conformation, in accordance with mathematical laws." (Skedros and Baucom 2007)

Wolff's statement and drawings implied that, as with the principal stresses, trabeculae crossed orthogonally (Figure 1.4) and their orientation was coincident with these stress trajectories. The surgeon even insisted to admonish von Meyer for not drawing lines of trabeculae crossing at 90° of each other (Skedros and Baucom 2007).

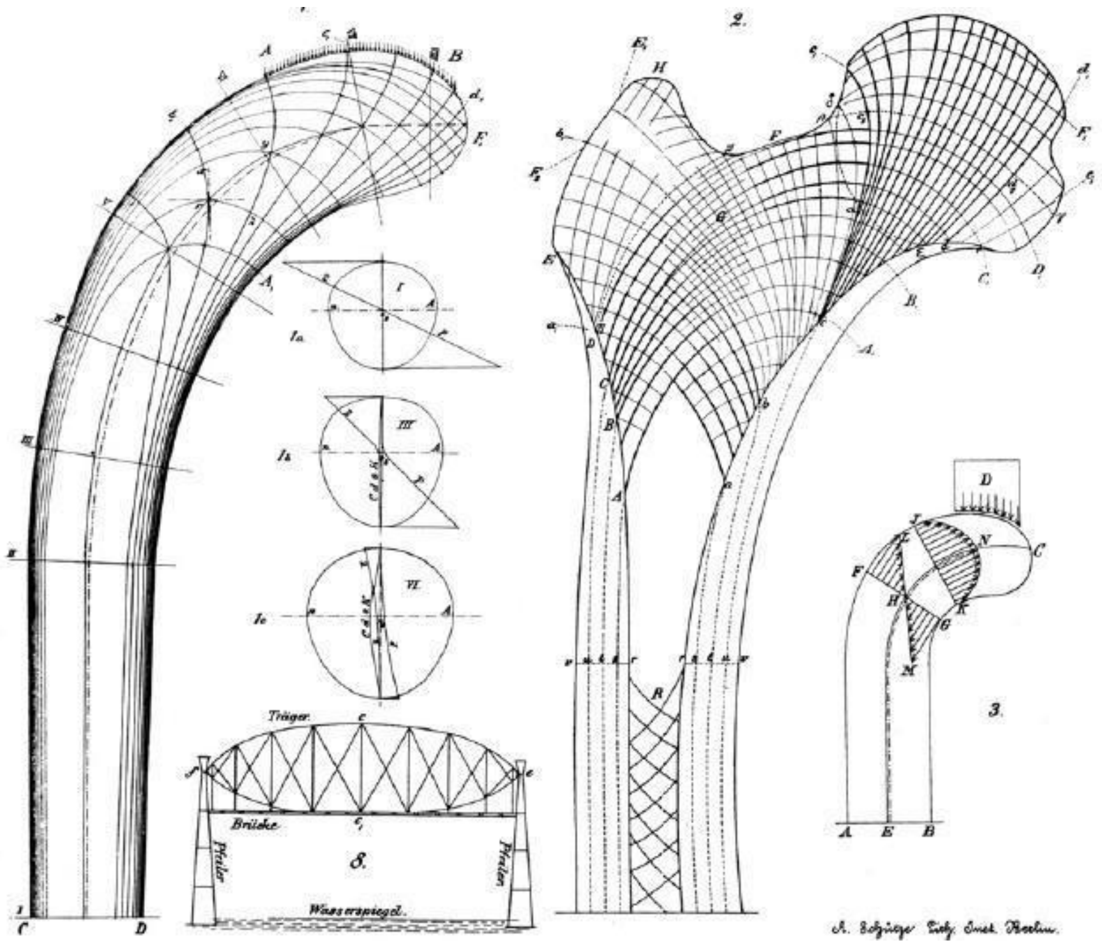

Figure 1.4 - Julius Wolff's drawings comparing the alignment of the trabecular structures with the principal stress directions of Culmann’s analysis of a Fairbairn crane (Skedros and Baucom 2007), taken from Wolff.

Julius Koch’s 1917 study of the stress trajectories and distributions in the proximal femur undergoing single leg stance (Koch 1917) was accepted as mathematical confirmation of the orthogonal arrangement of trabeculae (Figure 1.5), notwithstanding other contemporary observational studies stating that trabeculae do not necessarily cross at right angles (Jansen 1920). It is now accepted that the orthogonal configuration of trabeculae is optimal for simple loading (Pedersen 1989), although trabeculae intersect at acute angles in regions of complex loading in order to resist shear (Skedros and Baucom 2007). The same study by Jansen also introduced the idea that muscle pull could play an important role in bone formation, influencing the structure of the trabecular bone (Jansen 1920).

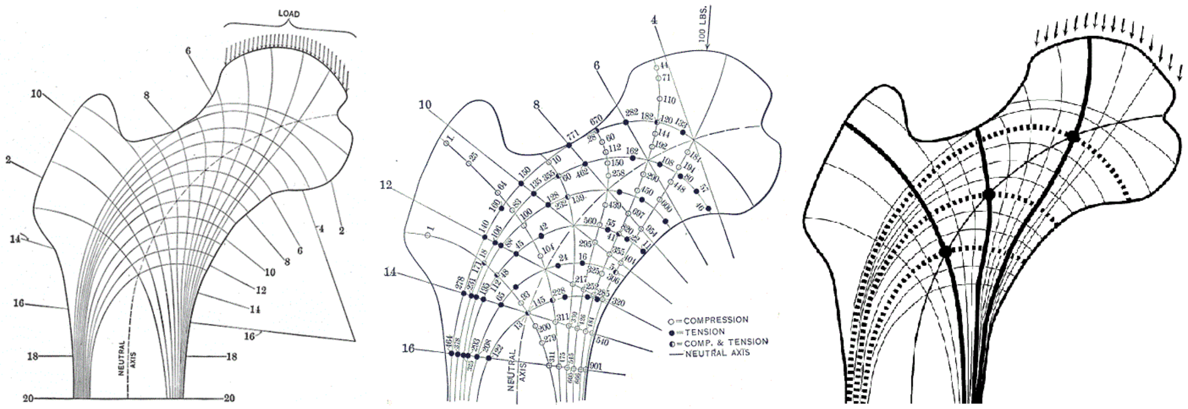

Figure 1.5 - Koch's calculations of the principal stresses and trabecular trajectories in the proximal femur (Koch 1917).

Tobin's work on the clinical significance of the internal architecture of the femur highlighted that the majority of femoral neck fractures he observed occurred through Ward's triangle. He also observed that this area becomes more distinct as bone maturity is reached, being particularly evident in osteoporotic women (Tobin 1955). Additionally, he considered the *calcar femorale* to be the true neck of the femur (Figure 1.6), composed of dense trabeculae with almost cortical hardness that resulted from the force exerted by the flexor and abductor muscles of the hip (Tobin 1955; Garden 1961).

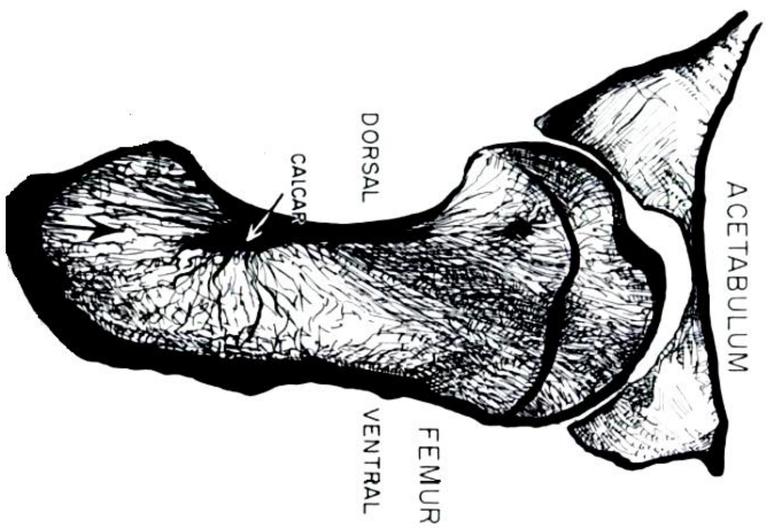

Figure 1.6 - A transverse section of the proximal femur with the existence of the calcar femorale highlighted (Tobin 1955).

Garden’s analysis of the function of the hip joint followed Ward’s observations to conclude that the femoral neck is angled in order to allow twisting and turning. This motion promotes the conversion of the weight bearing compressive stresses arising from the upright position from oblique to vertical (Garden 1961). He noticed that both the proximal end of the femur and the cortex of the femoral shaft had a spiral form configuration as a response to the load transfer at the hip joint. Further examinations by Garden showed that there is a decussation between arching lamellae in the femoral diaphysis, with the secondary trabecular groups crossing at acute angles, in agreement with Jansen, and not orthogonally, as Wolff and Koch suggested (Garden 1961).

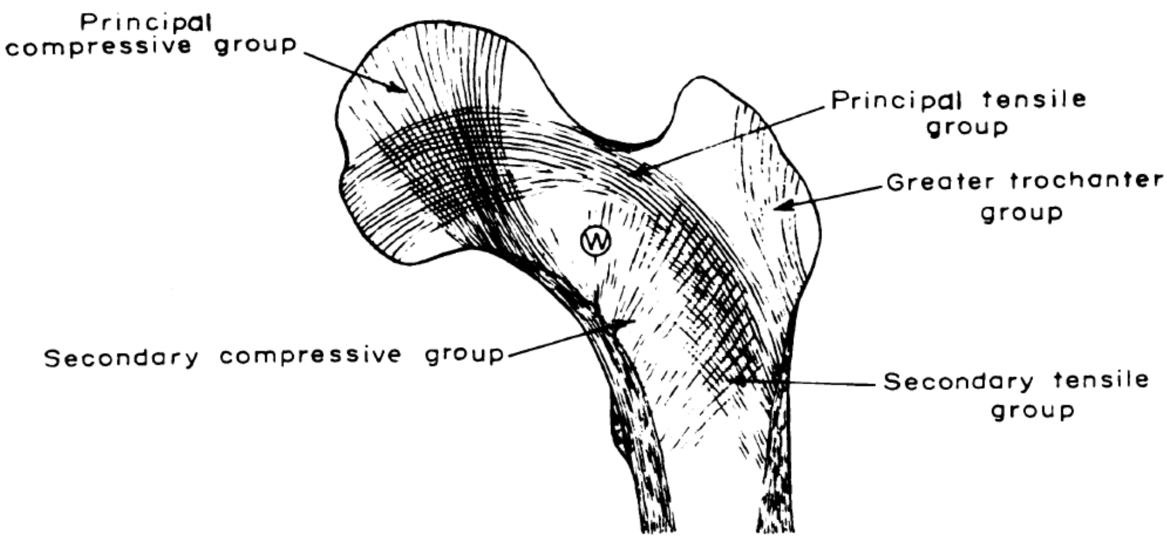

Figure 1.7 - Singh's representation of the trabecular compressive and tensile groups in the proximal femur. The circled W points to the Ward’s triangle (Singh et al. 1970).

A 1970’s publication by Singh classified in detail the trabecular bone structures that are arranged along the lines of compressive and tensile stresses resultant from weight bearing activities (Singh et al. 1970). Five main trabecular groups were described: the principal tensile and compressive groups, the secondary tensile and compressive groups and the greater trochanter group (Figure 1.7). Singh proposed that changes in the trabecular patterns could be used as an index to evaluate the stages of degradation of an osteoporotic bone (Singh et al. 1970).

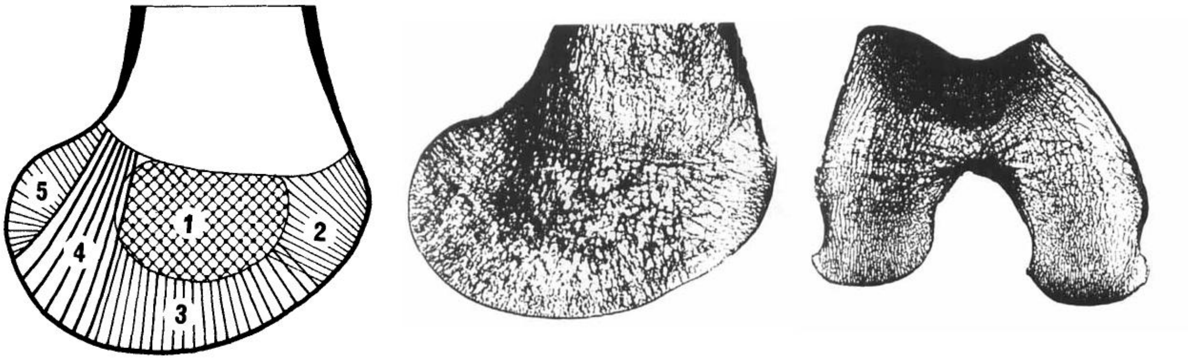

Figure 1.8 - Takechi's study of the bone structures in the distal femur (Takechi 1977).

Takechi extended the study of bone’s structures and geometry to the distal part of the femur, with special focus on the condyles, where five main trabecular features were described (Figure 1.8). It was concluded that the femoral condyles were adjusted to respond to both the compression and rotation movements the distal part of the femur is subjected to during daily living activities. Trabeculae were observed to run perpendicularly to the articular surface predominantly at both the patello-femoral and tibio-femoral joints, where pressure is predominant (Takechi 1977).

More recent work by Skedros and Baucom (Skedros and Baucom 2007) confirmed the observations that bone structures do not always cross at right angles (Jansen 1920; Garden 1961). The same study highlighted that this decussation may be a form of responding to the shear stresses induced by the many different load cases bone is subjected to (Skedros and Baucom 2007). It was also stated that the orthogonal crossing of trabecular groups occurs in areas of bone where a single load case is predominant. However, in areas where complex loading occurs, such as in the proximal femur, secondary groups crossing at non-orthogonal angles are required to resist the shear stresses induced by the combination of load cases it is subjected to (Garden 1961; Miller et al. 2002; Miller and Fuchs 2005; Skedros and Baucom 2007). This implies that bone’s structure is optimised to resist the strains and stresses arising from different daily activities.

1.2 Bone Remodelling and Adaptation

It was highlighted in the previous Section that the shape, geometry and internal structure of the femur are result of the bone's adaptation to its functions and the environmental loading it is subjected to during daily living activities. Many studies have made attempts to explain how this adaptation process occurs. The *Mechanostat* theory by Frost (Frost 1987) stated that bone optimises its structure in order to keep the strains resulting from its mechanical usage between certain thresholds. This process consisted in growth, modelling and remodelling towards a plateau (in a region between 1000 and 1500 µstrain) around a target strain where no bone is lost or gained (Figure 1.9) (Frost 1964; Frost 1987; Frost 2003). Frost described that mechanical loads stimulated the mechano-sensitive bone cells (osteocytes) which in turn would recruit bone apposition (osteoblasts) or resorption (osteoclasts) cells in order to achieve this proposed state of *minimum effective strain* (MES).

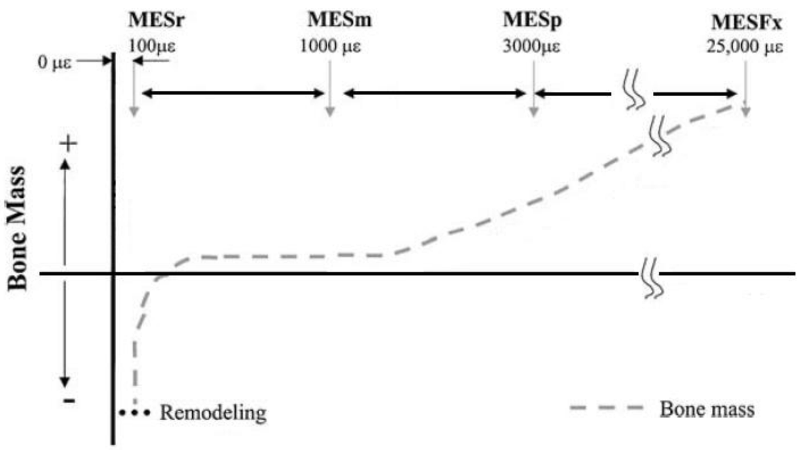

Figure 1.9 - Diagram showing the representation of the *Mechanostat* theory (Frost 2003).

If the strains are below the remodelling threshold – MESr (50 - 100 µstrain) bone is removed and converted to bone marrow. Strains above the operational micro-damage threshold – MESp (~3000 µstrain) promote woven bone formation. Extremely large strains – MESFx (25000 µstrain) will result in fracture. When strains are outside the modelling threshold - MESm (1000 - 1500 µstrain), mechanically driven modelling and remodelling occurs in order to bring them within the target range (Figure 1.9). This theory has been supported by many different studies. Long periods of bed rest result in a drastic drop in loading of the skeleton, leading to a rapid loss of bone mass (Burkhart and Jowsey 1967). Furthermore, in micro-gravity conditions during space flight, where bone is minimally loaded, substantial loss of bone mass has been measured (Vogel and Whittle 1976; Collet et al. 1997). The other extreme has also been documented: cortical thickness and bone size increases have been measured in professional athletes who subject their skeleton to continuous stimulation through sports (Krahl et al. 1994). Another study altered the walking patterns of sheep according to pre-determined conditions and observed the predicted changes in trabecular orientation at their joints (Barak et al. 2011). These changes in bone mass can also be induced locally, as many experiments in different animals suggest (Hert et al. 1971; Lanyon and Rubin 1984; Rubin and Lanyon 1987). Static loads were shown to have no effect on bone remodelling (Hert et al. 1971), and dynamic stimulus to play an important part in this process (Lanyon and Rubin 1984; Skerry 2006), as well as loading frequency (Rubin and Lanyon 1987; Skerry 2006). The same group also found the remodelling plateau to be around 1000 µstrain in avian bones, similar to the one proposed by Frost (Rubin and Lanyon 1985). Other factors such as strain rate, loading amplitude, duration of loading and alternation with resting periods have also been shown to influence bone growth and remodelling (Ehrlich and Lanyon 2002).

Many studies have focused on what might drive this mechano-adaptation (Currey 1984; Cowin 1986; Mullender and Huiskes 1995; Turner et al. 1997; Carter et al. 1998; Currey 2003; Skerry 2006; Skerry 2008). Osteocytes (OCY) have been put forward as the mechano-sensing cells in bone tissue (Mullender and Huiskes 1997; Bonewald 2002; Han et al. 2004; Skerry 2006; Skerry 2008), mediating the bone modelling process (Mullender and Huiskes 1997; Burger and Klein-Nulend 1999; Bonewald 2002; Skerry 2006; Skerry 2008) via osteoblasts (OB) and osteoclasts (OCL). Figure 1.10 shows a schematic representation of bone remodelling at the cellular level: in the steady state (A) that results from normal use, there is no OCL nor OB activity, since the OCYs do not sense any relevant changes in the mechanical environment. When the region surrounding the OCY is overused (B) OB are recruited, collagen is synthesised and bone apposition occurs, reducing the bone strains and returning the mechanical environment back to a steady state; when bone is not being loaded, i.e. in disuse (C), OCL migrate to the surface, promoting bone resorption via degradation of the bone matrix and collagen, decreasing bone mass and increasing strains so the steady state level can be reached (Burger and Klein-Nulend 1999).

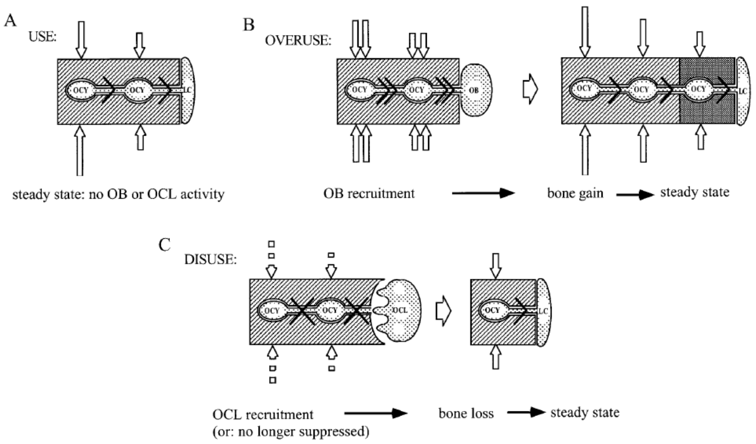

Figure 1.10 - Schematic representation on the regulation of bone modelling by the osteocytes (OCY) via recruitment of osteoblasts (OB), osteoclasts (OCL) and lining cells (LC) (Burger and Klein-Nulend 1999).

The mechanism of bone remodelling has been thoroughly discussed. Consensus on the stimulus that drives this process has yet to be reached. It is commonly accepted that loading of the bone results in changes in the strain gradient of the tissue (Currey 1984; Carter et al. 1989; Carter et al. 1998; Skerry 2008). The straining of the cellular matrix leads to a change in instraosseous pressure, promoting flow of fluid in the lacuno-canalicular porosities in the extracellular matrix where osteocytes are embedded (Frost 1964; Turner et al. 1997). It has been advanced that mechanisms such as cell wall shear stress, primary cilia, focal adhesions or metabolite transportation (Fritton and Weinbaum 2009) could enable the mechano-sensation in osteocytes. Experimental evidence suggests that this strain-driven flow through the lacuno-canalicular network that surrounds the OCYs activates the mechano-sensing cells (Skerry 2008) by increasing their calcium concentration (Burger and Klein-Nulend 1999; Cowin 2001). Nonetheless, there are other hypotheses that flow-induced shear stress in the bone marrow (Coughlin and Niebur 2012) might play an important part the trabecular remodelling. Independently of the bone remodelling mechanism at the micro-level, bone modelling or remodelling can be described as being driven by changes in strain, at the macro-scale (Huiskes et al. 2000).

1.3 Why Study the Femur?

Advances in modern medicine have resulted in increased life expectancy. Certain biomechanical complications have become more concerning with the ageing demographics. Osteoarthritis is a degenerative joint disease that can lead to the need to replace hip and knee joints in order to improve patients' life quality. Hip and knee replacements have become increasingly frequent procedures in orthopaedics in the last decade due to advances in the prosthesis design and surgical methods, which improve the outcomes of these procedures. In the United States (US) 327,000 hip and 676,000 knee replacements were performed in 2009 (National Center for Health Statistics 2009) whereas in the United Kingdom (UK), 76,759 hip replacements were carried out according to the National England and Wales Joint Registry (National Joint Registry 2011), with a mortality rate of 0.6 % in the first 90 days after the surgery and large financial burdens to the National Healthcare System (NHS). The UK also saw 81,979 knee replacements performed in the same year, with 4.9% of revisions by year seven and a mortality rate of 0.4% in the first 90 days after the surgery (National Joint Registry 2011). Both procedures can result in reduction of mobility and frequency of everyday activities for some patients, as well as changes in their gait profiles (Morlock et al. 2001; D'Lima et al. 2006). In some cases, the bone loss occurring during a total hip replacement procedure provokes fracture of the acetabulum, resulting in pelvic discontinuity (Berry et al. 1999). Another progressive systemic skeletal condition is osteoporosis. This disease affects between 16% and 30% of Caucasian women and leads to a decrease of bone mass and deterioration of micro-architecture. This results in increased fragility and chances of fracture, particularly at the hip joint, vertebrae and wrist (Kanis 1994; Boutroy et al. 2011). 75 million people in the developed world are affected by this disease which leads to 2.3 million osteoporotic fractures annually (WHO 1994). The frequency of osteoporotic related fractures increases with the ageing of the population and with loss of bone quality resultant from the progression of the disease (WHO 1994). These fractures can also be caused by fatigue, trauma or induced inactivity. Fractures of the femoral neck have an extremely high mortality rate within one year (between 20% and 35%) (Goldacre et al. 2002).

The conditions discussed above cause significant burdens in countries' healthcare systems and efficient solutions are required in order to improve their treatment. The progression of such degenerative diseases can only be understood with an improved knowledge of bone's mechanical behaviour in healthy and affected subjects. For instance, osteoporosis is characterised by loss in bone mass and elastic properties (Homminga et al. 2003). Changes to the trabecular architecture in an attempt to maintain structural integrity along the predominant loading directions have also been observed (Singh et al. 1970). However, there is evidence that selected physical activities can increase bone mass density and decrease the risk of osteoporosis or reduce the rate of bone decay in affected patients (Jämsä et al. 2006), in particular in the femoral neck region (Blain et al. 2009). Consequently, a more thorough understanding and description of the bone's structural and material properties is required (Singh et al. 1970; Ford and Keaveny 1996; Homminga et al. 2003; Pulkkinen et al. 2004; Boutroy et al. 2011; Hambli et al. 2012).

Many different studies in Biomechanics have targeted the femur in an attempt to define its response to complex loading environments. The development of instrumented prosthesis has provided more valuable information about the hip and knee joints (Bergmann et al. 1993; D'Lima et al. 2006). Bergmann released HIP 98, a package that provides the hip joint contact forces and moments for different trials of daily living activities (such as walking at slow, normal and fast speeds, standing up, climbing and descending stairs) performed by 4 different patients (Bergmann et al. 2001; Bergmann et al. 2004). Other studies implemented similar techniques at the knee (D'Lima et al. 2006; D'Lima et al. 2008; Kutzner et al. 2010). Musculo-skeletal models of the lower limb have been developed in an attempt to predict joint contact forces and moments as well as muscle activations and forces for different activities, using static optimisation and inverse dynamics (Delp 1990; Heller et al. 2001; Heller et al. 2005). These models have provided valuable insight into the biomechanics of the lower limb and the mechanical environment bones are subjected to. Validated open source musculo-skeletal models provide an additional valuable source of input data for loading of FE models of bone (Modenese et al. 2011).

There have been numerous studies that have measured bone's elastic material properties (Young's and shear moduli, Poisson's ratios) in the femur. These measurements have been undertaken either directly, via compression studies (Carter and Hayes 1977), nano-identation (Rho et al. 1997; Rho et al. 1999; Turner et al. 1999) and three-point bending (Cuppone et al. 2004), among others; or indirectly, using techniques such as acoustical imaging (Ashman et al. 1984), stereological analysis (Cowin and Mehrabadi 1989), micro-scale FE (μFE) analysis (van Rietbergen et al. 1995), fabric measurement (Kabel et al. 1999) or acoustic microscopy (Turner et al. 1999). Since the results of these studies depend on the technique used, sample size and shape, testing environment and bone and site of origin (Goulet et al. 1994; Morgan et al. 2003; Austman et al. 2008), consensus has yet to be reached on which values measured are the most representative of bone's material properties.

Elastic moduli can also be extracted from the Hounsfield Units (HU) produced by Computer Tomography (CT) (Keyak et al. 1990; Wirtz et al. 2000; Peng et al. 2006; Shim et al. 2007; Tabor and Rokita 2007; Baca et al. 2008; Hellmich et al. 2008), by determining a mathematical relationship between the HU values and the known density of different phantoms (Ciarelli et al. 2000). In order to assign a physiological distribution of material properties to FE models of bone, many regression equations have been fitted between the elastic properties measured and the CT-derived densities (Carter and Hayes 1977; Hodgskinson and Currey 1992; Dalstra et al. 1993; Kopperdahl and Keaveny 1998; Morgan et al. 2003). These were compiled in a review paper by Helgason (Helgason et al. 2008) (Figure 1.11). This same review suggests that it is difficult to accurately determine the relationship between bone density and its elastic properties (Helgason et al. 2008). A high resolution FE study also established that there is no single, universal relationship between Young's modulus and density across anatomical sites (Morgan et al. 2003). Furthermore, the HU values extracted from CT imaging are a scalar quantity resulting from a combination of local porosity and tissue mineralisation and, therefore, are not able to predict the directionally dependent elastic properties of bone required to model its structural directionality at a continuum level (Rohrbach et al. 2012).

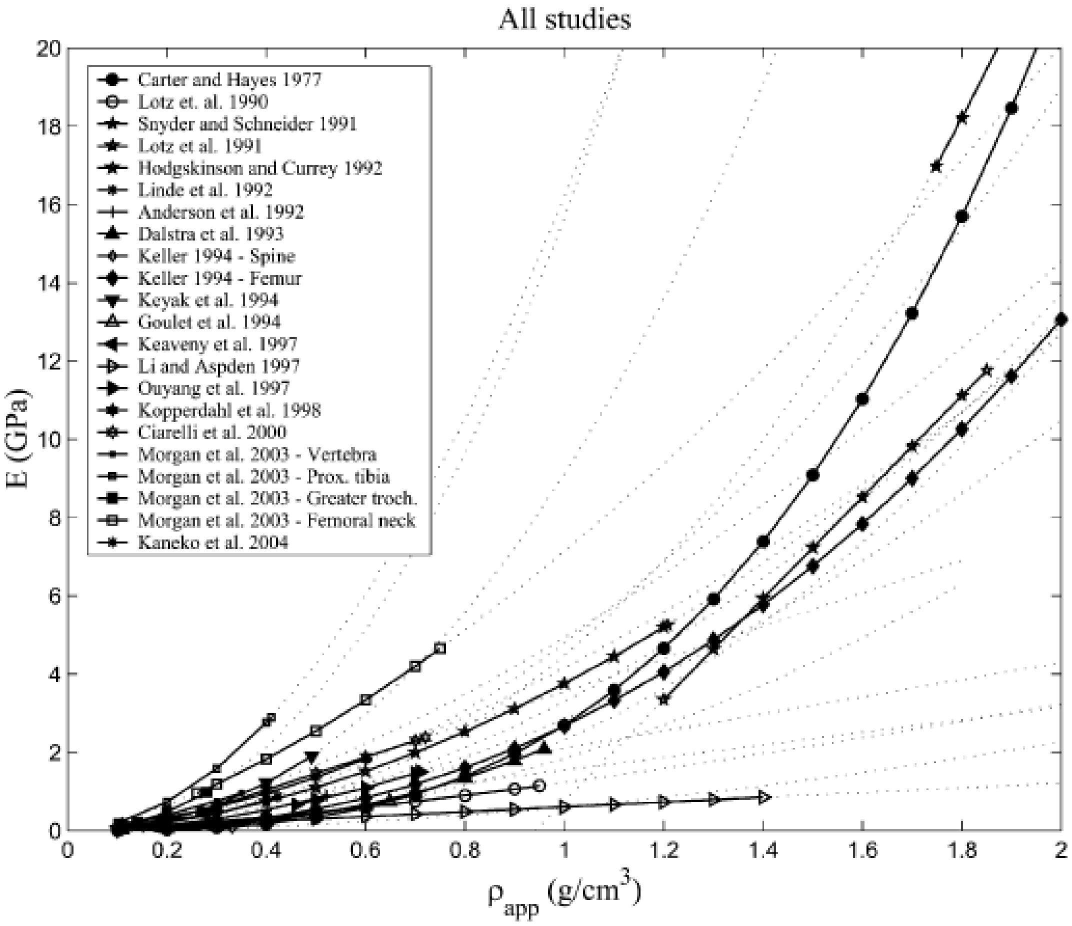

Figure 1.11 - Relationships between Young's modulus (E) and density (ρ_{app}) in Helgason's review (Helgason et al. 2008).

Optimisation algorithms incorporated with FE can be used to predict the material properties and structural orientation of the femur (Huiskes et al. 1987; Carter et al. 1989; Beaupré et al. 1990a; Beaupré et al. 1990b; Fernandes et al. 1999; Miller et al. 2002; Rossi and Wendling-Mansuy 2007; Coelho et al. 2009; Tsubota et al. 2009), as an alternative to using empirical relationships or the measurements by the techniques mentioned above. The predicted material properties and the structural directionality can be validated by comparison with CT and micro CT (μCT) images, respectively (Dalstra et al. 1995; Dalstra and Huiskes 1995; Miller et al. 2002; Coelho et al. 2009; Tsubota et al. 2009; Phillips 2012). The next Section describes in detail these algorithms and their limitations.

1.4 Bone Adaptation Algorithms and their Limitations

The femur's geometry and internal architecture have been thoroughly studied. The available data measured by instrumented prosthesis and predicted by musculo-skeletal models, and the many studies and measurements of its material properties, make this bone an ideal subject in the attempt to understand the process of bone adaptation.

Bone adaptation algorithms have been incorporated into FE studies in many areas of Biomechanics that focus on bone's morphogenesis (Beaupré et al. 1990a; Beaupré et al. 1990b) and reaction to altered loading conditions such as the behaviour of bone-implant interfaces (Huiskes et al. 1987; Scannell and Prendergast 2009), fracture initiation (Juszczyk et al. 2011; Hambli et al. 2012) and healing (Shefelbine et al. 2005). Huiskes merged bone remodelling theory with finite element analysis (FEA) and applied it to prosthetic design analyses. Bone was assumed to be a self-optimising linearly elastic continuum that responded to changes in strain energy density (SED) (Huiskes et al. 1987). FEA was used to find the SED distribution resultant from perturbations on the bone (such as mechanical loading or the existence of a resorption cavity) and to induce the changes in bone architecture that these perturbations promoted (Figure 1.12) (Huiskes et al. 1987).

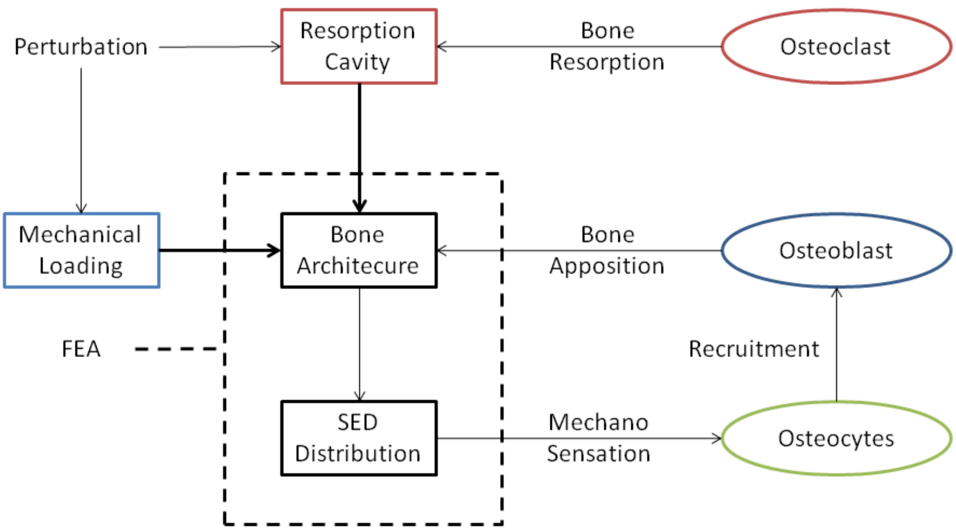

Figure 1.12 - Diagram representing the bone remodelling process proposed by Huiskes.

Beaupré implemented Frost's *Mechanostat* proposal that changes in local strain stimulus were the driving force for bone remodelling, with bone's natural state to be around a stimulus region where no bone is either lost or gained (Beaupré et al. 1990a; Beaupré et al. 1990b). Jang observed that bone remodelling using SED as stimulus can be mathematically matched with results derived from topology optimisation, showing that bone has, indeed, the self-optimising behaviour hypothesised (Jang et al. 2009). Beaupré's study also introduced the concept that strain should be considered as a stimulus when information about directionality of the structure is required. SED cannot provide such information because it is a scalar (Beaupré et al. 1990a; Beaupré et al. 1990b). Another two-dimensional FE study looked at the convergence problem of using SED as stimulus and concluded that strains were better suited as the driving stimuli of the adaptation process in FE (Weinans et al. 1992). McNamara concluded that a combination of both strain-adaptive and damage-adaptive remodelling seemed to give the best predictions at a micro-structural level (McNamara and Prendergast 2007). These studies indicate that strain-driven adaptation can provide the directional information required to model the femur's structure.

The process of bone adaptation may be modelled by considering bone's structure directionality to be influenced by multiple load cases. Carter superimposed different load cases and observed that trabecular orientations do not necessarily correspond to the principal stress directions of any individual load case (Carter et al. 1989). Bagge assigned anisotropic material properties and time-dependent loading to a 3D model of the proximal femur resulting in a stiffening of the bone in the vertical direction, in agreement with experimental measurements (Bagge 2000). Miller introduced an adaptation algorithm for an orthotropic material model of bone's fabric with directionality of its structures achieved by rotation of the orthotropic elastic constants in order to match the direction of the principal stresses resulting from multiple load cases (Miller et al. 2002).

Different optimisation criteria have been used throughout literature at different scales with multiple applications. Fernandes modelled bone's micro-structural parameters using homogenisation theory applied to cellular solids (Fernandes et al. 1999; Coelho et al. 2009). The heterogeneity of density distribution and structural anisotropy were predicted by using a homogenisation method that assumed bone to be composed of perforated micro-structures that attempt to maximise their own structural stiffness (Rossi and Wendling-Mansuy 2007). Damage-repair theory was implemented in another study on the proximal femur before and after total hip replacement, with bone starting as an isotropic material with uniform density distribution and whose porosity changed according to the minimum mechanical dissipation principle (Doblaré and Garcia 2001). Design space optimisation criteria implemented with a μFE model has also been applied in order to predict trabecular architecture with much shorter computational times for both 2D (Jang and Kim 2010) and 3D (Boyle and Kim 2011) models of the proximal femur. Trabecular fracture healing was studied by incorporating μFE with fuzzy logic, with tissue differentiation predicted from analysis of the local hydrostatic and octahedral strains (Shefelbine et al. 2005). Tsubota developed both large-scale pixel and voxel FE models with changes to the trabecular structure resulting from surface remodelling driven by the non-uniformity of local stress (Tsubota et al. 2002; Tsubota et al. 2009). Phillips introduced a 3D meso-scale structural model of the femur with cortical and trabecular bone represented by shell and bar elements respectively, providing a good description of the structures present with reduced computational times (Phillips 2012). Hambli incorporated FE at macroscopic level replaced with trained neural networks for meso-scale computations (Hambli 2011).

Different bone adaptation algorithms and optimisation techniques have been introduced and discussed. However, despite the application of such techniques in different fields in Biomechanics, there are still limitations and overlooked assumptions that are discussed in more detail below.

In order to simplify the analysis and reduce computational times, bone is usually assumed to have isotropic material properties when assumed a continuum (Huiskes et al. 1987; Beaupré et al. 1990a; Beaupré et al. 1990b; Dalstra et al. 1995; Dalstra and Huiskes 1995). This assumption does not explain the directionality of bone's internal structures observed (von Meyer 1867; Wolff 1892; Garden 1961; Singh et al. 1970; Skedros and Baucom 2007) and predicted (Doblaré and Garcia 2001; Miller et al. 2002). Anisotropic and orthotropic material properties for bone have been measured experimentally using techniques such as nano-identation (Rho et al. 1997; Rho et al. 1999; Turner et al. 1999), acoustical imaging (Ashman et al. 1984), acoustic microscopy (Turner et al. 1999) and three-point bending (Cuppone et al. 2004). FE macro and micro analysis have also confirmed the anisotropic nature of bone (van Rietbergen et al. 1995; van Rietbergen et al. 1998; Turner et al. 1999). Other studies have verified these findings by looking at the fabric properties of bone (Cowin and Mehrabadi 1989; Kabel et al. 1999; Yang et al. 1999). The orthotropic assumption does not explain the non-orthogonal intersection of the trabecular groups (von Meyer 1867; Pidaparti and Turner 1997; Skedros and Baucom 2007); however, it has been shown that orthotropic symmetry is a close approximation to bone's anisotropy in comparison with isotropy (Ashman et al. 1984). In addition, it has been demonstrated that the optimal orientation for orthotropic trabeculae under a unique load case corresponds to their alignment with the principal stress directions (Pedersen 1989). Furthermore, the isotropic assumption is insufficient in predicting the directionality and orientation of bone's microstructure, important factors when understanding bone's performance and mechanical behaviour (Nazarian et al. 2007).

This need for a more physiologically accurate representation of bone where its directional material properties are considered and correctly assigned has led to the development of different modelling methods. Taylor extracted the femur's orthotropic elastic constants by matching the FE model with experimentally measured natural frequencies under vibration (Taylor et al. 2002). Wirtz accounted for directionality by manually determining the principal stiffness directions in the femur after measuring its trabecular structures and Haversian systems orientations (Wirtz et al. 2003). Both these models produced a comparable qualitative match with the trabecular structures observed in CT scans. However, they are highly time-consuming and subject-specific.

The requirement of a more general approach to the prediction of directionally dependent material properties has led to the application of bone remodelling or optimisation algorithms (Weinans et al. 1992). Doblaré used damage-repair theory and demonstrated that trabeculae align themselves with the principal directions, although a non-realistic load scenario was considered and muscle and ligaments were not included in the model (Doblaré and Garcia 2001). Tsubota applied large scale pixel and voxel remodelling producing anisotropic structures resembling the ones found *in vivo*, although with extremely demanding computational power and only considering the proximal femur region (Tsubota et al. 2002; Tsubota et al. 2009).

Although the studies mentioned in this Section can describe the macro-scale heterogeneity of bone, they do not allow for accurate and physiological local directionality and material properties prediction, both key factors when modelling bone-implant interface or fracture mechanics, as well as providing a better understanding of bone's mechanical behaviour. Topology optimisation algorithms where bone maximises its own structural stiffness resulting in a good density distribution prediction have been proposed in different studies (Fernandes et al. 1999; Rossi and Wendling-Mansuy 2007; Coelho et al. 2009), but these either considered simplified load cases, 2D geometries or non-physiological boundary conditions applied at the distal part of the model. Miller succeeded in modelling trabecular stiffness orientation and bone density by applying a 2D bone remodelling algorithm to the proximal femur, considering orthotropic material properties that adapted their directional stiffness values in order to achieve a target strain plateau (Miller et al. 2002).

In an attempt to produce a physiological continuum model of bone's material properties distribution and structure orientation arising from the daily living activities the femur is subjected to, an iterative strain-driven orthotropic 3D bone adaptation algorithm with material orientations aligned with the principal stresses was developed (Chapter 2).

1.5 Finite Element Modelling Considerations

As discussed in the previous Section, bone adaptation algorithms have been incorporated into FE studies in Biomechanics in order to study bone's mechanical properties, behaviour and adaptation to changing mechanical environments. Independently of the criteria picked, these optimisation algorithms are all based on the same premise: that bone's natural state is its most functionally efficient state, where strength, stiffness, weight and global energy are optimised. In order to model such behaviour, the driving stimulus of the adaptation process needs to be accurately evaluated and, most importantly, physiologically meaningful.

This thesis describes a novel method of achieving a physiological orthotropic heterogeneous model of the femur by incorporating a bone adaptation algorithm within an FE model of the femur spanning the hip and knee joints. Independently of the driving stimulus for the optimisation process picked, the FE model of the bone being studied is required to be as close to the physiological state as possible. This involves careful selection of its constitutive representation, mesh, geometry and the loading and boundary conditions applied (Erdemir et al. 2012).

CT produces stacks of 2D images which can be segmented to generate accurate geometric topologies of bone (Shim et al. 2007). This geometry-based modelling technique has been validated against experimental studies (Lengsfeld et al. 1996; Lengsfeld et al. 1998). The Muscle Standardised Femur (Figure 1.13) has been made publically available in order to provide the scientific community with a generic anatomy of the human femur and its muscle insertions (Viceconti et al. 2003a; Viceconti et al. 2003b). Together with providing a geometry of the synthetic Sawbones femur (Gardner et al. 2010) to be used in computational research, this uniformisation allows for easier replication of previously undertaken research as well as cross-validation of numerical studies (Viceconti et al. 2003a). FE meshes with different densities, element types and sizes can be generated depending on the objective of the study (Ramos and Simões 2006).

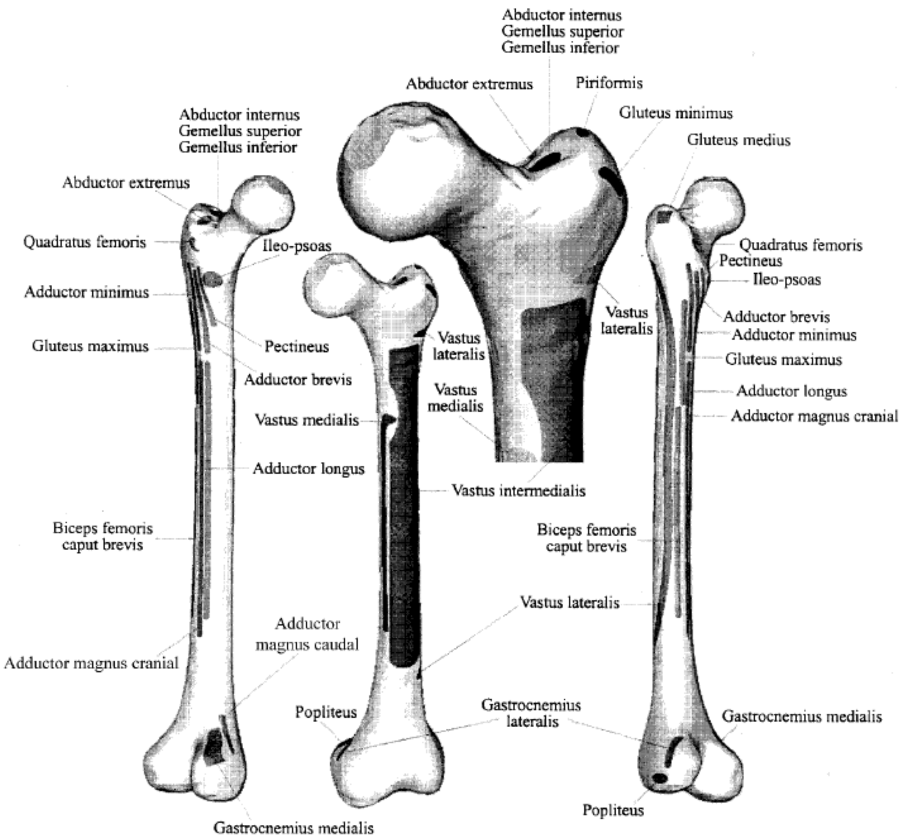

Figure 1.13 - The Muscle Standardised Femur with the muscle insertions highlighted (Viceconti et al. 2003a).

In order to model the behaviour of bone remodelling with FE models, the driving stimulus of the adaptation process needs to be physiologically meaningful (Bitsakos et al. 2005). Therefore, the FE model of the bone being studied is required to be as close to the physiological state as possible. This involves careful selection of the loading and boundary conditions applied. The improvements on the mechanical environment applied to FE models of the femur throughout literature are represented in Figure 1.14.

Taylor produced a 3D model of the femur fixed at the distal end and with the hip joint reaction force (HJR) and the iliopsoas, adductors and ilio-tibial tract forces included as point loads (Taylor et al. 1996) (Figure 1.14 (a)). Lengsfeld showed that the femoral strain pattern and principal stress orientation is sensitive to the resultant joint contact forces and muscle forces at the hip joint, particularly within the coronal plane, due to the effect of the ilio-tibial tract (Lengsfeld et al. 1996). Duda further demonstrated the importance of considering a fully balanced loading configuration in FE modelling of the femur in order to reproduce a physiological strain distribution (Duda et al. 1998), rather than other loading configurations. This was corroborated in other studies (Wirtz et al. 2003), with femoral head boundary conditions also shown to influence the strain distribution within the same bone (Simões et al. 2000).

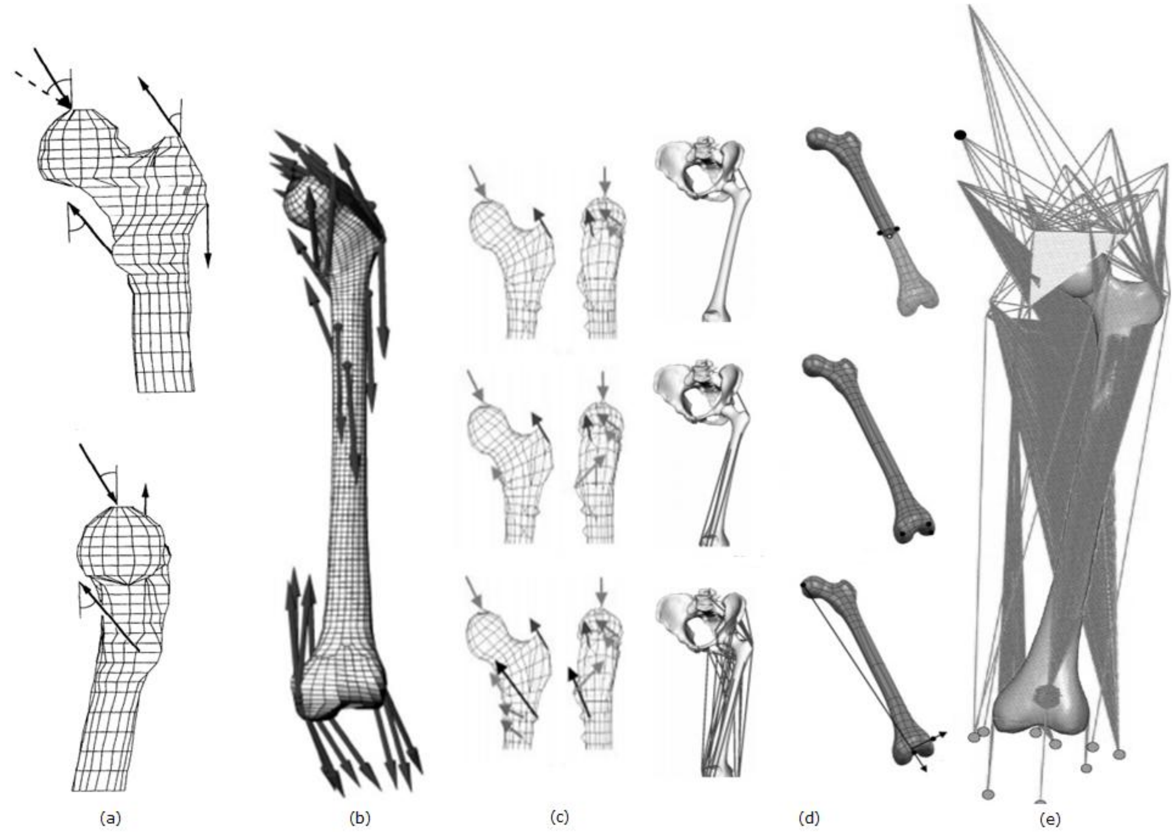

Figure 1.14 - Examples of the inclusion of joint and muscle forces and boundary conditions in FE modelling of the femur. Left to right: (Taylor et al. 1996; Kleemann et al. 2003; Bitsakos et al. 2005; Speirs et al. 2007; Phillips 2009).

Kleeman included all muscle forces as point loads, the HJR applied at the centre of the femoral head and the knee reaction force (KRF) equally distributed by the two condyles with compressive and tensile strains below 4000 μstrain (Kleemann et al. 2003) (Figure 1.14 (b)). Polgar found that when muscles with large attachment areas were modelled as point loads, the stress and strain distributions were affected not only in the surroundings of the load application point but also in the internal surface of the cortical shaft. Although computationally efficient, this simplification can result in unrealistic displacement and strain values, and the results from elements in the FE model surrounding the point of load application should not be considered (Polgar et al. 2003).

After testing FE models including an increasing number of muscles, Bitsakos also concluded that the loading configuration is a key factor in achieving a physiologically relevant remodelling signal (Bitsakos et al. 2005) (Figure 1.14 (c)). Speirs showed the effect of different boundary constraints in the deflection, strain patterns magnitudes and reaction forces of the intact femur. The inclusion of non-physiological constraints, such as fully constraining a node in each condyle or the cortical shaft, led to large reaction forces, altered strain patterns in the cortex and non-physiological deflections of the femur. It was also concluded that only the application of 'physiologically-based' boundary conditions and different combinations of muscle loading could result in physiological deflections and strain distributions (Speirs et al. 2007) (Figure 1.14, (d)). However, the deflection at the proximal femur was not assessed in the same manner as the study it was compared to Taylor's work (Taylor et al. 1996). Furthermore, the boundary conditions applied Speirs' study implied that the femur's movement was still constrained at many degrees of freedom and, therefore, cannot be said to be fully representative of its physiological state.

By explicitly including the ligaments and muscles spanning between the hip and knee joints, Phillips demonstrated that no absolute values above 3000 µstrain were found in the femur undergoing single leg stance (Phillips 2009) (Figure 1.14, (e)). In a study of the pelvis, this free boundary condition method was shown to produce more physiological and reduced stresses than those available in literature, since the bone in question is not constrained in non-physiological ways (Phillips et al. 2007).

Table 1.1 summarises the conclusions obtained in the studies discussed in this Section. It can be observed that boundary and loading conditions play an important role in the modelling of the stress and strain distributions in the femur, with an increase in their physiological significance associated with more physiological results. Nevertheless, all these studies assumed bone to be isotropic, ignoring the directionality of its material properties at a continuum level. Directionally specific material properties have been highlighted as being of key importance in FE modelling of the femur (Wirtz et al. 2000; Wirtz et al. 2003).

Table 1.1 - Different FE studies' loading and boundary conditions and their conclusions.

Study	Model	Conclusion
Taylor et al. 1996	Proximal femur model fixed at distal end. HJR, iliopsoas, adductors and iliotibial band as point loads.	Need to careful consider applied forces and their consequences on resulting stress and strain distributions.
Lengsfeld et al. 1996	Proximal femur and femoral shaft fixed at distal end. HJR, gluteus medias and iliotibial tract as point loads.	Femoral strain pattern and principal stress orientations sensitive to the resultant contact and muscle forces, particularly within sagittal plane.
Duda et al. 1998	Proximal femur and femoral shaft with three nodes fixed at distal end. HJR and thigh muscles included as point loads.	Important to consider a fully balanced loading configuration in order to reproduce a physiological strain distribution.
Kleeman et al. 2003	Complete femur with HJR and all muscle forces applied as point loads. KRF equally distributed by the two condyles.	Physiological principal compressive and tensile strains in the postero-medial aspect of the femur at different stages of the gait cycle.
Polgar et al. 2003	Complete femur with HJR and KRF applied as point loads. Muscle forces uniformly distributed along attachment area vs. point loads applied at centroid of attachment area.	The simplification of modelling muscle forces as point loads can result in large unrealistic displacement and strain values.
Bitsakos et al. 2005	Proximal femur fixed at distal end. Increasing number of muscles modelled as point loads.	Best remodelling signal obtained when more muscles are included in the model.
Speirs et al. 2007	Complete femur with varying boundary and loading conditions (physiological and non-physiological)	Application of physiologically based boundary conditions could result in physiological strain distributions.
Phillips 2009	Free boundary condition modelling of the complete femur. Muscles and ligaments included explicitly.	More physiological and reduced stress concentrations. No absolute strain values above 3000 μstrain.

The importance of each parameter defined in FE modelling in achieving physiologically significant driving stimuli for bone adaptation was discussed in this Section. Geometry and material properties, including directionally specific properties, play an important part in the results achieved computationally. A fully balanced loading configuration with all muscles and ligaments forces applied along their attachment sites, as well as boundary conditions that do not constrain the femur in non-physiological ways, also need to be considered.

1.6 Aims and Objectives

The previous Sections introduced functional adaptation in the femur, the attempts that have been made to model and understand this process and the reasons why this understanding might be important.

This thesis proposes a novel 3D iterative orthotropic strain-driven bone adaptation algorithm. A fully balanced loading configuration, with all muscles and ligaments forces applied over their attachment sites and physiologically relevant boundary conditions that do not constrain the femur in non-physiological ways is also considered. As result, a physiological orthotropic heterogeneous continuum model of the femur functionally adapted to the daily living activities was produced.

Listed in the subsections below are the aims and objectives of the development and release of such a heterogeneous orthotropic model of the femur.

1.6.1 Algorithm

Creation and development of a 3D iterative orthotropic strain-adaptive algorithm (Chapter 2):

- Material properties (Young's and Shear moduli, Poisson's ratio) updated proportionally to the local strain stimuli.
- Material orientations aligned with the local principal stresses.
- Definition of a convergence criterion.

Modification of the algorithm to allow modelling of multiple load cases (Chapter 4):

- Definition of a selection criterion for the driving frame of the local adaptation process, (when multiple load cases are considered).
- Development of a Shear Moduli adaptation algorithm.

1.6.2 Model

Creation of a working 3D FE model of the whole femur geometry with application of physiological loading and boundary conditions (Chapter 3):

- Physiological modelling at the hip, tibio-femoral and patello-femoral joints interfaces.
- Explicit inclusion and modelling of all muscles and ligaments spanning the femur
- Definition of physiological boundary conditions that represent the mechanical behaviour of the bone in question.

Modification of the model to allow modelling of multiple load cases (Chapter 4):

- Inclusion of multiple frames for different daily activities.

1.6.3 Validation

Validation of the FE model (Chapter 5):

- Analysis of the stress and strain distributions obtained.

- Comparison of calculated forces with published joint reaction forces, muscle forces and electromyography (EMG) data.

Validation of the bone adaptation algorithm (Chapter 6):

- Qualitative comparison of resultant material properties distribution and directionality with published literature (density distribution, elastic properties and micro-architecture).
- Quantitative comparison of resultant material properties distribution and directionality with CT and μCT data from a human femur specimen (density distribution, elastic properties, micro-architecture, fabric properties).

1.6.4 Multiple Load Case Investigation

Investigation of the influence of different instances of multiple load cases in the adaptation process and their topological influence in the trabecular shear modulus (Chapter 7).

Chapter 2

The Bone Adaptation Algorithm

Chapter 1 highlighted the need for the development of a 3D iterative orthotropic algorithm, with material properties updated proportionally to the local strain stimuli and material orientations aligned with the local principal stresses.

This Chapter outlines the development and implementation of the algorithm and its development from 2D to 3D, and analyses the results of its application to increasingly physiological models undergoing a single load case. Section 2.1 introduces the features to be included in the algorithm. Section 2.2 describes in detail each of the steps implemented in the adaptation algorithm, from building the initial template finite element (FE) model to the update of material properties and directionality, and the criteria for convergence of the optimisation process. A flow-chart and a brief overview of the pseudo-code adopted in the algorithm’s implementation can be read in Section 2.3. Section 2.4 describes the development of the algorithm and its application to simplified 2D and 3D models of the proximal femur, with increasing physiological relevance. Finally, Section 2.5 summarises the results produced by both models during the algorithm development and draws some conclusions on the method created.

2.1 Introduction

Adaptation algorithms have been incorporated in many studies in order to understand the biomechanics of the skeletal system and bone's behaviour in response to altered mechanical environments (Huiskes et al. 1987; Beaupré et al. 1990a; Beaupré et al. 1990b; Fernandes et al. 1999; Cowin 2001; Miller et al. 2002; Shefelbine et al. 2005; Tsubota et al. 2009).

These optimisation algorithms are based on Frost's *Mechanostat* hypothesis that bone's natural state is around a remodelling plateau where no bone is lost or gained (Frost 1987). Different driving-stimuli to this adaptation process have been put forward, such as strain energy density (SED) or strain. Despite providing an indication on the gradient of deformation, SED is a scalar function and, therefore, does not hold any directional information (Beaupré et al. 1990a; Beaupré et al. 1990b).

As seen in Chapter 1, directionality is of key importance when attempting to model bone's anisotropy accurately. The isotropic symmetry assumption allows for the representation of the overall density distribution (Huiskes et al. 1987). However, anisotropic and orthotropic material properties for bone have been measured experimentally (Ashman et al. 1984) and shown to be key when attempting to physiologically model bone's behaviour (Baca et al. 2008).

Miller succeeded in modelling trabecular architecture by applying a 2D bone remodelling algorithm to the proximal femur, considering orthotropic material properties that adapted their directional stiffness values in order to achieve a target strain plateau. The orthotropic material properties were assumed to follow *Wolff's Law*, and align themselves with the local principal stress directions (Miller et al. 2002). This approach produced material orientations in agreement with the trabecular structures observed in the proximal femur (Singh et al. 1970).

A novel iterative strain-driven orthotropic 3D bone adaptation algorithm was developed in an attempt to produce a physiological continuum model of the complete femur. The algorithm was tested for 2D models before its application in 3D studies.

In the orthotropic bone remodelling algorithm implemented in this study, trabecular directions of each element were determined by the principal stress directions and, simultaneously, local material properties were updated according to the associated local strain stimulus. The process was run iteratively until a predefined convergence criteria was met.

To implement the above, three software packages were used:

- MATLAB (v. R2007b, MathWorks, USA) – Software for pre- and post-processing of output data from Abaqus, updating material properties and orientations, checking for convergence and analysing results.

- Abaqus/CAE (v. 6.10, SIMULIA, Dassault Systèmes S.A., France) – Finite element solver with modules for mesh generation and editing, running jobs and displaying results.

- Python (v.2.5, Python software Foundation) – High level programming language used for data extraction from Abaqus output databases (ODBs) and alternated running of MATLAB and Abaqus during the iterative process.

2.2 The Algorithm

Following the initial template creation as an Abaqus input file, the bone adaptation process was implemented. After applying the intended loading and boundary conditions to the FE model of the bone in question, and extracting the resulting strain and stress distributions, the optimisation process took place. The adaptation algorithm matches each element's orthotropic material orientation with the local principal stress directions, and updates the directional material properties proportionally to the local associated strain stimulus. The material definition for each element is then updated and the algorithm checks if convergence is reached. If a converged solution is achieved, the optimisation process is considered complete; otherwise, the iterative process is repeated.

This Section describes in detail how the template model was built (Section 2.2.1) and each of the three main steps of the iterative strain-adaptive orthotropic algorithm for bone adaptation was implemented: updating the material orientations and properties (Sections 2.2.2 and Section 2.2.3) and checking for convergence (Section 2.2.4).

2.2.1 Building the Initial Model

The initial model geometry was extracted from the Standardised Femur (Viceconti et al. 2003a; Viceconti et al. 2003b). Loading and boundary conditions were then defined in Abaqus and material properties were assigned using a combination of MATLAB and Python software packages.

<u>Extract model geometry</u>

<u>Apply Loading and Boundary Conditions (Abaqus) for each instance modelled</u>

- Import 2D or 3D mesh of the femur
- Rotate and translate mesh, if 3D model used
- Add physiological structures
  - Define muscles and ligaments
  - Define hip, patello-femoral and tibio-femoral joints
- Add boundary conditions
  - Define boundary condition node and element sets
  - Define boundary condition type
- Add loading
  - Define loading application points
  - Apply loading profile

<u>Assign orthotropic material properties to each element</u>

- Define initial local material orientation directions matching global orientation
- Define initial material properties (Young's moduli, shear moduli, Poisson's ratios)

<u>Create initial (template) input file</u>

2.2.2 Material Directionality Update

In order to correctly model the structural properties of the femur at a continuum level, the orthotropic material properties were considered to be aligned with the local principal stress directions, following *Wolff's Law* (Wolff 1892; Koch 1917; Hayes and Snyder 1981; Cowin 1986). Notwithstanding different published observations that trabecular groups do not necessarily cross at orthogonal angles (Jansen 1920; Garden 1961; Pidaparti and Turner 1997; Skedros and Baucom 2007), it has been shown that this is the optimal orientation for an orthotropic material undergoing a single load case where shear stresses are not influential (Pedersen 1989). This approach was used in a two-dimensional study of orthotropic bone (Miller et al. 2002) and produced material orientations at a continuum level showing good agreement with the trabecular structures in the proximal femur (Singh et al. 1970).

At each iteration, the loading and boundary conditions were applied to the bone geometry and the model's strain and stress distributions extracted. This was achieved by accessing the Output Databases (ODBs) produced by the Abaqus FE solver via a custom Python script. Stress and strain distributions were written into separate text files and imported into MATLAB which post-processed the data.

The stress tensor, $\boldsymbol{\sigma}_{ij}$, and the strain tensor, $\boldsymbol{\varepsilon}_{ij}$, were extracted for each element of the mesh after each iteration. An eigen analysis of the stress tensor produced the local principal stress orientations, σ_{pv}, and corresponding principal stress values, σ_p (Equation 2.1).

$$eig\left(\boldsymbol{\sigma}_{ij}\right) = [\sigma_{pv} \quad \sigma_{pv}] = \begin{bmatrix} \sigma_{pv1}^{min} & \sigma_{pv1}^{med} & \sigma_{pv1}^{max} \\ \sigma_{pv2}^{min} & \sigma_{pv2}^{med} & \sigma_{pv2}^{max} \\ \sigma_{pv3}^{min} & \sigma_{pv3}^{med} & \sigma_{pv3}^{max} \end{bmatrix} \begin{bmatrix} \sigma_p^{min} & 0 & 0 \\ 0 & \sigma_p^{med} & 0 \\ 0 & 0 & \sigma_p^{max} \end{bmatrix} \qquad (2.1)$$

The element orthotropic material orientations were rotated to match with the calculated local principal stress orientations (Figure 2.1), following Miller's work for two dimensions (Miller et al. 2002; Geraldes and Phillips 2010).

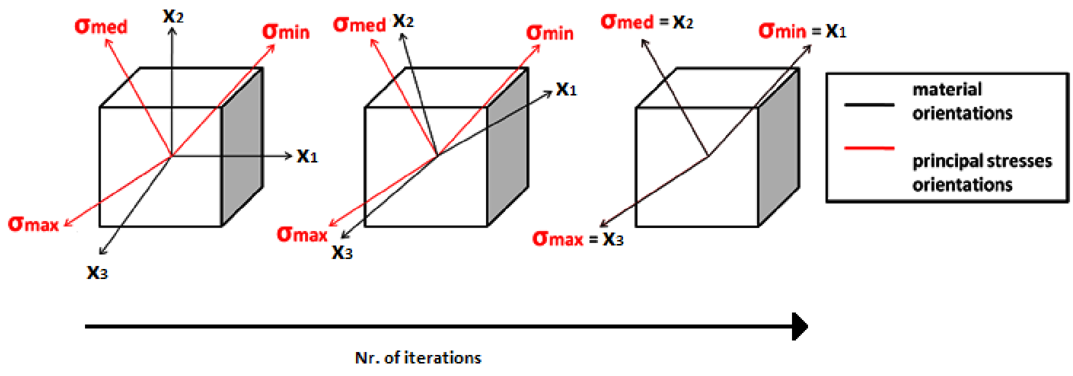

Figure 2.1 - Diagram representing the rotation of material properties (x_1, $x_{2,}$ x_3) in order to match the principal stresses orientations (σ_{min}, $\sigma_{med,}$ σ_{max}) along the iterative process.

The three orthotropic axes x_1, x_2, x_3 were associated with the minimum, σ_{pv}^{min}, medium, σ_{pv}^{med}, and maximum, σ_{pv}^{max}, principal stress vectors, respectively. This order was selected so that the first orthotropic axis was associated with the minimum principal strains resulting from compression, the predominant mode of loading of the femur (Taylor et al. 1996; Sverdlova and Witzel 2010).

The principal stresses were the target for rotation of the material orientations in agreement with Pedersen's proven optimum orientations for orthotropic materials (Pedersen 1989) and following Wolff's observations (Wolff 1892) which have been successfully implemented in 2D studies (Miller et al. 2002). The use of principal stress directions instead of principal strains avoids the problems caused by the 'flik-flaking' in principal strain orientations.

2.2.3 Material Properties Update

The algorithm performs the adaptation process by implementing the *Mechanostat* theory (Frost 1964; Frost 1987; Frost 2003) that bone optimises its structure in order to keep the strains resulting from its mechanical usage within upper and lower thresholds. This can be achieved for a continuum by increasing or decreasing the appropriate material property proportionally to the local driving stimulus for the remodelling process, driving strains towards a remodelling plateau where no bone is lost or gained (Huiskes et al. 1987; Beaupré et al. 1990a; Beaupré et al. 1990b; Miller et al. 2002).

At the end of each iteration, each element's material axes were rotated to match the local principal stress vectors. The local strain stimulus associated with the transformed orthotropic material axes, $\boldsymbol{\varepsilon}^*_{ij}$, was calculated for each element according to Equation 2.2 (Miller et al. 2002; Geraldes and Phillips 2010) (Equation 2.2).

$$\boldsymbol{\varepsilon}^*_{ij} = {\sigma_{pv}}^T \boldsymbol{\varepsilon}_{ij}\, \sigma_v \tag{2.2}$$

The orthotropic material orientations were found to converge quickly after 4 iterations and align with the principal stress directions, indicating that determination of the associated local strain stimulus, $\boldsymbol{\varepsilon}^*_{ij}$, might not be necessary after the initial stages of the iterative process.

Figure 2.2 introduces an explanative diagram for the key steps taken in defining the target directions to update the directionality of each element. The calculation of the strain values associated with the target orthotropic orientations is also depicted.

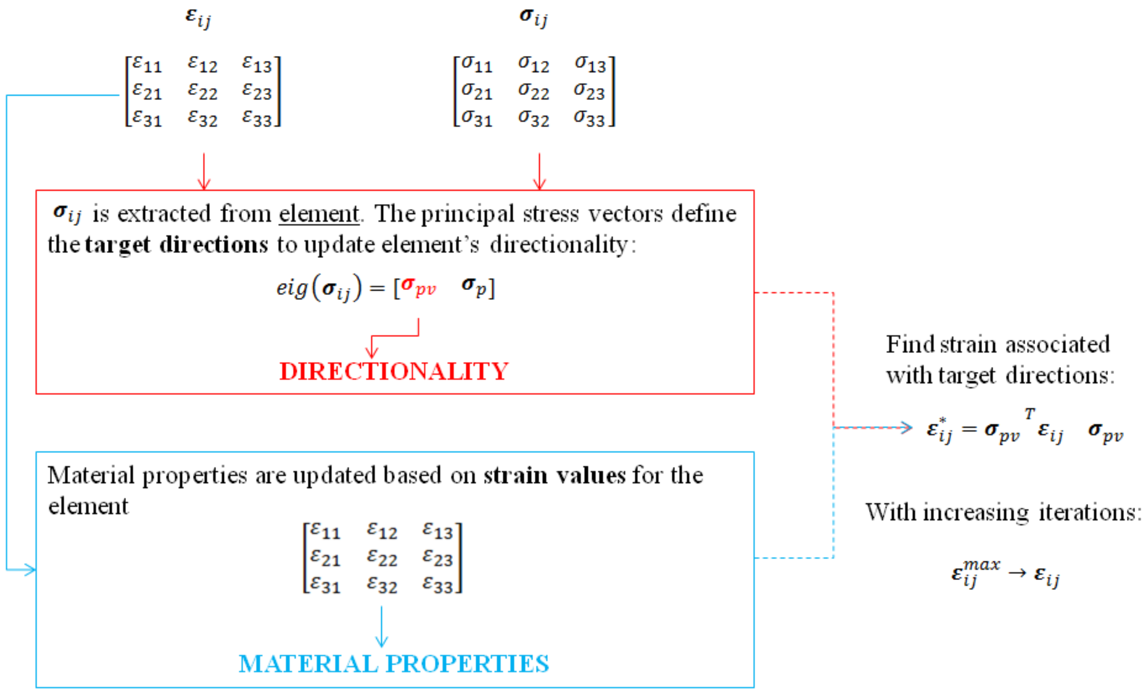

Figure 2.2 - Diagram highlighting the key steps in updating the orthotropic directionality and material properties.

2.2.3.1 Young's Moduli

After the strain stimuli associated with the new material orientations, $\boldsymbol{\varepsilon}^*_{ij}$, were calculated for each element, the material properties were updated in order to bring the local strains within the remodelling plateau, as proposed by Frost's *Mechanostat* theory (Frost 2003).

The remodelling plateau corresponds to a region around a target normal strain value, ε_{nt}. This region was proposed by Frost to be between 1000 and 1500 µstrain (Frost 1964; Frost 1987) and confirmed in experimental studies of bone remodelling in different animals (Lanyon and Rubin 1984; Rubin and Lanyon 1985). Target values within the range suggested by Frost have been used throughout literature with results showing good agreement with the material properties observed in the femur (Beaupré et al. 1990a; Beaupré et al. 1990b; Cowin 2001, Miller et al. 2002).

The proposed algorithm used a normal target strain, ε_{nt}, of 1250 µstrain, with a margin of μ_0 = ±20% in order to form the remodelling plateau ($\varepsilon_{nt} - \mu_0$ = 1000 µstrain to $\varepsilon_{nt} + \mu_0$ = 1500 µstrain), following Frost's proposed limits (Frost 1987). Each orthotropic Young's modulus, $E_i{}^{it}$, of the elements outside the remodelling plateau was updated proportionally to the absolute value of their associated strains (Equation 2.3). ${E_i}^{it}$ was initially limited between 10 MPa and 10 GPa (Miller et al. 2002; Geraldes and Phillips 2010). it corresponds to the current iterative step.

$$
{E_i}^{it} = {E_i}^{it-1} \frac{\varepsilon_{ii}{}^{*}}{\varepsilon_{nt}} \tag{2.3}
$$

Figure 2.3 shows a diagram representing the tri-linear profile of the adaptation process. When local strains are within the remodelling plateau no changes are imposed in the orthotropic material properties. However, when the local strains fall outside this plateau, the elements' Young's moduli are reduced or increased accordingly, driving the strains into the plateau region.

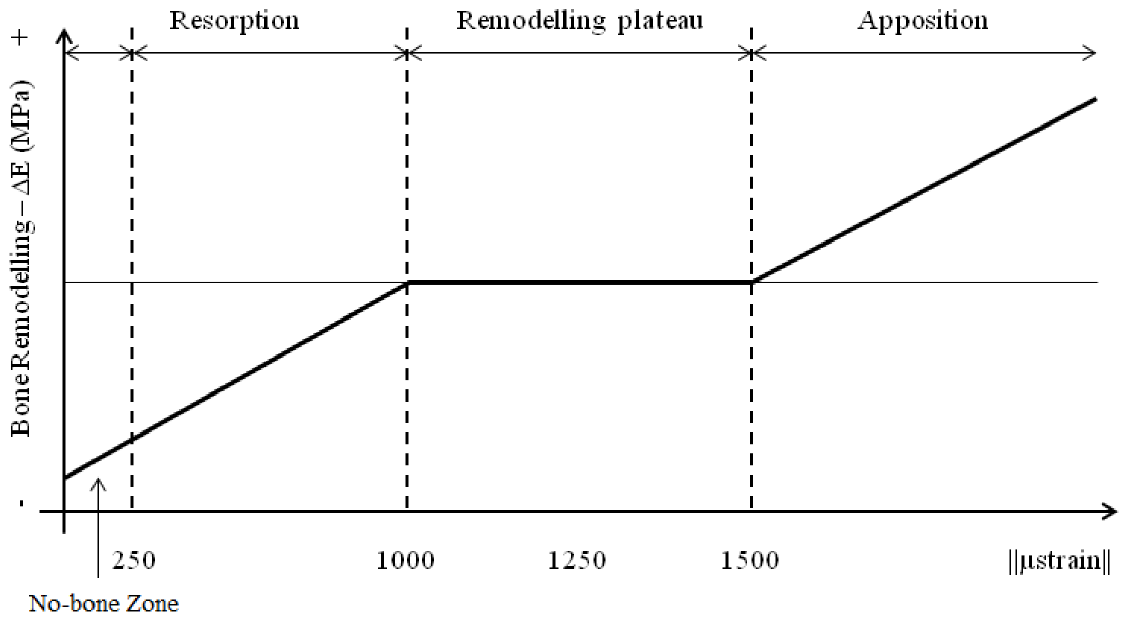

Figure 2.3 - Diagram highlighting the remodelling plateau, bone resorption, bone apposition and no-bone zone regions of the bone remodelling process.

${E_i}^{it}$, were based on the normal associated principal strains (${\varepsilon_{11}}^{*}$, ${\varepsilon_{22}}^{*}$ and ${\varepsilon_{33}}^{*}$). After a small number of iterations, the principal strain directions aligned themselves with the principal stress directions, and hence the orthotropic orientations. Therefore the normal strains (ε_{11}, ε_{22} and ε_{33}) could be used for computational efficiency.

2.2.3.2 Shear Moduli and Poisson's Ratios

Shear moduli were taken to be a fraction of the mean orthotropic Young's moduli according to experimental measurements (Ford and Keaveny 1996) (Equation 2.4).

$$G_{ij}{}^{it} = \frac{E_i{}^{it} + E_j{}^{it}}{4} \tag{2.4}$$

Since shear stresses are not influential in bone undergoing a single load case (Pedersen 1989; Skedros and Baucom 2007), an adaptation algorithm for shear moduli was not considered.

Because of the independent variation of the elastic modulus, $E_i{}^{it}$, (Section 2.2.3.1), some elements' Poisson's ratios, $\nu_{ji}{}^{it}$, were altered (Equation 2.5). This was implemented so that the compliance matrix remained always positive definite, in order to satisfy the thermodynamic restrictions on the elastic constants of bone (Lempriére 1968; Cowin and van Buskirk 1986; Miller et al. 2002; Geraldes and Phillips 2010).

$$\frac{E_i{}^{it}}{E_j{}^{it}} > \left(\nu_{ij}{}^{it}\right)^2 \tag{2.5}$$

Poisson's ratios for each element, $\nu_{ij}{}^{it}$, were assumed to less than or equal to 0.3 (Rho et al. 1997; Rho et al. 1999; Turner et al. 1999; Miller et al. 2002). In addition, if $E_j{}^{it}$ was greater than $E_i{}^{it}$, $\nu_{ji}{}^{it}$ was adjusted such that the equality constraint shown in Equation 2.6 was maintained.

$$\frac{\nu_{ji}{}^{it}}{E_j{}^{it}} = \frac{\nu_{ij}{}^{it}}{E_i{}^{it}} \tag{2.6}$$

The restrictions on the elastic constants implemented in Equation 2.5 and 2.6 add an upper limit constraint ($E_j{}^{it} = \frac{E_i{}^{it}}{0.3^2} = 11.1E_i{}^{it}$) to the adaptation process for the orthotropic Young's moduli.

2.2.4 Convergence

A ‘no-bone zone’ of elements was defined in order to exclude from the simulation elements of extremely low elastic stiffness and undergoing negligible strains. This no-bone zone was excluded from the adaptation process as it corresponded to areas where virtually no bone can be found and therefore, convergence problems could arise in a continuum representation.

An element was considered to be in the ‘no-bone zone’ when the maximum absolute normal strain values, ${\varepsilon_{ii}}^*$, were less than 250 μstrain and, simultaneously, its directional Young’s moduli, ${E_i}^n$, were all below 100 MPa.

The adaptation process was considered to achieve a state of convergence when the average change in Young’s moduli of all elements outside the no-bone zone was less than 2%.

2.3 Implementation

This Section outlines the pseudo-code that was used to implement the proposed algorithm undergoing a single load case. Abaqus, Python and MATLAB were the software packages used in this process. A flow chart representing the sequence of the different stages and processes of the algorithm discussed in Section 2.2 can be seen in Figure 2.4.

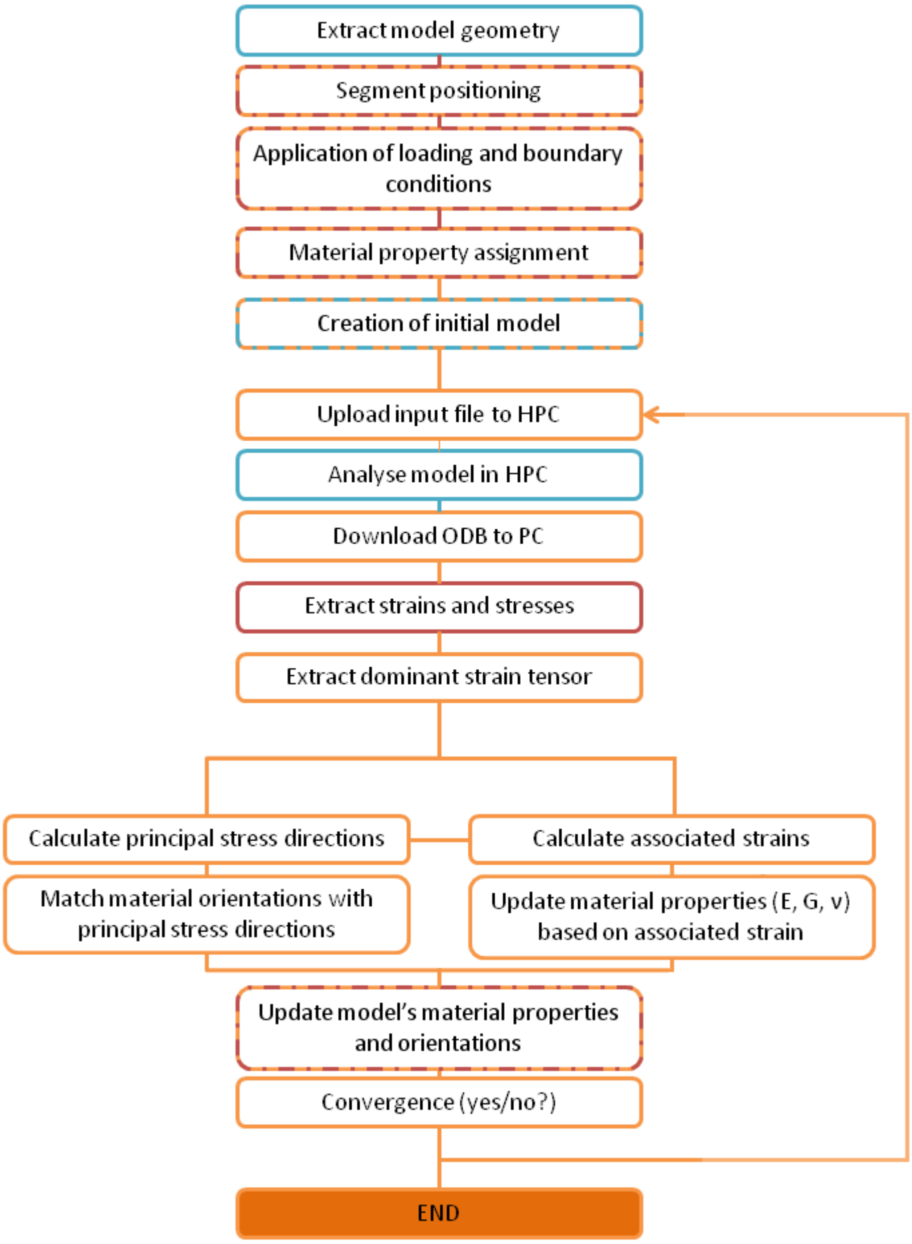

Figure 2.4 - Algorithm flow chart. Orange boxes refer to steps performed in MATLAB, red boxes to steps implemented in Python and blue boxes when Abaqus modules were implemented. Dashed boxes represent steps where more than one software package was involved. HPC indicates the stages when High Performance Computer was used.

A MATLAB script alternated between Abaqus and Python scripts in an iterative fashion (Figure 2.4). Abaqus processes the input file and analyses the model using an implicit solver. A Python script extracts the resulting strains and stresses for the centroid of each element into separate text files. MATLAB then updates the material properties and orientations in order to match the strain stimulus and principal stresses respectively, writes an updated input file and checks for convergence. The process repeats itself until a state of convergence is reached. The pseudo-code for the implemented tasks is described below.

Start Iteration (while loop)

Extract model strains and stresses (Section 2.1)

- Upload input file to Imperial College's High Performance Computer (HPC) node
- Solve Models in HPC using Abaqus
- Download Abaqus ODB to desktop PC
- Extract strain and stresses for each element using Python scripts developed for that purpose.

Extract previous material properties and orientations from input file

- Import input file into MATLAB
- Read and store material properties and orientations for each element

Update directionality (for each element) (Section 2.2.2)

- Find principal stress directions (eigen analysis)
- Rotate material orientations to match local principal stress directions

Update material properties (for each element) (Section 2.2.3)

- Calculate associated stimuli with the new local material orientations
- Update Young's moduli proportionally to the associated strain stimuli for each element
- Update shear moduli as an average of the calculated Young's moduli
- Limit values for Poisson's ratios and Young's moduli if required

Create new input file with updated material properties and orientations

Add 1 to the iteration number

Check for convergence (Section 2.2.4)

- Exclude elements in the no-bone zone
- Check convergence criteria
  - If convergence is not achieved, return to beginning of iteration loop
  - If convergence is achieved, finish iterative process

2.4 Development of the Algorithm

The algorithm was developed using simplified square and cube models with sets of loads and boundary conditions that would produce known material distributions and orientations (see Figure A. 1 and Figure A. 2 in the Appendix) and then verified by applying it to simplified 2D and 3D proximal femur models and analysing the resulting stiffness and directionality distributions. This Section will focus on the implementation and results of the 2D and 3D proximal femur models. All elements had the same initial material properties ($E_1 = E_2 = E_3 = 10$ MPa; $G_{12} = G_{13} = G_{23} = 5$ MPa) and material orientations (aligned with the global coordinate system). Both Young's and shear moduli were restricted between 10 MPa and 10 GPa. Both models had sets of loads extracted from literature applied as point loads. The resulting material properties distribution and orientations were qualitatively compared to bone structures documented in literature.

2.4.1 2D Proximal Femur

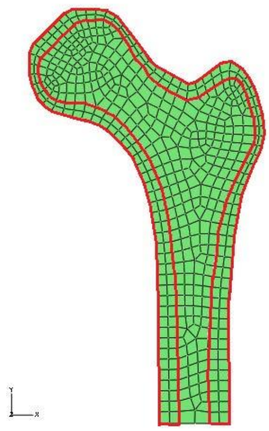

Figure 2.5 - The 2D proximal femur mesh. The elements representing cortical bone are highlighted in red.

The geometry used for the 2D proximal femur model was extracted from Sawbones (60 year old Caucasian male, 183cm, and 91kg) (Gardner et al. 2010) (Figure 2.5). A coronal plane slice was used as geometry, since the architecture of trabecular bone has been thoroughly described in this plane (Singh et al. 1970; Miller et al. 2002; Skedros and Baucom 2007). The 2D proximal femur model was assigned a section depth of 1 mm. Cortical bone was represented as a two-element layer with stiff material properties ($E = 18$ GPa, $\nu = 0.3$) (highlighted in red, Figure 2.5), since only adaptation in trabecular bone was considered initially. Both cortical and trabecular bone were modelled with 4-noded bilinear plane stress elements (CPS4), 366 for the trabecular region and 208 for the cortical region. Six nodes at the bottom of the proximal region of the femoral head were fixed against translation. The hip joint reaction force (HRF) was applied through a load applicator tied to the contact surface of the femur, simulating the interaction between the acetabulum and the femur. The load applicator was modelled with solid triangular elements with the same material properties as cortical bone (E = 18 GPa, ν = 0.3), with the exception of the layer in contact with the femoral head, which simulates the softer material of cartilage (E = 10MPa) (Figure 2.6, in red).

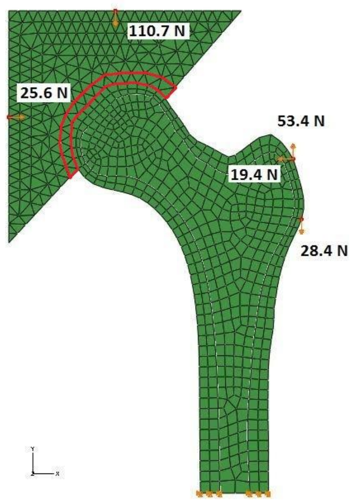

Figure 2.6 - The loads and boundary conditions applied to the 2D proximal femur model. The elements representing the cartilage layer are highlighted in red.

The magnitude and orientation of the HRF, the ilio-tibial tract (IIT) and the abductor group (AbG) forces were scaled from values presented in another study for the peak forces that arise during walking (10% of the gait cycle). (Duda et al. 1998) and applied as point loads. These loads needed to be scaled as they were being applied in a plane with finite width instead of a three-dimensional femur. This was implemented in order to avoid over-estimation of the results. The acetabulum was assumed to be in contact with half of a sphere (representing the femoral head) with a radius, r, of 22 mm and a section depth, d, of 1 mm in the 2D proximal femur model (Figure 2.7, left), with the contact force distributed as a sinusoidal function out of plane (Figure 2.7, right).

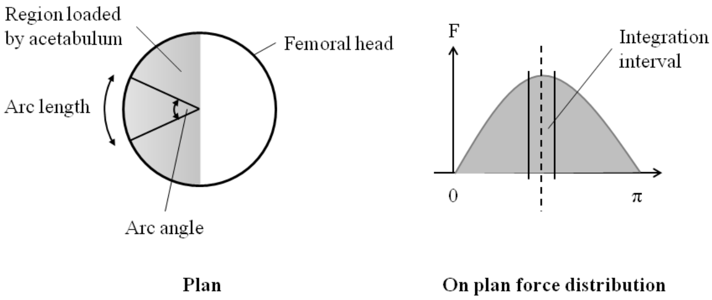

Figure 2.7 - Scaling of the hip contact force for a planar model.

The contact region of the slice with the acetabulum was considered to be an arc length, a_l, on a plan with the same length as the model width, 1 mm. This arc length corresponds to an arc angle, a_θ, of 0.04545 rads, according to Equation 2.6.

$$a_\theta = {}^{a_l}\!/_{r} \tag{2.7}$$

The scaling factor for the forces being applied, ϕ, was considered to be the integral of the sinusoidal distribution over the distance on the plane along which the HRF was integrated. The lower and upper integration limits were $\frac{\pi}{2} + \frac{a_\theta}{2}$ and $\frac{\pi}{2} + \frac{a_\theta}{2}$, respectively, resulting in a scaling factor of $\frac{1}{22}$ (Equation 2.7). The scaled values used to model the HRF, IIT and AbG are reported in Table 2.1 and can be seen in Figure 2.6.

$$\varphi = \int_{\frac{\pi}{2}-\frac{a_\theta}{2}}^{\frac{\pi}{2}+\frac{a_\theta}{2}} \sin x \, dx = \cos\left(\frac{\pi}{2} - \frac{a_\theta}{2}\right) - \cos\left(\frac{\pi}{2} + \frac{a_\theta}{2}\right) = \frac{1}{22} \tag{2.8}$$

Table 2.1 - Summary of the scaled components for the HRF, AbG and the ITT forces.

Force (F) Duda et. al 1998	**Magnitude (ϕ x F)**	**Angle with vertical axis**	**Vertical component**	**Horizontal component**
HRF = 2500 N	113.6	13˚	110.7 N	25.6 N
AbG = 1250 N	56.8 N	20˚	53.4 N	19.4 N
ITT = 625 N	28.4 N	0˚	28.4 N	N/A

In this model, a converged state was reached after 31 iterations. E_1 ranged from 10 MPa to 2962 MPa for trabecular bone, with the maximum values being obtained in elements in the lower part of the femoral head and the medial side of the epiphysis. E_2 varied between 10 MPa and 3933 MPa and the elements where higher values were found could be seen in the region below the greater trochanter (Figure 2.8). The representative Young's modulus, E_{rep}, was taken according to Equation 2.8.

$$E_{res} = \sqrt{{E_1}^2 + {E_2}^2} \tag{2.9}$$

As expected, the distribution of E_{rep} (Figure 2.9, left) reached its maximum values in the region below the greater trochanter and the lower part of the femoral head, with values ranging from 10 MPa to 4050 MPa. The lower values can be observed in the intra-medullary canal, the Ward's triangle and the greater trochanter, as expected. The anisotropy of Young's moduli, A, was taken as the ratio between E_1 and E_2 (Equation 2.9). The anisotropy distribution can be seen on the right hand-side of Figure 2.9, highlighting the local differences between elastic moduli. Both E_1 and E_2 can be over-estimated if the isotropic assumption is used. It is clear that the predominant stiffness modulus is E_1, associated with compression. The thermodynamic restriction imposed on the ratio of the elastic moduli created an upper limit constraint in their adaptation process of 11.

$$A = \frac{E_1}{E_2} \tag{2.10}$$

These results match with the compressive and tensile groups observed by Singh (Singh et al. 1970) in the proximal femur and modelled by Miller (Miller et al. 2002). Having been satisfied with the performance of the algorithm in a 2D model subjected to a single load case, the adaptation process was extended to a 3D model of the proximal femur.

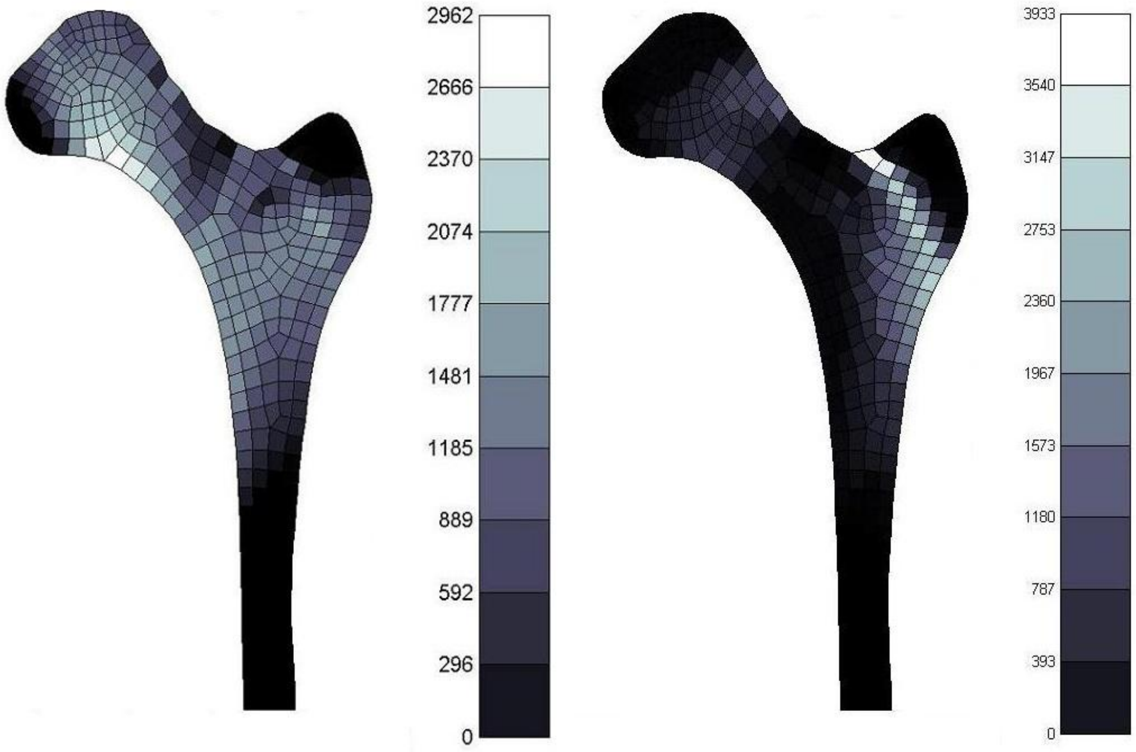

Figure 2.8 - Stiffness distribution (MPa) and orientations for the trabecular bone of the converged femur model (E_1, on the left, and E_2, on the right). The cortical layer was removed in order to improve visualisation of the results.

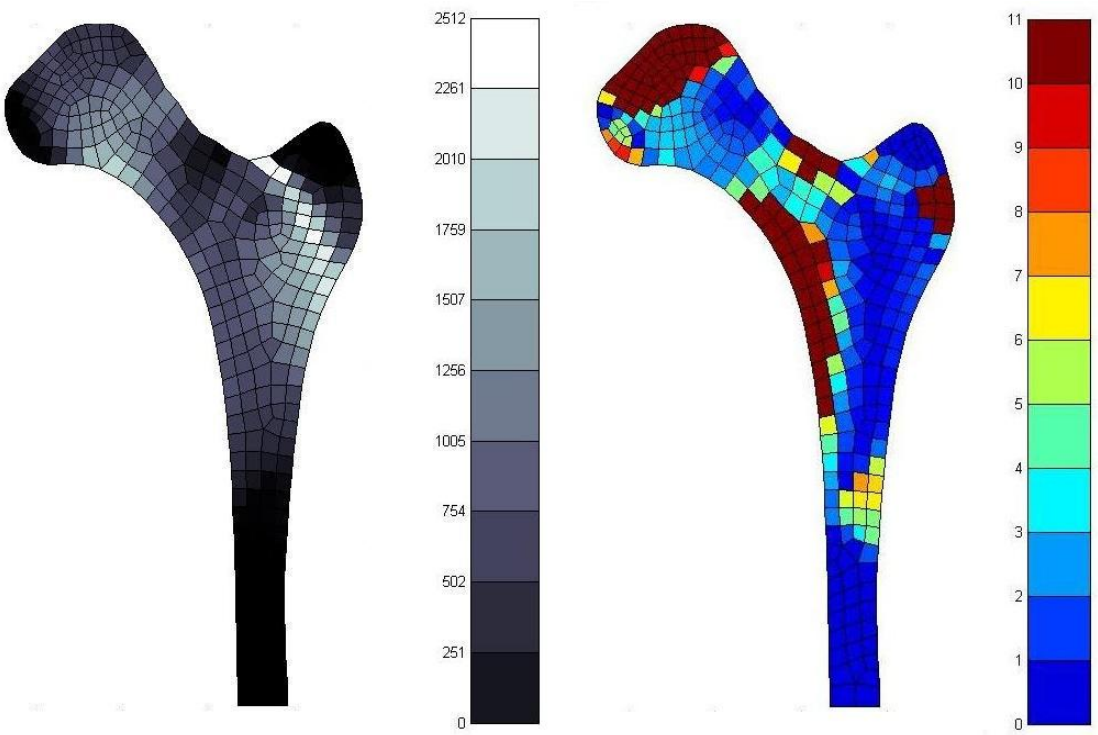

Figure 2.9 - Representative (left) and anisotropy distribution (right) for the elastic moduli of the trabecular bone. The cortical layer was removed in order to improve visualisation of the results.

2.4.2 3D Proximal Femur

The geometry used for the femoral head was extracted from Sawbones (60 year old Caucasian male, 183cm, and 91kg) (Gardner et al. 2010). The femoral head was composed of 36384 linear tetrahedral C3D4 elements. All the elements were considered to have the same initial material properties since, in simpler models, it was verified that the proposed adaptation algorithm could be applied to both trabecular and cortical bone. Sensitivity studies were also performed to confirm that the starting configuration of material properties did not affect the end results. The nodes along the distal end of the femoral head were fixed against translation. The forces applied were modelled as point loads (Duda et al. 1998). Un-scaled values for the forces used in the 2D femoral head model were used (Table 2.1). Table 2.2 shows the x, y and z components for each of the forces applied. A representation of the x, y and z components of the forces applied and the boundary conditions implemented in the model can be seen in Figure 2.10.

Table 2.2 - Summary of the forces applied to the 3D femoral head model.

Force (N)	X-axis component (N)	Y-axis component (N)	Z-axis component (N)
HRF = 2500	536.4	361.8	2414.8
AbG = 1250	427.5	0	1174.6
ITT = 625	0	0	625.0

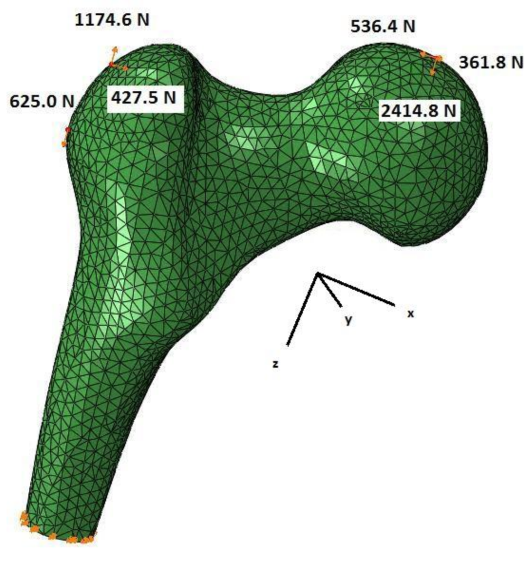

Figure 2.10 - The 3D proximal femur model.

Figure 2.11 shows Young's moduli orientations for E_1 associated with the minimum principal strains (left, black), E_2 associated with the medium principal strains (middle, blue) and E_3 associated with the maximum principal strains (right, red). These are shown in a coronal section of the femoral head, as this plane is where the principal and secondary compressive and tensile groups have been documented (Singh et al. 1970). E_1 associated orientations fan out the medial diaphysis side towards the greater trochanter and point towards the articular surface of the femoral head with the acetabulum. Both primary and secondary compressive groups can be observed. On the other hand, E_3 associated orientations (right, red) describe an arch through the femoral neck and epiphysis, connecting the lateral with the medial diaphysis and the greater trochanter. The primary and secondary compressive and tensile groups observed by Singh, as well as the greater trochanter group, arise. Below the contact region with the acetabulum and the Ward's triangle, E_3 directions rotate into the posterior-anterior plane, as a result of the direction the HRF is applied. This suggests that the trabecular architecture describes a helical shaped arch, in agreement with Garden's observations (Garden 1961). These results also match with the directionality observed in literature (Singh 1970) and obtained with similar algorithms in 2D (Miller et al. 2002).

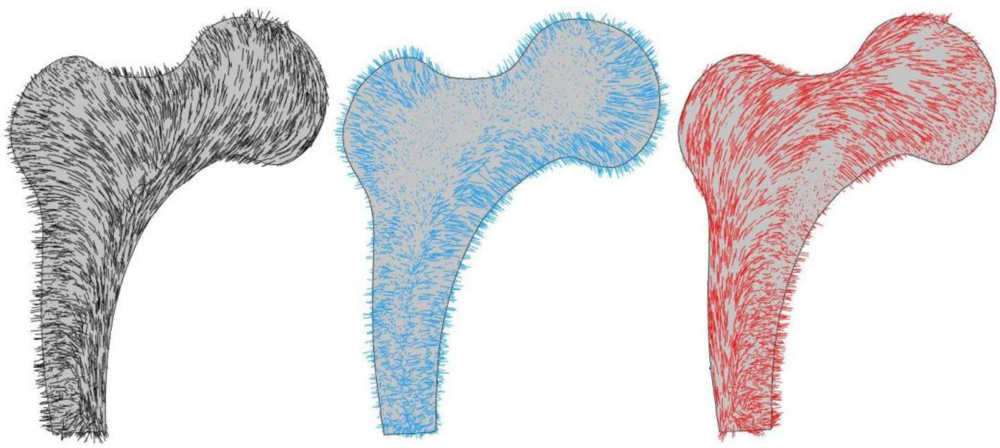

Figure 2.11 - Coronal plane representation of the orientations for E_1 (black), E_2 (blue) and E_3 (red).

E_1, E_2 and E_3 vary from 10 MPa to 10 GPa, whereas their representative equivalent varies between 17 MPa and 17.321 GPa. (Figure 2.12 to Figure 2.15). The coronal sections were extracted as 5 mm slices of the 3D proximal femur model along the coronal plane. The coronal slice representation of the E_1 distribution for the 3D femur model (Figure 2.12) shows the presence of the principal compressive group arching from the medial shaft of the femur upwards towards the upper portion of the femoral head as a dense high stiffness value zone. This corresponds to the high density trabecular arrangement expected. The secondary compressive group can also be seen as a less dense, more disperse region of high stiffness values, arching from the medial shaft towards the greater trochanter region, resulting from the thin loosely spaced trabeculae that form this group. The appearance of the femoral shaft as elements of high stiffness along the surface of the distal end of the model, and the intra-medullary canal as low stiffness elements in the centre of this region are also predicted.

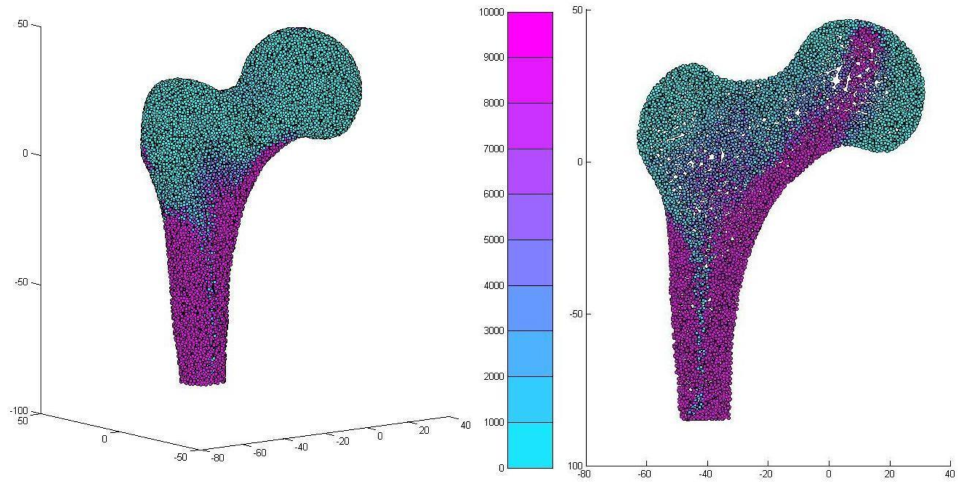

Figure 2.12 - E_1's distribution (in MPa) in 3D (left) and in the coronal plane (right).

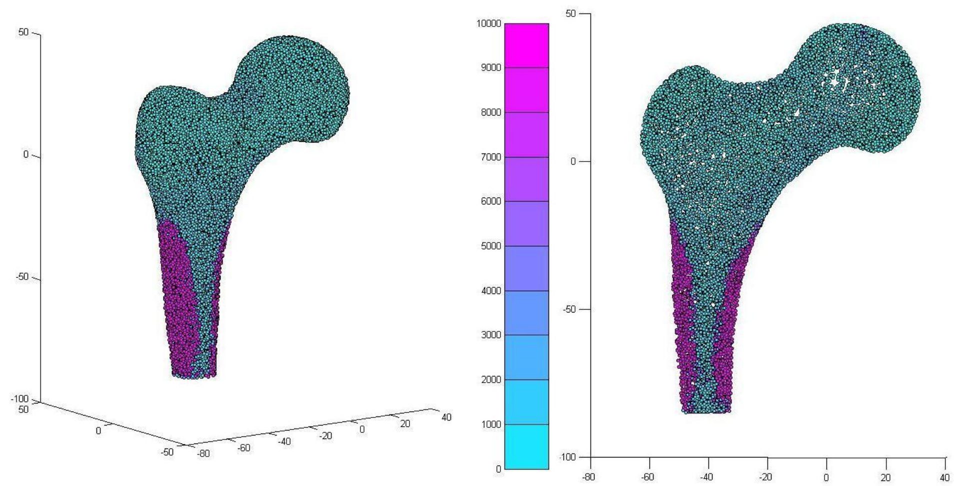

Figure 2.13 - E_2's distribution (in MPa) in 3D (left) and in the coronal plane (right).

The coronal cut for the 3D distribution of E_2 in the 3D femur model (Figure 2.13) shows the presence of the femoral shaft along the surface of the distal end of the model, and the intra-medullary canal as low stiffness distribution of elements in the centre of this region.

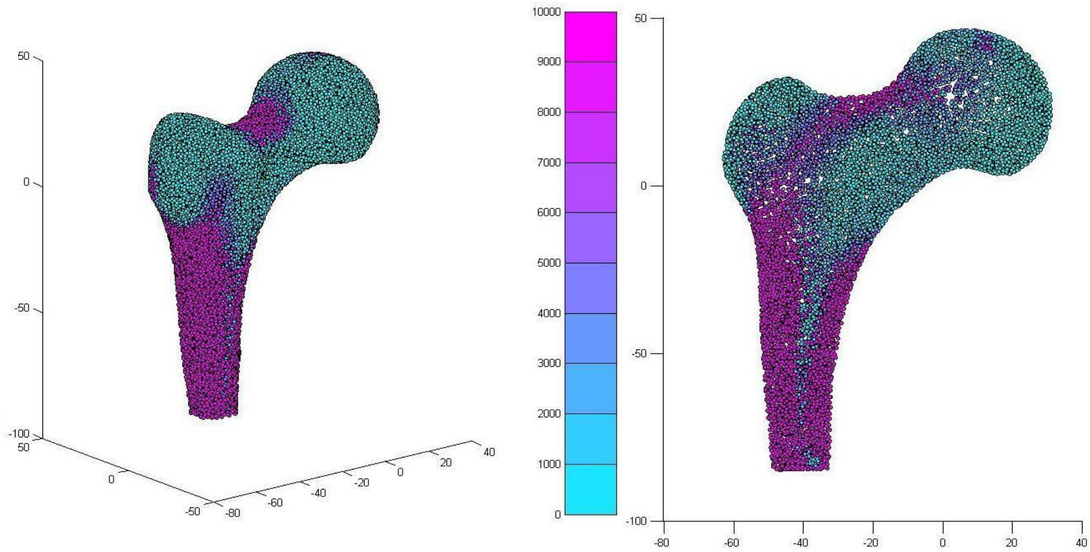

Figure 2.14 - E_3's distribution (in MPa) in 3D (left) and in the coronal plane (right).

The E_3 distribution for the 3D femur model (Figure 2.14), represented as a coronal section, shows the presence of the principal tensile group arching from the lateral shaft of the femur across the femoral neck towards the femoral head as a dense high stiffness value zone. This matches the expected high density trabecular arrangement. The secondary tensile group can also be seen as a less dense, more disperse region of high stiffness values starting right below the principal tensile group, arching from the lateral shaft across the mid-line of the femur, resulting from the thin groups of trabeculae that form this group. Along the greater trochanter, a region with elements of medium stiffness values matching the arrangement of thin trabeculae forming the greater trochanter group arises. In addition, the concentration of elements of high stiffness along the surface of the distal end of the model corresponding to the cortical femoral shaft is predicted. The intra-medullary canal composed by low stiffness elements in the centre of this region can also be observed.

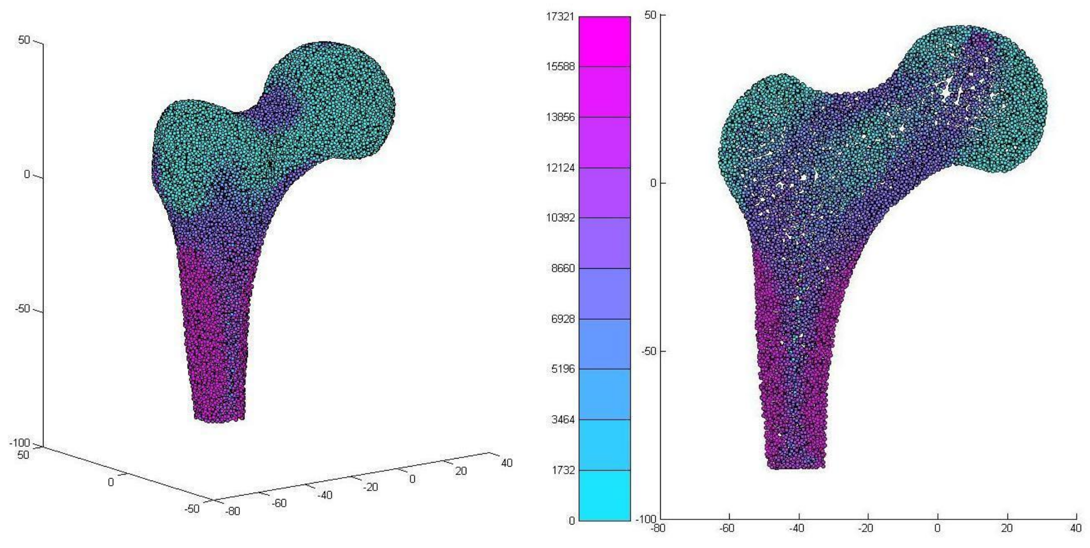

Figure 2.15 - Representative Young’s modulus distribution (in MPa) in 3D (left) and in the coronal plane (right).

The representative Young's modulus, E_{rep}, was calculated according to Equation 2.10.

$$E_{rep} = \sqrt{{E_1}^2 + {E_2}^2 + {E_3}^2} \qquad (2.11)$$

As expected, the distribution for E_{rep} (Figure 2.15) corresponds to a superposition of the compressive and tensile groups observed for the previous plots. Principal and secondary compressive and tensile groups are clearly present with a less evident greater trochanter also shown. The femoral shaft has elements with stiffness values similar to cortical bone, and the intra-medullary canal resemble the expected structure. Finally, a region with minimum stiffness values corresponding to the Ward’s triangle is also observed. This coronal representation shows good correlation and resemblance with the observed trabecular distribution in the proximal femur (Singh et al. 1970). The values for E_{rep} seem to reach its maximum in the region of the femoral shaft, hinting that the upper boundary for the limits applied in the material properties update needs to be revised.

2.5 Discussion and Concluding Remarks

By applying a single physiological load case (Duda et al. 1998), this algorithm was expected to reproduce the 2D and 3D trabecular architecture documented in literature (Wolff 1892; Singh et al. 1970) that arises as a response to the compressive loading of the acetabulum on the femoral head. The maximum values for the absolute elastic modulus were found in the region below the greater trochanter and the lower part of the femoral head. These are areas of high compression stresses due to the attachment of the abductor muscle group and ilio-tibial tract, in the first case, and the hip joint force, in the second. Lower values could be found in the intra-medullary canal, the greater trochanter and Ward's triangle region. These areas of the femur are known for being composed of thin and loosely arranged trabeculae, resulting in the lower stiffness distribution.

The 2D model's anisotropy plot shows that E_1 is up to 11 times higher than E_2 in the area of the femoral head in contact with the acetabulum (Figure 2.9), both sides of the neck, below the greater trochanter and along the internal diaphysis, as expected. These results match with the compression areas observed in other FE studies (Taylor et al. 1996; Sverdlova and Witzel 2010) and the anisotropy distribution predicted in a similar 2D algorithm (Miller et al. 2002). The isotropic assumption is not viable when studying physiological material properties because of the likelihood of over-estimating the directional elastic moduli. This reinforces the need for modelling bone as a material with orthotropic symmetry in an attempt to represent bone's anisotropy in continuum models. Since orthotropic material properties are dependent on the direction of the stiffness matrix, the stimulus required for the remodelling process put forward in this thesis needs to include directional information. This cannot be achieved by using SED because it is a scalar with no directional information. The use of strain as the driving stimulus of the adaptation process has been shown to allow for physiological prediction of material properties orientation (Beaupré et al. 1990a; Beaupré et al. 1990b; Miller et al. 2002; Geraldes and Phillips 2010).

In the 2D and 3D cases, both the greater trochanter and the principal and secondary compressive and tensile trabeculae groups documented (Singh et al. 1970) were predicted. In the E_1 plots, a slightly curved group of closely packed trabeculae originating in the medial cortex of the femoral shaft and ending in the superior part of the femoral head (principal compressive group), arises. A spaced trabecular group arising below the principal compressive group in the medial cortex of the femoral shaft and ending by the greater trochanter (secondary compressive group) can also be seen. If we look at the E_2 plot in the 2D model and the E_3 plot in the 3D model (both associated with tensile stresses), the three tensile groups are also represented: trabeculae originating in the lateral cortex below the greater trochanter and ending at its surface (greater trochanter group), a group of trabecular bone starting in the lateral cortex below the greater trochanter in the lower part of the femoral head and curving upwards and inwards across the next of the femur (primary tensile group) and trabeculae originating below the primary tensile group in the lateral cortex, arching upwards and medially across the upper end of the femur and ending irregularly after crossing the mid-line (secondary tensile group). The 3D model also shows that the material properties are not oriented exclusively in one plane but can be projected into other planes, as it can be seen in the E_3 plot for a coronal section of the proximal femur. This is a direct result from the direction of application of the abductor group and joint reaction forces. A twisted primary tensile group would reduce bending moments along the bone promoting the conversion of the weight bearing compressive stresses arising from the upright position from oblique to vertical (Ward 1838; Garden 1961). The representative Young's modulus distribution (Figure 2.15) showed a good correlation with the observed *in vivo* structures, with the zones of expected high stiffness (trabecular groups and cortical femoral shaft) and of low stiffness (Ward's triangle and intra-medullary canal) arising. However, the femoral shaft and intra-medullary canal cannot be observed as clearly as expected, which may be due to the application of non-physiological fixed boundary conditions to the whole base of the proximal femur. It is therefore recommended that a whole model of the femur should be developed where no non-physiological boundary conditions are applied directly to the bone. Because of the simplification of only applying a single load case in each model, shear modulus adaptation was not performed (Pedersen 1989).

2.5.1 Concluding Remarks

The results described above show that the algorithm proposed in this study can reasonably predict trabecular orientation and elasticity distribution in bone models for 2D and 3D. However, they were assessed only in the coronal plane and no information was obtained for the distal femur. The preliminary results discussed in this Chapter indicate that by including load cases and boundary conditions closer to the physiological state, zones with changing material properties and directionality could be modelled with a higher accuracy and resolution. These include multiple load cases such as walking, standing up or stairs climbing and descent (activities that generate high forces at a wide range of joint angles). This would require some modifications to be made to the algorithm, in particularly the development of a shear modulus adaptation algorithm to account for the resistance of certain trabecular groups to the shear stresses produced by the different daily activity cycles (Skedros and Baucom 2007). Furthermore, a selection method of the appropriate driving stimulus for each element also needs to be considered when upgrading the algorithm to include multiple load cases, in order to achieve a more physiological loading envelope.

Since the outcomes of the optimisation process rely on the stimulus calculated in the FE model, more realistic constraints can also produce more physiological strain distributions and, therefore, results closer to what can be observed *in vivo*. Some of the modifications could involve, for instance, the modelling of the complete femoral structure, inclusion of muscles and ligaments as free boundary conditions (Phillips 2005; Phillips 2009) and load application across muscle insertion zones instead of point loads. These have been discussed in Chapter 1 as necessary improvements to the current approaches to FE modelling of the lower limb. Mesh refinement and an increase of the limitation of the upper individual stiffness values from 10 GPa to 20 GPa, value measured in different studies (Rho et al. 1997; Rho et al. 1999), could also improve the accuracy of the bone models, following the guidelines for considerations to be taken during FE modelling as discussed in Chapter 1 (Erdemir et al. 2012). This method can prove to be an invaluable tool to assess directionality of trabecular structures and stiffness distribution in the femur or any other bone, allowing for a better understanding of the biomechanics of bone structures.

Chapter 3

Single Load Case 3D Femur Model

The previous Chapter outlined the development and implementation of an iterative 3D adaptation algorithm driven by strain, with bone considered to have orthotropic material properties.

This Chapter describes the application of the algorithm to a 3D finite element (FE) model of the whole femur undergoing single leg stance. The hip and knee joints, muscles and ligaments were included explicitly. Details on the model's definition can be read in Section 3.1. Section 3.2 describes the results obtained after running the adaptation algorithm with the single load case 3D femur model until convergence was achieved. Discussion of the results obtained, shortcomings of the model and further developments can be read in Section 3.3 with conclusions drawn in Section 3.4.

3.1 Single Load Case 3D Femur Model

Section 1.4 in Chapter 1 highlighted the need to carefully select the constitutive representation, mesh, geometry, loading and boundary conditions applied to a finite element model of bone, in order to produce a driving stimulus for the adaptation process as close to the physiological state as possible (Erdemir et al. 2012). Phillips proposed a free boundary condition approach to produce a self-equilibrating model of the femur with the ligaments and muscles spanning the hip and knee joints explicitly included. This method has been shown to produce reduced absolute strain values for the femur undergoing single leg stance (Phillips 2009), when compared with other studies (Polgar et al. 2003; Speirs et al. 2007). It also has been shown to produce physiological stresses in the pelvis (Phillips et al. 2007). A 3D FE model of the whole femur was created based on the same modelling approach. It is thought that this approach to modelling the femur represents more physiologically its mechanical environment, in comparison to models where fixed constraints or point loads are applied directly to the femur (Phillips 2009). The model was positioned and loaded under single leg stance conditions (Bergmann et al. 2001). This Section outlines the definition of the model's geometry, loading and boundary conditions in Abaqus. Figure 3.1 highlights the important anatomical landmarks of the femur discussed in this Chapter.

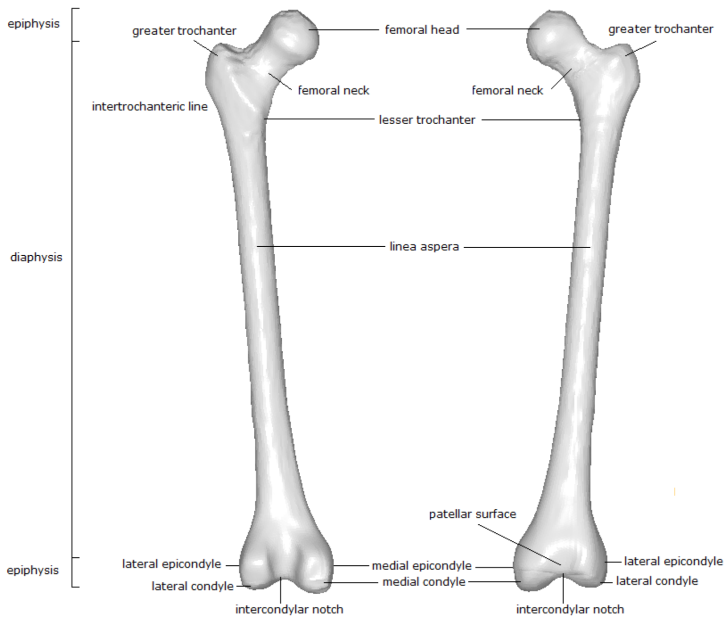

Figure 3.1 - Anatomical landmarks of the femur.

3.1.1 Geometry

3.1.1.1 Femur Mesh

The importance of geometry definition in FE modelling was highlighted in Section 1.4. Not only is a suitable definition of the bone in question required in order to produce reliable results (Erdemir et al. 2012), but it also can facilitate the replication of published research and the cross-validation of numerical studies (Viceconti et al. 2003b). The external geometry of the Muscle Standardised Femur (Viceconti et al. 2003a) was extracted and meshed with 326026 four-noded linear tetrahedral elements (C3D4), 62060 nodes. These had a mean element edge length of 2.37 mm. Mesh density and properties were within values found to be adequate for numerical modelling of the femur by a previous study (Ramos and Simões 2006). Sensitivity studies were also performed to assess the dependency of the predicted results with mesh properties and starting configuration of material properties. The mesh density considered in this model produced physiological strains, stresses, forces and material distributions whilst being computationally efficient. The starting configuration of material properties did not seem to influence the converged results.

The femur was positioned according to the International Society of Biomechanics (ISB) recommendations (Wu et al. 2002) (Figure A.3, in the Appendix): (i) the centre of the femoral head coincided with the origin of both the global reference space and the femoral reference space. (ii) The z axis was defined as the line joining the femoral origin and the mid-point between both femoral epicondyles (FEps), and pointing superiorly. (iii) The x axis was defined as the line joining both FEps, perpendicular to the z axis and pointing medially. (iv) The y axis was defined as the line perpendicular to both x and z axis, pointing anteriorly. The global and local reference systems were assumed to be coincident. The axis nomenclature and order was the same used by Phillips (Phillips 2009), in order to facilitate the model building and comparison between studies.

The angle of the femoral shaft was 10° in the coronal plane (Phillips 2009) and 7° in the sagittal plane (Cristofolini et al. 1995). The femur positioning was within the ranges used to measure the *in vivo* hip contact forces (HCFs) for single leg stance. All elements were assigned the same initial orthotropic elastic constants ($E_1 = E_2 = E_3 = 3000$ MPa, $\nu_{12} = \nu_{13} = \nu_{23} = 0.3$, $G_{12} = G_{13} = G_{23} = 1500$ MPa) and orientations matching the femoral axis system. Sensitivity studies confirmed that the starting material properties did not affect the converged material properties.

3.1.1.2 Cartilage at the Femoral Head and Condyles

Soft elastic layers were included to promote even load distribution at both the hip and knee joints, emulating the function of the cartilage structures present in these regions. All elements were assigned the same initial isotropic elastic constants ($E = 10$ MPa, $\nu = 0.49$). The cartilage surrounding the femoral head was modelled as the intersection between a sphere with 50 mm diameter projected from the centre of the femoral head and the femoral head itself. It was meshed with 1512 nodes, resulting in 5081 four-noded linear solid tetrahedral elements (C3D4) (Figure 3.2 (a), in yellow). The condylar cartilage was modelled as the intersection between two identical toroids (radius 10 cm, width 5 cm) merged together and the distal femur (Phillips 2009). The resultant shape was meshed with 120617 four-noded linear solid tetrahedral elements (C3D4), 23280 nodes (Figure 3.2 (b), in maroon).

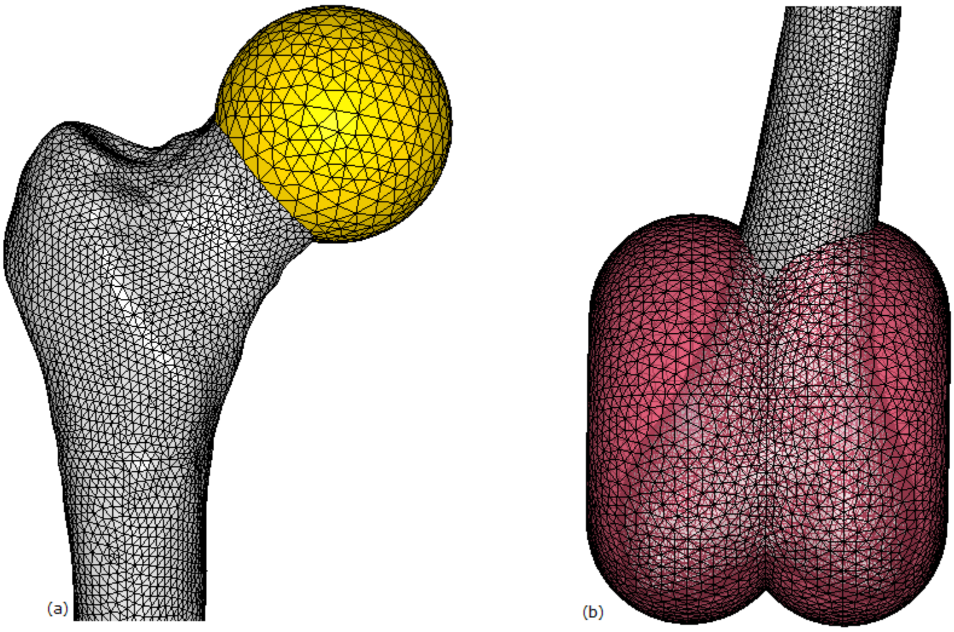

Figure 3.2 - Mesh of the femoral head (a) and condyles (b) cartilage.

3.1.2 Joints

In order to transfer the loads resulting from the application of body weight (BW) through the pelvis onto the proximal femur through to the distal femur, structures were defined at the hip and knee joints based on Phillips' model (Phillips 2009).

3.1.2.1 Hip Joint

An artificial load applicator representative of the acetabular region was created by intersecting a 25 mm radius hemisphere out of an equilateral wedge with 70 mm edge length. This elastic structure was modelled with 122059 four-noded linear solid tetrahedral elements (C3D4), composed by 23611 nodes (Figure 3.3 (a)). All elements had the same isotropic material properties (E = 5000 MPa, ν = 0.3). The pelvic tilt was 3° towards the medial side, based on Bergmann's positioning data (Bergmann et al. 2001).

Two-noded truss elements (C32D) with stiffness of 10^6 N/mm were used to connect this structure to muscle insertion points on the pelvis, sacrum and lumbar spine, creating the pelvic construct. Such high stiffness was considered so that the forces applied to any point in the pelvic region were transmitted to the whole construct. The pelvic region was also connected to a point between the L5 lumbar and S1 sacral vertebrae (L5S1) where BW was applied (see Section 3.1.4) (Phillips 2009).

The L5S1 point and the hip muscle insertion points were not constrained directly in any degree of freedom (Figure 3.3 (a)). This was implemented in order to allow free motion of the pelvic region around the femoral head (Phillips 2007; Phillips 2009). The action of the muscles spanning the hip joint helped to stabilise the pelvic movements (see Section 3.1.3), resulting in an equilibrated system (Figure 3.3 (b)).

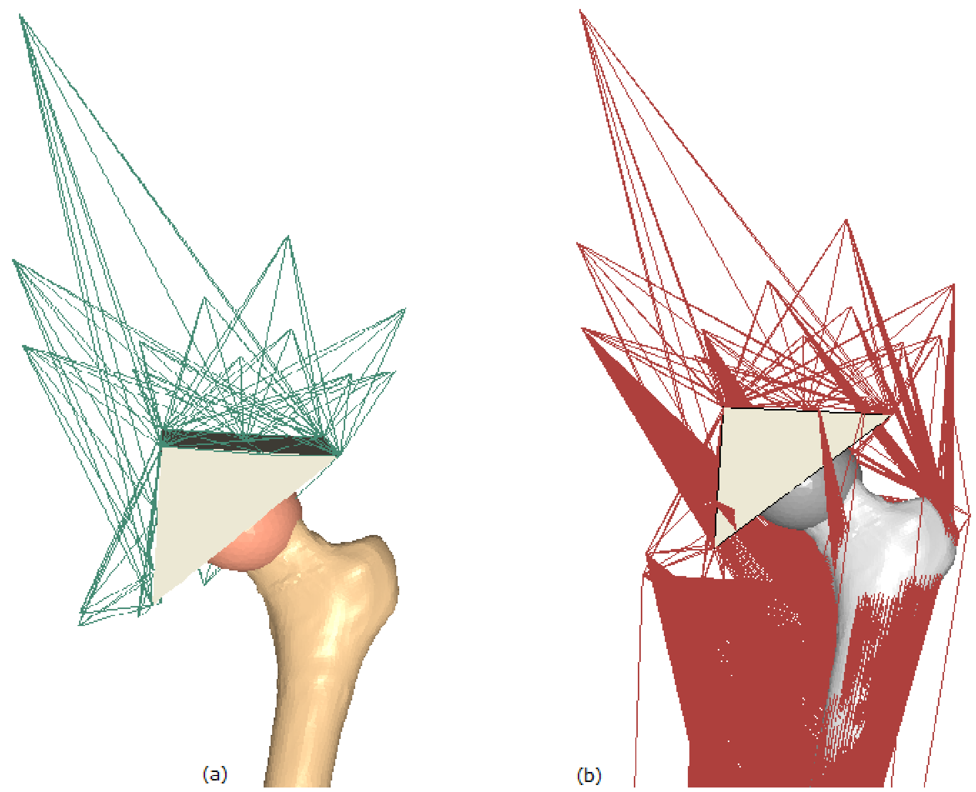

Figure 3.3 - The pelvic structure with the load applicator (a) and including the muscles spanning the hip joint (b).

3.1.2.2 Knee Joint

An artificial structure representative of the tibial plateau was created by intersecting the contact region of the condylar cartilage (Section 3.1.1.2) out of a rectangular solid (100 mm x 80 mm x 20 mm). The resulting 3D shape was meshed with 39777 four-noded linear solid tetrahedral elements (C3D4), composed by 8134 nodes (Figure 3.4, left). All elements had the same isotropic material properties (E = 5000 MPa, ν = 0.3).

A point in space, representative of the insertion point on the patella, was defined and connected to two other nodes in space with two-noded truss elements (C3D2) with stiffness of 10^4 N/mm. These formed a hinge-like triangular structure that allowed the transfer of the forces through the patella ligament and quadriceps muscles back to the femur whilst reducing the structural rigidity that would have been induced by higher stiffness trusses (as applied in the pelvic construct). This structure was then connected back to the articular surface of the condyles with the patella by using 240 C3D2 elements with significant stiffness in compression (10^6 N/mm) and negligible in tension (100 N/mm). This was undertaken in order to promote patello-femoral force transfer (Figure 3.4, right).

The insertion point on the patella was then connected to the corresponding muscle and ligaments insertion points (see Section 3.1.3).

The inclusion of a tibial plateau and a patellar structure allowed for force transfer across the knee joint and through the patello-femoral articular surface.

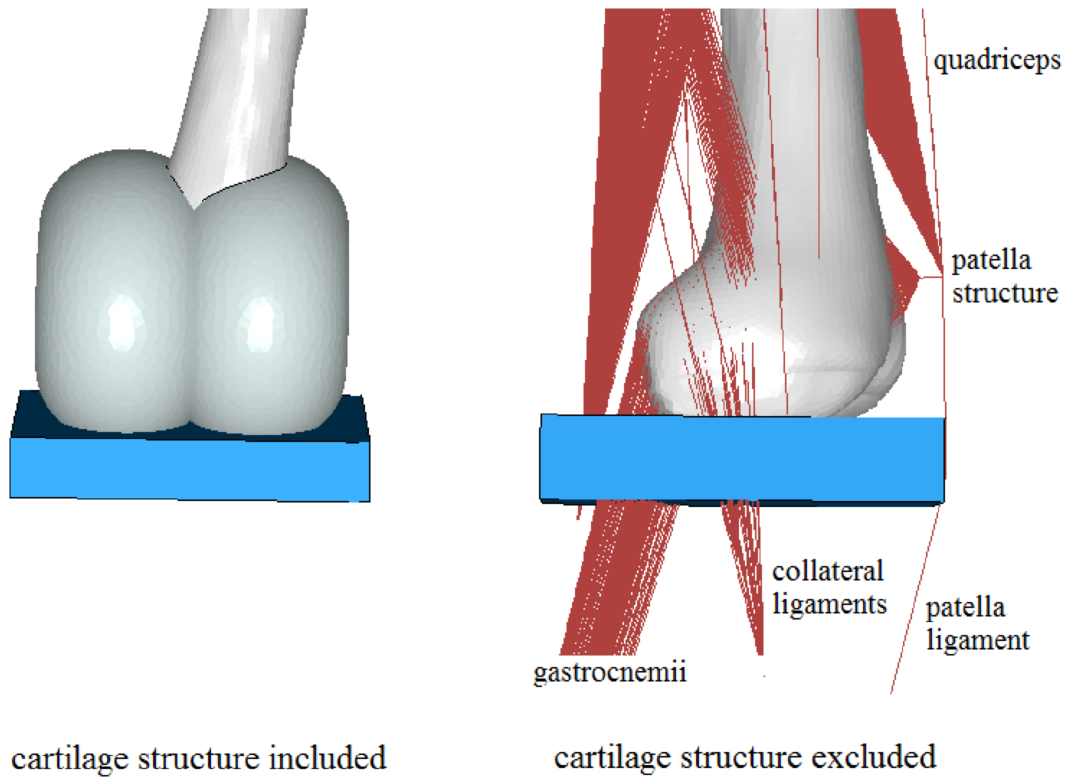

Figure 3.4 - Anterior view of the tibial plateau (left) and medial view of the distal femur joint definition (right) with patello-femoral and tibio-femoral joint representations.

3.1.3 Muscles and Ligaments

A total of 26 muscles and 7 ligamentous structures were included explicitly in the model as groups of spring connector elements (C3D2) (Phillips 2009). Muscle origination areas were extracted from the Standardised Femur (Viceconti et al. 2003a) and mapped onto the femoral mesh described in Section 3.1.1.1. Ligament origination areas and pelvic insertion points were defined as described by Phillips (Phillips et al. 2007; Phillips 2009).

3.1.3.1 Linear Definition of the Muscles and Ligaments

The modelling of muscles and ligaments as spring elements acting as passive actuators has been shown to produce consistent results with joint and muscle forces produced by balanced models and measured throughout literature (Phillips et al. 2007; Phillips 2009). Their inclusion as groups of spring elements allows for the development of equilibrated models which do not require input from musculo-skeletal models. A similar approach to the linear muscle definition proposed by Phillips was used in the single load case 3D femur model described in this Chapter. Each of the muscles was defined as a group of connectors with number proportional to their origination area. Figure 3.5 shows a typical force-displacement curve for the connectors. This curve is defined by a reference stiffness value, k_{iso}^{ML}, and a peak contractile force, F_{peak}^{M}, based on the linear free boundary condition implemented (Phillips 2009) and described here for completeness.

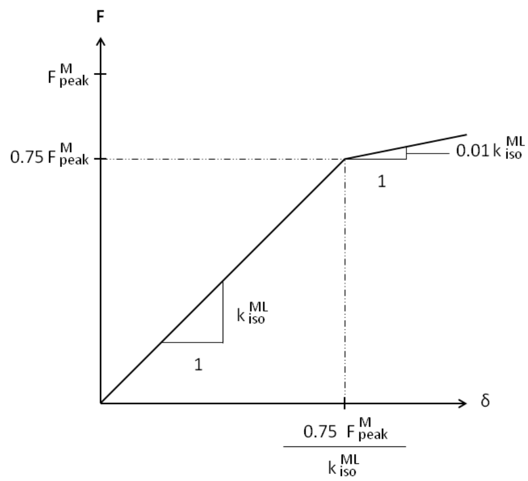

Figure 3.5 - Force-displacement relationship curve for each of the muscles (Phillips 2009).

Measurements of the hip contact forces (HCF) (Bergmann et al. 1993; Bergmann et al. 2001; Bergmann et al. 2004) and numerical investigations on muscle forces (Besier et al. 2009) and maximum voluntary torque (Anderson et al. 2007) suggest that muscles are not expected to reach their peak contractile force during daily living activities. In order to model this behaviour in the force-displacement curve, stiffness was lowered after $0.75F_{peak}^{M}$ to $0.01k_{iso}^{ML}$, promoting activation of other muscle groups as the force generated by each muscle approaches its maximum (Phillips 2009). This limit to 75% of peak muscle force is in agreement with muscle optimisation criteria for limiting muscle forces during daily activities (Crowninshield and Brand 1981; Heller et al. 2001). Given that muscles act in tension (Zajac 1989), stiffness values were considered to be negligible ($0.01k_{iso}^{ML}$) in compression. The number of elements, C, defined for each of the connector groups representing the muscles included in the model, was taken as the number of nodes within the origination areas. These were extracted from the Standardised Femur after mapping the later onto the femur mesh. The value for k_{iso}^{ML} for each muscle group was taken from Phillips' work (Phillips 2009). These were calculated according to Equation 3.1,

$$k_{iso}^{MT} = \frac{3.5}{0.1}\frac{F_{peak}^{M}}{L_{slack}^{T}} \tag{3.1}$$

where L_{slack}^{T} is the tendon slack length, defined according to Zajac (Zajac 1989) and calculated using published experimental measurements following cadaveric dissection (Wickiewicz et al. 1983; Delp 1990; Friederich and Brand 1990). The stiffness for each of the muscle, k_{iso}^{MT}, was divided by the number of connectors defined per muscle to generate the effective stiffness, ${k_{iso}^{MT}}_{eff}$, for each of the elements in a muscle. Table 3.1 outlines the reference stiffness, tendon slack length, number of connectors, peak force and effective stiffness for each of the muscle groups. The stiffness values for the ligaments included in the model were extracted from experimental measurements (Butler 1989) and validated models (Li et al. 1999; Mesfar and Shirazi-Adl 2006). The iliotibial tract stiffness was updated following measurements by Merican

(Merican and Amis 2009) and the peak force generated by the patella tendon obtained from Staubli's measurements of this structure's ultimate failure load (Stäubli et al. 1996). These can be seen in Table 3.2.

Table 3.1 - Properties of the muscles included in the model.

Muscle	F^M_{peak} **(N)** (Delp 1990)	L^T_{slack} **(mm)** (Zajac 1989)	k^{MT}_{iso} **(N/mm)** (Phillips 2009)	C	$k^{MT}_{iso\,eff}$ **(N/mm)**
Adductor brevis	285	20	499	127	3.93
Adductor longus	430	110	137	300	0.46
Adductor magnus caudalis	220	150	51	63	0.81
Adductor magnus cranialis	880	150	205	1396	0.15
Biceps femoris long head	720	341	74	1	74
Biceps femoris short head	400	100	140	299	0.47
Gastrocnemius lateralis	490	385	45	55	0.82
Gastrocnemius medialis	1115	408	96	148	0.65
Gemeli	110	39	99	77	1.29
Gluteus maximus	1300	132	345	406	0.85
Gluteus medius	1365	61	783	120	6.53
Gluteus minimus	585	31	660	99	6.67
Gracilis	110	140	98	1	98
Iliopsoas	430	90	177	50	3.54
Pectineus	175	20	306	92	3.33
Piriformis	295	115	90	28	3.21
Psoas	370	130	100	1	100
Quadratus femoris	225	24	328	37	8.86
Rectus femoris	780	346	79	2	39.5
Sartorius	105	40	92	1	92
Semimembranosus	1030	359	100	1	100
Semitendinosus	330	262	44	1	44
Tensor fascia latae	155	425	13	1	13
Vastus intermedius	1235	136	318	2578	0.12
Vastus lateralus	1870	157	417	695	0.6
Vastus mediatus	1295	126	360	330	1.09

Table 3.2. - Properties of the ligaments included in the model.

Ligament	F^M_{peak} **(N)**	k^{MT}_{iso}**(N/mm)**	C	$k^{MT}_{iso\,eff}$ **(N/mm)**
Gluteal iliotibial tendon	720	85	1	85
Iliotibial tract	430	97	2	48.5
Patella tendon	2500	1000	2	500
Anterior cruciate	N/A	200	13	15.38
Lateral collateral	N/A	100	26	3.85
Medial collateral	N/A	100	28	3.57
Posterior cruciate	N/A	200	17	11.76

3.1.3.2 Geometrical Definition of the Muscles and Ligaments

The mechanical surroundings of the numerical model in question need to be carefully defined in order to achieve physiological stress and strain distributions. Therefore, special attention was put into modelling the muscles lines of action and ligamentous structures in order to reflect their anatomical positions. Figure 3.6 and Figure 3.7 are included in order assist in the visualisation of the definition of the muscles geometry. The insertion points of the muscles originating from the femur were derived based on Duda (1996). Insertion points in the pelvis, tibia, fibula, calcaneus and the muscle via points were extracted from Phillips' pelvic and femoral free boundary condition models (Phillips 2005; Phillips et al. 2007; Phillips 2009). These were mapped from Dostal and Andrews study on pelvic and femoral bony landmarks (Dostal and Andrews 1981). The coordinates for these points and their anatomical location relative to the global reference system are outlined in Table 3.3, at the end of this Section. Muscle origination areas were extracted from the Standardised Femur (Viceconti et al. 2003a) and mapped onto the femoral mesh described in Section 3.1.1.1. Values for the effective stiffness shown in Tables 3.1 and 3.2 were normalised for the number of connectors of a given muscle or ligament group.

The iliotibial tract was split into two elements, one starting from its insertion on the pelvis to a point in space representing its turning point on the femur around the greater trochanter, and another running from the turning point to its insertion in the tibia. Elements with considerable stiffness in compression ($k = 10^6$ N/mm) connected the turning point of the iliotibial tract to the femur, simulating the load transfer generated by the wrapping of this band around the greater trochanter, similar to that implemented for the patella (Section 3.1.2.2 and Figure 3.4(b)). The tensor fascia latae was modelled by a single connector running from its insertion in the iliac crest to a point in space representing the turning point of the iliotibial tract. The gluteus maximus was divided into two parts of 203 connector elements each, originating from the femur and running to an insertion on the sacrum and to the turning point of the iliotibial tract at the greater trochanter. The second group was included to model the gluteus maximus contribution to the action of the iliotibial band. Two connectors representing the gluteal iliotibial tendon were associated with the two insertion points of the gluteus maximus and inserted into the turning point of the iliotibial tract. The piriformis muscle was also divided in two parts of 28 connectors each, both starting at its attachment area on the greater trochanter, and finishing at the point representing the sacrum and a point representing the superior margin of great sciatic notch.

The gluteus medius was split into three parts of 40 elements each, starting from its origination surface on the greater trochanter and inserting to three points representing the outer surface of the ilium and the anterior gluteal line. The gluteus minimus was also composed by three parts of 33 elements each fanning out from the origination area on the greater trochanter, and inserting on to three points along the outer surface of the ilium (Figure 3.6(a)). The vastus intermedius was composed of 2578 elements starting from the antero-lateral region of the femoral shaft. The vastus lateralus was split into 695 spring elements originating in the greater trochanter, inter-trochanteric line and linea aspera of the femoral shaft. The vastus mediatus was divided into 330 elements originating from the medial side of the femur (Figure 3.6(b)).

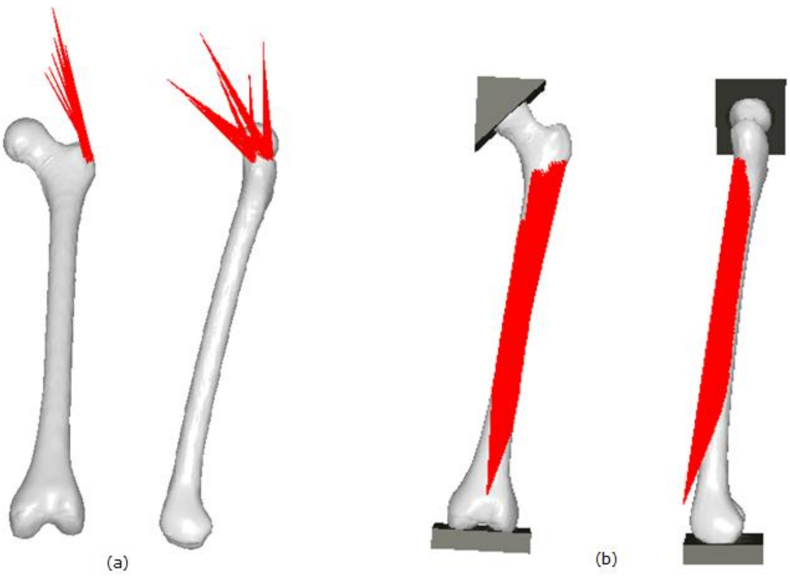

Figure 3.6 - Anterior and lateral views of the gluteus medius and minimus (a) and of the vasti muscle groups (b).

The patella tendon was divided into two connectors spanning between the insertion point of the quadriceps (rectus femoris and vasti) on the base of the patella to its insertion on the superior part of the tibial shaft. The gastrocnemius lateralis and the gastrocnemius medialis were partitioned into 55 elements starting at the lateral condyle and 148 connectors starting at the medial condyles, respectively. Both connector groups insert into a point in space representing the mid-posterior calcaneus (Figure 3.7(a)). The anterior cruciate, posterior cruciate, medial collateral and lateral collateral ligaments were represented by 27, 34, 56 and 52 connecting springs respectively, starting from their respective origination areas in the epicodylar and intercondylar areas of the distal femur and finishing at their respective insertions at the tibia and fibula (Figure 3.7(b)).

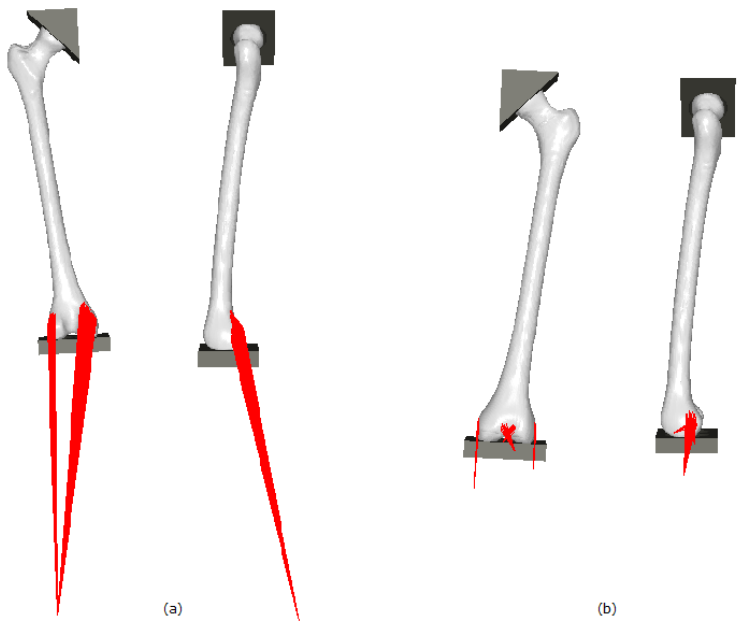

Figure 3.7 - Posterior and lateral views of the gastrocnemii (a); anterior and lateral views of the knee ligaments (b).

The quadratus femoris muscle was composed of 37 elements running between the ischial tuberosity and a region on the surface on the inter-trochanteric crest. The rectus femoris was modelled as two connectors running from the iliac spine to their insertion on the base of the patella. This insertion point in the patella was also connected to the different origination areas on the femur of the three vasti muscles. The long head of the biceps femoris was modelled as a single connector between the tuberosity of the ischium to the insertion point in the fibula. The short head of the same muscle was divided into 299 elements originating from the linea aspera region in the femoral shaft, and inserting in the same point in the fibula. The gracilis, sartorius, semimembranosus and semitendinosus muscles were modelled by single connectors starting from their respective insertion points in the ischium and terminating in fixed insertion points in the tibia. The gemeli were split into 77 elements extending from the greater trochanter to the ischium. 92 elements connected the superior pubic ramus to the pectineal line of the femur, forming the pectineus muscle. The iliopsoas was split into 50 connector elements running from the lesser trochanter to a point in space representative of its turning point at the edge of the iliac fossa. A single connector representing the psoas was then connected between this turning point and its insertion in the lumbar region. The adductor muscles all originated along the linea aspera of the femur and inserted on the pubic region. The adductor brevis and adductor longus were composed of 131 and 300 elements, respectively. The adductor magnus was split into two parts: the caudal part, composed by 63 elements, starting in the distal part of the femoral shaft; and the cranial part, split into 1386 elements, originating along the medial part of the femoral shaft.

Medial, anterior, lateral and posterior views of the femur model after the inclusion of the 26 muscles and 7 ligamentous structures can be seen in Figure 3.8.

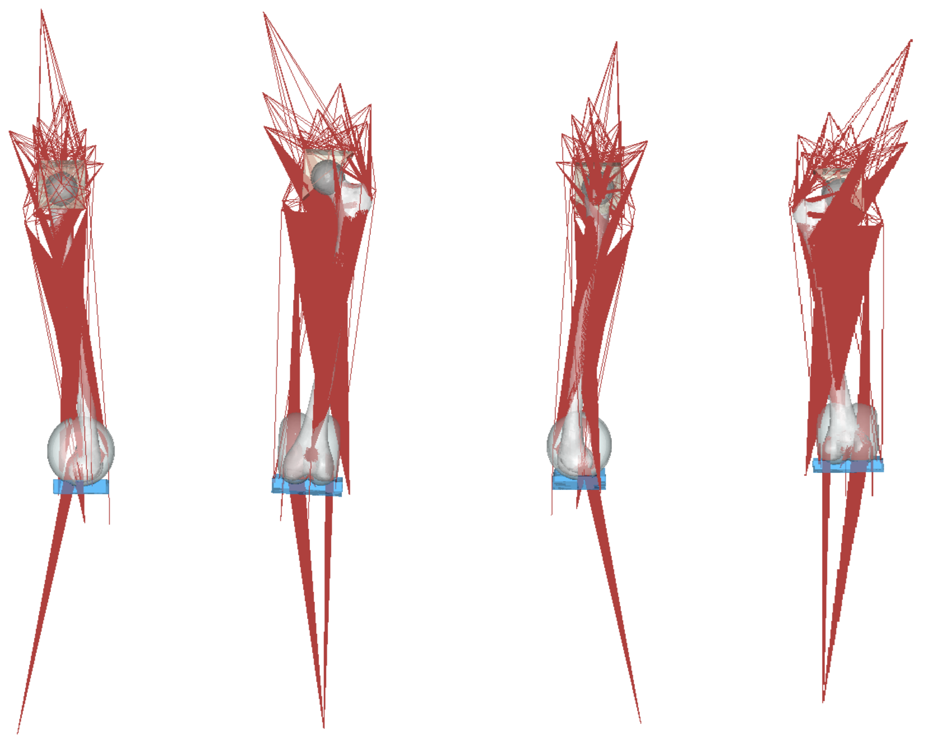

Figure 3.8 - Left to Right: medial, anterior, lateral and posterior views of the Single Load Case 3D Femur Model.

Table 3.3 - Spatial coordinates of the points used to model muscle and ligament origins, insertions and via points and their anatomical location. The coordinates presented are relative to the in the global reference system.

Point	Location	x (mm)	y (mm)	z (mm)
Adductor brevis	Pubic region	67	21	-45
Adductor longus	Pubic region	65	41	-31
Adductor magnus caudalis	Pubic region	44	-31	-61
Adductor magnus cranialis	Pubic region	34	-48	-59
Anterior cruciate	Intercondyloid eminence of the tibia	10	-5	-425
Biceps femoris 1	Tuberosity of the ischium	-54	-59	-442
Biceps femoris 2	Head of the fibula	13	-53	-36
Gastrocnemius medialis	Mid-posterior calcaneus	-35	-162	-788
Gastrocnemius lateralis	Mid-posterior calcaneus	-35	-162	-788
Gemeli	Ischium	19	-52	-4
Gluteus maximus	Sacrum	44	-87	68
Gluteus medius 1	Outer surface of the ilium	-62	27	102
Gluteus medius 2	Outer surface of the ilium	-18	-2	132
Gluteus medius 3	Anterior gluteal line	15	-48	97
Gluteus minimus 1	Outer surface of the ilium	-41	29	73
Gluteus minimus 2	Outer surface of the ilium	-20	-4	88
Gluteus minimus 2	Outer surface of the ilium	0	-26	71
Gracilis	Ischium	41	-14	-434
Iliopsoas	Outside the iliac fossa	-6	59	45
Lateral collateral	Head of the fibula	-5	-35	-435
Lumbar	Lumbar region	95	-30	240
Medial collateral	Medial condyle of the tibia	43	-25	-484
Patella tendon insert	Superior part of the tibial shaft	3	12	-492
Patella insertion	Base of patella	3	22	-392
Patella insertion hinge1	Base of patella	32	17	-390
Patella insertion hinge2	Base of patella	42	17	-390
Pectineus	Superior pubic ramus	38	44	-3
Piriformis	Great sciatic notch	47	-78	55
Posterior cruciate	Posterior intercondylar area of the tibia	-29	-27	-426
Quadratus femoris	Ischial tuberosity	15	-36	-46
Rectus femoris	Iliac spine	-26	43	37
Sacrum	Sacrum	95	-42	78
Sartorius	Ischium	42	-8	-435
Semimembranosus	Ischium	34	-29	-428
Semitendinosus	Ischium	40	-22	-433
Tensor fascia latae finish	Tibia	-33	22	-436
Tensor fascia latae start	Iliac crest	-56	45	78
Tensor fascia latae via	Outside the greater trochanter	-70	0	-18

3.1.4 Loading, Model Interfaces and Boundary Conditions

Body weight (BW) was considered to be 1000 N. Single leg stance was modelled by applying a downwards load (along the global z axis only) of 5/6 BW (835 N) to the L5S1 point (Phillips 2009).

The femur was not constrained, following the free boundary condition approach (Phillips et al. 2007; Phillips 2009). Surface to surface tie conditions were applied between the femur and the two cartilage structures at the femoral head and condyles. For both interaction definitions the master surface was considered to be the outer surface of the femur mesh with a position tolerance of 0.25 mm.

Small sliding frictionless penalty contact conditions were applied between the cartilage structure surrounding the femoral head, and the concave hemispheric surface representative of the acetabulum. Identical contact conditions were also applied between the cartilage structure surrounding the condyles, and the concave surface representative of the tibial plateau. These were discretised using the node to surface method. For both interactions, the master surface was considered to be the one on the load applicator (i.e. acetabular structure and tibial plateau, respectively). Hard contact pressure-overclosure with penalty constraint enforcement method was used (Clarke et al. 2012).

One node in the centre of the bottom part of the tibial plateau structure was fixed against displacement (totalling 3 degrees of freedom), allowing the femur to pivot about the tibial plateau. Fixed constraints were also applied at the insertion points of the muscles and ligaments on the tibia and fibula (biceps femoris, gastrocnemius medialis, gastrocnemius lateralis, anterior cruciate ligament, posterior cruciate ligament, medial collateral ligament, lateral collateral ligament, patella tendon, tensor fascia latae, gracilis, sartorius, semimembranosus and semitendinosus).

Figure 3.9 shows a representation of the Single Load Case 3D Femur Model with the load applied highlighted in red and the boundary conditions in orange.

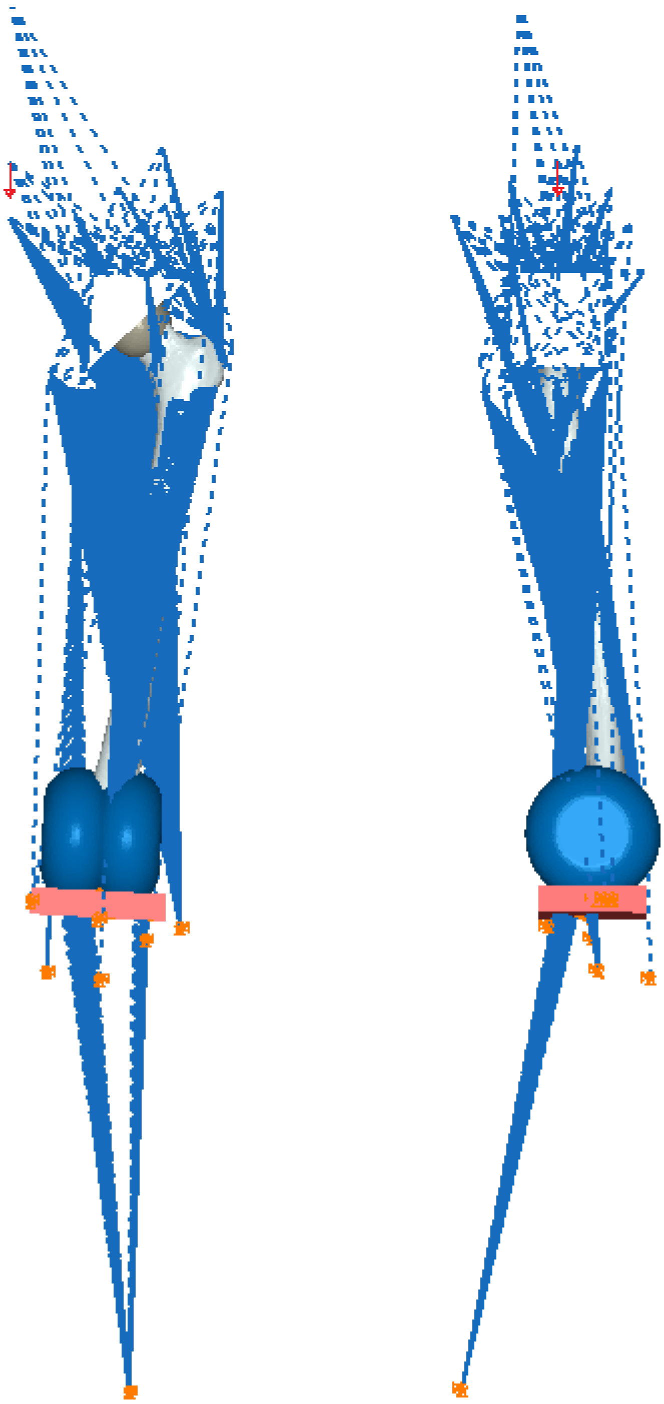

Figure 3.9 - Anterior and medial views of the Single Load Case 3D Femur Model, with loading (in red) and boundary conditions (in orange).

3.2 Results

The iterative bone adaptation algorithm proposed in Chapter 2 was applied to the Single Load Case 3D Femur Model undergoing single leg stance. The algorithm reached a state of convergence after the 27th iteration. This Section illustrates the von Mises stresses, strains, reaction and contact forces, muscle forces and material properties that resulted from this process.

3.2.1 Model Results

3.2.1.1 Stresses and Strains

Figure 3.10 displays up to the 99th percentile of the resulting von Mises stresses distribution for the converged femur model undergoing single leg stance. 99% of elements reported von Mises values below 46.88 N/mm^2. The maximum value for the von Mises stresses was 57.15 N/mm^2 and was found in the superior region of the medial femoral shaft.

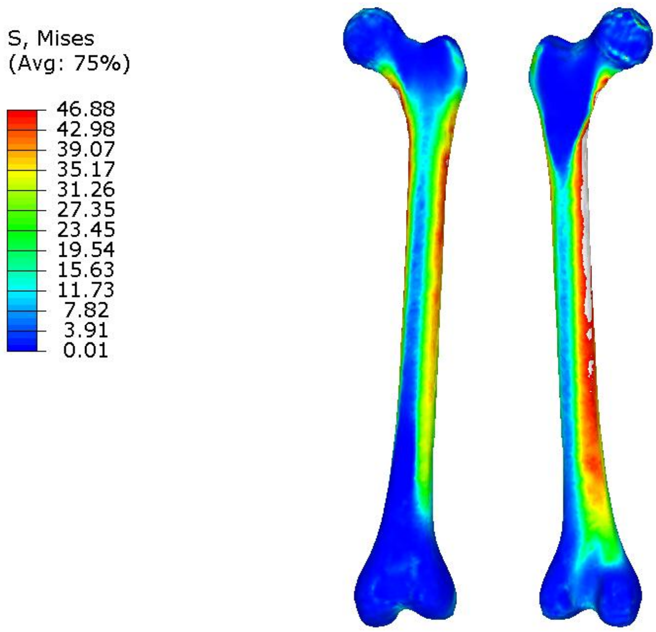

Figure 3.10 - Anterior and posterior view of the von Mises stresses (N/mm^2) of the femur undergoing single leg stance.

Figure 3.11 displays up to the 99th percentile of the resulting maximum (tensile) principal strains of the femur undergoing single leg stance. 99% of the resulting maximum strains were found below 1950 µstrain. The maximum value, ε_{max}, of 2861 µstrain was found in the superior part of the lateral femoral shaft.

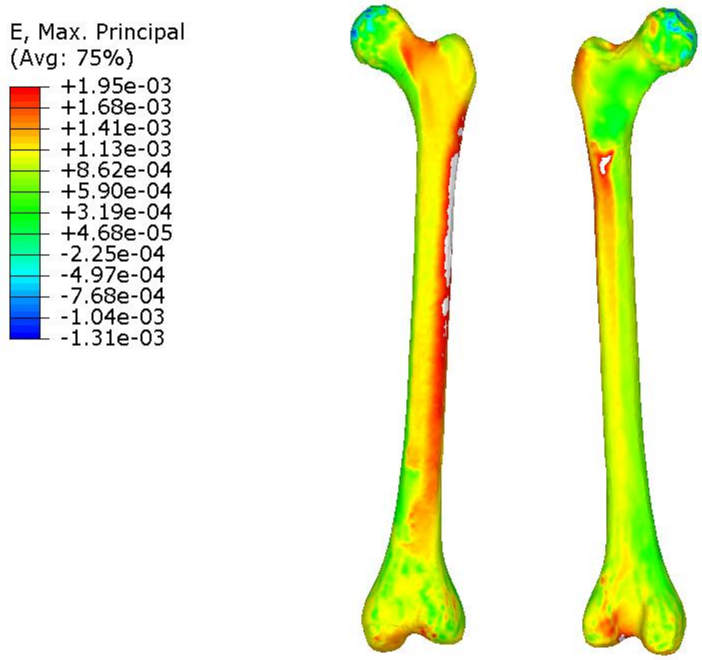

Figure 3.11 - Anterior and posterior view of the maximum principal strains of the femur undergoing single leg stance.

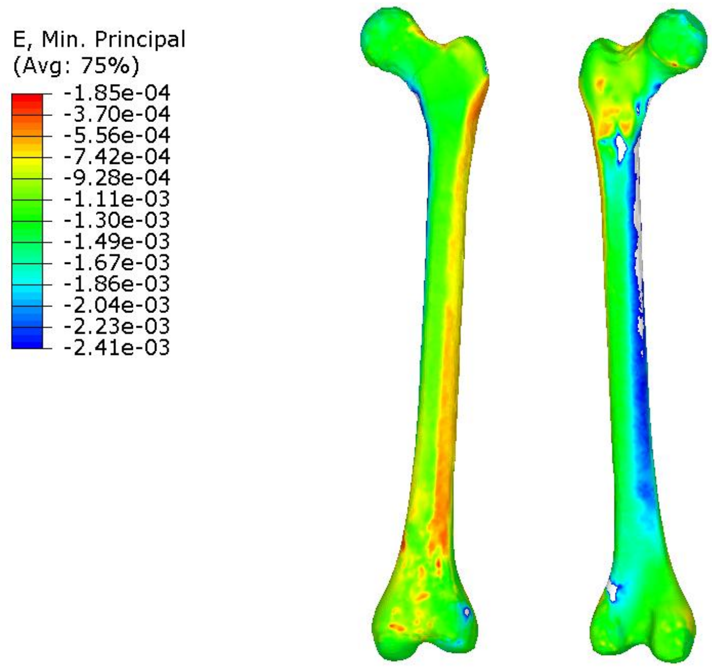

Figure 3.12 - Anterior and posterior view of the minimum principal strains of the femur undergoing single leg stance.

The resulting minimum (compressive) principal strains of the femur undergoing single leg stance are displayed in Figure 3.11. 99% of the values were found to be above -2410 μstrain. The minimum value, ε_{min}, of -5446 μstrain was found in an element in the greater trochanter region of the proximal femur. Nevertheless, only 5 elements (0.0015%) had values above 3000 μstrain.

3.2.1.2 Reaction and Contact Forces

The resultant predicted hip and knee contact forces converged quickly after 3 iterations (Figure 3.13). Table 3.4 summarises the values obtained for their resultant, x, y and z components (F_r, F_x, F_y and F_z, respectively), as well as the medial-lateral split in knee reaction forces. The split was obtained by calculating the pressures applied by both condyles on the tibial plateau.

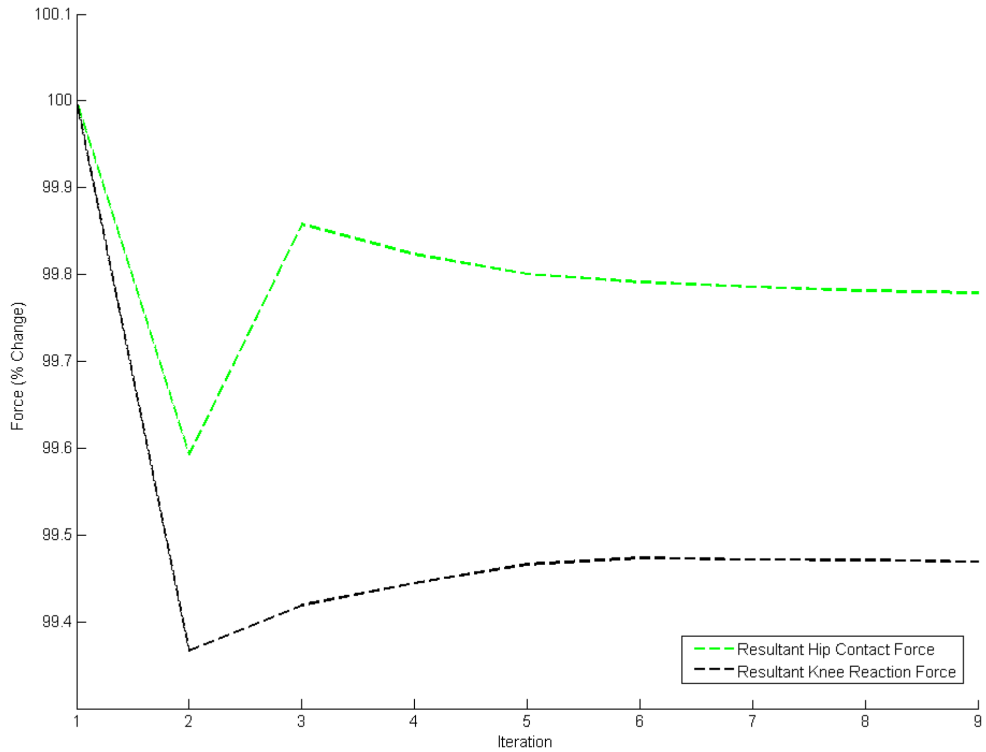

Figure 3.13 – Change in hip contact and knee reaction forces in respect to their peak value across all iterations. The forces converge quickly after three iterations.

Table 3.4 - Components of the contact forces at the femoral head and the condyles (N).

Component	F_x (%BW)	F_y (%BW)	F_z (%BW)	F_r (%BW)	Split (medial – lateral)
Femoral Head	56	-4	255	261	N/A
Condyles	8.3	-0.7	-278	278	51.3-48.7 (%)

3.2.1.3 Muscle Forces

The muscle and ligament forces resulting from the self-balanced free boundary condition model converged quickly after 3 iterations (Figure 3.14) and can be seen in Table 3.5. Resulting forces below 10 N were considered negligible and therefore were not reported.

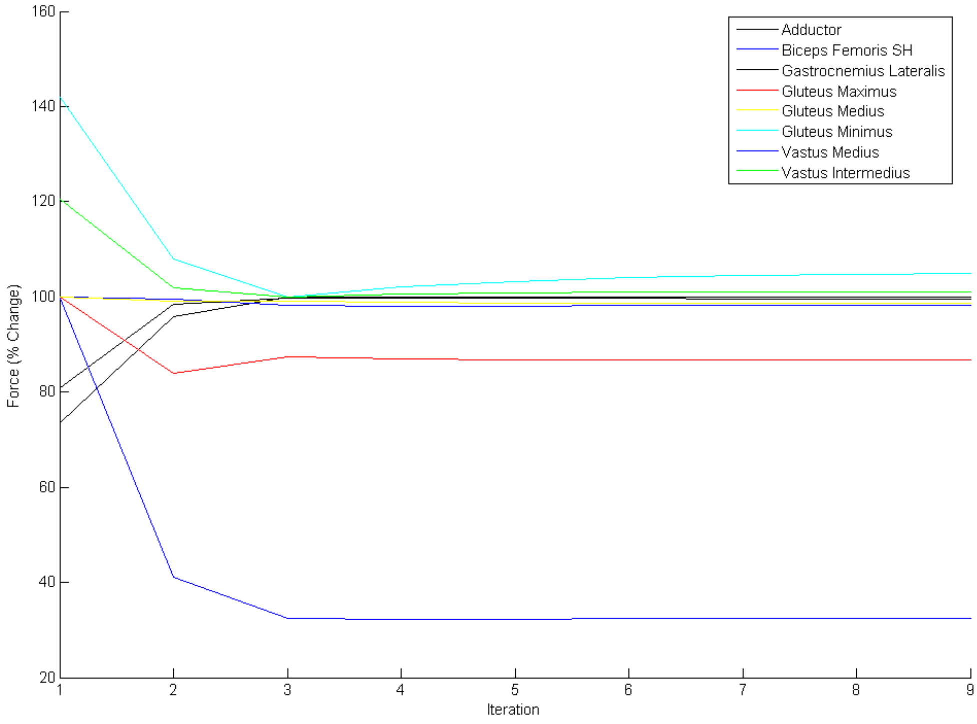

Figure 3.14 - Change in muscle forces in respect to their peak value across all iterations. The forces converge quickly after three iterations. The muscle forces converge quickly after three iterations.

Table 3.5 - Muscle and ligament forces for the femur undergoing single leg stance (N). Forces were not reported when they were found to be less than 10 N.

Muscle/Ligament	Force (N)
Adductor magnus	242
Biceps femoris (short head)	253
Gastrocnemius lateralis	78
Gluteus maximus	229
Gluteus medius	952
Gluteus minimus	324
Vastus medius	315
Vastus intermedius	237
Iliotibial tract	59
Anterior cruciate	77
Lateral collateral	48

3.2.2 Material Properties

The analysis started with all elements being assigned the same initial orthotropic elastic constants ($E_1 = E_2 = E_3 = 3000$ MPa, $\nu_{12} = \nu_{13} = \nu_{23} = 0.3$, $G_{12} = G_{13} = G_{23} = 1500$ MPa) and orientations aligned with the global coordinate system. Similarly to the predicted muscle and joint forces, material properties converged quickly after three iterations. Figure 3.15 shows the distribution of the dominant Young's moduli and their associated orientation for coronal slices of the whole femur, proximal femur and condyles. The dominant Young's modulus was selected as the highest value between E_1, E_2 and E_3. The directions for E_1, associated with compression, are plotted in red, whereas the directions for E_3, associated with tension, are plotted in blue. Elements with Young's moduli above 7 GPa were in grouped as cortical bone, in order to highlight the trabecular areas (Carter and Hayes 1977; Hodgskinson and Currey 1992). The maximum value for each of the Young's moduli was of 20 GPa. The regions where the high and low values can be found are summarised in Table 3.6 at the end of this Section.

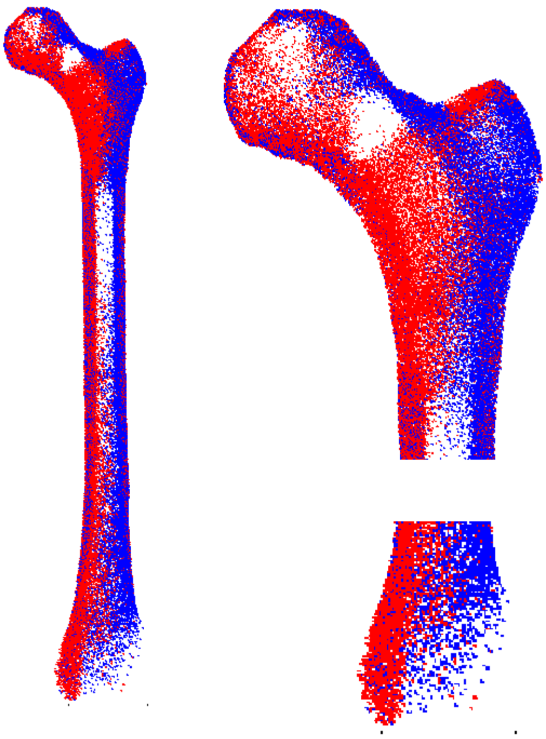

Figure 3.15 - Distribution of the dominant Young's moduli in MPa (E_1 in blue, E_3 in red) and their associated orientation for coronal slices of the complete femur, proximal femur and condyles.

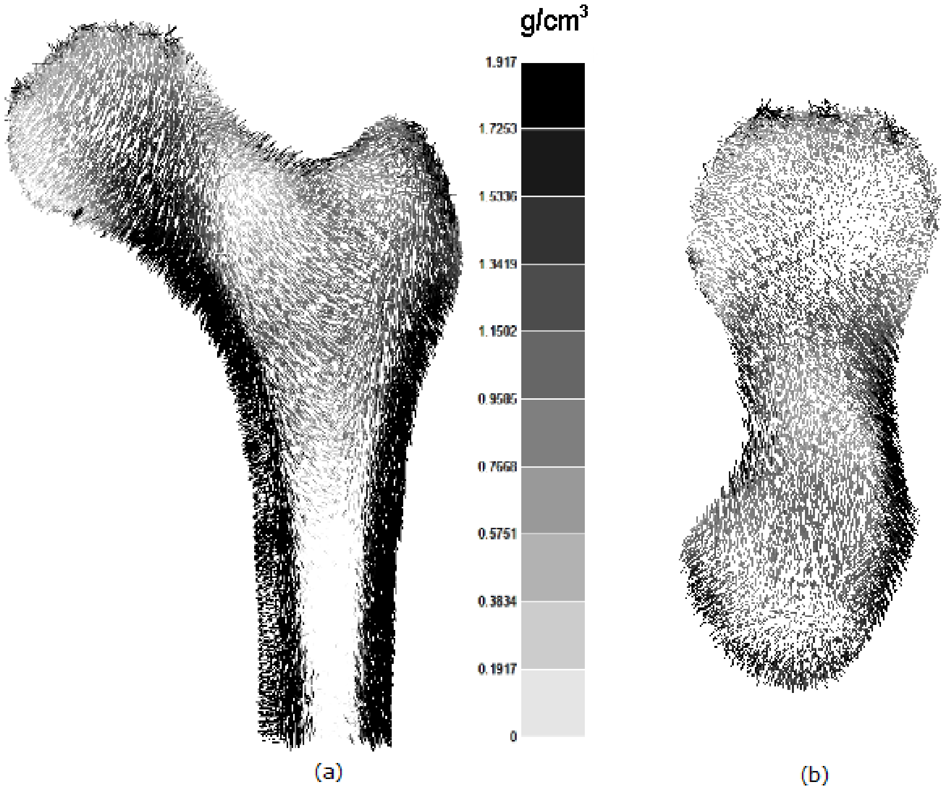

Figure 3.16 - Distribution of equivalent density (g/cm^3) and dominant directions for a coronal (a) and a transverse (b) slice of the proximal femur.

The distribution of the equivalent density and the dominant directions for a coronal (a) and a transverse (b) slice of the proximal femur can be seen in Figure 3.16. The colour scale varies in intensity between the lowest value (in white) and its maximum (in black). Density was calculated using the power relationship between the mean Young's modulus and density for the femoral neck. The empirical relation used was extracted from Morgan's study of the material properties in the proximal femur (Morgan et al. 2003) (Equation 3.2) below, where E_{mean} is the mean Young's modulus for each element (Equation 3.3).

$$\left(\frac{E_{mean}}{6.850}\right)^{\frac{1}{1.49}} = \rho \qquad (3.2)$$

$$E_{mean} = \frac{E_1+E_2+E_3}{3} \qquad (3.3)$$

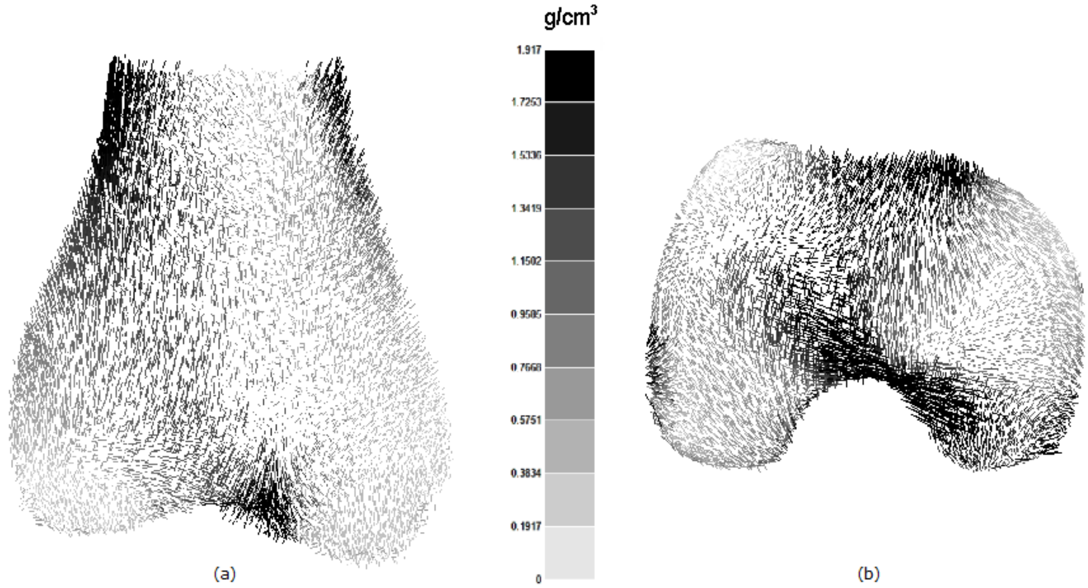

Figure 3.17 - Distribution of equivalent density (g/cm^3) and dominant directions for a coronal (a) and a transverse (b) slice of the distal femur.

Figure 3.17 illustrates the distribution of the equivalent density and the dominant directions for a coronal (a) and a transverse (b) slice of the distal femur.

The regions where the high and low values for density are located are collected in Table 3.6.

Table 3.6 - Summary of the regions of high and low density and stiffness values.

Regions	**Proximal femur**	**Femoral condyles**
High density / stiffness	Greater trochanter Centre of the femoral head Calcar femorale Superior and inferior part of femoral neck Cortical shaft	Intercondylar notch Articular surface of the patella Cortical shaft Medial condyle Epiphysis
Low density / stiffness	Centre of femoral neck Medial inferior part of the femoral head Lateral superior part of the femoral head Intra-medullary canal	Epiphysial line Lateral condyle Intra-medullary canal Metaphysis

Figure 3.18 shows the calculated cumulative density distributions for an orthotropic and isotropic adaptation process compared against a CT scan of an ethically obtained specimen of a male cadaveric femur, 27 years old, weight 75 kg and height 175 cm taken with a SOMATOM Definition AS+ scanner (Siemens AG, Munich, Germany) based in the Queen Elizabeth Hospital,

Birmingham, United Kingdom. The specimen was scanned at 120 kV and 38.0 mAs and with an effective spatial resolution of 0.71 mm. The specimen's density was calculated by converting the Hounsfield Units (HU) values obtained with the CT scan to density values, using a relationship calculated by Dalstra for different regions of the pelvic bone (Dalstra et al. 1993).

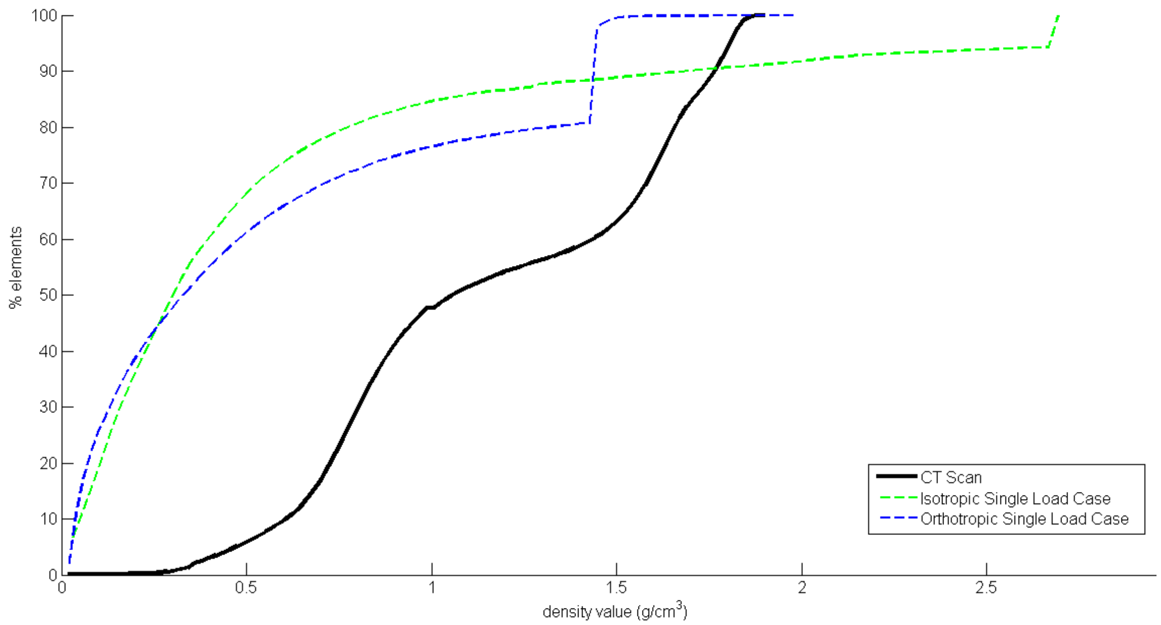

Figure 3.18 - Cumulative density distributions for an isotropic (green dashed line) and orthotropic (blue dashed line) adaptation algorithm were compared against the values obtained from a CT scan (black line).

A coronal slice representation of the density distributions resultant from the isotropic (a) and orthotropic (b) adaptation processes for a femur undergoing single leg stance can be seen in Figure 3.19.

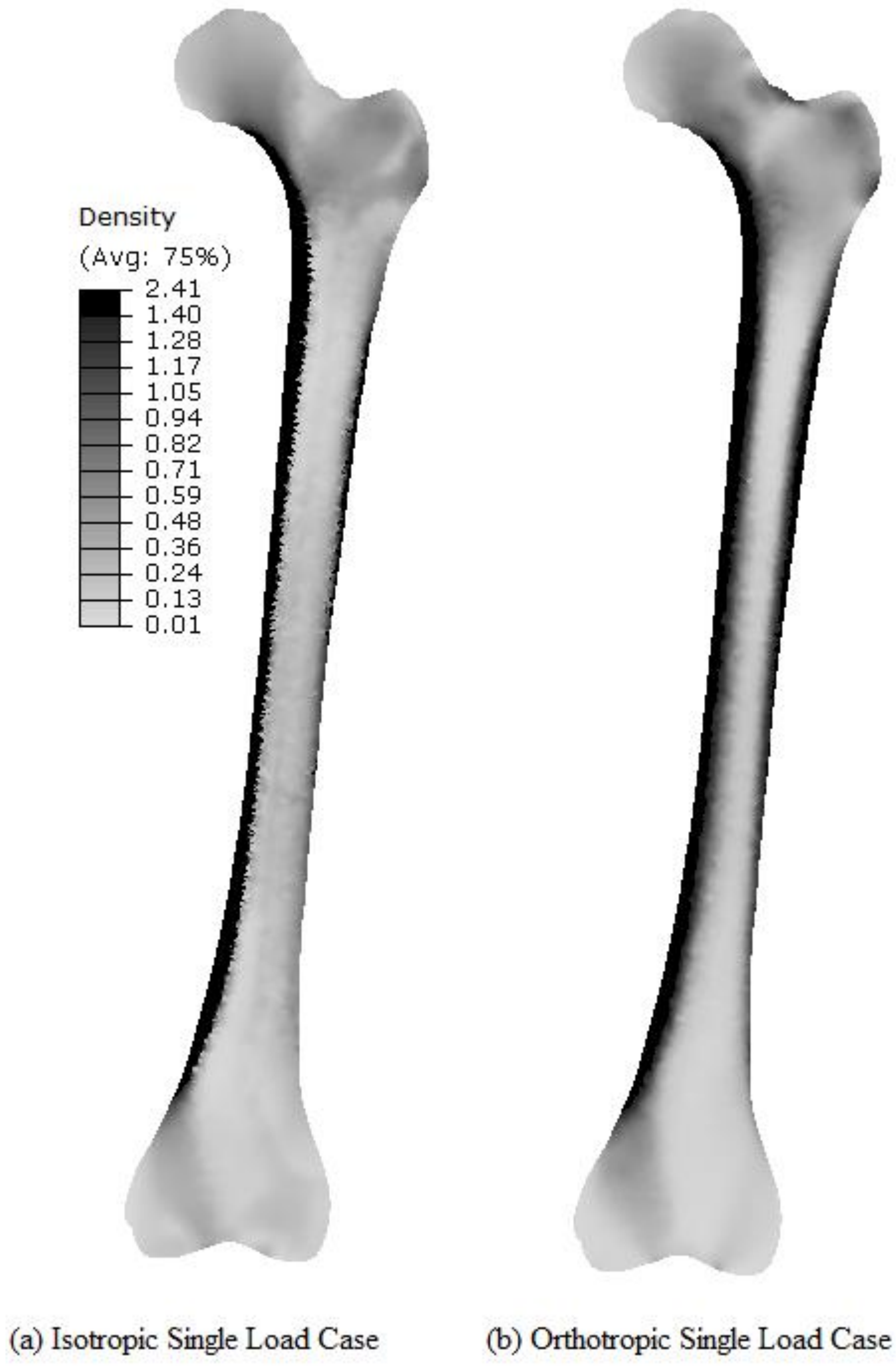

Figure 3.19 - Coronal slice representation of the density distributions resultant from the isotropic (a) and orthotropic (b) adaptation processes for a femur undergoing single leg stance.

3.3 Discussion

3.3.1 Model Results

Analysis of the von Mises stresses, maximum principal strains and minimum principal strains distribution (Section 3.2.1.1) indicates that bending occurs predominantly in the coronal plane during single leg stance. High absolute strain and stress values can be observed in the medial and lateral sides of the cortical shaft, as well as in the lesser trochanter. In comparison, significantly lower values can be found in the anterior and posterior sides of the cortex, the proximal femur and the condyles. Principal strains and von Mises stresses were found to be below 3000 µstrain and 60 N/mm^2, respectively, in agreement with the results obtained by Phillips (Phillips 2009). The resulting minimum principal strains showed a similar distribution overall. The target values for the remodelling plateau of the adaptation algorithm were set between 1000 and 1500 µstrain. Despite this, there are still regions where the absolute values for the femoral principal strains fall outside this range, below the limits defined by Frost for the initiation of micro damage process (Frost 1987). These are similar to studies where the adaptation process was not considered (Duda et al. 1998; Polgar et al. 2003; Speirs et al. 2007; Phillips 2009). This might suggest that the remodelling plateau is an optimum attractor state that bone attempts to optimise itself to, but not necessarily reach . The bodyweight of 1000 N assumed to generate the 5/6 BW downwards force applied at the L5S1 joint can be considered to be high and therefore generate higher strains than expected. Proportional reduction of strains and stresses approach the results obtained to the ones measured by Aamodt (Aamodt et al. 1997).

The positioning of the femur at a 7° angle in the sagittal plane increased bending in this plane which, together with the stabilising action of the muscles spanning the hip joint, could result in the increase of compressive strains in the lesser trochanter region and explain the differences in the F_y components (-4% compared to 18% - 30%) of the HCF (Bergmann et al. 2001). The predicted resultant HCF was 261% BW, close to the range of the peak contact forces measured for two patients (223% - 253% BW) (Bergmann et al. 2001). The x component, F_x, (56% BW) and the z component, F_z, (255% BW) of the contact force are close to Bergmann's measured equivalents (20% - 51% and 222% - 247%, respectively) (Bergmann et al. 2001). The predicted knee contact force of 278% BW was in agreement with the measurements by D'Lima (D'Lima et al. 2006; D'Lima et al. 2008) and calculated by Kutzner (Kutzner et al. 2010). The directional components F_x, F_y and F_z are also close to the ranges from the aforementioned works. Furthermore, a 51.3%-48.7% medial-lateral split in joint reaction forces in the tibial tray was found, providing a good comparison to the data collected in the same studies. The contact pressures (not shown) indicated that the maximum values found for the hip and knee joint contact pressures matched predicted areas of high contact pressures published in different numerical studies (Dalstra and Huiskes 1995; Pedersen et al. 1997; Clarke et al. 2012) and measured with *in vivo* prosthesis (Hodge et al. 1986).

Table 3.5 outlined the muscle and ligament forces above 10 N. These show good agreement with the ones published for a similar model (Phillips 2009). In particular, the gluteus medius, gluteus minimus and biceps femoris (short head) produced forces very close to the ones reported. Overall, the muscle forces are slightly higher, which might be explained from the increased bending in the sagittal plane resulting in activation of the abductor and adductor muscles that stabilise the hip. This increase could result from the inclusion of the sagittal tilt, increasing the moment arm resultant from the application of the HCF on the femoral head. Significant forces were produced by the abductors and iliotibial tract in order to maintain balance in the coronal plane, as predicted by Heller (Heller et al. 2001). Some muscle groups did not produce significant forces, which can be explained by the nature of the activity modelled. Single leg stance does not involve extenuate muscle activations, large contact forces or extreme bending resulting from high flexion angles (Bergmann et al. 2001). This is also reflected in the low forces generated by the ligaments included. Furthermore, the linear definition of the muscles and ligaments modelled does not take into account muscle synergies and co-contractions, as it converges to the minimum energy solution for the model's deformations. Nevertheless, this approach is considered to be a reasonable approach to model daily activities, where no extreme muscle activations are required.

3.3.2 Material Properties

A converged solution to the material distribution and directionality in the femur was obtained after the 27th iteration. The areas where medium or high stiffness and density values for the proximal femur can be found were located in the greater trochanter, along the lateral epiphysis, towards the articular surface of the femoral head, the inferior side of the femoral neck, the calcar femorale and along the diaphysis (Table 3.6). The regions where low stiffness and density values are present are the superior part of the greater trochanter, the intra-medullary canal, Ward's triangle, Babcock's triangle in the medial inferior region of the femoral head and the lateral superior region of the femoral head. High E_1 values associated with compression can be observed predominantly in the medial side of the proximal femur whereas the high E_3 values associated with tension are located mostly in the lateral side of the same region (Figure 3.13). The values for E_1 and E_3 seem to reach their higher limit in different regions of the femur, suggesting that their upper limit needs to be revised.

Figure 3.15 shows the elements associated with E_1 (associated with compression) and E_3 (associated with tension). The areas where medium or high stiffness values can be found for the proximal femur are areas of high compression or tension stresses. These high stresses result from the bending of the proximal femur because of the application of the HCF and the action of the attached muscle groups (Garden 1961; Skedros and Baucom 2007). The lower value regions observed correspond to regions known for being either composed of thin and loosely arranged trabeculae, or where virtually no trabecular bone can be found (Singh et al. 1970).

The main documented trabecular groups (Singh et al. 1970) are also clearly represented: The primary and secondary compressive groups in blue; the primary and secondary tensile groups as well as the greater trochanter group in red (Figure 3.15). These arise as a structural response to the necessity to transfer load along the femur from an oblique to a vertical direction (Ward 1838; Garden 1961; Takechi 1977). These predictions correlate with other 2D and 3D studies of the proximal femur (Huiskes et al. 1987; Fernandes et al. 1999; Miller et al. 2002; Tsubota et al. 2009).

Because of the orthotropic assumption, the intersection of trabeculae in the region below the epiphysis is, in effect, orthogonal. Although this agrees with Wolff's trajectorial theory, other studies have measured the angle of decussation to be acute (Garden 1961; Skedros and Baucom 2007). This is the limitation of assuming bone to be a continuum with local orthotropic symmetry under simple loading. However, orthotropy has been shown to be a closer approximation to bone's anisotropy than the isotropic assumption (Ashman et al. 1984).

Finally, the perpendicular arrangement of trabeculae along the articulate surface of the condyles and the surface in contact with the patella is clearly present (Figure 3.14 and Figure 3.15), particularly in the medial side, in response to the compression caused by the weight bearing function of the femur (Takechi 1977). The high stiffness distribution around the epiphyseal line is a result of the thicker and coarser trabeculae that can be found in this region. In contrast, finer and denser trabeculae were also observed towards the metaphysis. Lastly, the trabeculae radiating from the intercondylar notch towards both condyles were also predicted. The low stiffness distribution in the lateral condyle matches the lower density expected for the region (Takechi 1977).

The advantage of using orthotropic material properties instead of isotropic symmetry is highlighted in Figure 3.18 and Figure 3.19. The isotropic assumption results in 5% of the elements achieving a very high stiffness/density (Figure 3.18). This permits a greater number of elements in comparison to the orthotropic adaptation to have a low stiffness and density but not necessarily accurately represent the density distribution for a coronal slice (Figure 3.19). The isotropic assumption does not predict the dense cortical distribution along the lateral shaft, superior aspect of the femoral neck and the greater trochanter. It is evident that the distinction between cortical and trabecular bone is lost when using the isotropic adaptation algorithm. The almost vertical increase observed at 1.4 g/cm^3 for the orthotropic adaptation process corresponds to the elements of high stiffness predicted along the femoral shaft. The previous Section highlighted this abrupt transition between the intra-medullary canal where virtually no bone is found and the stiff cortical layer.

Material properties converged quickly after three iterations. This explains the coinciding convergence of muscle forces and joint contact forces: the structure is reaching its structural integrity, with changes in material distributions becoming increasingly small with the progression of the iterative process. The iterative process could, therefore, be cut short earlier if the adaptation simulation is under severe time constraints.

The use of a single load case is a limitation when describing the complex mechanical environment the femur is subjected to physiologically. This is demonstrated by the under-prediction of stiffness at the distal femur, in particularly in the lateral condyle. Reduced wall thickness in the anterior and posterior aspects of the cortical shaft was also observed as a result of the simplified loading applied. Inclusion of more load cases for a variety of frequent daily activities will allow a more accurate prediction of the distribution of the mechanical properties and associated orientations. This will improve predictions particularly in the condyles, the distal part of the femur adapted to both mechanical compression and rotary movements (Takechi 1977). However, the inclusion of more daily activities will result in an increase in the shear stresses in the femur, with the resistance of the trabecular structures to shear potentially playing a more important role than in the single load case model (Skedros and Baucom 2007).

3.4 Concluding Remarks

This Chapter outlined the creation of a 3D FE model of the whole femur undergoing single leg stance, where the hip and knee joints, muscles and ligaments were explicitly included. The iterative orthotropic strain-adaptive algorithm developed in Chapter 2 was applied to this model. The principal strains, von Mises stresses, joint reaction forces, and muscle and ligament forces produced by the model are coherent with the ranges measured in literature and reported in published work. The forces and material properties predicted by the model and the adaptation algorithm were shown to quickly converge after three iterations.

The orthotropic assumption was shown to produce more physiological density distributions than when isotropic symmetry was considered. The orthotropic algorithm is capable of clearly predicting the appearance of the cortical layers and trabecular groups expected in a coronal section of the whole femur whereas the isotropic assumption either over-estimates the density and stiffness of cortical bone while producing density distributions that resemble less what has been observed *in vivo*. Furthermore, the fact that the directionality of the femoral structures can be extracted with this method is a product from considering bone to have orthotropic material symmetry. The isotropic assumption could not produce such directional information.

Despite the inclusion of an adaptation algorithm targeting a remodelling plateau around a target normal strain, absolute principal strains were still found outside these values, similarly to other FE studies that did not considered an iterative process. Furthermore, it was also shown in this Chapter that the stiffness distribution and structure directionality for the whole femur may be correctly assessed, with results approaching those observed and measured *in vivo*.

However, further development to this method is required in order to improve the predictions obtained with this method. The inclusion of more load cases, creating a loading envelope more representative of what the femur is subjected to *in vivo*, is expected to allow better predictions of the femur's material properties and orientation distributions, in particularly for its distal part. The upper limit for the directional orthotropic Young's moduli also needs to be revised.

Chapter 4

Multiple Load Case 3D Femur

It has been demonstrated that the loading configuration of finite element (FE) models is of key importance in order to physiologically reproduce the mechanical environment surrounding bone (Polgar et al. 2003) and achieve the best driving signal for bone remodelling (Bitsakos et al. 2005). The results obtained for the Single Load Case 3D Femur Model (Chapter 3) indicate that the use of a single load case might be limiting when describing the complex mechanical loading of the femur. Observation of the material properties distribution and their associated orientations for the same model suggest that inclusion of more load cases for daily activities might allow for a more accurate prediction, particularly in the distal region of the femur.

In an attempt to represent the full loading environment on the femur more accurately, modifications were performed to the Single Load Case 3D Femur Model (Chapter 3) and to the strain-adaptive orthotropic bone adaptation algorithm (Chapter 2). These implementations were required in order to allow for modelling of multiple instances of frequent daily activities, resulting in the creation of the Multiple Load Case 3D Femur. Level walking and stair climbing were chosen as the load cases to be modelled, since they are the most frequent daily activities that generate hip contact forces above 200% BW (Morlock et al. 2001).

The femoral geometry, mesh, initial material properties and coordinate system remained the same as for the Single Load Case 3D Femur Model. Section 4.1 describes how the hip and knee joints were re-defined in order to allow for modelling of different frames of daily activity cycles. Section 4.2 focuses on the modifications implemented to the muscle structures defined in Chapter 3. The definition of the multiple activity frames loading and positioning is explained in Section 4.3 and the boundary conditions applied to the model detailed in Section 4.4. Finally, the changes to the adaptation algorithm proposed in Chapter 2 in order to accommodate multiple load cases are outlined in Section 4.5.

4.1 Joint Definition

The inclusion of multiple load cases instead of a unique frame representing single leg stance requires an increase in the number of loads being applied to the femur and a wider envelope of femoral orientations. In order to model multiple load cases and positions, the hip and knee joints were re-defined. The modifications at the hip joint allow for the transfer of the inter-segmental forces and moments acting between the pelvis and the femur. The knee joint was modified to improve stability in activities with high flexion angles and knee reaction forces, a shortcoming of Single Load Case 3D Femur Model. This Section describes the key changes made to these structures in order to allow the modelling of the femur undergoing different instances of two different load cases (level walking and stair climbing).

4.1.1 Hip Joint

A 2 mm thick bi-layered structure was projected from the contact surface of the femoral head with the acetabulum, with its centre coincident with the centre of the femoral head (Figure 4.1, (a) and (b)). A 1 mm thick internal isotropic elastic layer representing cartilage ($E = 5$ MPa, $\nu = 0.49$) was modelled with 2965 six-noded wedge elements (C3D6) and can be seen as the red region in Figure 4.1(a). A 1 mm thick external isotropic elastic cortical bone layer ($E = 18$ GPa, $\nu = 0.3$) was also modelled with 2965 hexahedral C3D6 elements, and can be seen in grey in Figure 4.1(a,b). The 1532 nodes on the surface of the external layer were connected to the centre of the femoral head (coincident with the global origin) via stiff truss elements (T3D2) ($E = 10$ GPa, $\nu = 0.3$), with a cross-sectional area of 0.785 mm^2 (radius of 0.5 mm) seen in beige in Figure 4.1(a).

An artificial stiff truss structure, representing the acetabular region, was modelled according to the free boundary condition modelling approach (Phillips 2009) using stiff truss T3D2 elements ($E = 10$ GPa, $\nu = 0.3$), and is highlighted in red in Figure 4.1 (c). The same truss elements connected the acetabular structure to muscle insertion points on the pelvic bone, sacrum, lumbar spine and a point representative of the L5S1, as proposed by Phillips (Phillips 2009). The acetabular structure was connected via two-noded linear beam elements (B31) with a cross-sectional area of 10mm^2 ($E = 20$ GPa, $G = 10$ GPa) back to the centre of the bi-layered structure. The inclusion of the beam elements allowed for the moments and inter-segmental forces applied to the centre of the femoral head to be transferred back to the acetabular structure (highlighted in Figure 4.1(c)).

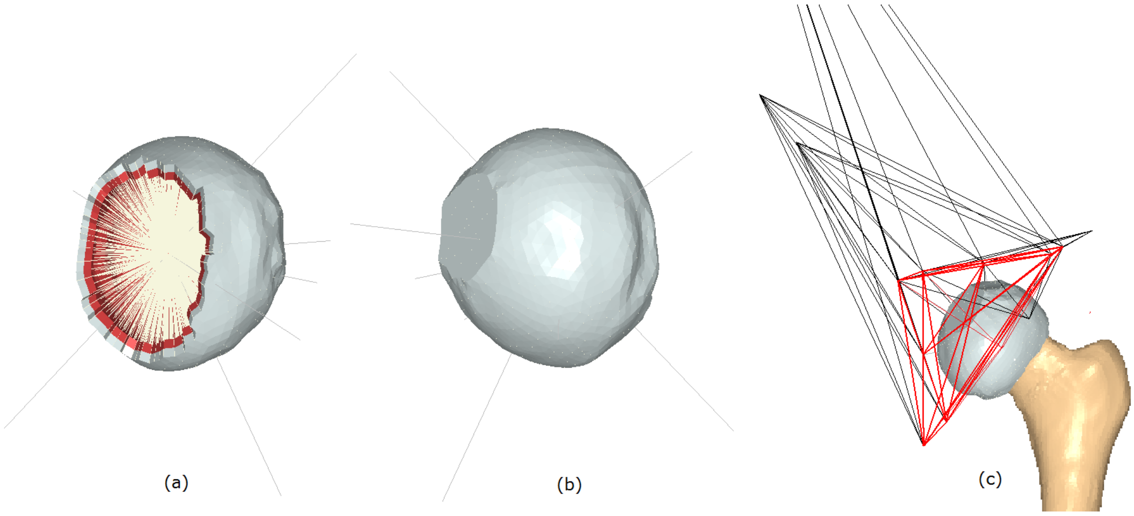

Figure 4.1 - Two different views of the bi-layered structure surrounding the contact area of the femoral head (left, middle) and the same structure with the acetabular and pelvic constructs also included (right).

Similar to what was described in Chapter 3, the acetabular and pelvic regions, together with the hip muscle insertions on the pelvic structure, were not constrained in any degree of freedom. This was implemented so that the free motion of the pelvis around the femoral head could be mimicked. The inclusion of the muscles spanning the hip joint stabilised the pelvic movements, resulting in a balanced model (Figure 4.2).

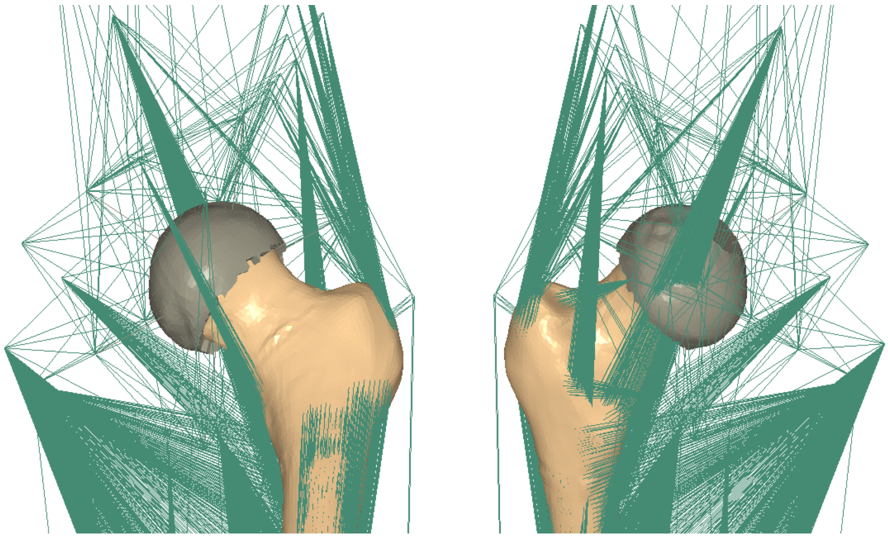

Figure 4.2 - Anterior and posterior views of the pelvic region after the muscles spanning the hip joint were included.

4.1.2 Knee Joint

The knee region was divided into two main structures modelling the tibio-femoral and the patello-femoral joints. These were defined similarly to the hip joint structure described in Section 4.1.1.

4.1.2.1 Tibio-Femoral Joint

A 2 mm thick bi-layered structure, representing the cartilage surrounding the condyles and the action of the tibial plateau, was projected from an anatomically appropriate hand-picked surface in the distal femoral region. This structure was defined with two sets of 2656 hexahedral elements with the same material properties as in the structure defined for the hip joint (Figure 4.3, cartilage layer in red and cortical layer in green).

The condylar axis is the axis along which tibio-femoral flexion movement occurs (van Campen et al. 2011) and was scaled to this model based on Klein Horsmann's measurements (Klein Horsman et al. 2007). This axis was introduced in order to restrict the tibio-femoral movements to the flexion/extension plane (in a hinge-like fashion) and allow for comparison with the forces produced by Modenese's musculo-skeletal model (Modenese et al. 2011). This formulation is also considered to be more realistic than the contact interaction defined for the Single Load Case 3D Femur Model (Chapter 3).

1420 truss elements connected the 710 surface nodes to two points along the condylar axis in the medial and lateral condyles (Figure 4.3, in beige), in order to simulate this interaction. These two nodes along the functional knee joint axis were connected with a B31 beam element in order to transfer the moments between them. The medial node was fixed against displacement. The boundary conditions and surface interactions are described in Section 4.4.

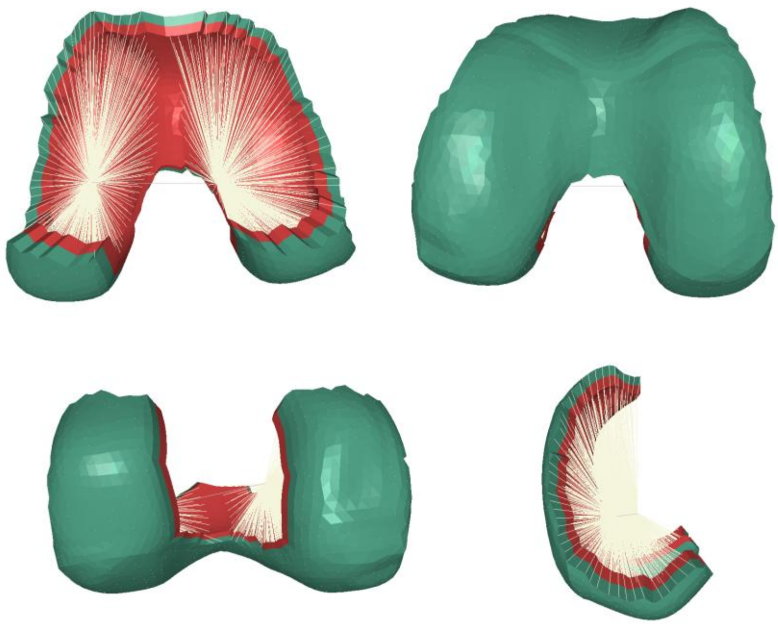

Figure 4.3 - Different views of the tibio-femoral joint structure.

4.1.2.2 Patello-Femoral Joint

Similarly to the tibio-femoral joint, a 2 mm thick bi-layered structure representing the patello-femoral joint, was projected from an anatomically appropriate hand-picked surface in the distal femoral region, corresponding to the contact surface of this region with the patella during sliding (Li et al. 2007). This structure was defined with two layers of 836 C3D6 elements similarly to the hip and the tibio-femoral joint. Figure 4.4 shows the cartilage layer in red and a stiff cortical layer as the one defined for both the hip and the tibio-femoral joint (E = 10 GPa, $\nu = 0.3$) in grey. The 474 external surface nodes were connected by two sets of B31 elements to two points along the patellar axis (Figure 4.4, in grey). The patellar axis was defined as two points either side of the centre point of a sphere of best fit for the external patellar surface, using the mean least square method. The orientation of the patello-femoral joint functional axis was scaled from Klein Horsmann's measurements (Klein Horsman et al. 2007). 14 extremely stiff two-noded axial connector elements (C3D2) (E = 1000 GPa) were included to create a hinge-like trapezoid structure, representing the region of the patella connected to the patellar ligament and the quadriceps, and allowing for force transfer back to the femur (Figure 4.4 (c)).

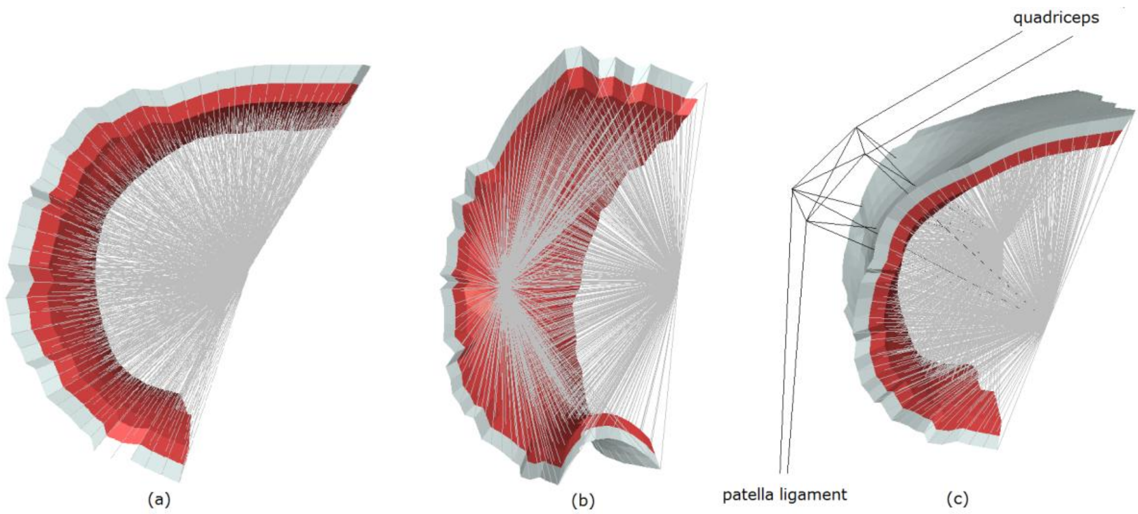

Figure 4.4 - Different views of the patello-femoral joint structure and its connections to the patella ligament and quadriceps.

A frontal and view of the distal region of the femur after inclusion of the patello-femoral and tibio-femoral structures and the muscles and ligaments spanning the knee joint can be seen in Figure 4.5.

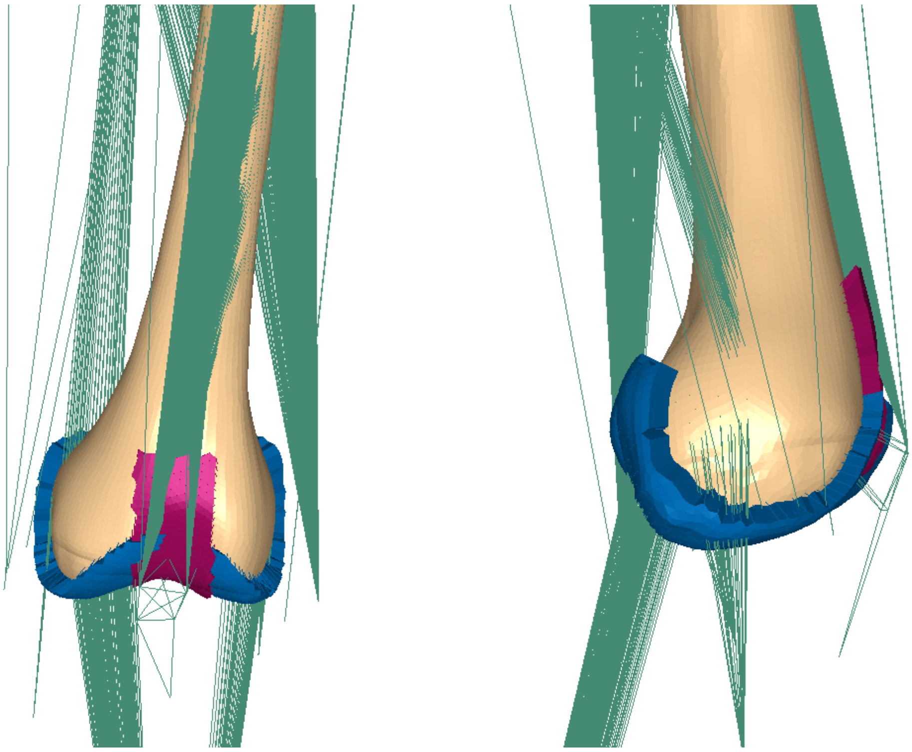

Figure 4.5 - Frontal and medial views of the distal region after inclusion of the muscles and ligaments (green) spanning the knee joint and the tibio-femoral (blue) and patello-femoral (magenta) joints.

4.2 Muscle Definition

Similar to the Single Load Case 3D Femur Model described in the previous Chapter, a total of 26 muscles and 7 ligamentous structures were included explicitly. These were modelled as groups of spring (C3D2) elements (Phillips 2009), spanning between the muscle origination areas extracted from the Standardised Femur (Viceconti et al. 2003a). The Standardised femur's muscle origination areas were mapped onto the femoral mesh. The muscles insertion points in the pelvic and tibial region were based on the Single Load Case 3D Femur Model detailed in the previous Chapter. Changes were applied to some muscles' definition in order to represent their anatomical position and function more physiologically when multiple load cases were considered. These changes were included to allow muscle wrapping around the greater trochanter and increase stability of the knee joint during high flexion positions.

The iliotibial tract structure was modelled with three connector elements: the first, running from the insertion point on the pelvis to a point representing its turning point at the greater trochanter, and two elements spanning between this turning point and the structure's insertion point at the tibia. This increase of the number of elements running along the femoral shaft was necessary in order to decrease bending of the femur in the medial-lateral plane (Merican and Amis 2009).

The tensor fascia latae was modified to allow wrapping around the greater trochanter and transfer force back to the femur. This region of the muscle contact was modelled as a bi-layered structure composed of 1250 C3D6 elements with a soft 1 mm thick internal isotropic elastic layer ($E = 5$ MPa, $\nu = 0.49$) and a 1 mm thick isotropic elastic layer ($E = 10$ GPa, $\nu = 0.3$) (Figure 4.6, left), tied to the contact area with the greater trochanter, similarly to the joint structures defined in Section 4.1. The structure was connected to the wrapping axis via T3D2 elements ($E = 10$ GPa, $\nu = 0.3$), with linear elasticity modified so that compressive stresses could not be generated, and a cross-sectional area of 0.785 mm^2. The wrapping axis was defined as a line perpendicular to the anterior-posterior plane going through the centre of a sphere fitted to the external surface of the greater trochanter. This axis was then connected to a hinge-like truss structure, functioning as the via-point where the tensor fascia latae meets the iliotibial tract (Figure 4.6, right).

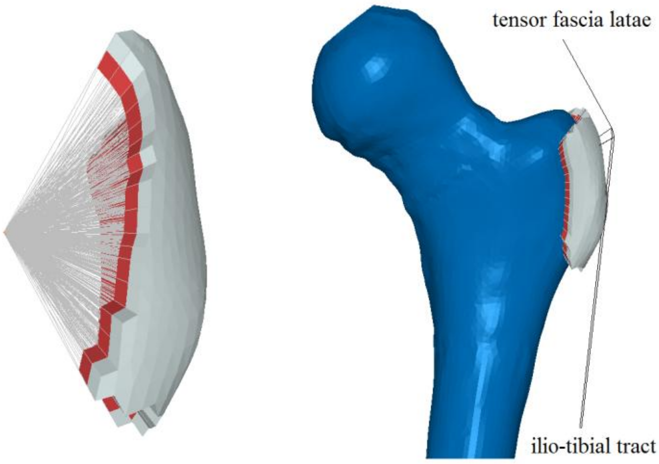

Figure 4.6 - The tensor fascia latae structure (left) and its positioning in the proximal femur (right).

The point in space representing the insertion at the lumbar spine was connected to ground via a spring element with a stiffness of 10 N/mm in the anterior-posterior direction, and negligible stiffness in the other two directions (0.1 N/mm), in order to simulate the balancing action provided by the upper torso during the different gait activities (Callaghan et al. 1999). The resulting model with all the joints, muscles and ligamentous structures can be seen in Figure 4.7.

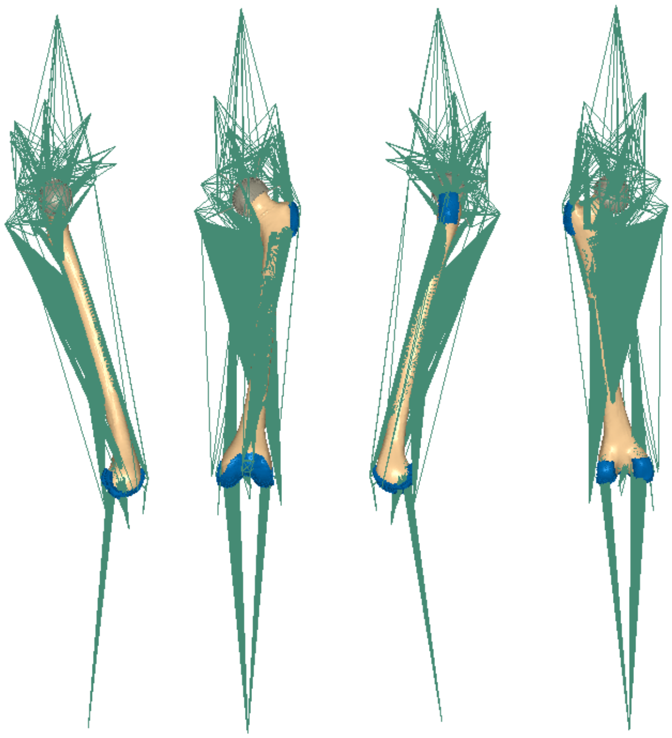

Figure 4.7 - Medial, anterior, lateral and posterior views of the Multiple Load Case 3D Femur Model.

4.3 Multiple Load Cases

Eighty loading configurations corresponding to forty time steps for each of two activity cycles (level walking and stair climbing) were modelled. The sampling rate of the load cycle signal was considered in accordance with the Nyquist-Shannon sampling theorem (Shannon 1949). This theorem states that an analogue signal can be accurately reconstructed if the sampling rate exceeds 2n, where n is the highest frequency of the continuous Fourier Transform of that signal. Since 99.7% of the human gait contact forces signal power is below the 7th harmonic (7 Hz) (Winter et al. 1974), the required sampling rate to reproduce this signal reliably would be of 14 samples per second. The lowest sample rate for both activities modelled was of 26.5 samples per second (40 frames modelled for 1.51s of gait cycle), comfortably above the minimum requirements for this signal sampled from Bergmann's HIP 98 published data (Bergmann et al. 2001). The frame where the peak hip joint force was measured for each of the activities considered was included in the forty samples taken.

The segment positioning and orientation were extracted from Modenese's analysis of the data published in HIP 98 (Bergmann et al. 2001; Modenese et al. 2011), where data collected by instrumented prosthesis implanted in four subjects was made publicly available. Two daily activities were selected and sampled for the same subject (HSR) – level walking (HSRNW4 trial) and stair climbing (HSRSU6 trial). HSR was the chosen subject, since the data produced from his trials has been considered in other studies (Heller et al. 2001; Heller et al. 2005; Modenese et al. 2011). The inter-segmental moments and forces were extracted from an open source musculo-skeletal model[1] (Modenese et al. 2011; Modenese 2012) developed in OpenSim (Delp et al. 2007), which has been validated against the same public dataset. Inverse dynamics analyses were performed on Bergmann's published kinematic and kinetic data for the same subject's trials, and the inter-segmental forces and moments between the pelvis and the femur were extracted. It is important to note that the inter-segmental forces and moments are independent of the muscle definitions implemented in that model.

[1] https://simtk.org/home/low_limb_london

4.3.1 Segment Positioning

The models were split into three segments: the femur, the pelvic region and the tibial region, with each feature of the model (bone, insertion and origin points for the muscles, via points) assigned to one of them.

The global coordinate system and femur segment local coordinate system used were the same as discussed in Section 3.1.1.1 and are coincident for the neutral position (see Figure A.3 in the Appendix).

The local pelvic segment coordinate system was coincident with the femoral coordinate system for a neutral position and defined according to ISB recommendations (Wu et al. 2002) as follows: (i) the origin was considered to be coincident with the centre of the femoral head (which was assumed to be the hip centre of rotation) (Klein Horsman et al. 2007). (ii) The x axis as a line parallel to the line connecting both pelvic anterior superior iliac spine bony landmars (ASIS) and pointing medially. (iii) The y axis as a parallel line to the line defined by the mid-point of the two ASISs and the midpoint of the right and left posterior superior iliac spine (PSIS) bony landmarks, perpendicular to the x axis and pointing anteriorly. (iv) The z axis as the line perpendicular to both x and y axis, pointing superiorly.

The tibial segment flexion axis was defined as the functional knee axis proposed by Horsman (Klein Horsman et al. 2007), in agreement with Modenese's model from where the segment position data was extracted (Modenese et al. 2011). A diagram explaining the local coordinate systems for a neutral position of the femur is included in Figure A.4 in the Appendix.

The kinematics of the lower limb movements for level walking and stair climbing were extracted from Modenese's analysis of the data published in HIP 98 (Bergmann et al. 2001; Modenese et al. 2011), and adjusted in order to match the coordinate system of this model. The rotation angles for the pelvis (θ_x, θ_y, θ_z), femur (α_x, α_y, α_z) and tibia (β) can be seen in the Appendix in Table A.1 and Table A.2 for the two activities modelled. Flexion/extension was determined by rotation about the x axis, abduction/adduction about the y axis and internal/external rotation about the z axis.

The points in the pelvic region were rotated in Abaqus about an axis whose origin coincided with the origin of the coordinate system. The same was implemented for the femoral rotation. The tibial rotation was applied about the transformed functional knee axis, after the femoral rotation was performed.

In order to achieve the segment positioning in Abaqus, a single rotation angle and a single rotation axis were extracted from the direction cosine matrix (DCM), or rotation matrix, used to achieve the segment positioning in Modenese's model (Modenese et al. 2011). The DCM was calculated for each of the segments, using the rotation angles applied in the same order as in Modenese et al. 2011: abduction, rotation and flexion.

A MATLAB function developed by James Tursa, *angleaxis.m* (Tursa 2007) was then used to calculate the equivalent Abaqus rotation angle (φ) and rotational axis (r_1, r_2, r_3) from the DCM. The Abaqus rotation angles and axes for the femur and pelvis for both load cases considered can be seen in Table A.3 and Table A.4 in the Appendix. A second rotation of angle β about the transformed functional knee axis was then applied to all the translated points in the tibial segment.

The final segment positions were checked for arbitrarily chosen instances of the load cases modelled and their correct positioning confirmed. The muscle lines of action were also verified in order to assess whether the connector elements crossed the femur model in non-physiological paths.

Lateral views of the final femoral positions for the models generated for both level walking and stair climbing can be seen in Figure 4.8 and Figure 4.9.

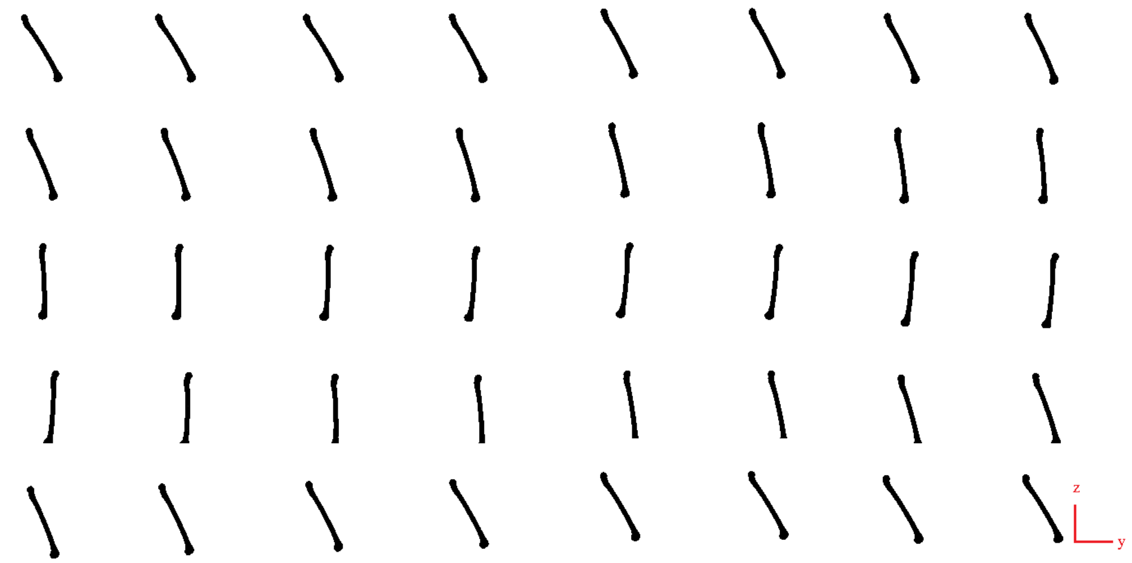

Figure 4.8 - Lateral views of the femur positions for level walking (HSRNW4), increasing from 1 to.

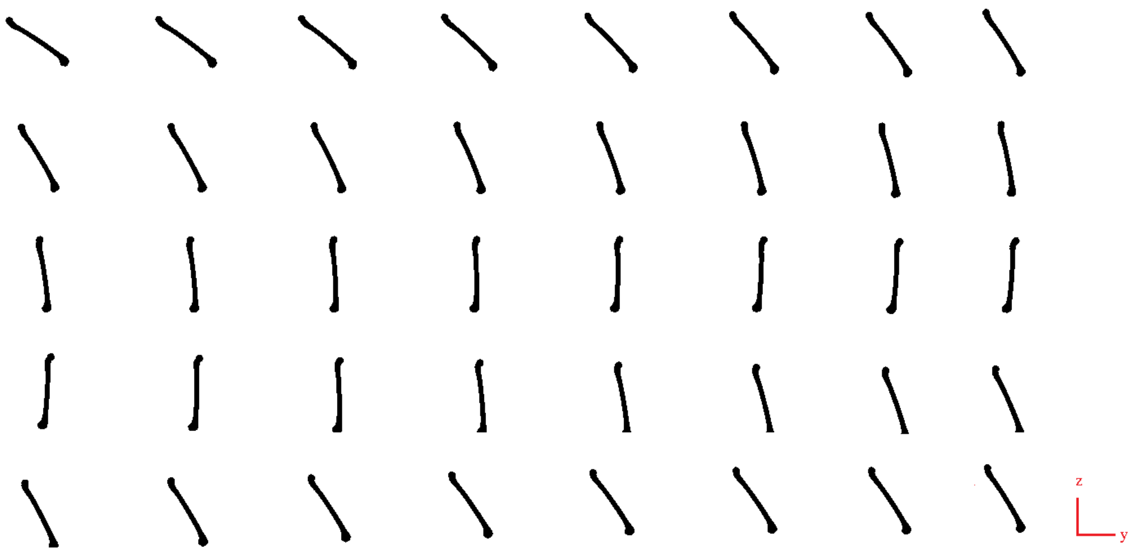

Figure 4.9 - Lateral views of the final femur positions for stair climbing (HSRSU6), increasing from 1 to 40.

4.3.2 Loading

The application of a single downwards 5/6 BW load to the point representing the L5S1 vertebrae in the Single Load Case 3D Femur Model was an oversimplification, as it ignores the role of the upper body. Nevertheless, this simplification was considered to be representative of the mechanical loading on the femur during static activities, such as single leg stance (Phillips 2009).

However, for daily activities where higher ranges of motion are present, such as the ones modelled in the Multiple Load Case 3D Femur Model, the inertial action of the controlateral leg and the missing torso need to be considered (Heller et al. 2001; Modenese et al. 2011), in order to equilibrate the segments modelled during the static analysis without influencing muscle recruitment. Inter-segmental forces and moments calculated with Modenese's model (Modenese et al. 2011; Modenese 2012) were extracted for the two activities in question (HSRNW4 and HSRSU6). This model has been validated against the *in vivo* hip contact forces measured by instrumented prosthesis available in HIP 98 (Bergmann et al. 2001) for all patients in the study. The use of these inter-segmental forces and moments also allows for direct comparison with the hip contact forces measured and calculated in the aforementioned studies, and validation of the mechanical environment modelled.

The inter-segmental forces and moments were applied at the centre of the bi-layered hip joint structure described in Section 4.1.1 and extracted from the trials of subject HSR in HIP 98 (Bergmann et al. 2001). The values used for the models representing the level walking load case are relative to the HSRWN4 trial and can be seen in Figure 4.10 and Table A.5 (in the Appendix); the values used for the modelling of the stair climbing activity correspond to the HSRSU6 trial and are reported in Figure 4.11 and Table A.6 (in the Appendix). A representation of the global coordinate system used to apply these forces and moments can be seen in Figure A.3 (Appendix).

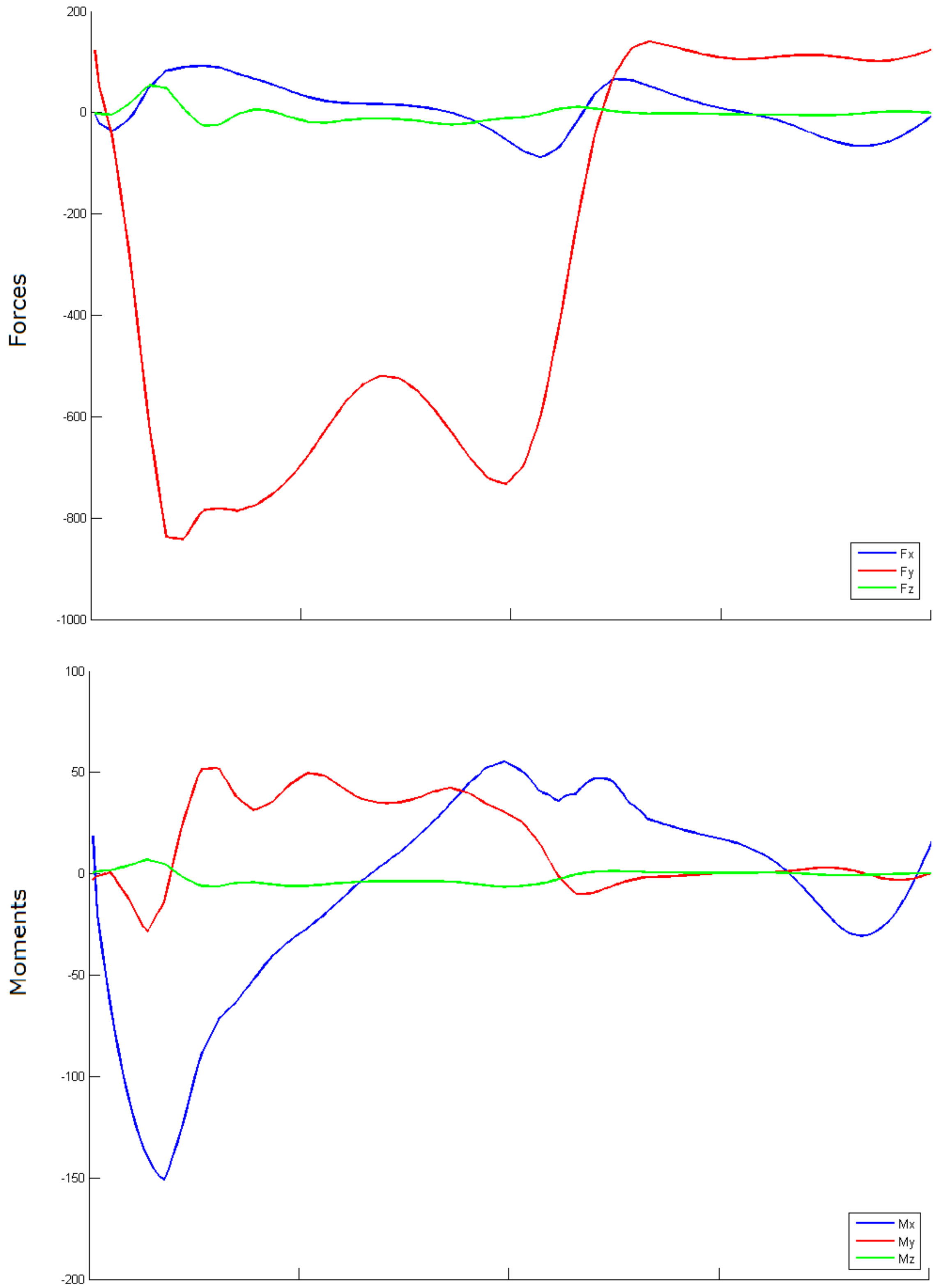

Figure 4.10 – Inter-segmental forces (N) (top) and moments (N/m) (bottom) components for HSRWN4 trial in the global coordinate system (Modenese 2012). Planes: x – medial/lateral; y – anterior/posterior; z – superior/inferior.

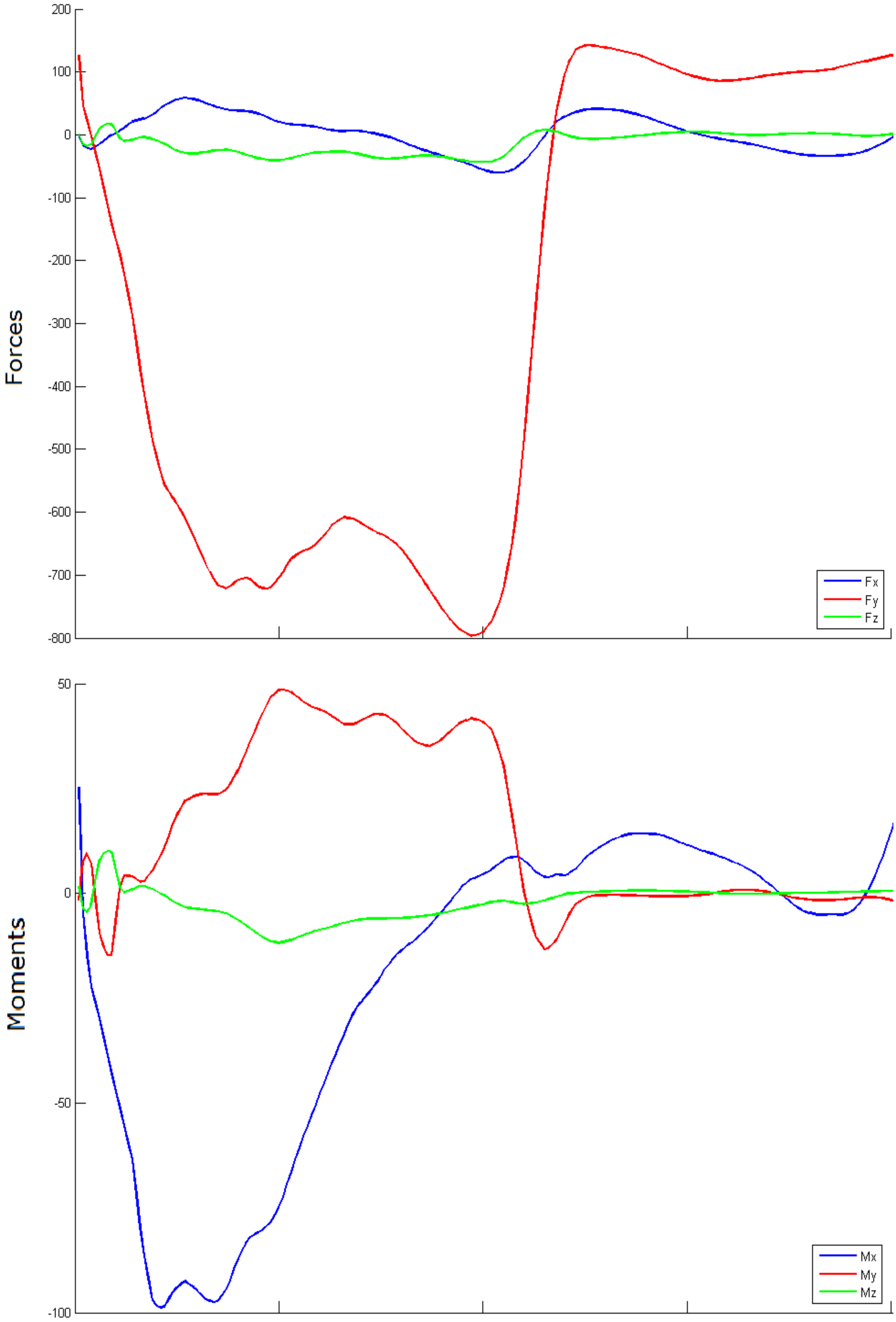

Figure 4.11 - Inter-segmental forces (N) (top) and moments (N/mm) (bottom) components for HSRSU6 trial in the global coordinate system (Modenese 2012). Planes: x – medial/lateral; y – anterior/posterior; z – superior/inferior.

4.4 Boundary Conditions

Surface to surface tie conditions of both displacement and rotational degrees of freedom, were applied to the contact surfaces between the femur and the joint structures modelled. The master surface was considered to be the outer surface of the femur mesh with a position tolerance of 0.25 mm. Analyses of the stress distributions at the joints determined that the bi-layered structures included produced load distributions along the contact surfaces with the femur statically equivalent to the ones generated by frictionless contact modelling. Therefore, contact conditions were not considered in order to reduce computational time, in accordance with Saint-Venant's principle. This theorem states that at sufficiently long distances, the difference between the effects of two statically equivalent loads can be ignored, (Love 1927).

A node along the tibio-femoral axis in the medial condyle was fixed against displacement in all directions, allowing the knee to pivot around the medial condyle in accordance with a study by Johal (Johal et al. 2005) and *in* vivo measurements taken by instrumented prosthesis (D'Lima et al. 2006; D'Lima et al. 2008).

The two nodes along the patello-femoral joint axis that connected to the external bi-layered structures' surface were constrained, restricting the patellar displacement solely to an arc in the plane perpendicular to the axis. This followed the implementation of a hinge-like joint in the musculo-skeletal model produced by Modenese et al. (2011). The two nodes along the tensor fascia latae wrapping axis were also constrained against rotation in the other two directions, allowing for motion only in the wrapping plane of the muscle around the greater trochanter.

Similarly to the Single Load Case 3D Femur Model, fixed constraints were also applied at the insertion points of the muscles and ligaments inserting on the tibia and fibula.

4.5 Algorithm Update

Bone is optimised to resist the stresses resulting from the different daily activities it is subjected to (Skedros and Baucom 2007). Multiple load cases were included in an attempt to reproduce the mechanical environment of the femur and achieve a more physiological envelope of the driving signal for bone remodelling, resulting from the local influence of different load cases in different regions in the bone.

The adaptation algorithm proposed in this work is based on the theory that each element's material orientations will rotate in order to match the local principal stress directions. Since multiple instances of daily activity cycles are considered, a guiding frame (i.e. the frame which produced the highest absolute normal strain value) was defined for each element of the femoral mesh during each iteration of the adaptation process.

The maximum strain values across all frames were selected for each element in order to produce an envelope containing maximum driving stimuli for the material properties and orientations update. This stimulus envelope was used instead of an average strain envelope resulting from the combination of multiple load cases since bone is assumed to be adapted to resist the maximum strains it is subjected to (Fehling at al. 1995; Judex and Zernick 2000; Honda et al. 2001).

Material orientations aligned with the principal stress directions have been shown to be the optimal configuration for an orthotropic material undergoing a single load case (Pedersen et al. 1997). However, in regions where multiple load cases may be influential, trabeculae have been observed to cross at different angles and are suggested to resist the shear stresses that arise (Skedros and Baucom 2007). In order to approach the orthotropic continuum modelling of bone to describe its structural anisotropy, a shear modulus adaptation algorithm was also included in the remodelling process.

These modifications were implemented in an attempt to achieve the optimised material distribution found *in vivo* that allows bone to achieve the highest structural integrity with the least amount of material possible.

4.5.1 Selection of the Guiding Frame and Directionality Update

For each load frame, all the models representing equally spaced instances of the load cases in question were analysed in parallel using the Abaqus standard solver running on Imperial College's High Performance Computer (HPC). After completion of the task, the Output Databases (ODBs) for each load case were copied back to the desktop where the rest of the analysis was carried out. For each one of the ODBs, the strains and stresses found using Abaqus were extracted using a custom developed Python script and processed in MATLAB.

The guiding frame, g, for the adaptation process in each element was selected as the one where the maximum absolute normal strain value, $\boldsymbol{\varepsilon}_n^{max}$, could be found (Equation 4.1).

$$\boldsymbol{\varepsilon}_n^{max} = max\left(\left|\varepsilon_{11}^{1\to nmax}\right|, \left|\varepsilon_{22}^{1\to nmax}\right|, \left|\varepsilon_{33}^{1\to nmax}\right|\right) \qquad (4.1)$$

Only normal components were considered, since the alignment of the orthotropic material axis with the principal stress directions will result in the diagonal components of the strain matrix tending towards the principal strain values. The number of frames, n, ranged between 1 and the total number of models used in the analysis, $nmax$, which was 80, in this case.

After selecting the guiding frame for each of the elements in the femoral mesh, the guiding stress tensor, $\boldsymbol{\sigma}_{ij}^{g}$, was defined as the stress tensor resultant from that frame (Equation 4.2).

$$\boldsymbol{\sigma}_{ij}^{g} = \begin{bmatrix} {\sigma_{11}}^{g} & {\sigma_{12}}^{g} & {\sigma_{13}}^{g} \\ {\sigma_{12}}^{g} & {\sigma_{22}}^{g} & {\sigma_{23}}^{g} \\ {\sigma_{13}}^{g} & {\sigma_{23}}^{g} & {\sigma_{33}}^{g} \end{bmatrix} \qquad (4.2)$$

Similarly to the single load case algorithm (Chapter 2), the principal stress orientations, $\boldsymbol{\sigma}_{pv}^{g}$, for each element can be found by performing an eigen analysis of the guiding stress tensor (Equation 4.3).

$$eig\left(\boldsymbol{\sigma}_{ij}^{g}\right) = [\,\boldsymbol{\sigma}_{pv}^{g} \quad \boldsymbol{\sigma}_{p}^{g}] \tag{4.3}$$

These were defined as the target directions for the rotation of the orthotropic material axes orientations. This step is highlighted in red in the diagram depicted in Figure 4.12.

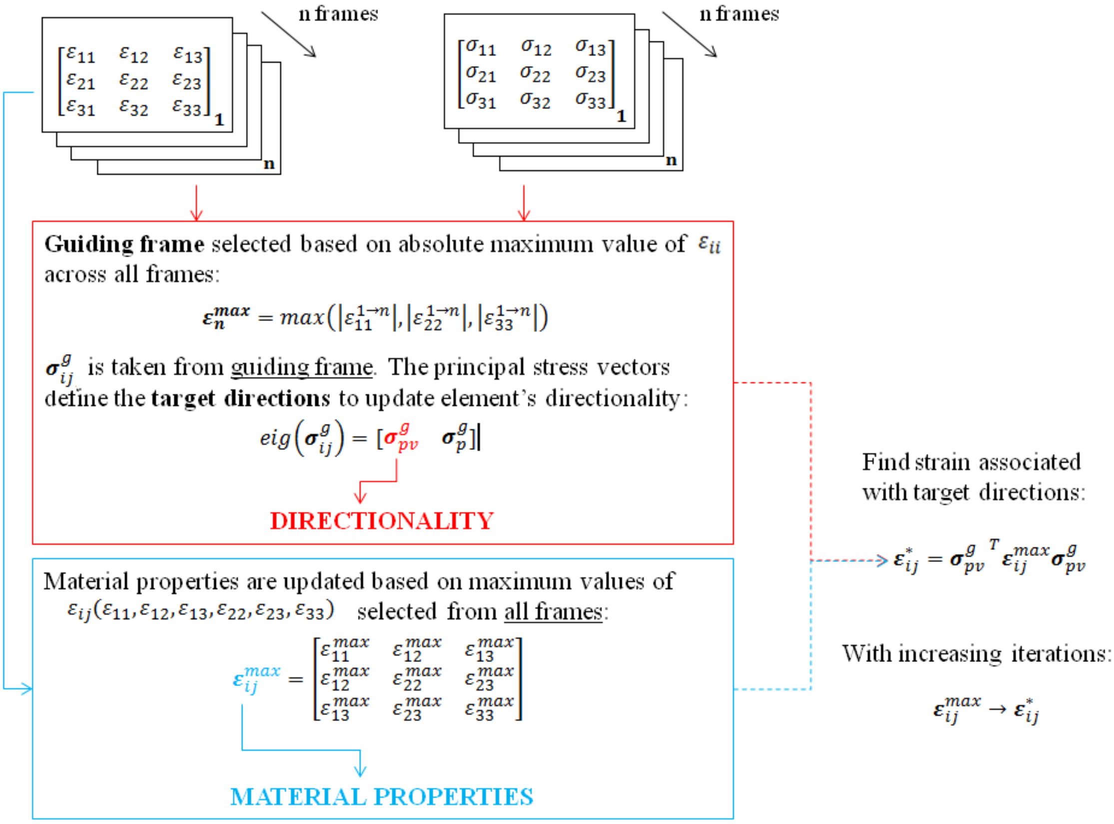

Figure 4.12 - Diagram highlighting the key steps in updating the orthotropic directionality and material properties for the multiple load case adaptation process

4.5.2 Selection of Driving Stimulus

For each element of the femoral mesh, the maximum absolute values, ${\varepsilon_{ij}}^{max}$, for each of the strain components, $\boldsymbol{\varepsilon}_{ij}$, were chosen from across all frames (Equation 4.4).

$$ {\varepsilon_{ij}}^{max} = max\left(abs\left({\varepsilon_{ij}}^{n=1}, {\varepsilon_{ij}}^{n=2}, {\varepsilon_{ij}}^{n=3}, \dots, {\varepsilon_{ij}}^{nmax}\right)\right) , 1 \leq n \leq n_{max} \qquad (4.4) $$

The maximum absolute strain tensor, $\boldsymbol{\varepsilon}_{ij}^{max}$, then becomes

$$ \boldsymbol{\varepsilon}_{ij}^{max} = \begin{bmatrix} {\varepsilon_{11}}^{max} & {\varepsilon_{12}}^{max} & {\varepsilon_{13}}^{max} \\ {\varepsilon_{12}}^{max} & {\varepsilon_{22}}^{max} & {\varepsilon_{23}}^{max} \\ {\varepsilon_{13}}^{max} & {\varepsilon_{23}}^{max} & {\varepsilon_{33}}^{max} \end{bmatrix} \qquad (4.5) $$

The maximum absolute strain tensor does not represent a specific frame but rather the absolute maximum strain envelope bone optimises itself to (Fehling at al. 1995; Judex and Zernick 2000; Honda et al. 2001). The stimulus tensor, $\boldsymbol{\varepsilon}_{ij}^{*}$, associated with the target directions was calculated following the method introduced in Chapter 2 (Equation 4.6).

$$ \boldsymbol{\varepsilon}_{ij}^{*} = {\sigma_{pv}^{g}}^{T} \boldsymbol{\varepsilon}_{ij}^{max} \, \sigma_{pv}^{g} \qquad (4.6) $$

The set of stimulus tensors for all elements was used as the driving stimulus of the adaptation process. After the 4th iteration, the orthotropic material axes directionality stopped changing significantly, fluctuating around a certain configuration. Therefore, transformation of the strain stimulus into the maximum stress orientations was no longer required and $\boldsymbol{\varepsilon}_{ij}^{*} = \boldsymbol{\varepsilon}_{ij}^{max}$.

This step is highlighted in blue in the diagram depicted in Figure 4.12.

4.5.3 Material Properties Update

Bone material properties adaptation then progressed similarly to the algorithm proposed in Chapter 2, using the stimulus strain tensor, $\boldsymbol{\varepsilon}^*_{ij}$, as the driving stimulus for the material properties of each element, as explained in Section 2.2.3, and the target directions, $\boldsymbol{\sigma}^g_{pv}$, as the target for the rotation of the orthotropic material orientations. The upper limit for the directional Young's moduli was raised to 30 GPa, consistent with non-invasive measurements for the longitudinal modulus of long bones (Rudy et al. 2011; Rohrbach et al. 2012). Poisson's ratios were updated following the same method defined in Section 2.2.3.

The potential importance of trabeculae in resisting the resulting shear strains from the multitude of load cases bone is subjected to has been highlighted in literature (Skedros and Baucom 2007). Orthogonal crossing of trabecular groups occurs in areas of bone that are simply loaded. However, in areas where complex loading occurs, such as in the proximal femur, non-orthogonal secondary groups crossing at acute angles are required to resist the shear stresses induced by a multitude of load cases (Garden 1961; Miller et al. 2002; Miller and Fuchs 2005; Skedros and Baucom 2007). Notwithstanding the orthotropic assumption being a closer approximation to bone's anisotropy (Ashman et al. 1984), it implies that the decussation in trabecular structures observed cannot be modelled properly, since trabeculae are inherently assumed to cross at 90° under a single load case. In an attempt to model this resistance to shear, shear modulus adaptation was introduced. Similar to the Young's modulus adaptation process, a remodelling plateau for shear modulus towards a target shear strain value, ε_{st}, was inferred as follows.

Octahedral shear strain has been applied in bone remodelling (Shefelbine et al. 2005). The equation for mathematical octahedral shear strain is shown below (Equation 4.7). This relationship is considered to hold throughout the elastic regime, since the von Mises yield criterion has been used to study failure in bone (Keyak 2001; Tomaszewski et al. 2010).

$$\gamma_o = \frac{2}{3}\sqrt{(\varepsilon_{11}-\varepsilon_{22})^2 + (\varepsilon_{22}-\varepsilon_{33})^2 + (\varepsilon_{33}-\varepsilon_{11})^2 + 6({\varepsilon_{12}}^2 + {\varepsilon_{23}}^2 + {\varepsilon_{13}}^2)} \quad (4.7)$$

The target for normal strains, ε_{nt}, was defined in Chapter 2 as 1250 µstrain. Therefore, for monotonic axial loading $(\varepsilon_{22} = \varepsilon_{33} = \varepsilon_{12} = \varepsilon_{13} = \varepsilon_{23} = 0; \varepsilon_{11} = \varepsilon_{nt})$, the corresponding octahedral shear strain target, γ_o, can be found (Equation 4.8).

$$\gamma_o = \frac{2\sqrt{2}}{3}\varepsilon_{nt} \tag{4.8}$$

Similarly, under monotonic shear loading $(\varepsilon_{11} = \varepsilon_{22} = \varepsilon_{33} = \varepsilon_{13} = \varepsilon_{23} = 0,\ \varepsilon_{12} = \varepsilon_{st})$, the corresponding octahedral shear strain can also be obtained (Equation 4.9).

$$\gamma_o = \frac{2\sqrt{6}}{3}\varepsilon_{12} \tag{4.9}$$

In order to maintain integrity of octahedral shear strain under the two different cases (equating Equation 4.9 and Equation 4.10), the following relationship can be extracted (Equation 4.10) for the equivalent engineering shear strain target, γ_{st}.

$$\gamma_{st} = 2\varepsilon_{12} = 2\frac{\varepsilon_{nt}}{\sqrt{3}} \tag{4.10}$$

The shear moduli components of each element, ${G_{ij}}^{it}$, were updated following the same method used for the directional Young's moduli described in Chapter 2, with a target shear strain, γ_{st}, of 1443 µstrain (Equation 4.12) and a target plateau between 1154 and 1732 µstrain ($\gamma_{st} - \mu_0$ and $\gamma_{st} + \mu_0$, $\mu_0 = 0.2\gamma_{st}$). Similarly to the limits proposed for the Young's moduli, ${G_{ij}}^{it}$ values were limited between 10 MPa and 30 GPa, where it is the iteration number.

$${G_{ij}}^{it} = {G_{ij}}^{it-1}\frac{{\varepsilon_{ij}}^{*}}{\gamma_{st}} \tag{4.11}$$

4.5.4 Algorithm Flowchart

The flowchart of the bone adaptation algorithm for multiple load cases can be seen in Figure 4.13.

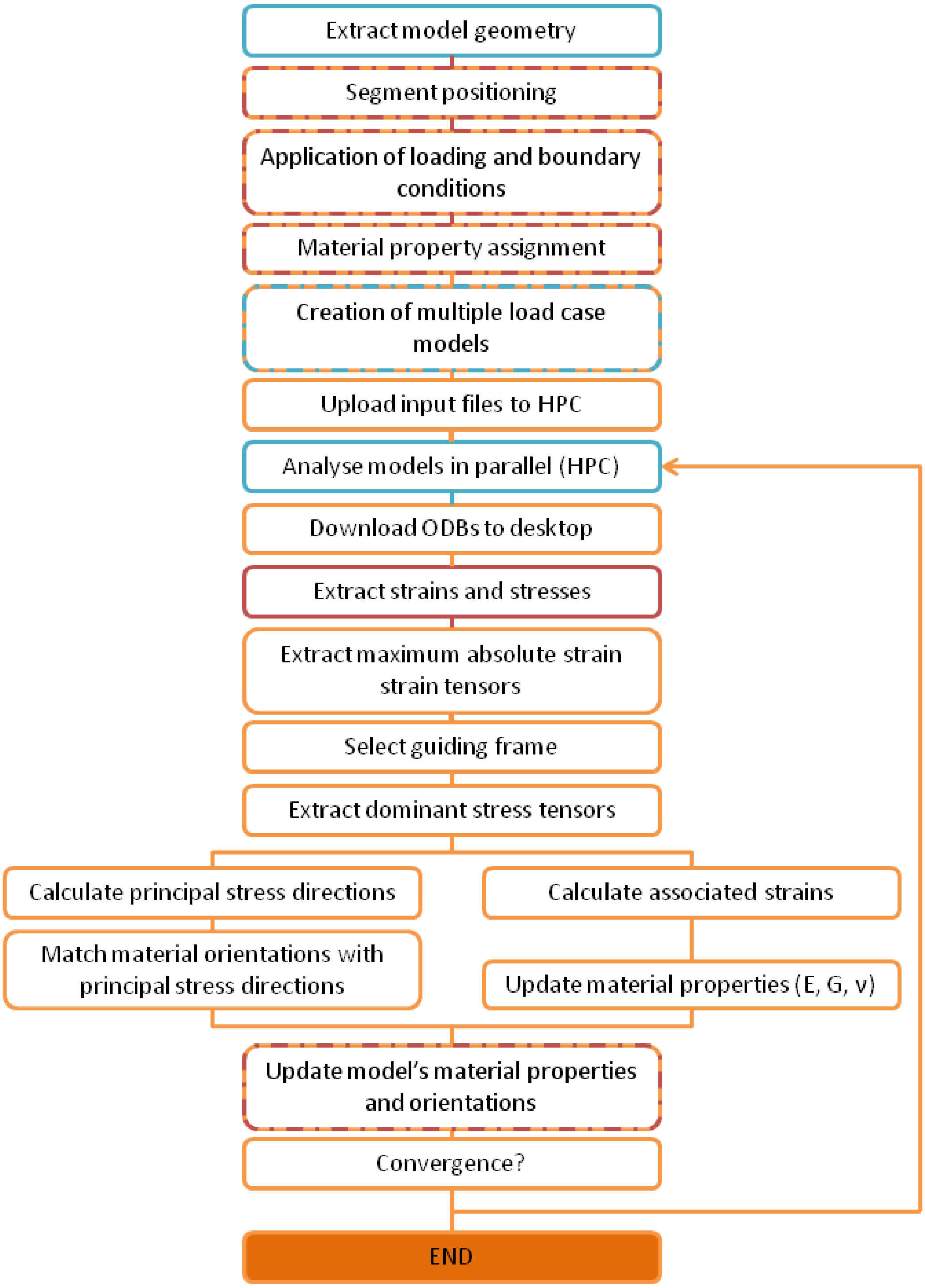

Figure 4.13 - Algorithm flowchart of the bone adaptation algorithm for multiple load cases. The steps undertaken in MATLAB can be seen in orange, Abaqus in blue and Python in red. Dashed lines represent steps where multiple software packages were involved.

Chapter 5

Finite Element Model Results

Chapter 4 introduced the modifications performed on the Single Load Case 3D Femur Model and the orthotropic strain-adaptive algorithm in order to allow for modelling of multiple load cases.

A Multiple Load Case 3D Femur Model was created with modifications at the hip and knee joints in order to allow application of the inter-segmental forces and moments arising from level walking and stair climbing. These were extracted from inverse dynamics analysis using an open source musculo-skeletal model of the lower limb. Some muscles definitions were also updated in order to allow for muscle wrapping at the greater trochanter, increase stability at the knee joint for load cases where high femoral flexion angles were involved, and to represent more physiologically their anatomical position and function.

The adaptation algorithm presented in Chapter 2 was also modified to allow for shear modulus adaptation. The change was implemented in order to model the trabecular structural resistance to the shear stresses and strains arising from multiple load cases at a continuum orthotropic level.

A method of selection of a guiding frame for the stimulus guiding the remodelling algorithm in each element of the femur mesh was also introduced. This alteration was undertaken with the intention of producing an envelope containing the maximum driving stimuli for the adaptation process in an attempt to achieve the optimised material distribution found *in vivo*.

In order to achieve physiologically meaningful material properties distributions and orientations with adaptation algorithms, the driving stimulus of the remodelling process needs to be appropriate and representative of what the bone is subjected to *in vivo*. This requires the finite element (FE) model of the bone being studied to be as close to the physiological state as possible.

This Chapter introduces the validation of the FE model developed by analysing the stress and strain distributions, joint contact and reaction forces, and muscle and ligament forces produced.

These were compared with data from other FE models, instrumented prosthesis and musculo-skeletal models available in literature.

Section 5.1 analyses the envelopes of stress and strain distributions produced by the FE model after convergence was achieved. Section 5.2 compares the hip contact and reaction forces generated for two daily activities with data measured *in vivo* by instrumented prosthesis, and calculated by a validated musculo-skeletal model. The muscle and ligament forces obtained for level walking and stair climbing are scrutinised in Section 5.3 and compared with data provided by a musculo-skeletal model validated at the hip joint. Finally, conclusions on the validation of the Multiple Load Case 3D Femur Model are drawn in Section 5.4.

5.1 Stress and Strain Distributions

The 3D orthotropic strain-adaptive bone adaptation algorithm was run iteratively for 80 instances of two frequent daily activities. Level walking (trial HSRNW4) and stair climbing (HSRSU6) trials were modelled with the segment positioning extracted from the kinematic data of Modenese's model (Modenese et al. 2011; Modenese 2012).

The inter-segmental forces and moments applied were selected from the results of the inverse dynamics of an open source musculo-skeletal model (Modenese et al. 2011) for the same subject (HSR). This model has been validated at the hip joint for the same trials chosen for this analysis (Modenese et al. 2011; Modenese and Phillips 2012). Convergence was achieved after the 29th iteration.

Results envelopes were created by finding the combined envelope of von Mises stresses and the maximum absolute values of principal strains across all frames modelled for each of the elements.

Similarly to the selection process of the guiding frame, the stress and strain distributions were extracted for each one of the Abaqus (v6-10, Dassault Systèmes, 2010) output databases (ODBs), N, for the converged model. Then, for each element, x, the principal strain, ε_p^N, and principal stress, σ_p^N, values were found by performing an eigen analysis on the strain, $\boldsymbol{\varepsilon}_x^N$, and stress tensor, $\boldsymbol{\sigma}_x^N$, respectively (Equation 5.1 and Equation 5.2). The value of N ranged between 1 and 80 for this analysis.

$$\begin{bmatrix}\varepsilon_v^N & \varepsilon_p^N\end{bmatrix} = eig(\boldsymbol{\varepsilon}_x^N) \tag{5.1}$$

$$\begin{bmatrix}\sigma_v^N & \sigma_p^N\end{bmatrix} = eig(\boldsymbol{\sigma}_x^N) \tag{5.2}$$

The maximum absolute values for the principal strains, $\varepsilon_{i_x}^*$, and stresses, $\sigma_{i_x}^*$, across all frames, were found according to Equation 5.3 and Equation 5.4, respectively, for each element.

$$\varepsilon_{i_x}^{*} = max\left(abs\left(\varepsilon_{i_x}^{n=1}, \varepsilon_{i_x}^{n=2}, \varepsilon_{i_x}^{n=3}, \dots, \varepsilon_{i_x}^{N}\right)\right) \tag{5.3}$$

$$\sigma_{i_x}^{*} = max\left(abs\left(\sigma_{i_x}^{n=1}, \sigma_{i_x}^{n=2}, \sigma_{i_x}^{n=3}, \dots, \sigma_{i_x}^{N}\right)\right) \tag{5.4}$$

Finally, the envelope of the von Mises stresses produced, $\sigma_{vM_x}^{*}$, was found by calculating the von Mises stresses using the maximum absolute values for the principal stresses, $\sigma_{i_x}^{*}$ (Equation 5.5).

$$\sigma_{vM_x}^{*} = \sqrt{\frac{(\sigma_{1_x}^{*} - \sigma_{2_x}^{*})^2 + (\sigma_{2_x}^{*} - \sigma_{3_x}^{*})^2 + (\sigma_{1_x}^{*} - \sigma_{3_x}^{*})^2}{2}} \tag{5.5}$$

The envelope of the von Mises stresses was calculated in such way that the principal stresses components used could come from different frames. This can produce a stress state that could not exist in reality, but gives a good indication of the variability of stresses across different regions.

An envelope of results for the converged model comprising the maximum absolute values for the maximum and minimum principal strains, as well as the envelope for the von Mises stresses was thus achieved. This Section analyses these distributions.

5.1.1 von Mises Stresses

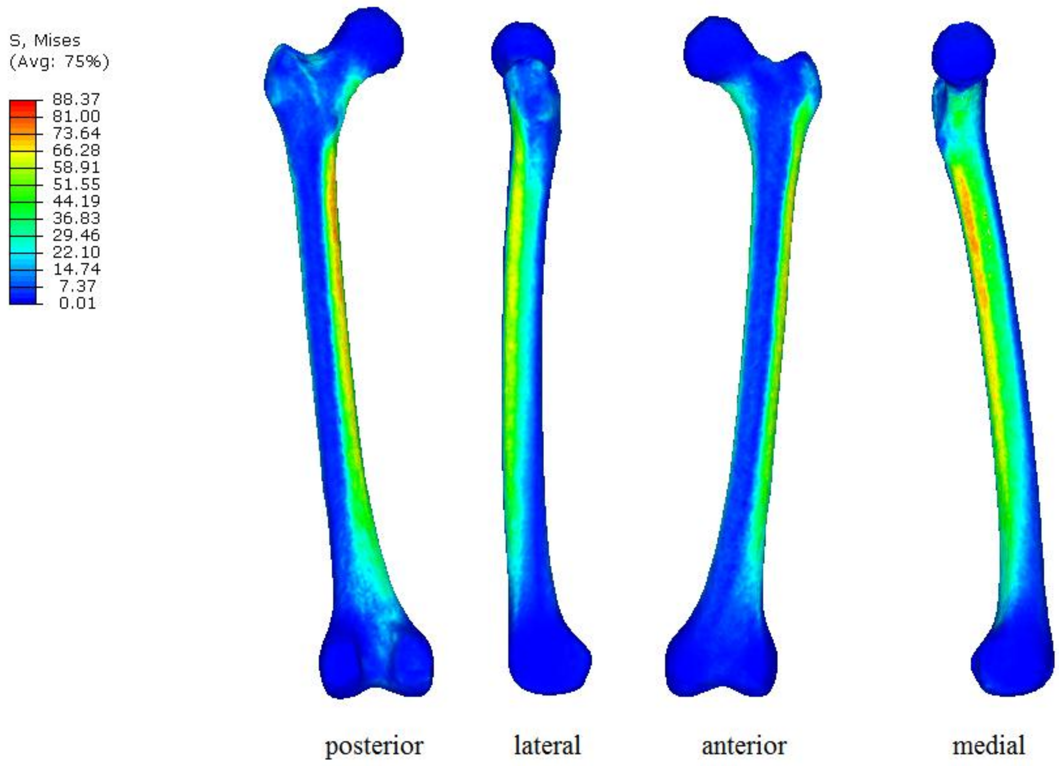

Figure 5.1 - Posterior, lateral, anterior and medial view of the von Mises stresses (N/mm^2) envelope of the femur.

Figure 5.1 shows the 99th percentile of the resulting combined von Mises stresses distribution envelope for the converged femur model across all 80 frames. 99% of elements reported von Mises stresses values below 88.37 N/mm^2. The maximum value for the von Mises stresses was 128.73 N/mm^2 and was found in the superior region of the medial femoral shaft. These are within the ranges calculated by Taylor (less than 90 N/mm^2) for a single leg stance (Taylor et al. 1996). However, they are found to be approximately double of the maximum values reported by Phillips for single leg stance (Phillips 2009). A possible explanation for this might be the fact that the contact forces applied on the femur are larger for the two load cases in this analysis than for single leg stance. The von Mises stress distribution resembles the patterns obtained for the model of the femur undergoing single leg stance (Chapter 3), with the larger values found in the medial and lateral aspects of the femoral shaft, as well as the inferior part of the femoral neck. This indicates that the highest elastic energy of distortion occurs predominantly in the coronal plane, where high bending stresses are expected during level walking and stair climbing.

5.1.2 Principal Strains

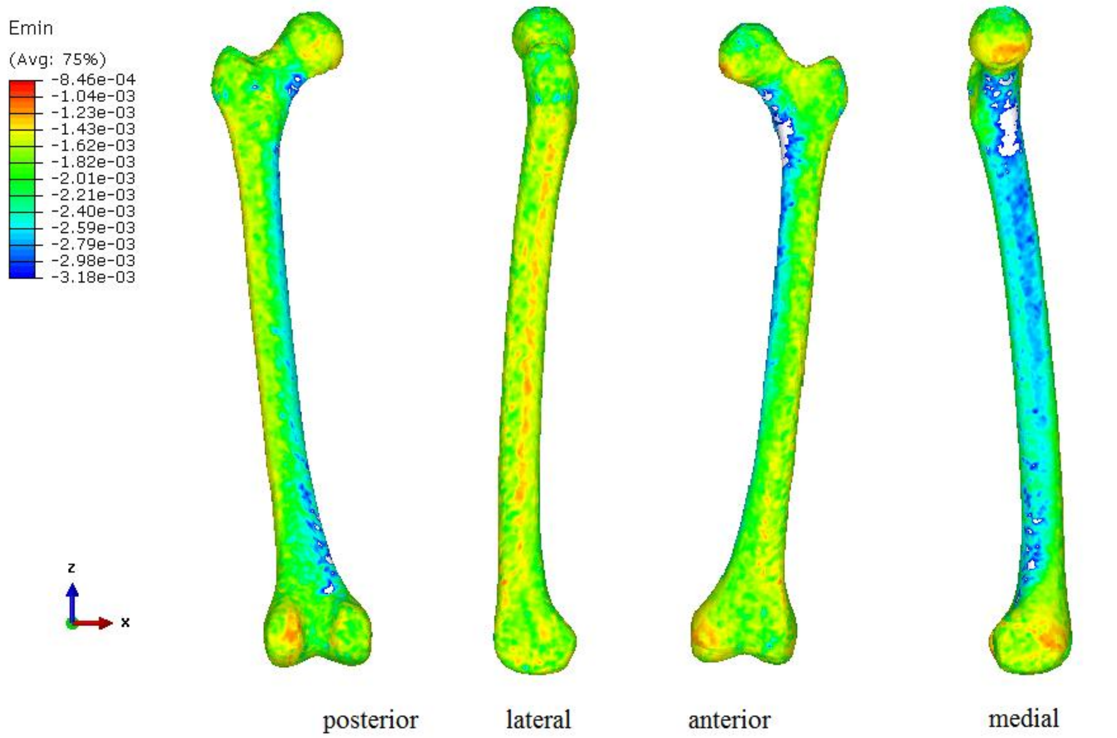

Figure 5.2 - Posterior, lateral, anterior and medial view of the minimum principal strains, ε_{min}, envelope of the femur.

The resulting combined minimum (compressive) principal strains, ε_{min}, of the femur are displayed in Figure 5.2 for the 99th percentile of the elements. 99% of the values were found to be above -3180 µstrain, with the highest absolute values concentrated in the medial part of the femoral shaft. The minimum value of -5860 µstrain was found in an element in the inferior part of the femoral neck. Figure 5.3 displays the 99th percentile of the resulting combined maximum (tensile) principal strains, ε_{max}, of the femur for the analysis. 99% of the resulting maximum strains were found below 2720 µstrain. The maximum absolute value of 5660 µstrain was found in the superior part of the lateral femoral shaft.

These values are within the ranges reported by Speirs for walking and stair climbing (below 3400 µstrain in tension and above -5000 µstrain in compression for stair climbing) with higher compressive strains found in the superior region of the femoral cortex and the femoral neck, as well as the inferior posterior region of the cortical shaft. Speirs also found high tensile strains in the medial and inferior anterior aspects of the femoral shaft (Speirs et al. 2007), similar to the results presented in Figure 5.2 and Figure 5.3.

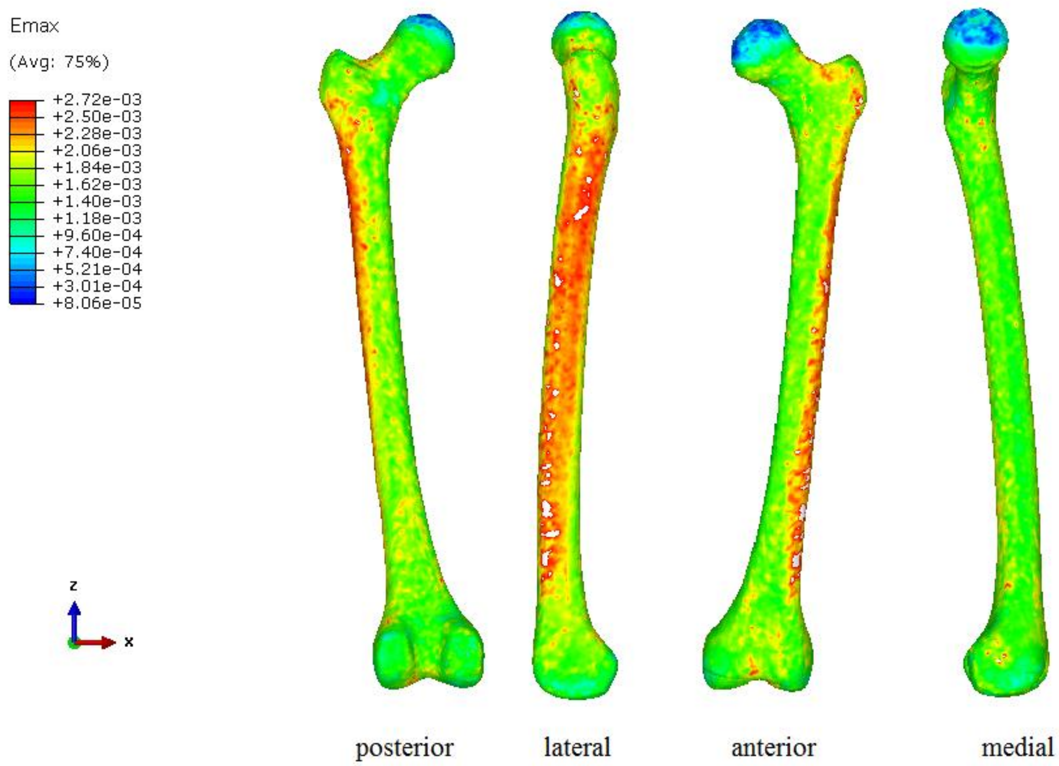

Figure 5.3 - Posterior, lateral, anterior and medial view of the maximum principal strains, ε_{max}, envelope of the femur.

Phillips study for a unconstrained femur undergoing single leg stance produced very similar tensile and compressive strain distributions in the medial and lateral aspects of the cortical shaft, with the highest values also found in the superior parts of both sides (Phillips 2009). The largest values reported for this analysis for the 99th percentile are in agreement with the largest values for the compressive and tensile principal strains reported in the same study (-2797 µstrain and 2585 µstrain, respectively). Younge implemented a similar free boundary condition model, obtaining very similar results (-3000 µstrain in compression and 2500 µstrain in tension) (Younge 2012).

5.1.3 Discussion

Both von Mises and principal strains distribution patterns agree with similar numerical models (Taylor et al. 1996; Speirs et al. 2007; Phillips 2009; Younge 2012), with the areas where the higher values were found matching convincingly. Aamodt measured *in vivo* the strain on the lateral cortex of two female subjects (Aamodt et al. 1997). An ε_{max} value of 1500 µstrain was found just below the greater trochanter. This study found values around 2720 µstrain for the tensile strains in this same region. An explanation for the disparity in the results could be the fact that the body weight of the subject used in this analysis (860 N) is potentially much higher than the patients in Aamodt's study. A reduction of body weight to a value more appropriate for female subjects (around 600 N, for instance) could result in a proportional reduction in the principal strains to values within the range of the ones measured. Similarly to the Single Load Case model discussed in Chapter 3, despite setting the target values for the remodelling plateau of the adaptation algorithm between 1000 and 1500 µstrain, there are still regions where the absolute values for the femoral principal strains fall outside this range. E_1 and E_3 values associated with the tensile and compressive strains, respectively, were found to max out in the medial and lateral aspects of the femoral shaft (see Chapter 6). This might suggest that the remodelling plateau is an optimum attractor state that bone attempts to optimise itself to, but not necessarily reach, with remodelling happening constantly.

Table 5.1 - Maximum values for the von Mises stresses, maximum (ε_{max}) and minimum (ε_{max}) principal strains found in literature and for the 99th percentile in this analysis. Because of the different load cases modelled, * indicates that this study is not directly comparable.

Study	Von Mises (N/mm^2)	ε_{min} (µstrain)	ε_{max} (µstrain)
Taylor et al. 1996	90	-3000	2500
Speirs et al. 2007	N/A	-5000	3400
Phillips 2009	49.97	-2797	2585
Younge 2012	N/A	-3000	2500
This study	88.37*	-3180	2720

Table 5.1 compiles the results reported in this Section and in the literature discussed. It can be seen that the Multiple Load Case 3D Femur Model produces strain and stress values within what has been calculated in similar numerical studies.

The studies mentioned in this Section assumed trabecular and cortical bone to have homogeneous isotropic material properties. The material distributions produced by Multiple Load Case 3D Femur were heterogeneous and orthotropic and are discussed in Chapter 6. Direct comparisons between models need to be conservative (Baca et al. 2008). However, experimental studies have validated that the overall behaviour of the femur can be predicted by homogeneous synthetic models (Cristofolini et al. 1995; Gardner et al. 2010; Juszczyk et al. 2011). Stress is likely to be more comparable across the studies as it is less dependable on material properties (Clarke et al. 2011). However, the other studies do not report the principal stresses obtained, so direct comparison cannot be done.

Nevertheless, the comparison between these studies and the results reported in this Section is considered satisfactory (Taylor et al. 1996; Speirs et al. 2007; Phillips 2009; Younge 2012). Therefore, it is concluded that the strains and stresses produced by this model can be considered reliable as the driving signal of the remodelling process.

5.2 Joint Contact and Reaction Forces

Chapter 1 introduced the functional adaptation of bone and its trabecular structures to the forces that it is subjected to during daily living activities. The femur's geometry (Ward 1838; Garden 1961), material properties distributions and structural directionality (Wolff 1892; Skedros and Baucom 2007) are optimised to the envelope of forces that are transmitted between the hip and the knee joints. In order to create physiological models of the remodelling process, an appropriate stimulus definition is required (Duda 1996; Lengsfeld et al. 1996; Huiskes et al. 2000; Bitsakos et al. 2005). Therefore, a physiological definition of the loading of the FE model of the bone being studied is also required (Erdemir et al. 2012).

In order to evaluate the ability of the Multiple Load Case 3D Femur Model to produce the correct loading conditions and, consequently, appropriate driving stimulus for the adaptation process, the joint contact and reaction forces produced were compared with data available in literature. These include forces and stresses measured by *in vivo* instrumented prosthesis for the hip (Bergmann et al. 2001; Kutzner et al. 2010) and knee (D'Lima et al. 2006; D'Lima et al. 2008) joints, hip contact forces calculated by musculo-skeletal models (Heller et al. 2001; Heller et al. 2005; Modenese et al. 2011; Modenese and Phillips 2012) and theoretical calculations (Ahmed et al. 1987). Comparison data was taken for the same trials, as reported in this study.

This Section compares the joint contact and reaction forces obtained by the proposed model and analyses its capability to reproduce the mechanical environment at the hip and knee joints for the two load cases in question (level walking and stair climbing).

5.2.1 Hip Joint

The hip contact forces (HCFs) calculated were extracted by inserting a two-noded (C3D2) probe connector element at the centre of the femoral head and connected to ground. The resultant, x, y and z components (F_r, F_x, F_y and F_z, respectively) of the force measured at the centre of the femoral head were then compared with the data measured *in vivo* for the same load cases modelled (trial 4 for level walking, HSRWN4, and trial 6 for stair climbing, HSRSU6, for subject HSR) with instrumented prosthesis, and made available in the HIP 98 package (Bergmann et al. 2001). In addition, the same components of the hip contact forces were compared with the forces calculated by the musculo-skeletal model that provided the inter-segmental forces and moments applied based on the same trials (Modenese et al. 2011). The signals were compared qualitatively by analysing the magnitude, shape and profile of the curves and quantitatively by calculating the Root Mean Squared Error (RMSE), as well as the mean Pearson's correlation coefficient. Two comparisons were made: the model's force curve vs. Bergmann's measured force curve and the model's force curve vs. Modenese's calculated force curve for a quadratic objective function. The RMSE was calculated according to Equation 5.6 for each of the stages, $i = 1, 2, \ldots n$, of the gait cycle analysed. The number of frames modelled, n, was 40 for each activity.

$$RMSE = \sqrt{\frac{\sum\left(curve1(i) - curve2(i)\right)^2}{n}} \tag{5.6}$$

Pearson's correlation coefficient gives a measure of the linear correlation between two variables. The coefficient ranges between -1 and +1 (+1 being the best possible match), and it measures how strong the linear dependence is between two variables (Rodgers and Nicewander 1988). Pearson's *r*, as it is otherwise known, was calculated using the function *corr.m* available in MATLAB. Figure 5.4 shows the comparison between the resultant, x, y and z component of the HCFs calculated by the Multiple Load Case 3D Femur Model and the forces measured *in vivo* by Bergmann and calculated by Modenese.

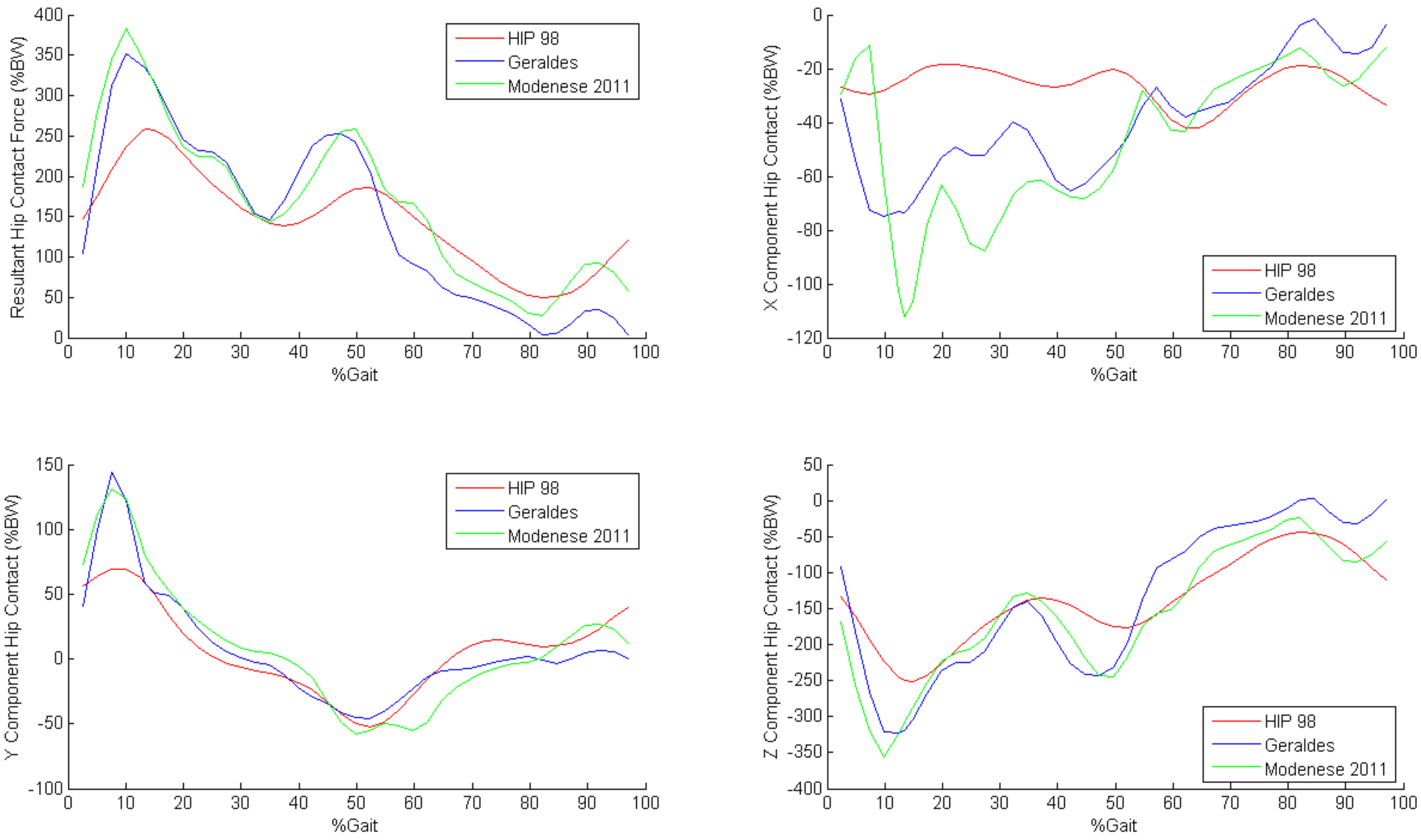

Figure 5.4 - Resultant, x, y and z components of the HCFs measured by Bergmann (red), calculated by the proposed model (blue) and by Modenese's musculo-skeletal model (green) for the level walking (HSRNW4) load case.

Qualitative observation of the curves for each of the components of the HCFs in Figure 5.4 shows a good match of the different phases of level walking recorded. The two peaks characteristic of walking (Bergmann et al. 1993; Bergmann et al. 2001) corresponding to the heel contact and toe-off phases, are clearly present for the resultant force and its z component. The mid-stance phase (dip in the curve between the two peaks) and the swing phase (between toe-off and heel strike) are also represented. There is a slight delay in phase between the predicted forces and the measured data, similarly to the delay reported by Modenese (Modenese et al. 2011).

The force curve produced by this model can be found in between the two other curves for most of the gait cycle, with Bergmann's as its lower limit and Modenese's as its upper limit. Hip contact forces were generally over-predicted in relation to data recorded by Bergmann's instrumented prosthesis, particularly at the peaks (353 %BW compared to 257%). For the peak resultant force, an over-estimation of 37% was recorded. This value is close to the over-prediction ratio of 33% reported by Heller for the same subject (Heller et al. 2001). Furthermore, this model's predictions were found to be consistent with Modenese's calculated forces (353 %BW compared to 382 %BW) (Modenese et al. 2011), as well as with other musculo-skeletal models (Heller et al. 2001; Heller et al. 2005) and FE studies (Pedersen et al. 1997).

The force curve relative to the x component (F_x) seems to differ significantly from the measured data. The absolute values of the forces predicted by this model are higher than the ones measured by Bergmann. A possible explanation for this could be the fact that the superior-inferior wrapping aspect of the gluteus muscles around the femoral head was not implemented in the FE model. The action of the gluteus muscles along this plane would reduce their medial-lateral contribution to the HCFs. The definition of the muscles as connectors along straight lines between their origination and insertion points results in the definition of direct paths. In muscles such as the gluteus, where the moment arm applied on the femur is dependent on the geometry defined, this method of muscle definition could produce un-realistic muscle forces (Phillips 2009). Furthermore, the femur geometry used in this study is not the same as the subject HSR, but extracted from the

Muscle Standardised Femur and, therefore could contribute to the hip contact forces over-prediction.

Table 5.2 compiles the Pearson's correlation coefficient (and corresponding *p* value) and the RMSE between the model's predicted force curves and Bergmann's measured, as well as the force curves calculated by Modenese. Apart from the comparison of the F_x component with Bergmann's data, all other comparisons resulted in high Pearson's correlation coefficients (with $p < 0.000001$). This shows a strong correlation within the two sets of curves. Furthermore, the RMSE value between the model predictions and the measured data is considered acceptable and within the ranges of Modenese's published values for the same subject (Modenese et al. 2011). Good correlation and low RMSE were found when comparing the predicted HCF curves with Modenese's data. This model reported similar issues with the modelling of the gluteal muscles (Modenese 2012).

Table 5.2 - Pearson's ρ, p value, and RMSE (%BW) between the two curves for the model vs. Bergmann and model vs. Modenese comparisons for level walking.

Comparison	Component	x	y	z	Resultant
Model vs. Bergmann	Pearson's ρ	-0.0991	0.8897	0.9286	0.9230
	p	0.5429	1.65E-14	6.02E-18	2.35E-17
	RMSE (%BW)	27.00	19.93	53.89	58.08
Model vs. Modenese	Pearson's ρ	0.7591	0.9551	0.9534	0.96305
	p	1.37E-08	1.11E-21	2.24E-21	2.98E-23
	RMSE (%BW)	19.90	15.23	38.11	37.01

Comparison of the curves for each of the components of the HCFs in Figure 5.5 shows good agreement with for the different components of the stair climbing load case. The two peaks measured by Bergmann for the same subject (HSR) can be predicted by the model for both F_z and F_r, as well as the swing phase (Bergmann et al. 1993; Bergmann et al. 2001). The three force curves compared are found to be extremely close, overlapping at some points.

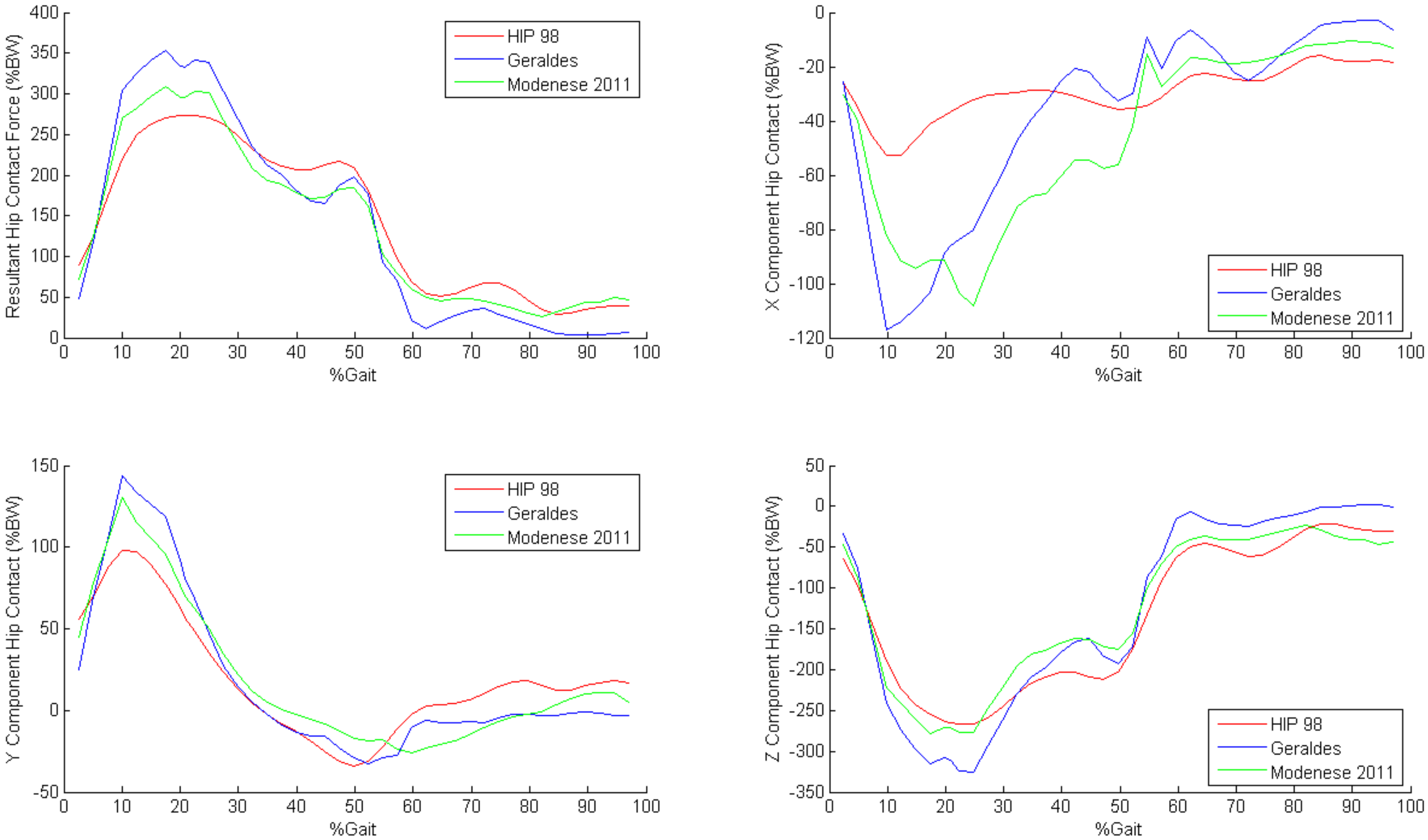

Figure 5.5 - Resultant, x, y and z components of the HCFs measured by Bergmann (red), calculated by the proposed model (blue) and by Modenese's musculo-skeletal model (green) for the stair climbing (HSRSU6) load case.

Hip contact forces were slightly over-predicted in relation to data recorded by Bergmann, particularly at the first peak (352 %BW compared to 274 %BW), with an over-estimation of 28%. This over-estimation falls within the range reported by Heller for the HSR subject (Heller et al. 2001). The predicted peak resultant was found to be consistent with Modenese's calculated forces (352 %BW compared to 308 %BW) (Modenese et al. 2011) and with other musculo-skeletal comparison studies (Heller et al. 2001; Heller et al. 2005). Similarly to the level walking load case, F_x seems to be the component to differ most significantly from the measured data. A reason for this peculiarity was put forward earlier in this Section.

Table 5.3 compiles the correlation coefficients and the RMSE between the model's predicted force curves and Bergmann's measured, as well as the force curves calculated by Modenese, for stair climbing. Comparisons show high Pearson's correlation coefficients (with $p < 0.000001$). This implies a strong correlation within the two sets of curves. The low RMSE values found are within the published range for the same subject (Modenese et al. 2011).

Table 5.3 - Pearson's ρ, p value and RMSE (%BW) between the two curves for the model vs. Bergmann and model vs. Modenese comparisons for stair climbing.

Comparison	**Component**	**x**	**y**	**z**	**Resultant**
Model vs. Bergmann	Pearson's ρ	0.8660	0.9429	0.9811	0.9765
	p	5.40E-13	9.83E-20	1.07E-28	6.21E-27
	RMSE (%BW)	28.76	19.47	35.74	43.01
Model vs. Modenese	Pearson's ρ	0.8913	0.9785	0.9964	0.9972
	p	1.27E-14	1.17E-27	3.12E-42	1.53E-44
	RMSE (%BW)	17.96	11.08	29.91	28.59

Qualitative and quantitative observations suggest that the HCFs for both the level walking and stair climbing load cases are consistent with the values measured *in vivo* (Bergmann et al. 1993; Bergmann et al. 2001) and calculated in different musculo-skeletal studies validated against the same data (Heller et al. 2001; Heller et al. 2005; Modenese et al. 2011; Modenese and Phillips 2012).

5.2.2 Knee Joint and Lumbar Forces

Figure 5.6 and Figure 5.7 show the resultant knee reaction force (KRF), the force measured at the lumbar connector in the anterior-posterior plane, the patello-femoral joint forces (PFJF) and the force acting through the patellar ligament for level walking and stair climbing, respectively.

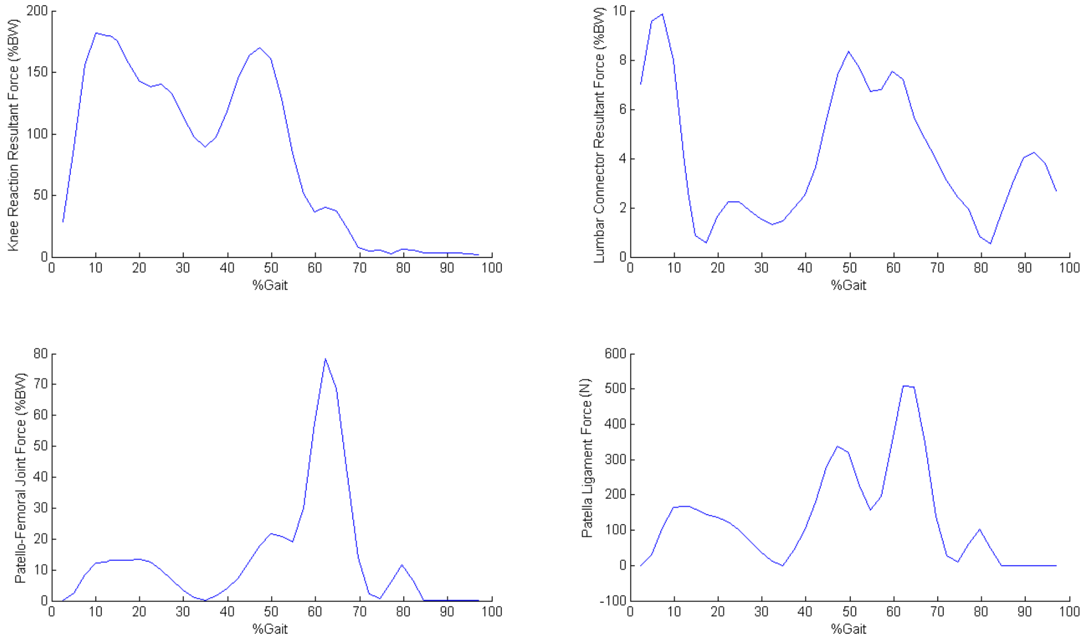

Figure 5.6 - Knee joint and lumbar forces for the level walking load case.

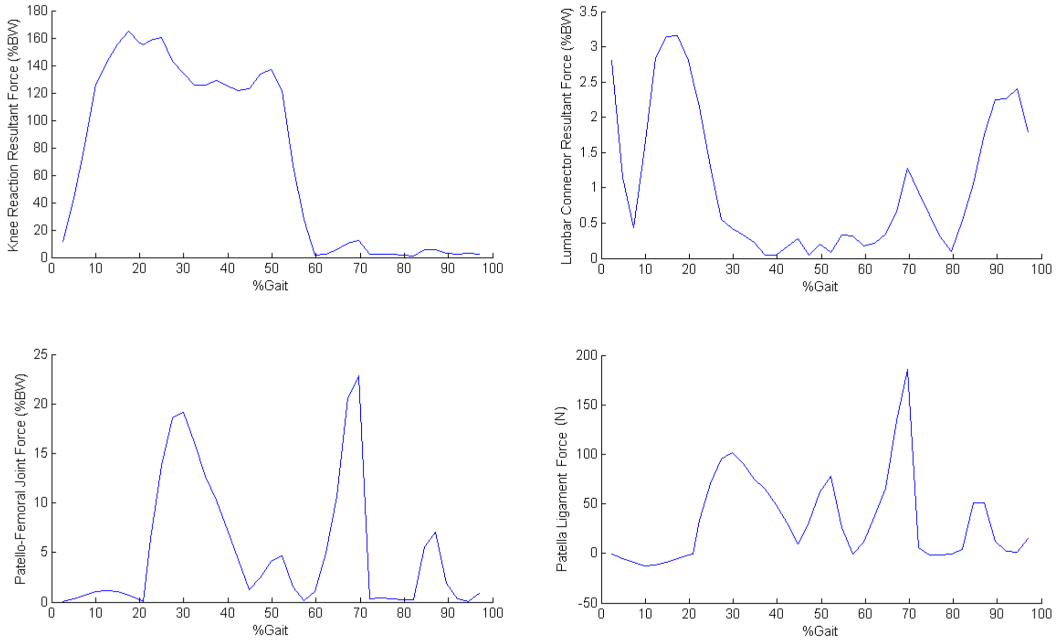

Figure 5.7 - Knee joint and lumbar forces for the stair climbing load case.

The peak KRFs produced by the model were of 179 %BW and 165 %BW for level walking and stair climbing, respectively, and occurred in the same frame as the first peak of HCF for both activities. These correspond to the heel-strike phases of the gait cycles modelled, when larger ground reaction forces are transmitted through the tibia (D'Lima et al. 2006; D'Lima et al. 2008; Kutzner et al. 2010). The measured peak reaction forces were higher than the ones obtained by Phillips' single leg stance model (Phillips 2009) and reproduced by Younge (Younge 2012). The fact that the forces arising from single leg stance are lower than the ones produced by the two load cases considered could provide a justification for this difference. Both force curves under-estimated the KRFs in comparison with data measured using instrumented knee prosthesis. D'Lima reported 217 (±20) %BW for level walking and 250 %BW for stair climbing. A similar study by Kutzner measured higher values for the same forces: [220 – 297 %BW] for level walking and [298 – 345 %BW] for stair climbing. The patello-femoral peak forces obtained in this model were 78 %BW and 24 %BW. These were also lower than published analyses of the static equilibrium at the knee joint (Reilly and Martens 1972; Ahmed et al. 1987; Miller et al. 1997) and measurements of the tension of a cable screwed to the patella of an equilibrated cadaveric femur in flexion (Miller et al. 1997). A potential explanation for the lower tibio-femoral and patello-femoral forces calculated by the proposed model could be that, by fixing the medial node along the knee functional axis in all translation directions, the movement of the distal part of the femur becomes restricted. The restriction of the tibio-femoral movement to its functional axis (Klein Horsman et al. 2007) and of the medial condyle node against translation introduced an artificial constraint which could result in less physiological significance of the movement of the knee region. This, in turn, could produce lower forces in the muscles inserting and originating at the knee, reducing the contact forces measured. The patella ligament peak forces were of 59 %BW and 22 %BW occurring in the same stages of the gait cycles as the peak patello-femoral forces. These values were within the ranges measured (Stäubli et al. 1996; Merican et al. 2009) and predicted (Ahmed et al. 1987) in literature. Finally, forces in the lumbar connector did not exceed 10 %BW in the anterior-posterior plane, within the ranges calculated by Callaghan (Callaghan et al. 1999) and highlighting the stabilising function of the upper torso during walking.

5.2.3 Discussion

Hip contact forces are usually over-predicted in comparison with Bergmann's data (Heller et al. 2001; Heller et al. 2005; Modenese et al. 2011; Modenese and Phillips 2012). One of the reasons for this over-prediction is the fact that the biomechanics of the hip have been altered as the subjects of the study all underwent hip arthroplasty (Bergmann et al. 2001). Subject-specific hip geometry has also been found to influence the calculation of the HCFs (Lenaerts et al. 2008). The fact that the geometry of the FE model of the femur modelled in this study was based on the Muscle Standardised Femur (Viceconti et al. 2003a; Viceconti et al. 2003b) and not representative of the geometry of the subject from which the kinetic and kinematic data were extracted may also explain the variations observed.

The definition of certain muscles as straight paths of action instead of their anatomical wrapping configuration can also influence the resulting HCFs (Phillips 2009). The use of the FE method ignores the synergism and co-contractions between muscles and, therefore, is an inaccurate representation of their behaviour (Phillips et al. 2007; Phillips 2009). Furthermore, the representation of muscles as bundles of spring connector elements ignores the passive effect of muscle volume on the femoral structure. The inclusion of fixed boundary conditions at the medial condyle node and restrictions of the tibio-femoral movement about its functional axis could reduce movement in the distal part of the equilibrated finite element model, resulting in underestimation of muscle forces and, therefore, the patello-femoral and tibio-femoral contact forces.

Nevertheless, qualitative and quantitative comparison of the forces produced at the hip and knee joints produced by the Multiple Load Case 3D Femur Model show that both the level walking and stair climbing load cases show reasonable agreement with the values measured *in vivo* and calculated using musculo-skeletal models or static equilibrium analysis. It can be concluded that the Multiple Load Case 3D Femur Model is capable of producing a physiological loading environments at the hip and knee joint, a key stepping stone in the attempt to produce a physiologically meaningful driving stimulus for the adaptation process of bone.

5.3 Muscle and Ligament Forces

The importance of the contribution of muscle and ligament forces to the definition of bone's mechanical environment was discussed in Chapter 1. In order to model bone adaptation in a physiologically significant manner, the signal driving the remodelling process needs to be accurate (Bitsakos et al. 2005). Experimental studies have ascertained the effect of the application of lateral muscle loading in femoral strain distributions (Szivek et al. 2000), and the influence of the thigh muscles in the axial strains measured in the femur (Cristofolini et al. 1995). Lengsfeld showed that the femoral strain patterns and principal stress orientations are sensitive to the effect of the ilio-tibial tract (Lengsfeld et al. 1996). Duda further demonstrated the importance of the inclusion of muscles in FE modelling in order to reproduce a physiological strain distribution (Duda et al. 1998). Other studies have reported similar observations (Simões et al. 2000; Polgar et al. 2003; Wirtz et al. 2003). A total of 26 muscles and 7 ligamentous structures were included explicitly in the Multiple Load Case 3D Femur Model as passive actuators, allowing for the development of an equilibrated model which does not requires input from musculo-skeletal optimisation models. The linear muscle definition was based on the approach proposed by Phillips (Phillips et al. 2007; Phillips 2009) and extensively described in Chapters 3 and 4.

This work proposes an iterative adaptation algorithm driven by a strain stimulus extracted from a FE model of the femur undergoing different instances of daily activities. Special focus needs to be put on physiologically modelling the loading conditions the FE model is subjected to (Erdemir et al. 2012). Section 5.2 assessed if the proposed model could replicate the hip and knee contact forces arising during level walking and stair climbing. In this Section, the muscle and ligament forces produced for the same activities were analysed and compared with the forces calculated by the open source musculo-skeletal model that provided the inter-segmental forces and moments applied (Modenese et al. 2011), as well EMG measurements of the activations of some of the muscles modelled (Wootten et al. 1990) for level walking.

5.3.1 Level Walking

Figure 5.8 shows the comparison of the muscle forces predicted by the model proposed in this thesis (in blue) and recorded EMG profiles (in black), ranging from 0 to 1 (Wootten et al. 1990) for level walking. The forces produced by the model developed by Modenese using a quadratic objective function for muscle recruitment (Modenese et al. 2011) are shown for interest (in red). Modenese's model has mainly been assessed against hip contact forces and while it has been compared to EMG, inconsistencies do occur (Modenese et al. 2011; Modenese 2012). The EMG data was available for the rectus femoris, semitendinosus, vastus mediatus and lateralus, the long head of the biceps femoris, gluteus maximus and medius and the two gastrocnemii.

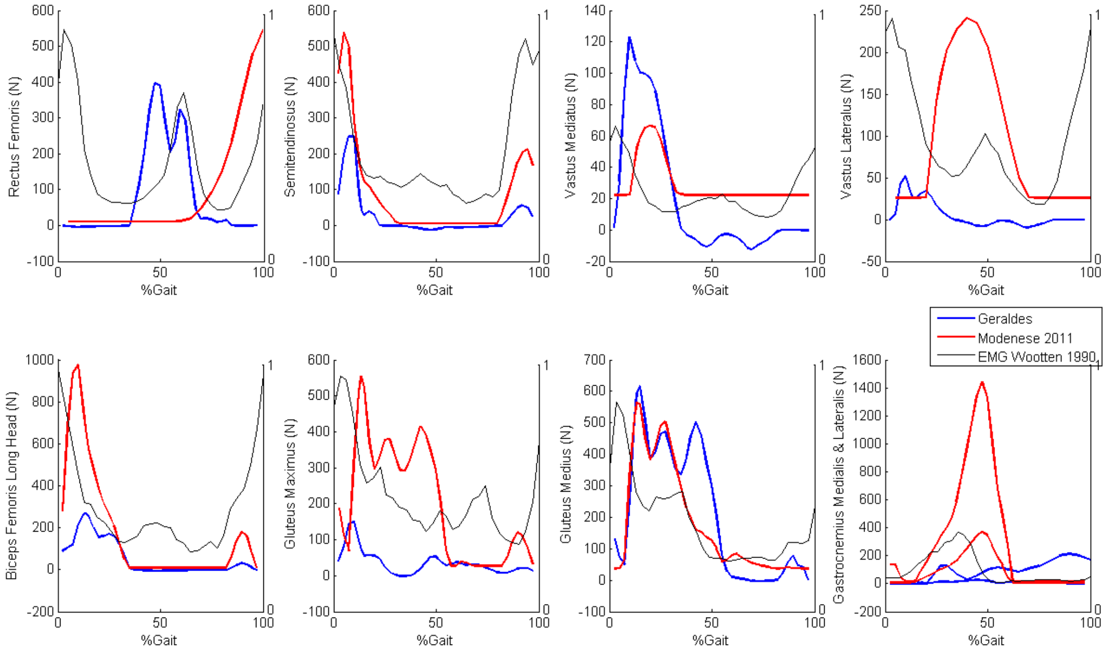

Figure 5.8 - Some of the predicted muscle forces by the Multiple Load Case 3D Femur Model (blue), the model developed by Modenese (red) and EMG profiles for walking published by Wootten et al. (thin black lines).

When comparing the forces predicted by the Multiple Load Case 3D Femur Model and the EMG profiles, it can be observed that the mono-articular muscles activation profiles are comparable to the EMG patterns for both muscles crossing the hip joint (gluteus maximus and gluteus medius) (Wootten et al. 1990). The other mono-articular muscles crossing the knee joint (vastus mediatus, vastus lateralus and gastrocnemii) show good agreement in activation timings for the first half of the gait cycle. Two possible explanations for the apparent inactivation in the second half are proposed: the reduced movement at the distal femur induced by the fixed boundary conditions applied at the medial condyle (and discussed in the Section 5.2.2). This, associated with the almost vertical position of the femur during the toe-off phase, promotes direct load transfer through the femur without the need for the stabilizing effect of the muscles inserting at the knee. Because of the self-balancing nature of the FE model proposed, these produce lower muscle activations in the distal region. Nevertheless, the activation of the vasti and rectus femoris muscles highlights their action in stabilising the femur during the extension phase of the gait cycle (Heller et al. 2001). The bi-articular muscles in Figure 5.8 show activation patterns matching the ones measured by Wootten (Wootten et al. 1990), in particular for the semitendinosus and the long head of the biceps femoris. These two muscles' activities peak in the weight bearing phase of gait and in good timing with the EMG profiles. However, they seem to be almost inactive throughout the swing phase, as is the rectus femoris. This could be associated with the lower inter-segmental forces applied at the centre of the femoral head during this period. The rectus femoris inactivation during the initial phase of the gait cycle does not match the EMG data shown in Figure 5.8 but is in accordance with other measurements (Perry 1992).

Figure 5.9 shows the muscle forces calculated for the other muscles for both the proposed model and Modenese's musculo-skeletal lower limb model (Modenese et al. 2011) for level walking. If the contribution of the shorter head of the biceps femoris is superimposed with the forces produced by the long head bundle, a closer match between the predicted muscle activation and the EMG recordings (Wootten et al. 1990) is obtained as well as similar peak forces to the ones calculated by Modenese (Modenese et al. 2011). Muscles such as semimembranosus, gluteus minimus, sartorius, pectineus, iliacus and both parts of the adductor magnus have activation patterns matching Modenese's predictions. The gluteus minimus force distribution exhibits a negative component in the first 20% of the gait cycle. This could arise from the antagonistic joint action of the adductor muscles, which force the acetabular structure to rotate in the superior-anterior direction, opposite to the gluteus minimus line of action. Because of the particular definition of these models, when large displacements are experienced by the connector elements, negative forces could be produced. The inter-segmental moments applied at the centre of the femoral head could have produced such displacements. This is a limitation of the muscle definition proposed by Phillips (Phillips et al. 2007; Phillips 2009) and used in this work.

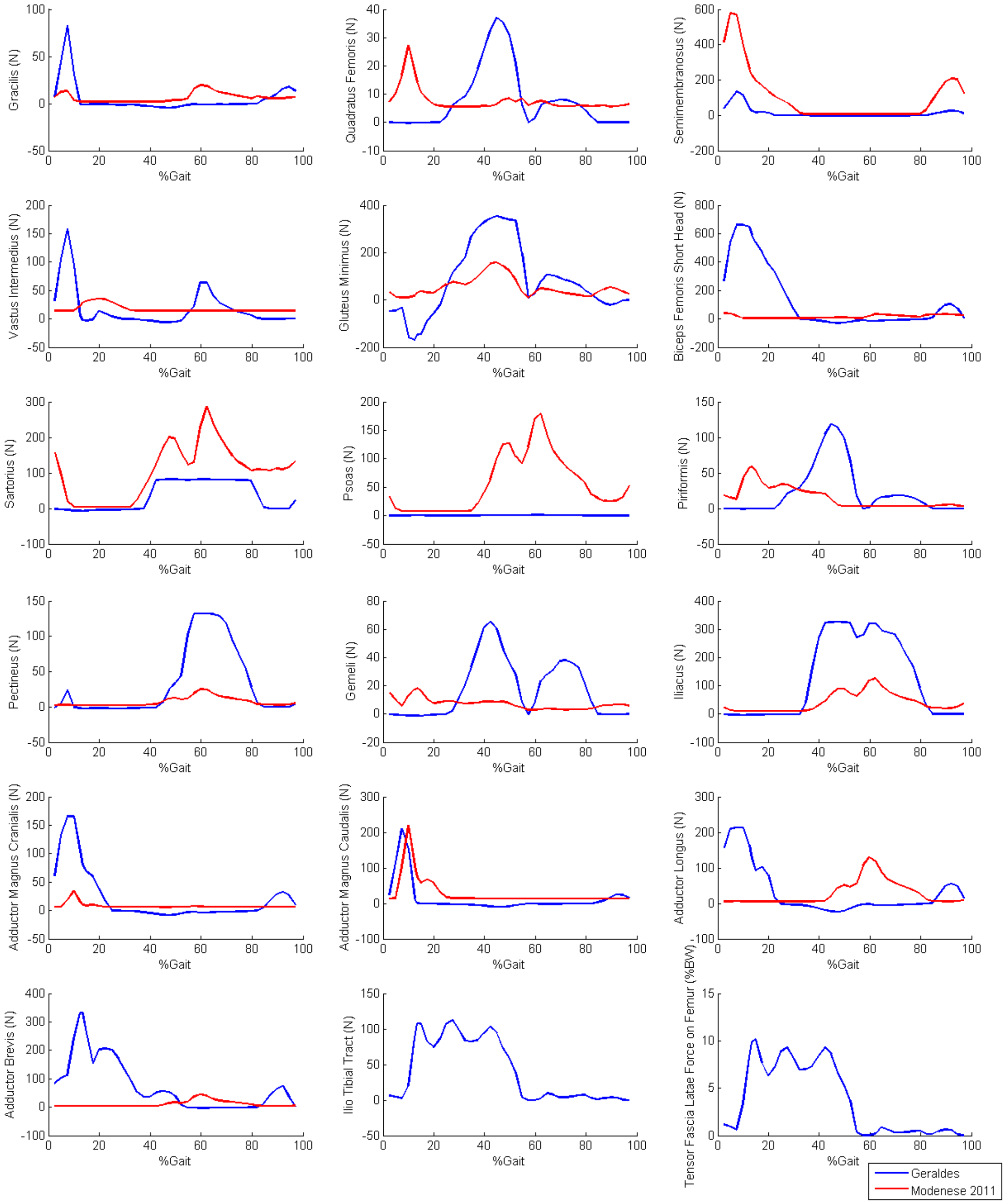

Figure 5.9 - Some of the predicted muscle forces by the Multiple Load Case 3D Femur Model (blue) and the model developed by Modenese (red) for level walking.

The sartorius seems to reach its limit throughout its activation stage suggesting that the value used for its peak force of 105 N (Delp 1990) may need to be revised. Modenese increased this value to 400 N, proportional to the muscle's cross-sectional area. The wrapping effect of the tensor fascia latae was achieved by including the modifications to this muscle proposed in Chapter 4, as up to 10 % BW is transmitted back to the femur. This wrapping action, together with the profile displayed by the ilio-tibial tract, increased stability in the coronal plane (where most bending of the femur occurs due to its compression).

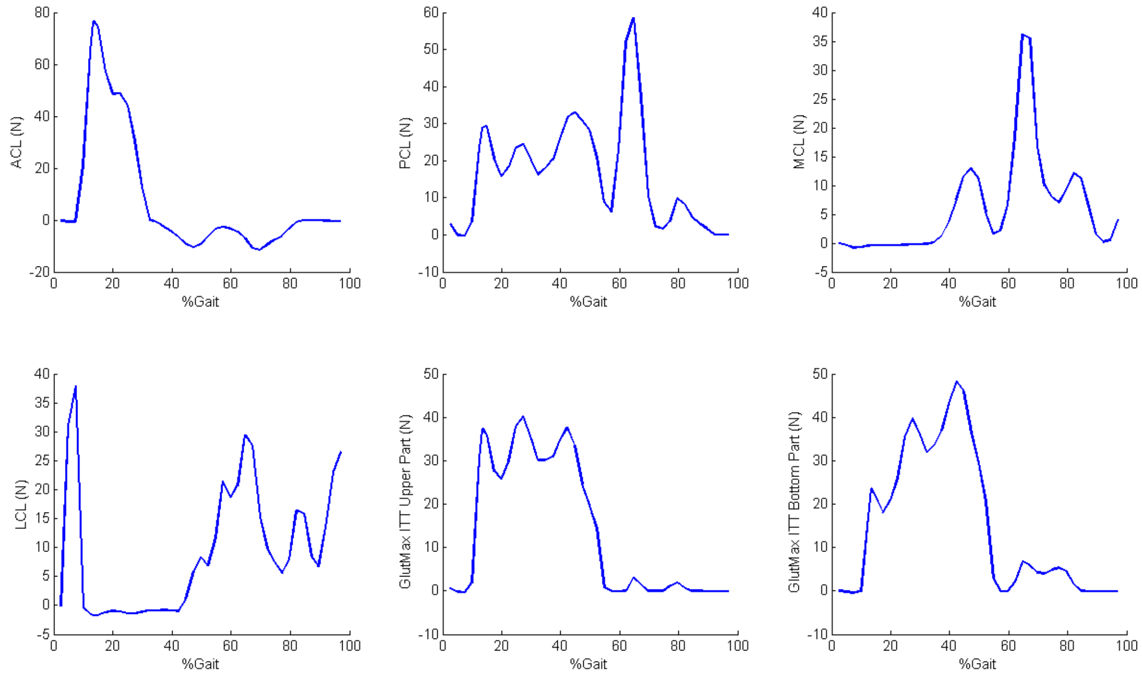

Figure 5.10 - Predicted ligamentous structures forces by the Multiple Load Case 3D Femur Model for level walking.

Figure 5.10 shows the predicted forces in the ligamentous structures modelled, with the low forces produced by the cruciate and collateral ligaments highlighting the stability of the knee joint. These forces are lower than the ones predicted in Phillips' single leg stance free boundary condition model (131 N for the anterior cruciate ligament, ACL, and 96 N for the lateral collateral ligament, LCL) (Phillips 2009). An explanation for this could be that the contact conditions modelled by Phillips would increase the instability in the distal region of the femur, therefore requiring larger forces by the ligaments to maintain the equilibrium.

5.3.2 Stair Climbing

Figure 5.11 shows the comparison of the muscle forces predicted by the Multiple Load Case 3D Femur Model (in blue) and the musculo-skeletal model developed by Modenese (in red) (Modenese et al. 2011) for stair climbing.

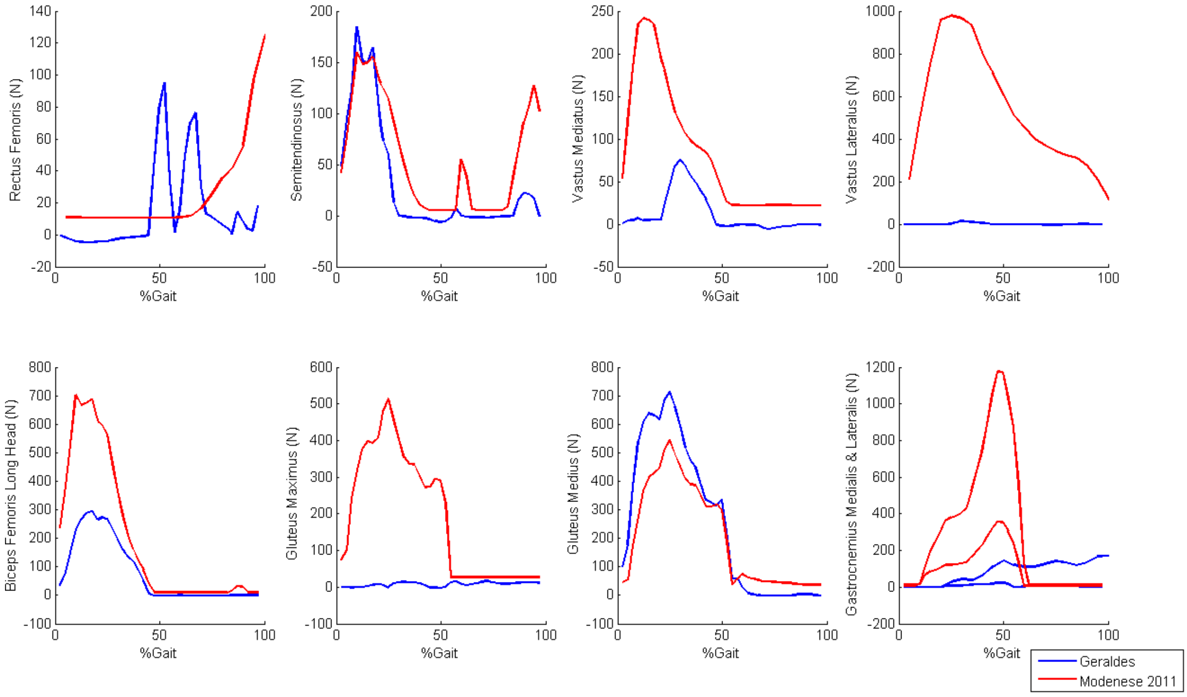

Figure 5.11 - Some of the predicted muscle forces by the Multiple Load Case 3D Femur Model (blue) and the model developed by Modenese (red) for stair climbing.

When comparing the forces predicted by the Multiple Load Case 3D Femur Model and the profiles produced by Modenese, it can be observed that the gluteus medius, the long head of the biceps femoris, the vastus mediatus and the semitendinosus muscles activation profiles are comparable, with the mono-articular hip joint muscles producing similar peak forces. The other mono-articular muscles crossing the knee joint (vastus lateralus and gastrocnemii) show very low to practically zero activation patterns. The possible explanations for the apparent inactivation have already been proposed in the previous subsection.

The forces predicted for the other muscles during stair climbing for both the proposed model and Modenese's musculo-skeletal lower limb model (Modenese et al. 2011) are represented in Figure 5.12.

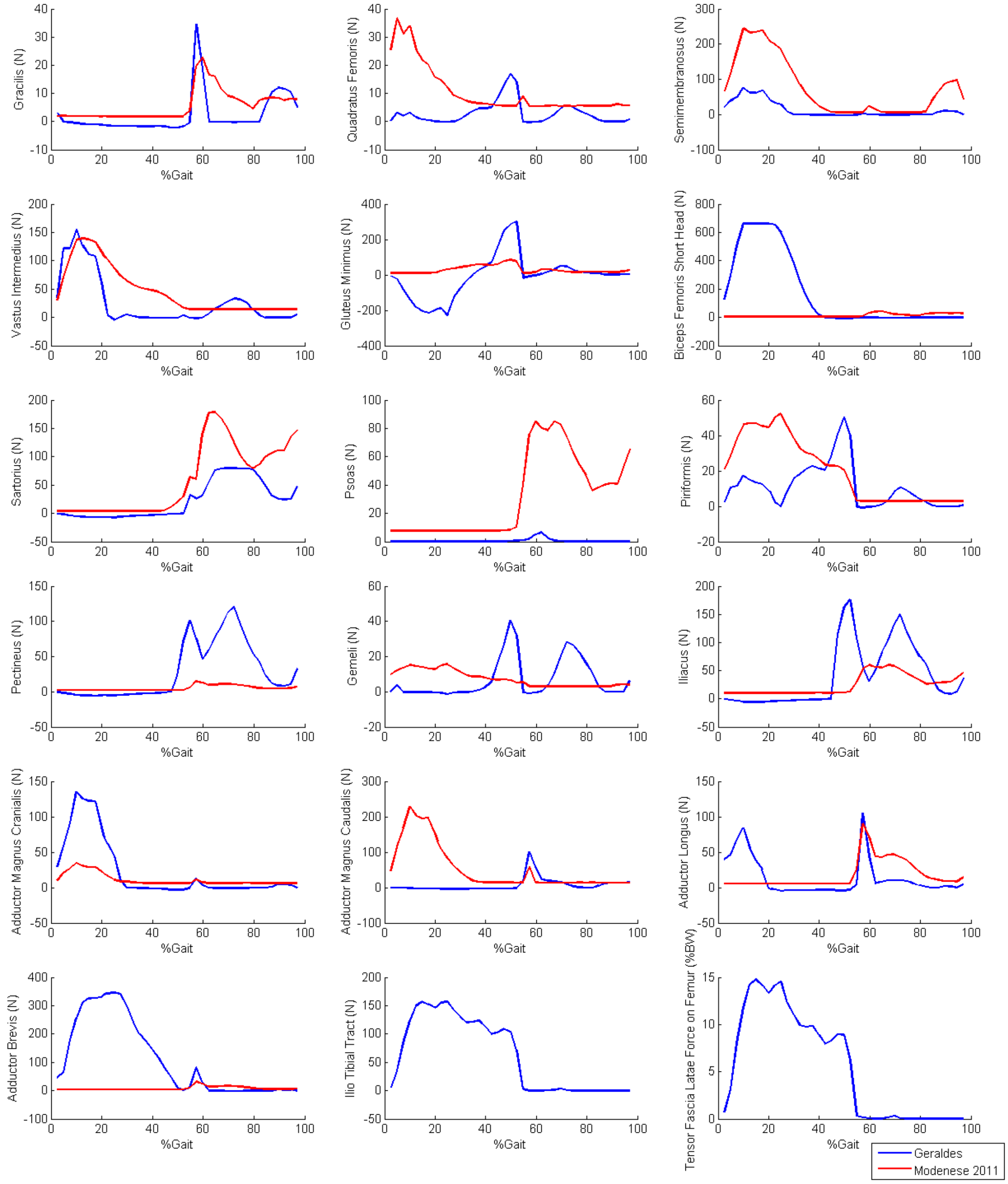

Figure 5.12 - Some of the predicted muscle forces by the Multiple Load Case 3D Femur Model (blue) and the model developed by Modenese (red) for stair climbing.

Similarly to what was observed for level walking, if the contribution of the shorter head of the biceps femoris is added to the forces produced by the long head bundle, a closer match is found between the predicted muscle force curves. Muscles such as gracilis, semimembranosus, vastus intermedius, sartorius and piriformis have activation patterns and muscle forces matching

Modenese's predictions (Modenese et al. 2011). The gluteus minimus shows a similar negative component in the first 20% of the gait cycle to the level walking load case and, just as for that load case, this profile could arise from the antagonistic action of the adductor muscles, very active when compared to Modenese's results. The short head of the biceps femoris seems to reach its limit throughout its activation stage suggesting that either the way the split of this muscle was modelled or the value used for its peak force of 400 N (Delp 1990) may need to be improved. The wrapping effect of the tensor fascia latae was also present with up to 15 % BW transmitted back to the femur. Stair climbing involves higher contact forces (Bergmann et al. 2001; Heller et al. 2001) and, therefore, more instability in the medial-lateral plane (where most bending occurs). Therefore an increase in the forces produced by these muscles is expected for this activity.

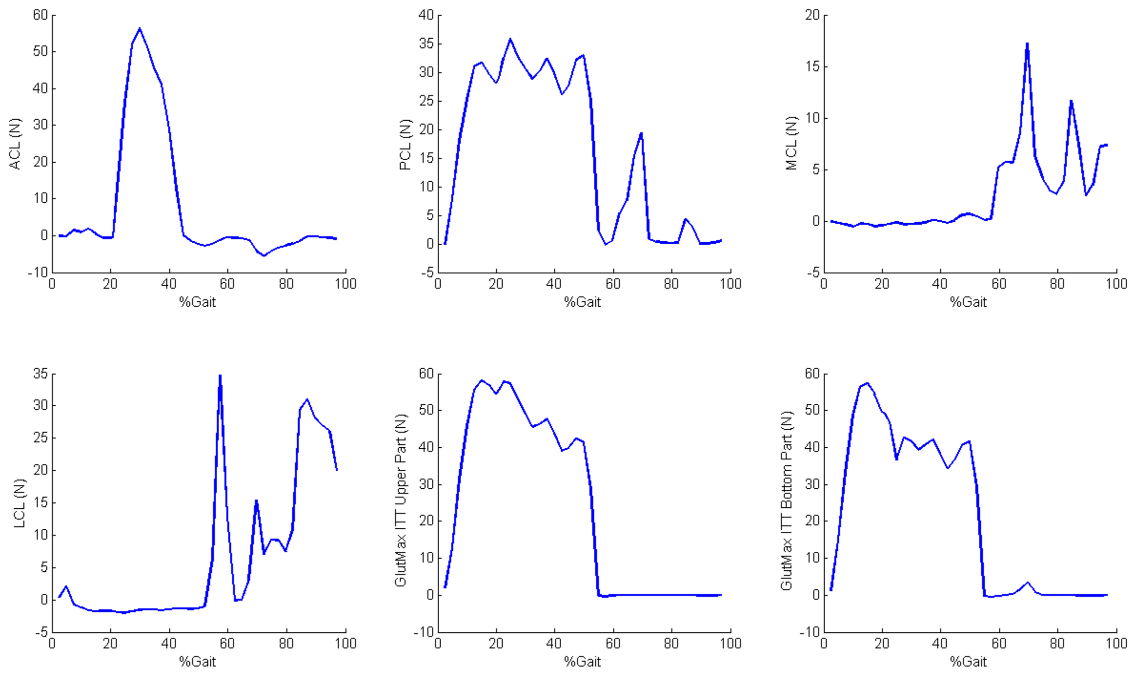

Figure 5.13 - Predicted ligamentous structures forces by the model for stair climbing.

Figure 5.13 shows the predicted forces in the ligamentous structures modelled and are very similar to the profiles obtained during level walking load case, accentuating once again the reduced displacements occurring at the knee joint.

5.3.3 Discussion

The higher inter-segmental forces and flexion angles generated during the daily activities modelled in this Chapter result in increased muscle force activation in comparison to the single leg stance modelled in Chapter 3. The differences between the muscle profiles produced by the Multiple Load Case 3D Femur Model and the forces calculated by musculo-skeletal models or activation profiles measured by EMG can be narrowed down to two types of causes: the FE model and the muscle definitions.

There are some limitations in the way the muscles anatomical positioning and behaviour were defined. The definition of certain muscles as straight paths of action instead of their anatomical wrapping configuration can produce different force profiles and lines of action. This is particularly evident in the gluteus muscles.

The same muscles highlighted the problems arising from the definition proposed by Phillips (Phillips 2009) when movements occur in the opposite direction, creating extreme negative displacements and producing compressive forces. Another limitation to Phillips' linear definition is that the passive effect of muscle volume on the femoral structure is ignored when modelling of muscles as bundles of spring connector elements. Finally, since the muscle forces calculated result from an equilibrated FE model, muscle co-contraction is not considered.

The imposition of fixed boundary conditions at the node in the medial condyle instead of allowing the distal region of the femur to balance on the tibia, restricts the movement of this part of the femur. Because of the way muscles were defined, this restriction in displacement of the connector elements inserting in the knee results in lower distal muscle and ligament forces than might be expected.

Table 5.4 outlines the peak forces obtained by the proposed model for the two load cases analysed. These are coherent with the muscle forces calculated by musculo-skeletal models (Heller et al. 2001; Modenese et al. 2011) and "equilibration" type models (Duda et al. 1998; Phillips 2009; Younge 2012). Furthermore, the activation patterns of some muscles are in agreement with measured EMG profiles for the level walking load case (Wootten et al. 1990; Perry 1992).

Table 5.4 - Peak values of the muscle and ligament forces calculated by the Multiple Load Case 3D Femur Model for both level walking and stair climbing.

Muscle / Ligament	**Level walking (N)**	**Stair climbing (N)**
ACL	77	76
Adductor Brevis	332	344
Adductor Longus	214	97
Adductor Magnus Cranialis	165	137
Adductor Magnus Caudalis	211	102
Biceps Femoris Long Head	270	293
Biceps Femoris Short Head	663	663
Gastrocnemius Lateralus	215	179
Gastrocnemius Mediatus	26	23
Gemeli	65	40
Gluteus Maximus	151	27
Gluteus Maximus ITT Bottom Part	48	56
Gluteus Maximus ITT Upper Part	40	55
Gluteus Medius	616	729
Gluteus Minimus	354	302
Gracilis	83	40
Iliacus	326	169
ITT	113	148
LCL	38	30
MCL	36	17
PCL	52	35
Pectineus	132	122
Piriformis	119	50
Quadratus Femoris	37	17
Rectus Femoris	396	93
Sartorius	82	80
Semimembranosus	136	70
Semitendinosus	248	172
Tensor Fascia Latae	88	121
Vastus Intermedius	158	153
Vastus Lateralus	52	3
Vastus Mediatus	123	27

Notwithstanding the limitations discussed in this Section, the muscle force profiles obtained by the model proposed in this thesis are considered to be acceptable representations of *in vivo* loading during level walking and stair climbing.

5.4 Conclusion

The chosen driving stimulus of bone adaptation needs to be derived based on an accurate representation of *in vivo* loading, in order to achieve physiologically meaningful material property distributions and orientations. This Chapter analysed the muscle and ligament forces, the joint contact and reaction forces and the stress and strain distributions produced by the model. Although a number of limitations are discussed in Section 5.3, the resulting muscle force profiles for both walking and stair climbing were considered to be acceptable representations of what occurs *in vivo*. Section 5.2 compared the forces produced at the hip and knee joints produced for both the level walking and stair climbing load cases to conclude that, despite their over and under prediction, these are consistent with the values measured *in vivo* and calculated using musculo-skeletal models and other static equilibrium analysis. Finally, both combined principal strains distribution patterns for the converged model agree qualitatively and quantitatively with similar numerical models.

It is therefore proposed that the developed Multiple Load Case 3D Femur Model provides a suitable platform for the prediction of bone material properties and orientations.

Chapter 6

Bone Adaptation Results

Chapter 4 discussed the modifications introduced in the remodelling algorithm from Chapter 2 in order to model the effect of multiple load cases in the adaptation process. A selection criterion for a guiding frame was defined for each element of the femoral mesh during each iteration of the adaptation process. Orthotropic material orientations were rotated to match the local dominant principal stress directions and the material properties (Young's moduli, shear moduli and Poisson's ratios) modified proportionally to the local associated strain stimulus. In order to model the optimised material distribution that allows bone to achieve the highest structural integrity with the least amount of material possible, the stimulus that drives the bone remodelling is required to be physiologically meaningful and the results produced by the adaptation process comparable with clinical observations *in vivo*. Chapter 5 concluded that the Multiple Load Case 3D Femur Model can produce a reliable driving signal of the remodelling process, by comparing the combined von Mises stresses and combined principal strain distributions, joint contact and reaction forces and muscle and ligament forces produced with data from instrumented prosthesis (Bergmann et al. 2001; D'Lima et al. 2006) and EMG (Wootten et al. 1990) measured *in vivo*, Modenese's musculo-skeletal model (Modenese et al. 2011; Modenese and Phillips 2012) and other models found in literature (Heller et al. 2001; Polgar et al. 2003; Speirs et al. 2007; Phillips 2009). This Chapter attempts to assess if the adaptation process was satisfactorily achieved for the Multiple Load Case 3D Femur Model. Section 6.1 analyses the distributions of the directional Young's moduli calculated whilst Section 6.2 shows the results obtained for the orthotropic shear moduli. Section 6.3 looks at the equivalent density distributions, particularly in the proximal and distal regions of the femur. Section 6.4 assesses whether the directional information produced by the algorithm is reliable, by comparing it with observational studies and micro CT images (μCT) of the same regions, together with published literature. Conclusions on the material properties distribution and directionalities produced by the algorithm are drawn in Section 6.5.

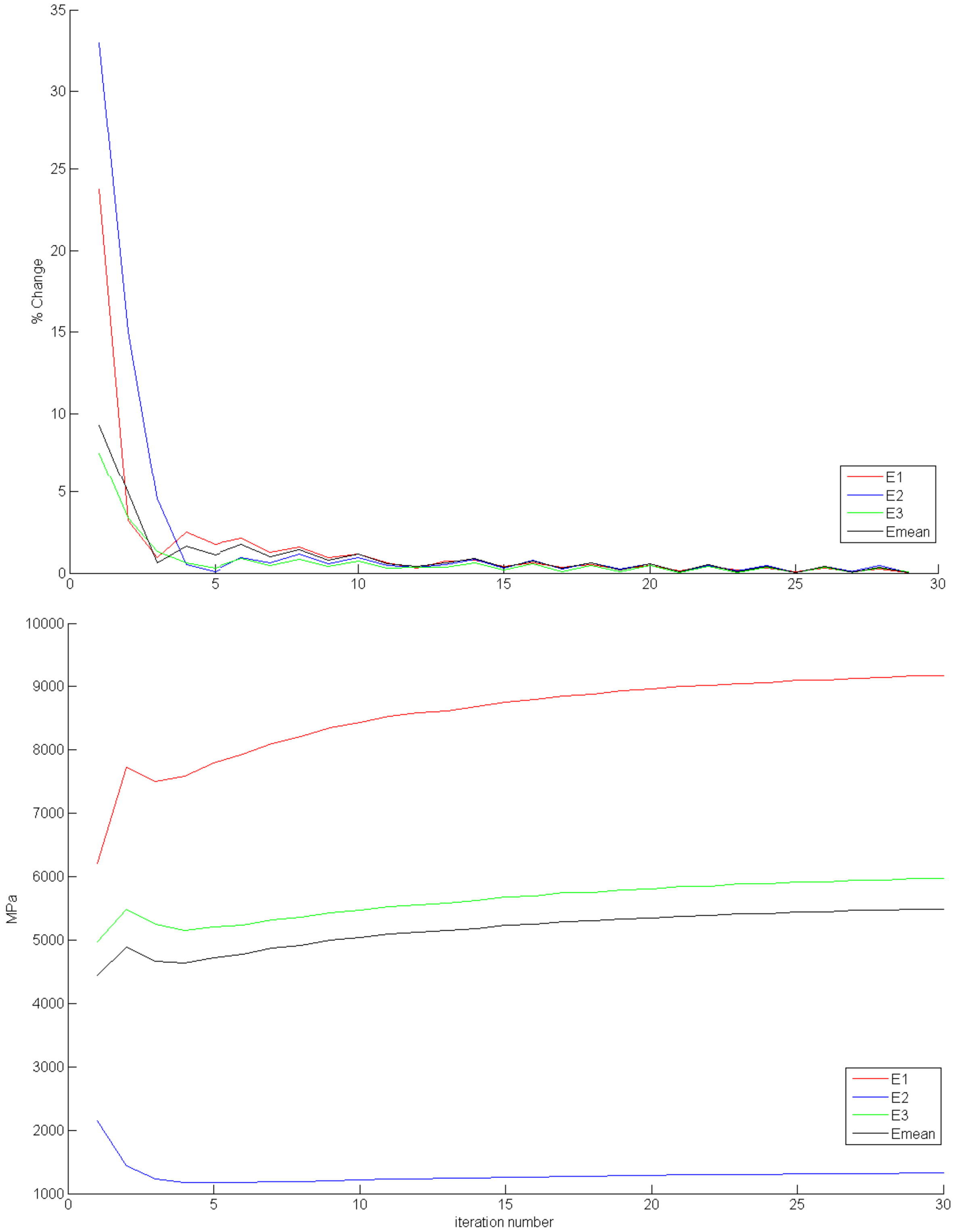

Figure 6.1 - Convergence curves: average changes (top) and mean value (bottom) of E_1, E_2, E_3 and E_{mean} in all elements with increasing iteration number.

6.1 Young's Moduli

The proposed adaptation algorithm updated the directional Young's moduli along each element's orthotropic material orientations proportionally to the local strain associated with principal stress directions. The analysis started with all elements being assigned the same initial orthotropic elastic constants ($E_1 = E_2 = E_3 = 3000$ MPa, $\nu_{12} = \nu_{13} = \nu_{23} = 0.3$, $G_{12} = G_{13} = G_{23} = 1500$ MPa) and local orthotropic orientations matching the global reference system. The femur's main anatomical features are shown in Figure A.6 (in the Appendix).

The orientation of each element was found to converge quickly after 4 iterations, indicating that the principal strain directions had aligned with the principal stress directions after this stage. Elements of extremely low elastic stiffness also undergoing negligible strains were grouped into a 'no-bone zone' and excluded from the simulation convergence criteria, since they represent areas where virtually no bone can be found. Convergence was achieved at the 29^{th} iteration, when the average change in Young's moduli of elements outside the no-bone zone was considered to be negligible (<1%).

Figure 6.1 shows the average changes in the Young's moduli (top) and the evolution of their mean values (bottom) with increasing iteration number. E_{mean} was calculated as the average of the three orthotropic Young's moduli: E_1, E_2 and E_3. It can be seen that all curves achieve the pre-determined convergence criteria, with an oscillating behaviour observed in the top part of Figure 6.1 as the model attempts to reach the remodelling plateau. Similar curves were obtained by Miller's 2D orthotropic bone remodelling algorithm when applied to the proximal femur (Miller et al. 2002).

The distribution of E_1, the directional Young's modulus associated with minimum principal strains, is depicted in Figure 6.2. The areas where medium or high values are present can be seen along the medial aspect of the femoral shaft, distributed between the medial side of the epiphysis and the articular surface of the femoral head, beside the inferior part of the femoral neck, along the greater trochanter and around the intercondylar notch. These correspond to regions where compression is expected to be the predominant mode of loading and, therefore, producing higher minimum principal strains (Taylor et al. 1996). The high compressive strains are a consequence of the bending of the femur resulting from the transfer of the compressive hip contact force applied on the articular surface of the femoral head to the femoral shaft (Ward 1838; Garden 1961), from the action of the muscles attached to the greater trochanter (Skedros and Baucom 2007) and the compressive stresses arising from the application of the tibio-femoral reaction force (Takechi 1977).

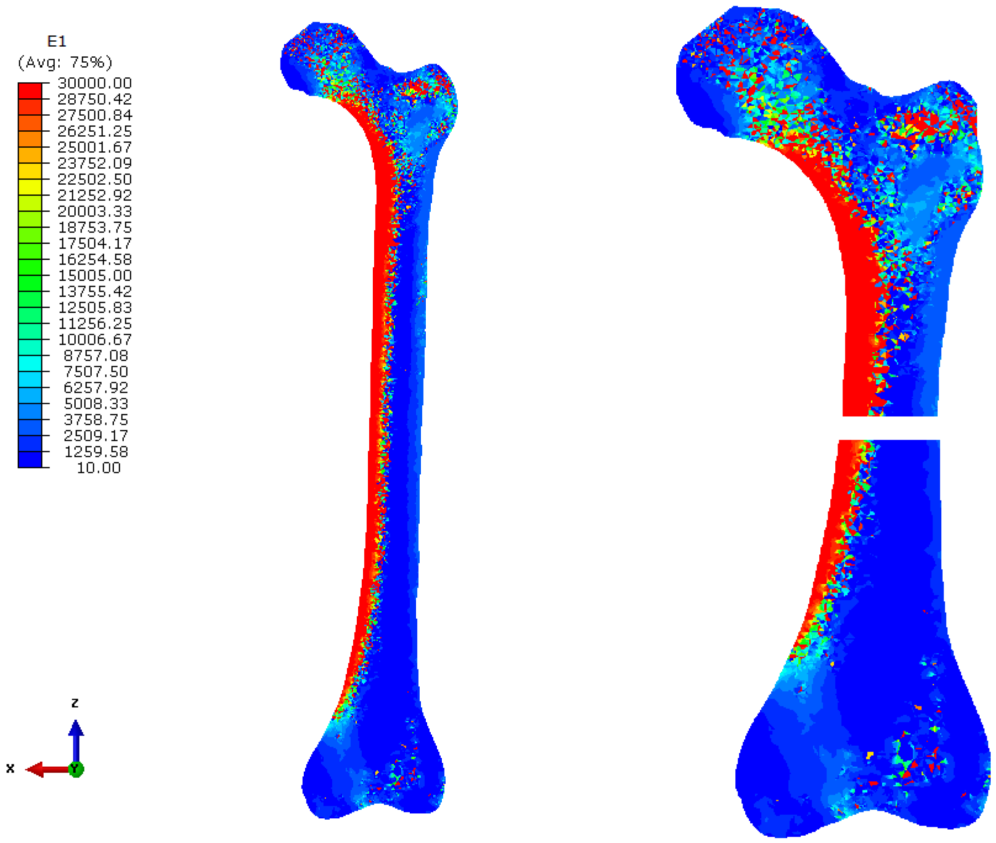

Figure 6.2 - Coronal representation of the distribution of E_1 (MPa) for the whole femur (left) and detailed for the proximal (top right) and the distal (bottom right) regions.

The areas where medium or high values for E_3, the directional Young's modulus associated with maximum principal strains, can be seen in Figure 6.3 and are located along the lateral aspect of the cortical shaft, the superior side of the femoral neck, the calcar femorale and the lateral condyle. These are regions where high tensile strains are expected, on the opposite side of the compressive strains (Ward 1838; Garden 1961; Takechi 1977; Taylor et al. 1996)

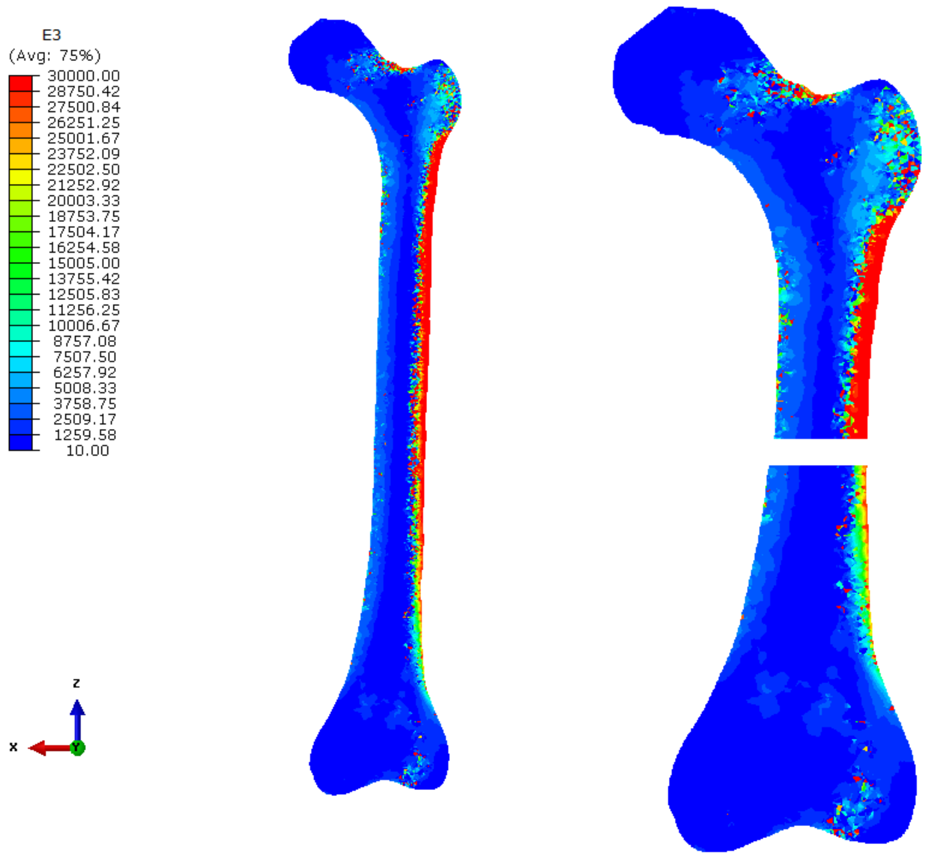

Figure 6.3 - Coronal representation of the distribution of E_3 (MPa) for the whole femur (left) and detailed for the proximal (top right) and the distal (bottom right) regions.

The distribution of E_2, the directional Young's modulus associated with medium principal strains resulted in values relatively low in comparison with the other directional Young's modulus, increasing slightly in the medial and lateral sides of the femoral shaft.

The high values for the directional Young's moduli found along the femoral shaft are within the ranges [23.6 - 36.0 GPa] calculated for the longitudinal Young's modulus of long bones by studies employing non-invasive measuring techniques such as ultrasonic wave propagation [27 – 32 GPa] (Rudy et al. 2011), acoustic microscopy [23.6 – 28.6 GPa] and synchrotron radiation μCT [30.0 –36.0 GPa] (Rohrbach et al. 2012). Invasive techniques such as nano-indentation [24.0 – 27.4 GPa] (Rho et al. 1997; Rho et al. 1999) and modal analysis of frequencies resulting from induced vibration [22.9 GPa] (Taylor et al. 2002) measured lower ranges in the longitudinal direction [22.9 – 27.8 GPa].

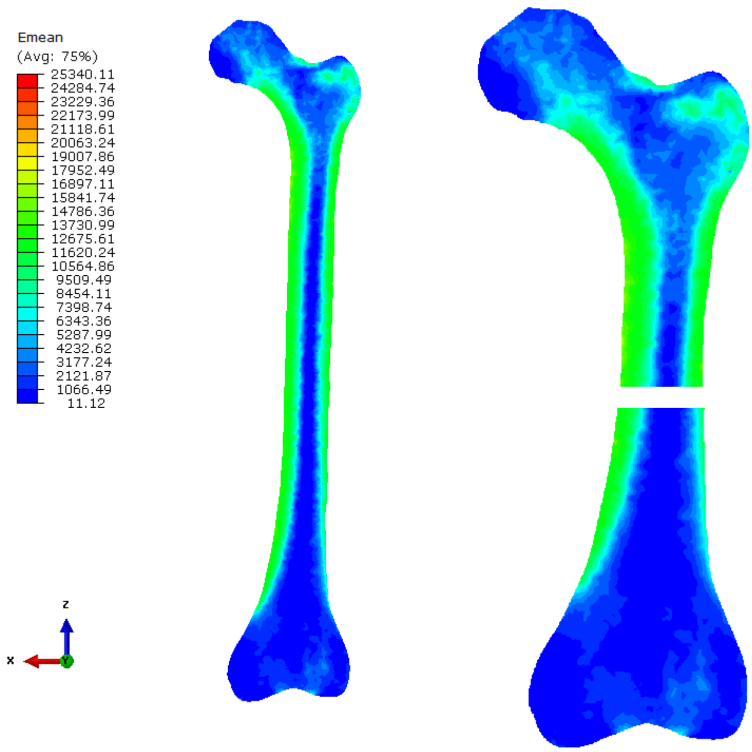

Figure 6.4 - Coronal representation of the distribution of Emean (MPa) for the whole femur (left) and detailed for the proximal (top right) and the distal (bottom right) regions.

Figure 6.4 shows the distribution of E_{mean} for a coronal slice through the whole femur. The resultant Young's modulus, E_{rep}, used in Chapter 3 is thought to over-estimate the joint effect of the directional Young's moduli, since an element with the same orthotropic Young's moduli in all three directions ($E = E_1 = E_2 = E_3$) should behave as an isotropic element with a Young's modulus of E. The regions where low stiffness and density values are present are the superior part of the greater trochanter, the intra-medullary canal along the femoral shaft, Ward's triangle, Babcock's triangle in the medial inferior region of the femoral head and the lateral superior region of the femoral head. The lower value regions predicted correspond to regions known for being either composed of thin and loosely arranged trabeculae, or for being virtually absent of any trabecular bone (Singh et al. 1970; Takechi 1977). The regions where the higher values can be found result from the superposition of the three directional Young's moduli figures. The features modelled in the mean Young's modulus distribution are in agreement with other 2D and 3D predictive studies of the proximal femur (Huiskes et al. 1987; Fernandes et al. 1999; Doblaré and Garcia 2001;

Miller et al. 2002; Tsubota et al. 2002; Wang and Mondry 2005; Rossi and Wendling-Mansuy 2007; Tsubota et al. 2009) and models which have assigned material properties from CT scans (Bitsakos et al. 2005; Behrens et al. 2009). Figure 6.4 also shows that the orthotropic material assumption can generate E_{mean} distributions consistent with the ones achieved by assuming bone to be isotropic either via bone remodelling algorithms (Huiskes et al. 1987; Beaupré et al. 1990a; Beaupré et al. 1990b; Behrens et al. 2009) or direct assignment of material properties from CT scans (Carter and Hayes 1977; Peng et al. 2006; Baca et al. 2008). However, these models do not give any directional information on the bone's material properties.

The anterior and posterior surface distributions of E_{mean} for the whole femur can be seen in Figure 6.5. It is observed that there is a line at both sides of the femoral shaft where low stiffness values are found. This line seems to be in between the regions under compression and tension, along a neutral axis which separates the two loading modes. Since the strains calculated for these regions and shown in Chapter 5 are within the remodelling plateau, it seems that bone along this region will not increase or decrease its stiffness.

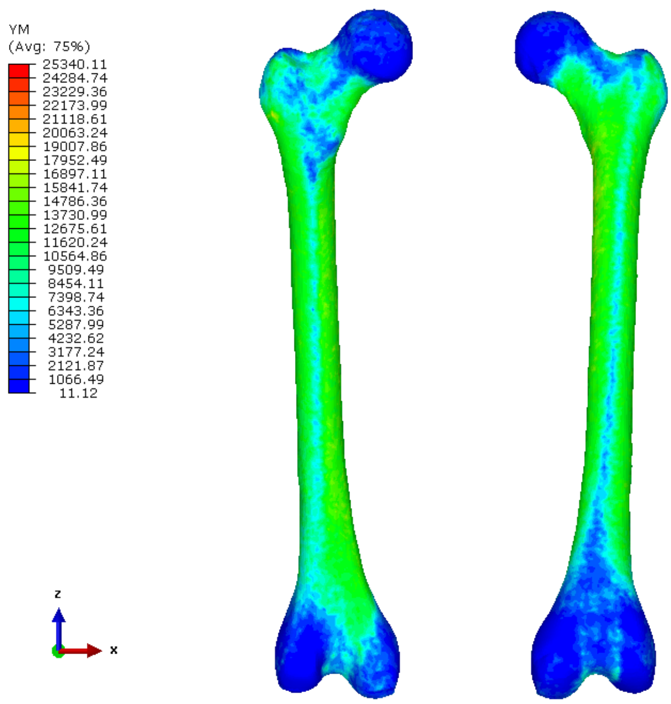

Figure 6.5 - Anterior (left) and posterior (right) representations of the distribution of E_{mean} (MPa) for the whole femur.

Some muscles attaching along the linea aspera or the anterior aspect of the femoral shaft were highlighted not to fully activate in the two load cases modelled (Chapter 5). The author therefore proposes that future work should investigate the modelling of daily activities where higher activation of muscles such as the quadriceps, gluteus maximus, pectineus or the adductors is expected. These occur during activities where higher flexion angles are involved (standing up from a chair) or extreme muscle activation occurs (running) (Blain et al. 2009).

It is interestingly noticed that the low stiffness values found coincide with regions where fractures occur more frequently. Femoral neck fractures often initiate in the anterior-posterior plane of the femoral neck (Wolff 1892; Klenerman and Marcuson 1970; Kyle et al. 1994; Juszczyk et al. 2011); inter-trochanteric fractures are also commonly observed (Wolff 1892; Taggart and Beringer 1984). Less common helicoidal (Salminen et al. 1997) or stress fractures (Daffner and Pavlov 1992; Nieves et al. 2010) in the femoral shaft and in the distal femur (Martinet et al. 2000) have also been reported and shown to also be associated with reduced survival in elderly patients (Streubel et al. 2011).

6.2 Shear Moduli

Despite the adaptation of the orthotropic Young's moduli to resist axial stresses arising from the compressive action of the hip contact and knee reaction forces on the femur, trabeculae have been suggested to also resist the shear stresses emerging from the range of load cases that bone is subjected to (Skedros and Baucom 2007). Trabeculae have shown to align themselves orthogonally and along the directions of the principal stresses in regions where bone is simply loaded (Pedersen 1989). However, non-orthogonal secondary groups crossing at acute angles can be observed in areas where complex loading occurs, such as in the proximal femur or in the condyles (Ward 1838; von Meyer 1867; Wolff 1892; Garden 1961; Takechi 1977; Miller et al. 2002; Miller and Fuchs 2005; Skedros and Baucom 2007; Skedros and Brand 2011).

Orthotropic material symmetry was assumed, since it is a closer approximation to bone's anisotropy (Ashman et al. 1984) than the commonly used isotropic approach. However, at a continuum level, the observed decussation in trabecular structures cannot be modelled fully, since trabeculae are inherently assumed to cross at 90°. In an attempt to model this resistance to shear and, therefore, to approach the continuum model to a structural representation, the iterative algorithm was modified to include adaptation of the orthotropic shear moduli (G12, G13 and G23) towards a remodelling plateau around a target shear strain value of 1443 µstrain (Chapter 4). Similarly to the Young's moduli adaptation process, the elements with extremely low shear modulus undergoing negligible strains were grouped into a 'no-bone zone' and excluded from the simulation. The same convergence criteria applied to Young's moduli was used.

Figure 6.6 (top) shows the average changes in the shear moduli with increasing iteration number. It can be observed that all curves decreased with an oscillating behaviour until the pre-determined convergence criterion was achieved. The curves seem to quickly reach a value closer to the convergence limit quickly, notwithstanding taking more than double of the number of iterations for the Young's moduli optimisation process, highlighting the complexity of the adaptation to shear strains in comparison with the axial strains. The mean value for the shear moduli can also be seen to converge (Figure 6.6, bottom).

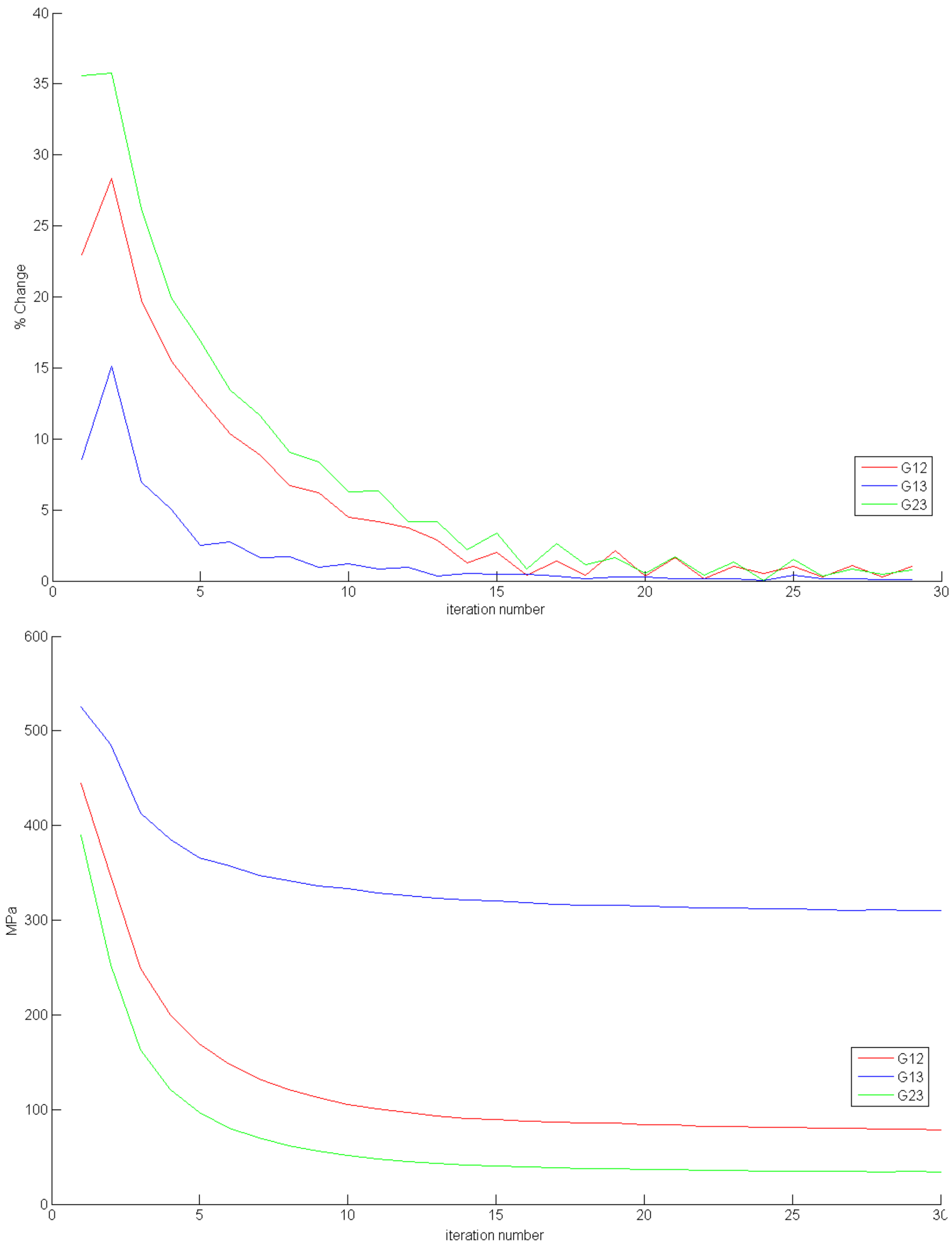

Figure 6.6 - Convergence curves: average changes (top) and mean values (bottom) of G_{12}, G_{13} and G_{23} (MPa) in all elements with increasing iteration number.

Figure 6.8 to Figure 6.11 display the distribution of G_{12}, G_{23} and G_{13} (MPa), respectively, for the whole femur. For the coronal slices representations of the proximal and distal femur all the elements with shear modulus above 10 GPa were grouped in order to highlight the areas where trabeculae were adapted to shear.

Shear modulus values were higher for G_{13} than for G_{12} and G_{23} and spanned ranges reported in literature for trabecular bone [0.4 – 6.2 GPa] (van Rietbergen et al. 1995; van Rietbergen et al. 1998; Kabel et al. 1999; Taylor et al. 2002; Rohrbach et al. 2012) (Figures 6.8 to 6.10).

G_{13} showed higher values than G_{12} and G_{23}, as expected, since shear strains should be higher between the two predominant modes of loading of bone (compression, E_1, and tension, E_3) than between the other two less significant combinations.

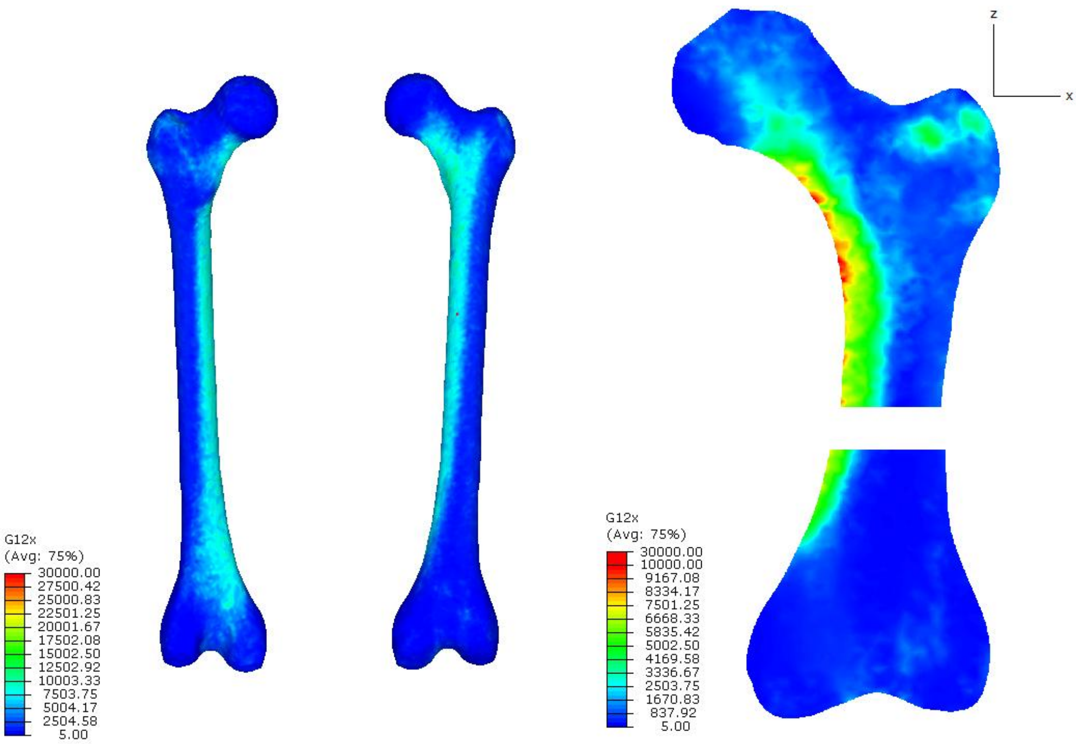

Figure 6.7 - Anterior (left), posterior (middle) and coronal (right) representations of the distribution of G_{12} (MPa) for the whole femur.

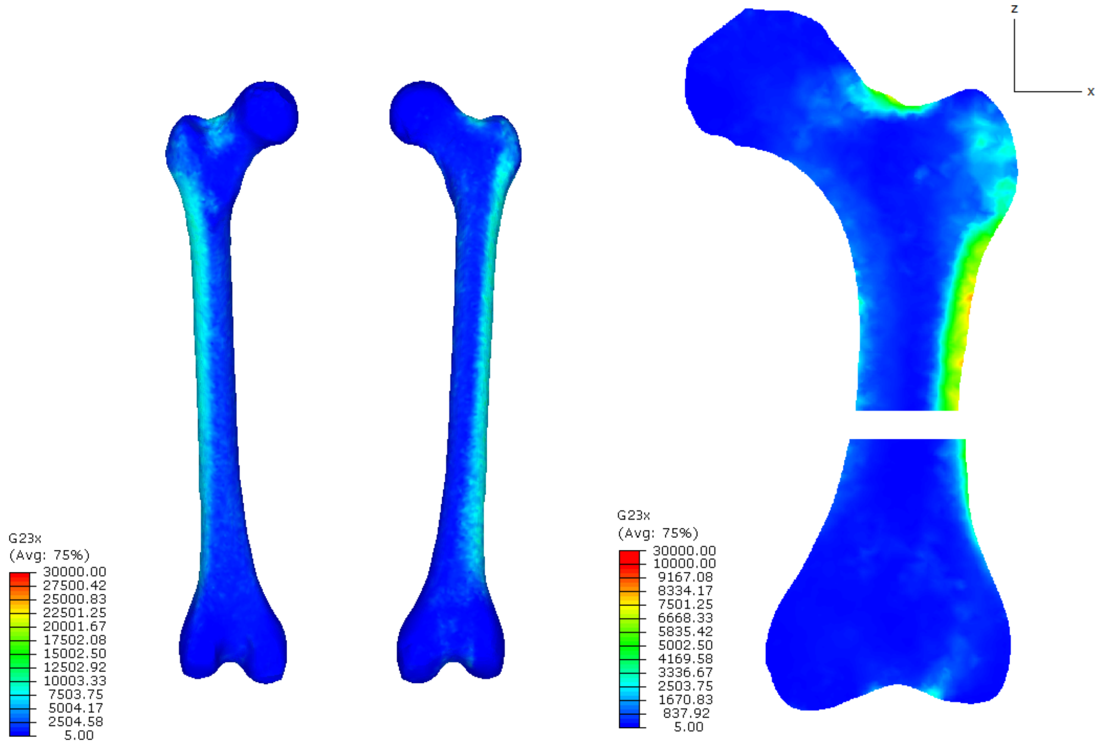

Figure 6.8 - Anterior (left), posterior (middle) and coronal (right) representations of the distribution of G_{23} (MPa) for the whole femur.

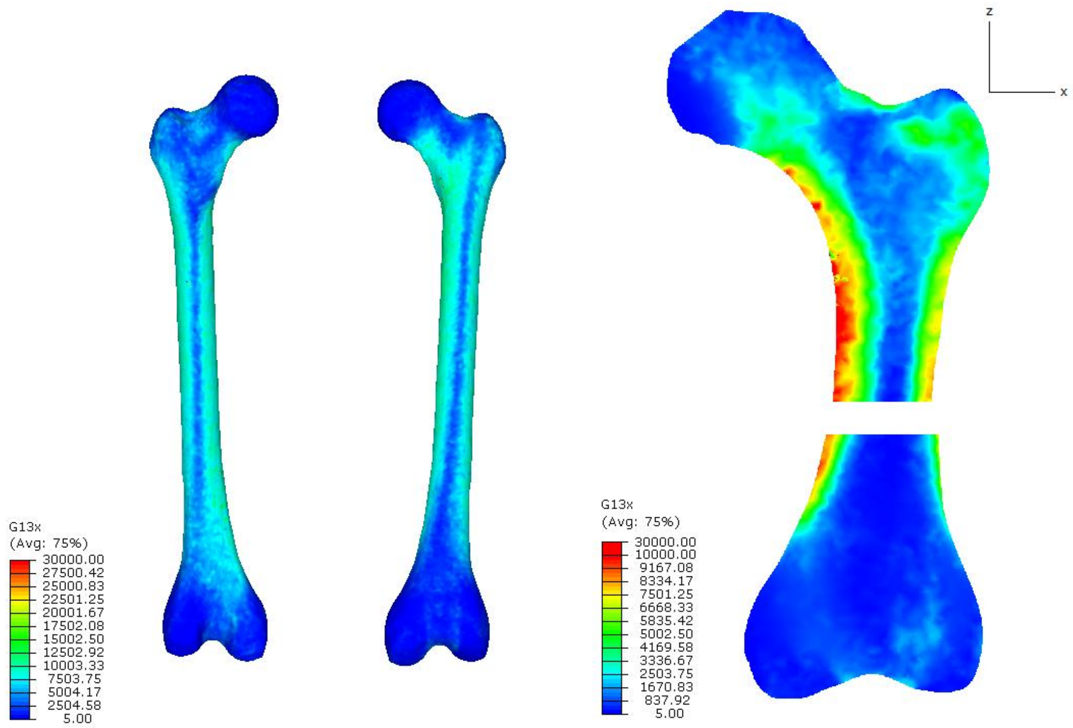

Figure 6.9 - Anterior (left), posterior (middle) and coronal (right) representations of the distribution of G_{13} (MPa) for the whole femur.

Figure 6.9 shows G_{13}, the shear modulus associated with the plane defined by the directions associated with E_1 and E_3 for each element. This is the plane where non-orthogonal trabecular crossing has been observed (von Meyer 1867; Tobin 1955; Garden 1961; Skedros and Baucom 2007) and suggested to be an adaptive response to the shear stresses arising from multi-axial loading (Pidaparti and Turner 1997; Skedros and Baucom 2007). The continuum model's orthotropic shear moduli were adapted to the shear strains arising from the multiple load cases modelled. The regions where high shear moduli were reported correspond to the regions where high shear forces (femoral neck) and torsional moments (femoral shaft) have been calculated using a structural analysis package (OASYS) (Younge 2012).

At a structural level, the non-orthogonality of trabecular crossing results from adaptation to shear (Skedros and Baucom 2007). A correspondence between zones of high shear moduli and non-orthogonal trabecular trajectories can therefore be drawn. The values for the trabecular shear modulus are particularly high in the superior and inferior femoral neck regions, the greater trochanter and along the femoral shaft. Relatively low values were also predicted in the inter-trochanteric region of the proximal femur, at the articular surface of the femoral head and at the condyles. The regions where high values of G_{13} are observed correspond to areas where non-orthogonal trabecular trajectories are expected. In contrast, regions where low values are predominant coincide with documented orthogonal crossings (Garden 1961; Singh et al. 1970; Takechi 1977; Skedros and Baucom 2007). More information on the directionality of the trabeculae can be read in Section 6.4. The relationship between shear modulus and directionality is further explored in Chapter 7.

6.3 Density

The proposed model was evaluated to assess whether an accurate density distribution could be obtained from the calculated orthotropic Young's and shear moduli. Models with physiological density predictions can then be used in many different areas of biomechanics such as the prediction of the degradation of bone due to the effects of osteoporosis (Folgado et al. 2004) or the changes induced in bone by implants and prosthesis (Huiskes et al. 1987; Behrens et al. 2009; Kluess et al. 2009; Scannell and Prendergast 2009).

As discussed in Chapter 1, density can be calculated using a power relationship between Young's modulus and density (Carter and Hayes 1977; Hodgskinson and Currey 1992; Dalstra et al. 1993; Goulet et al. 1994; Kopperdahl and Keaveny 1998; Anderson et al. 2005; Helgason et al. 2008). Since shear moduli adaptation was included, it is possible for certain elements to converge with higher values of shear moduli than those that what might be expected when basing their adaptation on the directional Young's modulus. This was taken into account in the attempt to calculate a representative value of Young's modulus, E_{rep}, from which the equivalent density was calculated. The criterion presented below was selected as the best representation of the element's Young's modulus after a sensitivity study involving different criteria was performed (Ho 2012).

The mean Young's modulus, E_{mean}, was calculated for each element as the average of the three orthotropic Young's moduli. Simultaneously, the mean shear modulus, G_{mean}, was calculated as the average of the three orthotropic shear moduli. An equivalent Young's modulus, E_{equi}, value was found according to Equation 6.1.

$$E_{equi} = 2(1 - \nu)G_{mean} \tag{6.1}$$

E_{rep} was taken as the maximum value between E_{mean} and E_{equi} (Equation 6.2) for each element.

$$E_{rep} = max\,(E_{equi}, E_{mean}) \tag{6.2}$$

Five different isotropic density-modulus relationships were then used and their cumulative distribution across all elements plotted in Figure 6.10. These included relationships calculated in studies for different parts of the femur (Morgan et al. 2003; Kaneko et al. 2004), or pooled between different bones (Morgan et al. 2003). The calculated cumulative distributions were compared against a CT scan of an ethically obtained specimen of a male cadaveric femur, 27 years old, weight 75 kg and height 175 cm taken with a SOMATOM Definition AS+ scanner (Siemens AG, Munich, Germany) based in the Queen Elizabeth Hospital, Birmingham, United Kingdom. The specimen was scanned at 120 kV and 38.0 mAs and with an effective spatial resolution of 0.71 mm. The specimen's density was calculated by converting the Hounsfield Units (HU) values obtained with the CT scan to density values, using a relationship calculated by Dalstra for different regions of the pelvic bone (Dalstra et al. 1993).

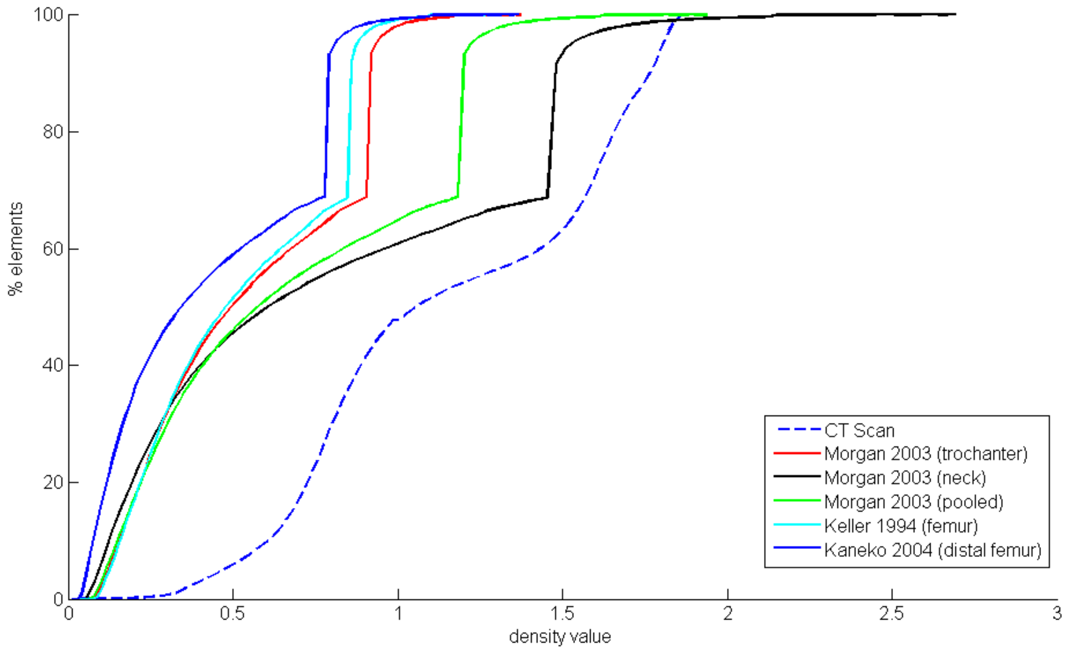

Figure 6.10 - Cumulative distributions of density values for different E_{mean} - density relationships (solid lines) versus the cumulative distribution extracted from a CT scan (dashed line) in g/cm^3.

Morgan's relationship for the femoral neck was chosen as it was found to give the closest match to the density distribution given by the CT scan (Morgan et al. 2003) and can be seen in Equation 6.3 below.

$$\rho = \left(\frac{E_{rep}}{6.850}\right)^{\frac{1}{1.49}} \tag{6.3}$$

The cumulative distribution predicted by the model was obtained by applying Morgan's relationship to all the elements not included in the 'no-bone zone' and can be seen in Figure 6.11. It was also compared with the predicted cumulative distribution resulting from the Single Load Case model.

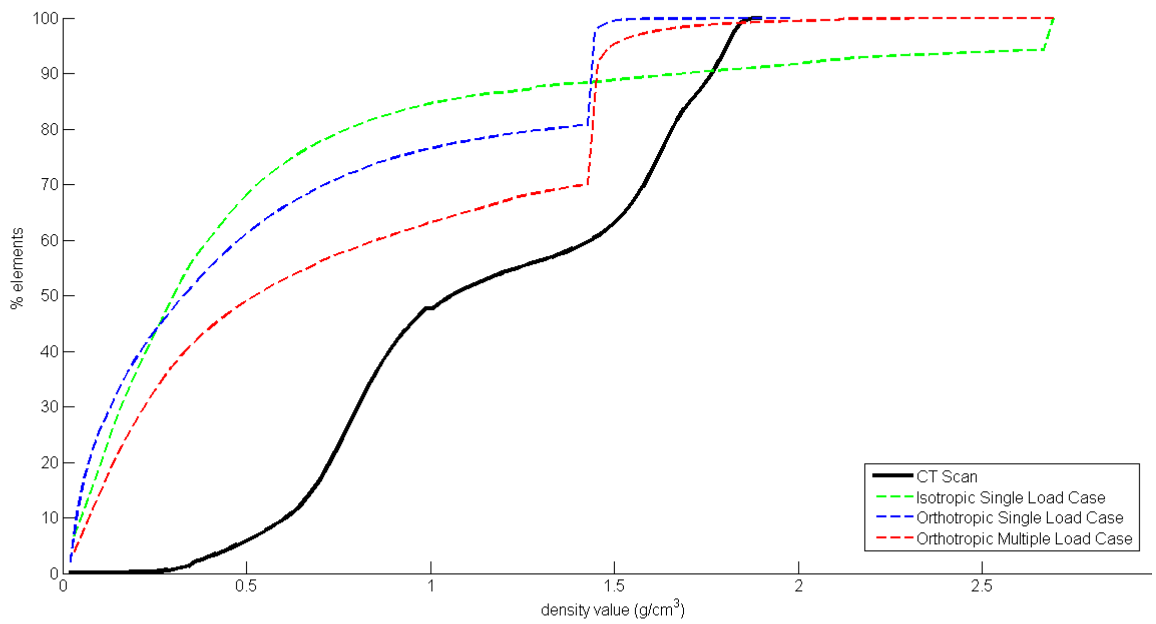

Figure 6.11 - Cumulative distributions of predicted density values and the density values extracted from CT (black) in g/cm^3 for a model undergoing a single load case with isotropic (green) and orthotropic (blue) material properties and an orthotropic adaptation algorithm undergoing multiple load cases (red).

The almost vertical increase observed at 1.4 g/cm^3 corresponds to the elements of high stiffness along the femoral shaft. The previous Section highlighted this abrupt transition between the intra-medullary canal where virtually no bone is found and the stiff cortical layer. A similar split between trabecular and cortical bone is observed in both curves although trabecular bone density is more uniformly distributed in the model predictions than in the CT measurements. A possible explanation for this could be the fact that the continuum model cannot accurately represent the empty spaces observed in the CT scans. The inclusion of multiple load cases in the analysis clearly improved the predictions, producing a more efficient orthotropic heterogeneous model of the femur (Figure 6.11). The improvements to the predictions by considering orthotropic adaptation and including multiple load cases are clearly observed in Figure 6.12.

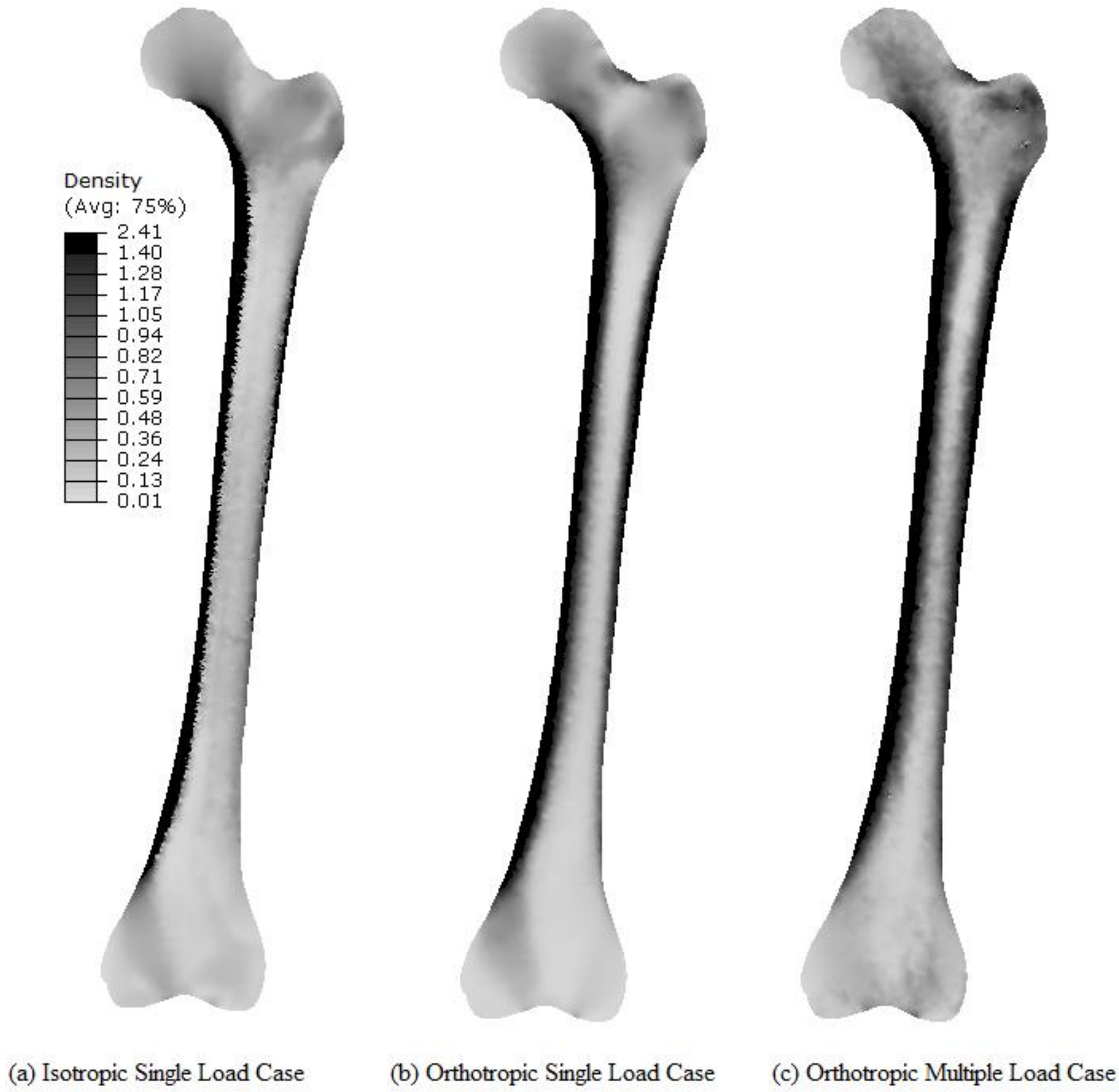

Figure 6.12 - The improvements to the predicted density distributions for a coronal section of the whole femur by considering orthotropic material properties and multiple load cases are clearly represented.

Figure 6.13 shows a comparison between a coronal slice of the CT scan of the femur specimen previously mentioned and the model predictions for the same region (with details of the proximal and distal regions). All elements with density above 1.4 g/cm^3 were grouped together as cortical bone, for the reasons already mentioned. All the important density distribution features observed in the CT scans were correctly predicted. Low density regions in the intra-medullary canal, Ward's triangle, Babcock's triangle, the region just above the principal compressive group in the femoral head and medial to the superior part of the femoral neck, as well as the epicondylar regions for both condyles, are all present in the model predictions. Furthermore, the thick femoral shaft and the denser regions in the superior and inferior regions of the femoral neck, along the surface of the greater trochanter and around the intercondylar notch all seem to be coherent with the CT observations.

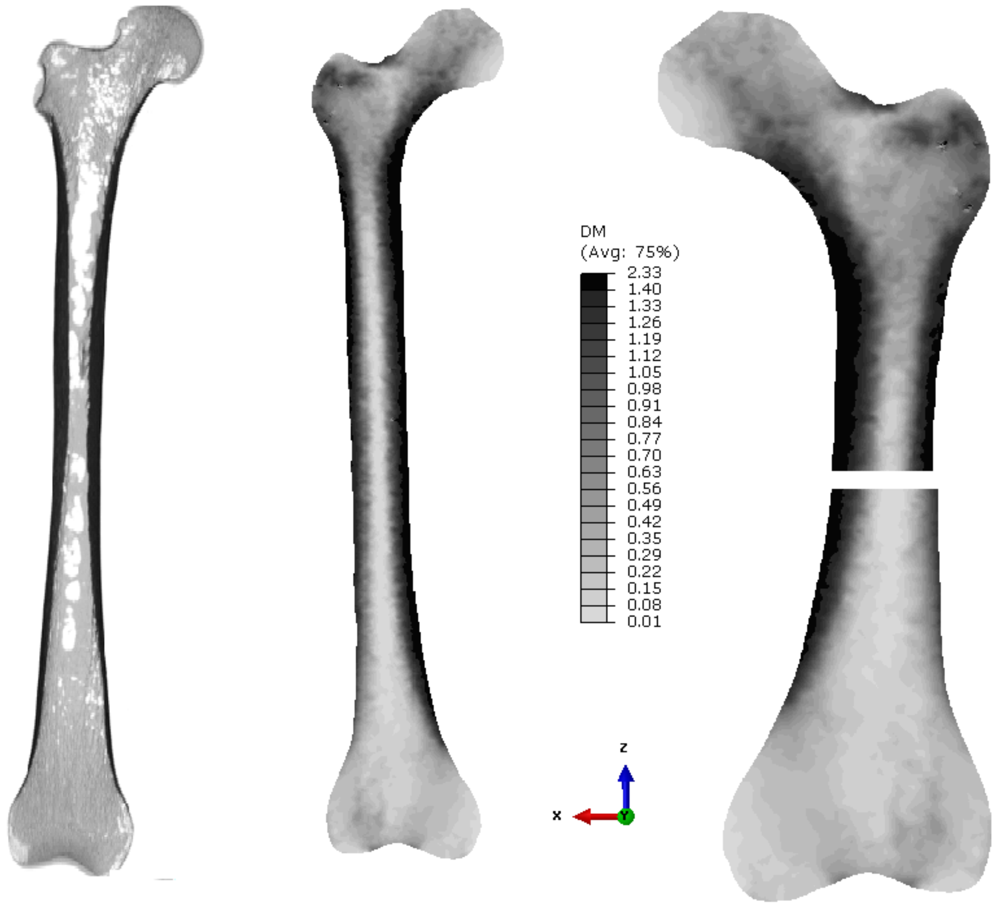

Figure 6.13 - Coronal slice of the CT scan of the femoral specimen (left), model predictions for a similar region (middle) and detail of the proximal femur (top, right) and the distal femur (bottom, right) in g/cm^3.

It should be highlighted that the geometries of the femurs in question are different, which can lead to differences in the results, particularly along the femoral shaft, since it is much straighter in the synthetic femur compared to the natural one. Furthermore, despite the best effort to compare the same coronal sections of the femur, an exactly identical cut could not be achieved, a possible explanation to why the medial aspect of the shaft seems much thicker than its lateral counterpart. In addition, the effect of muscle wrapping and high activation in the greater trochanter region can justify the higher density values observed in this part of the femur. The passive muscle action of the tensor fascia latae wrapping smoothly at the greater trochanter could be over-predicted by the tied conditions implemented between the artificial structure defined in Chapter 4 and the surface of the femur.

Finally, similar to the E_{mean} distribution discussed in the previous Section, it is observed that there are regions of low density values at both anterior and posterior aspects of the femoral shaft, inter-trochanteric line and anterior and posterior sides of the femoral neck (Figure 6.14, right).

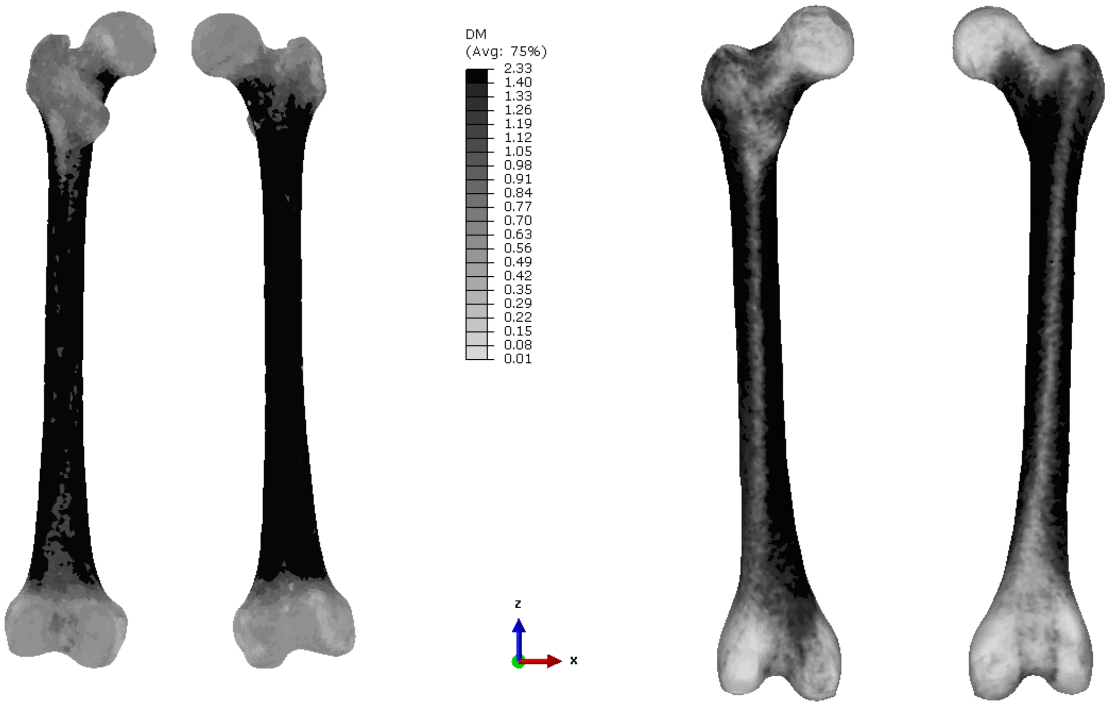

Figure 6.14 - Anterior and posterior representations of the CT scan measurements (left) and predicted density distribution (g/cm^3) (right) for the whole femur.

Interestingly, regardless of the different geometries of the femurs compared in this Chapter, some of the features of the femoral density in the cortical shaft are still predicted, in particular in the anterior side of the distal region and along the inter-trochanteric line (Figure 6.14). Figure 6.15 highlights the same regions of low density in four CT slices taken along the femoral shaft, showing why the cortical density at the external surface of the femoral shaft does not compare so clearly, predominantly in the posterior side of the cortical shaft. However, lower density regions are still observed in the interior surface.

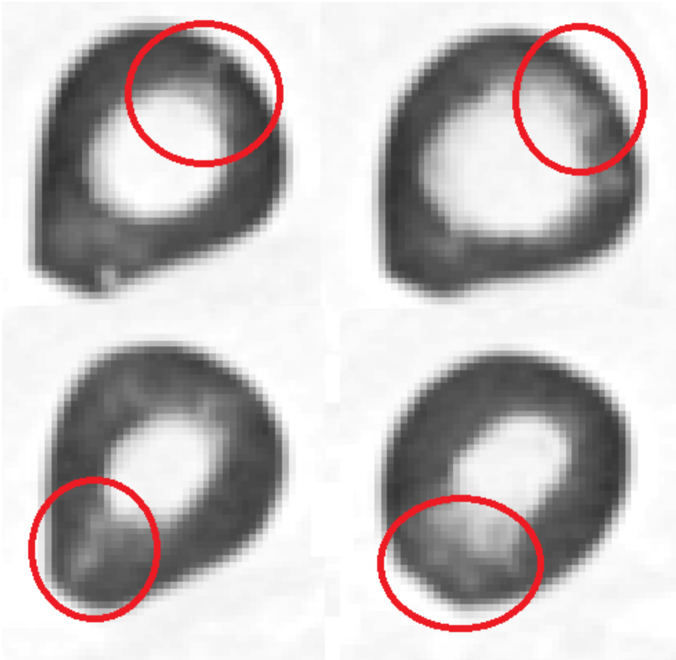

Figure 6.15 - Four CT slices highlighting the low density regions along the cortical shaft.

The combined effect of low density and low stiffness in the region in question might explain the occurrence of fractures initiated in these regions (Klenerman and Marcuson 1970; Taggart and Beringer 1984; Kyle et al. 1994; Martinet et al. 2000; Pulkkinen et al. 2004; Boutroy et al. 2011).

The cumulative and topological distributions predicted by the model seem to be in good agreement with data extracted from CT scans. However, inclusion of a more comprehensive envelope of daily activities could improve the predictions, in particular for the anterior and posterior aspects of the femoral shaft. It is tentatively concluded that the algorithm can physiologically predict the density distribution in a femur.

6.4 Directionality

The previous Sections in this Chapter assessed whether the proposed algorithm produced physiological orthotropic material properties at a continuum level. Young's moduli, shear moduli and density distributions were shown to be coherent with published data and a CT scan of the whole femur. It has been previously mentioned that bone was modelled as a material with orthotropic symmetry in an attempt to approach the continuum model to its structural anisotropy. The orthotropic material orientations were rotated in order to match the principal stress directions resulting from the application of multiple load cases. It is, therefore, necessary to assess whether the optimised directionality of the converged femur model is comparable to what has been observed and described (Garden 1961; Singh et al. 1970; Takechi 1977), in order to determine if the trabecular structures and groups are satisfactorily predicted.

The orthotropic orientations of the converged model were compared with μCT data for the same specimen discussed in the previous Section. The proximal and distal regions of a male cadaveric femur, 27 years old, weight 75 kg, height 175 cm were scanned using a HMXST 225 CT cone beam system with a 4MP Perkin Elmer Detector (Nikon Metrology, Tring, UK) based in the Natural History Museum, London, United Kingdom. The specimen was scanned at 145 kV and 150 μA and with an effective spatial resolution of 78.7 μm. The sample relatively large sizes produced a maximum resolution that does not allow for individual trabecular visualisation but produced enough information about the structures present. Coronal, transverse and sagittal slices of 2 mm thickness were reconstructed in 3D for both regions scanned, using ImageJ (Rasband 1997-2012). A user-defined threshold was applied to binarise the μCT slices. These were then reconstructed into 3D using a plugin available within the programme.

Simultaneously, the dominant directions of each element were projected for equivalent 2 mm thick regions of interest from the converged model. Since multiple load cases were considered during the adaptation process, different guiding frames were selected for each element target material orientations. Therefore, the dominant orthotropic axes will not necessarily cross orthogonally (unlike the simple load case presented in Chapter 3), since they can come from any of the 80 frames considered. In order to compare local trabecular orientations with μCT, a grid of points of interest was superimposed on the predicted slices and the representative directionality of a 4 x 4 x 2 mm rhomboid around each of the points calculated as follows:

- All the elements with centroids within the volume of interest (VOI) around each of the points in the grid were selected;

- For each VOI, each element's orthotropic axis ([x_1, x_2, x_3; y_1, y_2, y_3; z_1, z_2, z_3]) and Young's modulus (E_1, E_2 and E_3, respectively) were extracted;

- The orthotropic axes were collapsed onto the plane of interest (x_1-x_3 (x-z) plane for coronal [x_1, x_3; y_1,y_3; z_1, z_3], x_1-x_2 (x-y) plane for transverse [x_1, x_2; y_1, y_2; z_1, z_2] and x_2-x_3 (y-z) plane for sagittal [x_2, x_3; y_2,y_3; z_2, z_3] slices) and their norm (n_1, n_2, n_3) calculated;

- The dominant orthotropic axis for each element was selected as the axis with the largest norm components in the plane of interest (n_{max});

- For each VOI, all its elements' dominant orthotropic axes were averaged, giving the local trabecular orientation for that region;

- Simultaneously, the E_{mean} were also calculated for each VOI by averaging the associated directional moduli for each of the elements within that volume.

The predicted trabecular orientations were projected on to the reconstructed μCT slices with increasing intensity according to the value of their mean dominant directional moduli (E_1 in red and E_3 in blue). For some of the anatomical planes studied, the angles at which certain dominant orthotropic axes crossed were measured using the angle measuring tool provided by ImageJ. A schematic representation of the section cuts used to compare the predicted directionality with the μCT slices (Figure A.5) and their main anatomical features (Figure A.6) can be seen in the Appendix.

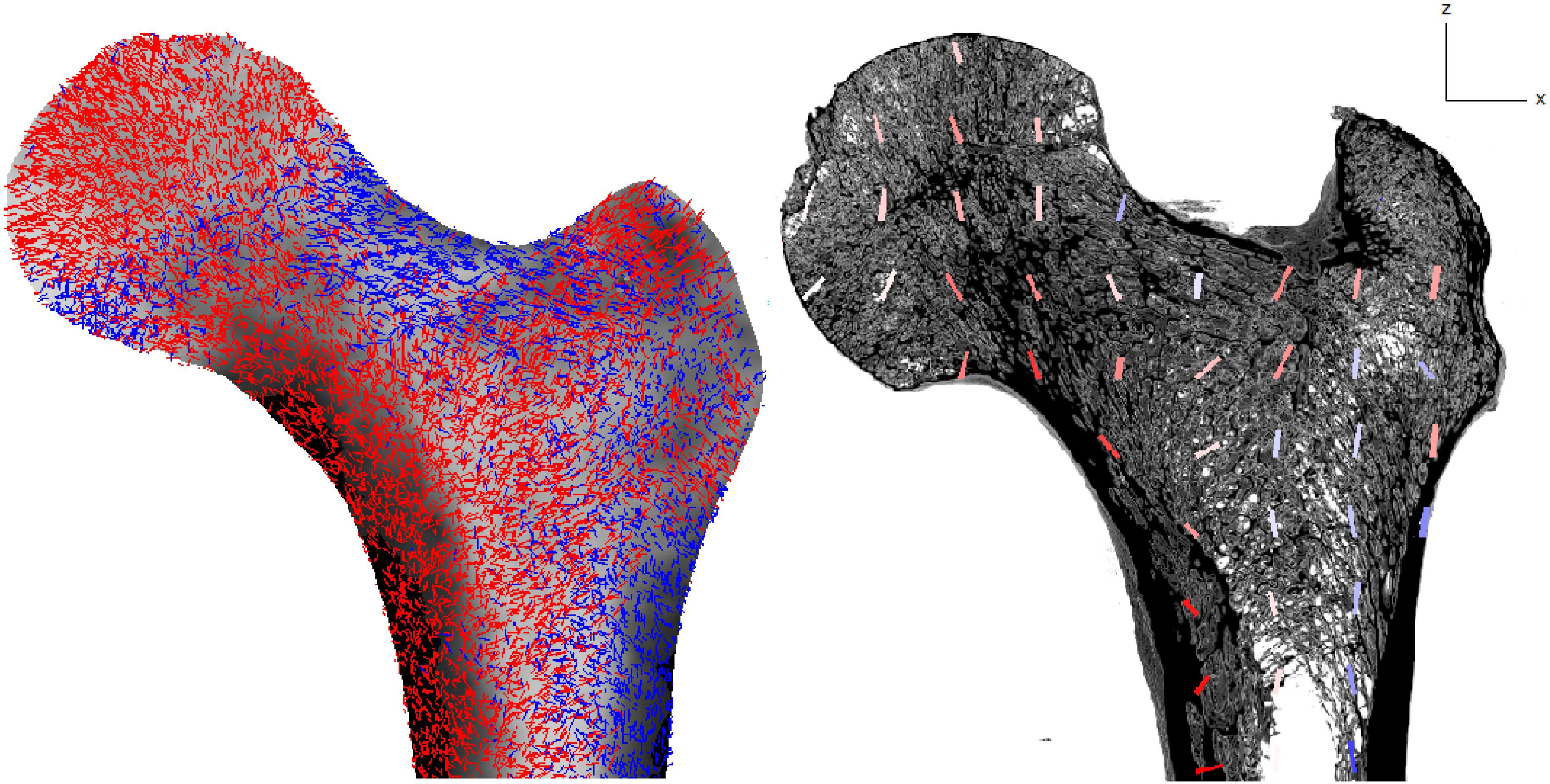

Figure 6.16 - Predicted dominant orthotropic axes superimposed with the density distribution for a 2 mm thick coronal slice of the proximal femur (left); an equivalent slice of the proximal femur specimen (right) with the predicted trabecular orientations superimposed, colour intensity proportional to the value of the dominant directional Young's modulus (E_1 in red, E_3 in blue).

6.4.1 Proximal Femur

Figure 6.16 shows the dominant orthotropic axes predicted by the algorithm in comparison with a μCT reconstruction for a similar coronal slice of the proximal femur. All main trabecular groups documented by Singh were predicted (Singh et al. 1970): (i) the principal compressive group, composed of stiff, densely packed trabeculae arching from the medial cortex of the shaft towards the articular surface of the femoral head. This group is aligned in this form because of the compressive effect of the hip contact force being applied at the contact surface of the femoral head with the acetabulum. (ii) The secondary compressive group, formed by the rest of the compressive trabeculae arising from the medial cortex of the shaft, right below the principal compressive group, and curving superiorly and laterally towards the superior region of the femoral neck and the greater trochanter. This group is less stiff than the principal compressive group. (iii) The principal tensile group, composed by trabeculae arching from the lateral cortex upwards across the neck of the femur and ending in the inferior part of the femoral head arises from the tensile stresses resulting from the transfer of the oblique hip contact force to the vertical cortical shaft. (iv) The secondary tensile group, originating in the lateral cortex just inferiorly to the principal tensile group, arching upwards and medially towards the mid-line of the upper end of the femur is also present. (v) The greater trochanter group, made by poorly defined trabeculae along the greater trochanter region can also be seen in blue. Some other interesting features were also satisfactorily predicted. The cortical thickness seems to be a good match with the one observed in the μCT slice. Trabeculae can be seen radiating from the centre of the femoral head and meeting its superior surface at perpendicular angles (Tobin 1955; Garden 1961).

Finally, decussation angles between 59°-88° were measured in the region of the femoral neck where both principal groups calculated meet. Figure 6.17 highlights some of the lines used in the measurement of the decussation angles. Skedros determined the intersection angles for the same region to be between 51°-90° (Skedros and Baucom 2007). Additionally, compressive and tensile trabeculae crossed in the region of the lesser trochanter predominantly at orthogonal angles, producing decussation angles between 78°-108°, coherent with the orthogonal crossings (82°-

105°) calculated in the same study (Skedros and Baucom 2007) and observed in different publications (von Meyer 1867; Wolff 1892; Tobin 1955; Garden 1961). The decussation angles predicted decrease as one moves towards the apex of the inter-trochanteric arch or towards internal aspect of the cortical shaft, in agreement with visual observations (Tobin 1955; Garden 1961; Skedros and Baucom 2007). The transfer of the compressive forces arising from the wrapping of the tensor fascia latae around the greater trochanter allows for the meeting of the inter-trochanteric compressive and tensile groups to be correctly predicted, when compared to the Single Load Case 3D Femur Model.

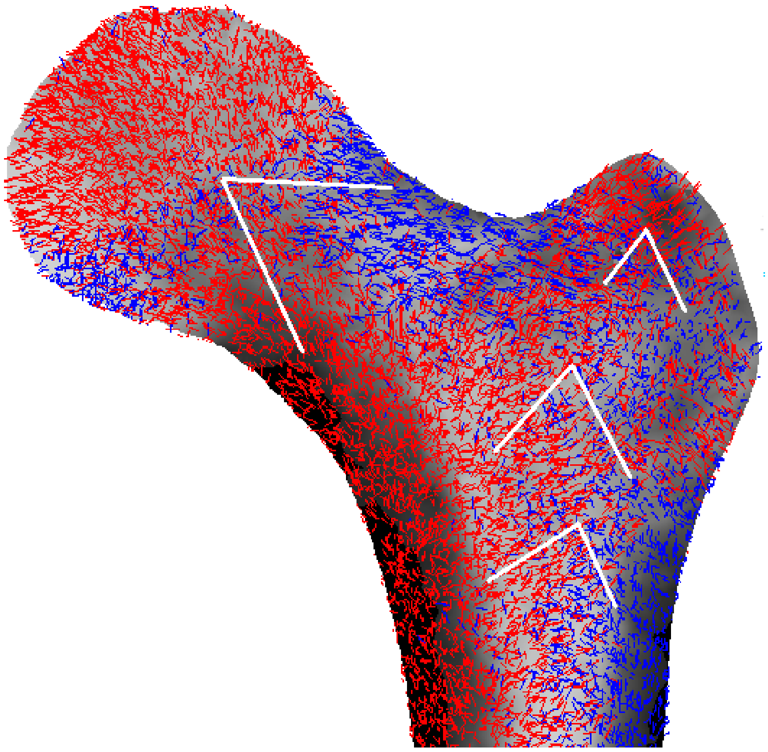

Figure 6.17 – Diagram highlighting the some of the lines used to calculate the decussation angles.

However, there are VOIs in the superior part of the femoral neck and the lateral side of the mid-line whose dominant trabecular orientation doesn't seem to match the trajectory of the principal tensile group despite the dominant Young's moduli in both VOIs being associated with tension (E_3). The dominant direction for each element was calculated by selecting the collapsed axis associated with the largest norm components on the plane in question (coronal, or x-z, plane in this example). This method excludes axes which are coming out of the plane. There have been observations that the tensile group might also arch anteriorly as well as medially in order to transfer the hip contact force from the oblique direction it is applied to the vertical orientation of the femoral shaft (Tobin 1955; Garden 1961). This arching feature of the tensile group can be observed in Figure 6.18. This three-dimensional twisting would not be spotted with the technique used when selecting the trabecular direction for these volumes of interest. Nevertheless, the fact that the superior part of the femoral neck is predominantly in tension (associated with E_3, in blue) is picked up by the selection criteria used.

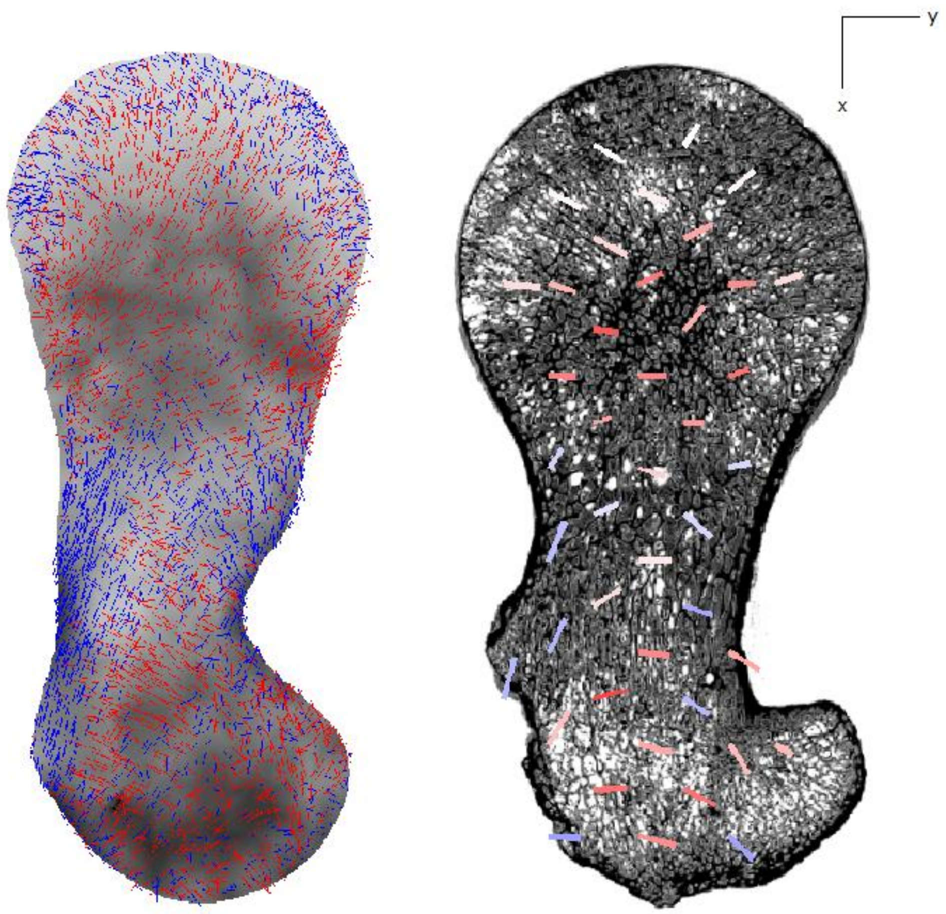

Figure 6.18 - Predicted dominant orthotropic axes superimposed with the density distribution for a 2 mm thick transverse slice of the proximal femur (left); a transverse slice of the proximal femur specimen (right) with the predicted trabecular orientations superimposed, colour intensity proportional to the value of the dominant directional Young's modulus (E_1 in red, E_3 in blue).

The dominant orthotropic axes predicted by the algorithm in comparison with a μCT reconstruction for a similar transverse slice of the proximal femur can be seen in Figure 6.18. The main features documented by Tobin and Garden were all convincingly predicted for the transverse plane. The highly dense, closely packed, stiff, compressive group of trabeculae in the centre of the femoral head and the tensile trabeculae aligned along both anterior and posterior sides of the femoral neck are present (Singh et al. 1970). Trabeculae arching outwards from the centre of the femoral head and meeting at perpendicular angles with the articular surface are also correctly predicted (Tobin 1955; Humphry 1856). The extremely dense region of the calcar femorale can be found, transferring the forces applied by the muscles attached along the inter-trochanteric line down towards the femoral shaft (Tobin 1955). This feature is also known as the 'true neck of the femur' because of its importance in load transfer (Garden 1961). Furthermore, the transverse slices used for the comparison also show two interesting features: the meeting of the secondary compressive group and the tensile greater trochanter group at the apex of the inter-trochanteric arch (Garden 1961), and the meeting of the principal tensile and compressive groups in the centre of the femoral head (Singh et al. 1970), with a similarly dense crescent-shaped region contained between the epiphyseal scar, formed by the epiphyseal plate during the years of growth, and the medial surface (Tobin 1955).

Figure 6.19 draws a comparison between the predicted trabecular orientations for a sagittal cut through the mid-line of the upper end of the femur and what is observed in the scanned specimen. The trabeculae that transfer load from the lesser trochanter down to the femoral shaft are clearly present. Furthermore, the thickness of the cortical layer in both the anterior and posterior walls, as well as the orientation of the trabeculae originating from them, seems to be accurately predicted. Additionally, the transition between compressive and tensile groups from the superior region in tension to the inferior region in compression can also be observed.

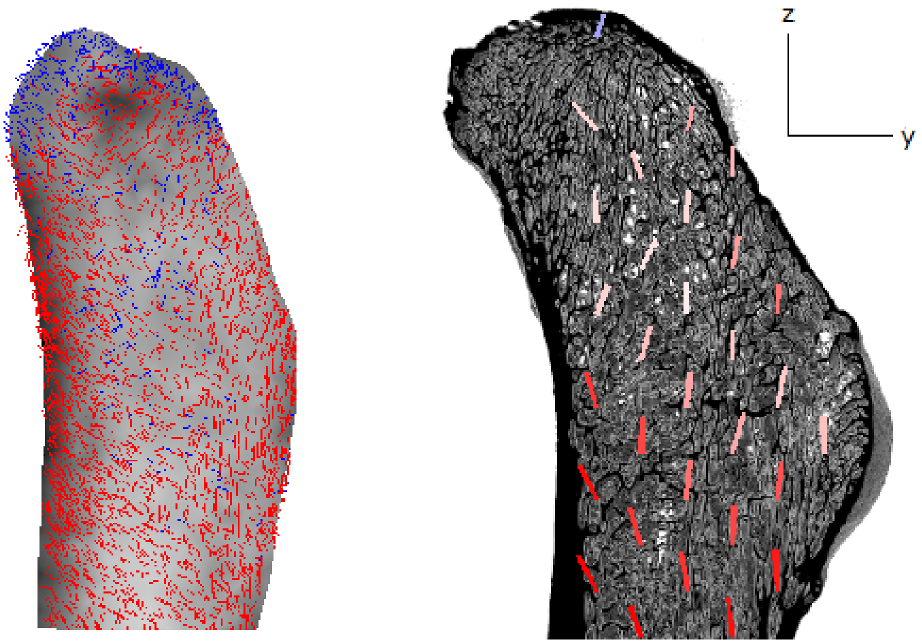

Figure 6.19 - Predicted dominant orthotropic axes superimposed with the density distribution for a 2 mm thick sagittal slice of the proximal femur (left); a sagittal slice of the proximal femur specimen (right) with the predicted trabecular orientations superimposed, colour intensity proportional to the value of the dominant directional Young's modulus (E_1 in red, E_3 in blue).

The proximal femur scanned by μCT has distinctively different geometry when compared to the Muscle Standardised Femur. The specimen used has a femoral head with a larger diameter, a prominent greater trochanter and more protuberant calcar femorale and lesser trochanter. Nevertheless, accounting for the possible discrepancies that different geometries might induce in the comparisons, it is tentatively concluded that trabecular directionality is physiologically and accurately predicted by the proposed algorithm, for the three main anatomical planes of the proximal femur.

6.4.2 Distal Femur

Most remodelling algorithms have been applied to study the material properties distributions at a portion of the femur, with particular emphasis on the proximal femur (Huiskes et al. 1987; Fernandes et al. 1999; Miller et al. 2002; Tsubota et al. 2002; Folgado et al. 2004; Coelho et al. 2009; Tsubota et al. 2009). Complete models of the femur have not been more widely used in bone adaptation because of the time consumption that the adaptive process involves (Tsubota et al. 2009), the application of non-physiological fixed boundary conditions at either end of the partial model used (Fernandes et al. 1999; Folgado et al. 2004; Coelho et al. 2009) and the fact that the loading conditions at the hip are more extensively described (Bergmann et al. 2001; Heller et al. 2001; Modenese et al. 2011; Modenese and Phillips 2012).

Chapter 5 concluded that the use of a balanced model such as the one proposed by Phillips (Phillips 2009) and developed in this thesis can produce a physiological loading environment for the whole femoral construct. This allows for bone adaptation to be predicted for a complete model of the bone without the effect of non-physiological stimulus induced in the remodelling process by the application of fixed boundary conditions.

The following pages intend to assess whether the proposed algorithm can predict bone's structural anisotropy at a continuum level for the complete femur, by looking at the converged orthotropic directions at the distal region of the femur model. These were compared with slices reconstructed from μCT scans of the distal region of the same femur specimen used for the assessment of the quality of predictions for the proximal femur, as well as with Takechi's extensive documentation of the trabecular features in the knee joint (Takechi 1977).

Figure 6.20 displays the dominant orthotropic axes predicted by the algorithm in comparison with a μCT reconstruction for a similar coronal slice of the distal femur. It is interestingly noticed that the vertical alignment of the tensile and compressive trabecular groups parallel to the bone axis, in order to transfer the loads arising from the daily activities through the knee joint, is correctly predicted. The perpendicular arrangement of the trabecular with the articular surface is also present. Trabeculae are seen to be thicker and coarser near the epiphyseal line, as expected. The trabeculae radiating from the intercondylar notch are also coherent with Takechi's observations (Takechi 1977).

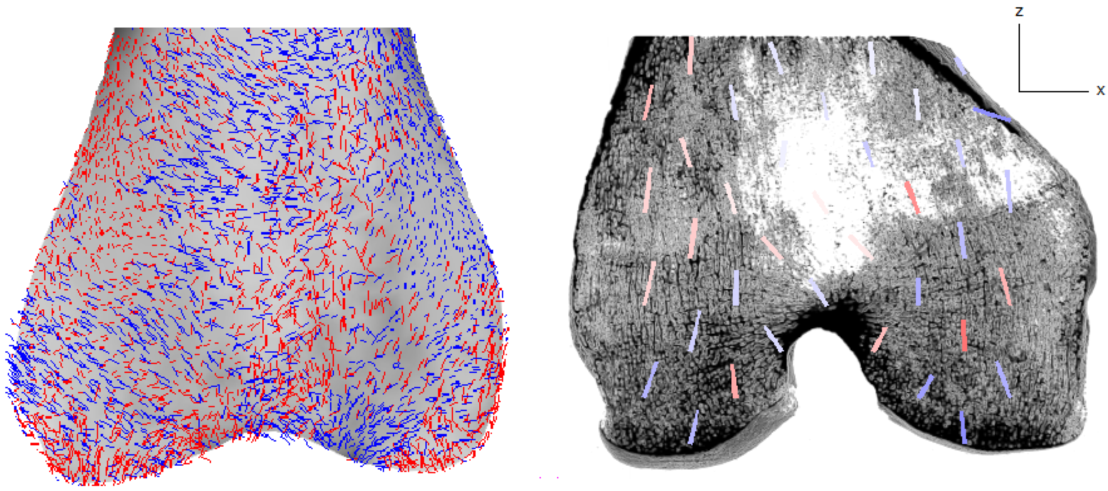

Figure 6.20 - Predicted dominant orthotropic axes superimposed with the density distribution for a 2 mm thick coronal slice of the distal femur (left); a coronal slice of the distal femur specimen (right) with the predicted trabecular orientations superimposed, colour intensity proportional to the value of the dominant directional Young's modulus (E_1 in red, E_3 in blue).

The five trabecular arrangements documented by Takechi for the sagittal section of the condyles (see Figure 1.8 in Chapter 1) are observable in Figure 6.21 (Takechi 1977). The central network of trabeculae crossing orthogonally below the epiphyseal line is observed in the lack of dominant directional Young's modulus, meaning this region is composed by both compressive and tensile trabecular groups. The less significant presence of dominant axes perpendicular to the long axis of the bone could be improved by modelling loading activities with more extreme flexion angles, where higher quadriceps activations resulting in higher patello-femoral forces would be expected, such as standing up from a chair or stair descent (Ahmed et al. 1987; Stäubli et al. 1996; Kutzner et al. 2010). Nevertheless, the perpendicular trabeculae running orthogonally to the articular surface of the patella are also correctly predicted by the orthotropic adaptation algorithm. Also clearly present are the trabeculae perpendicular to the tibio-femoral articular surface, supporting the compressive forces produced in this region. The fine and dense trabeculae that arise from the posterior margins of the condyles as a response to the rotary movement of the distal region of the femur are also successfully predicted by the alignment process of the algorithm. Finally, an angle of 19.5° (highlighted in green in Figure 6.21) was measured for trabecular running between the posterior side of the condyles and their mid-line. This angle is comparable to the 20° measured by Takechi (Takechi 1977).

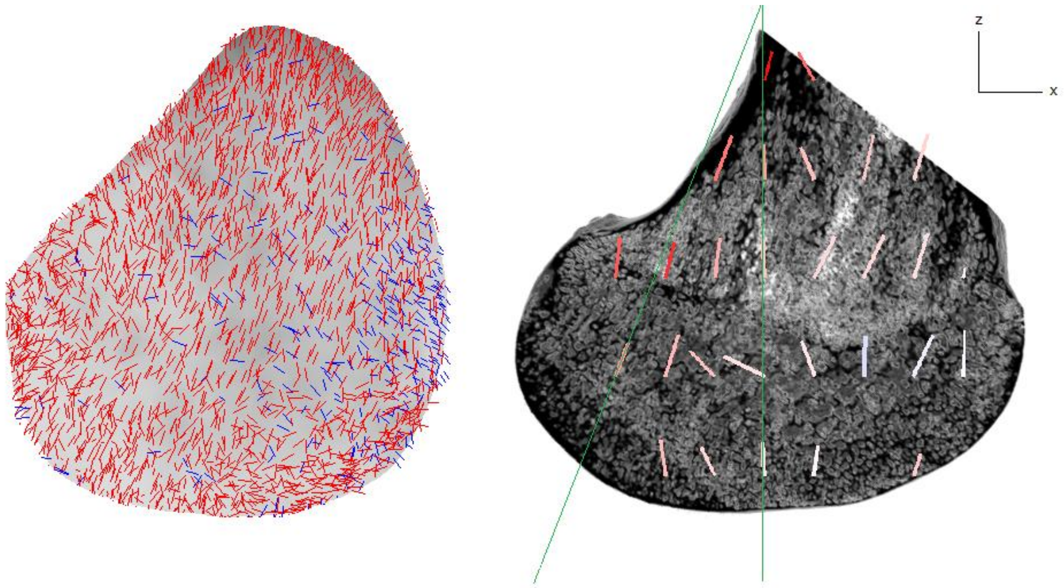

Figure 6.21 - Predicted dominant orthotropic axis superimposed with the density distribution for a 2 mm thick sagittal slice of the distal femur (left); a sagittal slice of the distal femur specimen (right) with the predicted trabecular orientations superimposed, colour intensity proportional to the value of the dominant directional Young's modulus (E_1 in red, E_3 in blue).

Figure 6.22 shows the main trabecular directionalities predicted by the model for a transverse slice of the condylar region. The same four patterns of trabecular orientation documented by Takechi were accurately predicted (Takechi 1977). The group of trabeculae originating from the posterior surface of both condyles and running in the anterior-posterior plane in a parallel arrangement to the outer contour of the epicondylar region is correctly displayed. This group is formed by fine and denser trabeculae near the joint surfaces and thick and coarse in the region in between. The second and third trabecular groups accurately predicted have already been described for the other slices: the trabeculae aligned perpendicular to the contact surface with the patella and the structures radiating from both sides of the intercondylar notch. The fourth group is formed by the fine and short, yet dense trabeculae that radiate from epicondyles, the attachment sites of both collateral ligaments. Finally, the central area of the femur formed by rather coarse and fine trabeculae is also clearly observed.

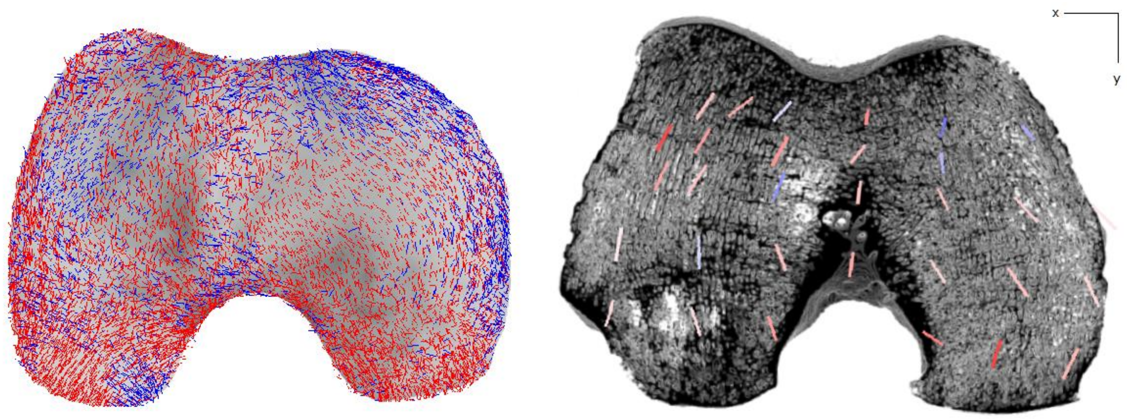

Figure 6.22 - Predicted dominant orthotropic axis superimposed with the density distribution for a 2 mm thick transverse slice of the distal femur (left); a transverse slice of the distal femur specimen (right) with the predicted trabecular orientations superimposed, colour intensity proportional to the value of the dominant directional Young's modulus (E_1 in red, E_3 in blue).

The geometry of the specimen scanned was similar to the femur model used, allowing for a more clear comparison between the dominant orthotropic orientations predicted by the model and what is observed in the μCT reconstruction. As expected, the prediction of the trabecular features at the distal region of the femur was much improved with the modification of the load application along the tibio-femoral surface, the inclusion of the patello-femoral joint structure and the modelling of different instances of daily activity cycles. There is, however, still room for improvement, namely by modelling more extreme load scenarios, where high flexion angles, quadriceps muscle activations and patello-femoral forces would approach the predicted density, stiffness and structures even more to their *in vivo* arrangement. This notwithstanding, it is reasonably concluded that trabecular directionality for the three main anatomical planes of the distal femur is physiologically and accurately predicted by the proposed algorithm.

6.5 Conclusion

This Chapter attempted to assess whether the adaptation process was accurately achieved by the orthotropic iterative algorithm proposed in this thesis. Young's moduli, shear moduli and density distributions were analysed and compared with what has been observed *in vivo* and documented in literature. This was undertaken in order to evaluate whether the orthotropic assumption can model bone's properties at a continuum level. Directionality of the trabecular structures was compared with μCT slices along the three main anatomical planes for the proximal and distal femur regions of the same specimen, in an attempt to assess the ability of the proposed algorithm to reproduce the femur's structural anisotropy at a continuum level.

The orthotropic orientations converged quickly after 4 iterations, implying that after a certain number of iterations the principal strains match with the principal stresses directions, allowing for some running time reduction. Furthermore, the mean changes in the Young's moduli (Figure 6.1) and shear moduli (Figure 6.7) hint that a state of near-convergence is achieved within the first 10 iterations, again allowing for reduction of the running times of the algorithm if required. The values of the orthotropic Young's and shear moduli were found to be within what has been measured in literature, with their distributions also matching what would be expected. Stiffer bone was found where cortical bone and load carrying trabecular groups have been documented and regions of low Young's modulus in areas where virtually no bone is found, such as the Ward's triangle and the intra-medullary canal. These distributions are very similar to what has been predicted using the isotropic assumption. However, the orthotropic modelling of bone's material symmetry also provides directional information, which is overlooked when assuming bone to be isotropic. The orthotropic assumption can then be said to be more advantageous, since not only is it a more accurate representation of bone's elastic symmetry, it can give information about the directional stiffness in any of the three orthotropic directions whilst still reproducing results achieved by the isotropic assumption. Interestingly, higher shear moduli occurred in regions where trabeculae are not expected to cross at orthogonal angles. The relationship between predicted shear moduli and directionality, as well as the feasibility of representing bone's structural anisotropy as an optimised orthotropic material with Shear modulus adaptation will be discussed further in Chapter 7. The cumulative and topological density distributions predicted by the model seem to be in agreement with data extracted from a CT scan. Differences between both could be attributed to differences in geometry. Furthermore, the fact that there is no unifying accurate regression relationship between stiffness and density for both cortical and trabecular bone, and that these relationships vary according to the position in the femur, could explain the differences observed. Finally, the fact that only a limited number of load cases were considered and that the passive compressive action of the muscles cannot be modelled by bundles of spring connector elements might have affected these predictions. The trabecular structures predicted for both the proximal and the distal femur regions were considered to be accurately predicted, by observing their agreement with the measurements and observations published in literature. However, the method used was shown not to be very accurate when trying to assess directionality of trabecular groups that come out of the anatomical plane under scrutiny.

The inclusion of multiple load cases greatly improved the predictions in the condylar regions, and it is suggested that the modelling of more extreme activities where higher flexion angles, quadriceps muscles activations and patello-femoral forces are involved could further improve the directionality of the structures predicted at the condyles, as well as the stiffness and density calculated along the inter-trochanteric line and the linea aspera. Further comments on the influence of different load cases in the material properties and orientations generated by the orthotropic adaptation algorithm will be made in Chapter 7. Finally, the use of a balanced model allows for the prediction of the adaptation process for the whole femur, without artefacts induced by the application of fixed boundary conditions. Additionally, this can be achieved accurately for the three main anatomical planes. This is a step forward in the current way bone adaptation is achieved, since, to the author’s knowledge, there are no adaptation algorithms that can represent bone’s structural anisotropy at a continuum level, with physiological material properties and directionality predicted in three dimensions for a whole model of a bone. It is therefore concluded that this model can reliably produce the observed optimised structures in the femur.

Chapter 7

Influence of Load Cases in Bone Adaptation

Chapter 5 confirmed that the Multiple Load Case 3D Femur Model can provide a suitable platform for the prediction of bone material properties and orientations, and Chapter 6 concluded that this model can reliably reproduce the femur's structural anisotropy at a continuum level in the three main anatomical planes. An orthotropic three dimensional model of the whole femur was produced as a result of the implementation of the adaptation algorithm described in this thesis.

This Chapter analyses the converged material properties distribution and directionality predicted and studies their relationship with the load cases modelled. Section 7.1 discusses the relationship between the predicted mean shear modulus and directionality, as well as the feasibility of representing bone's structural anisotropy as an optimised orthotropic material with shear modulus adaptation. The topological influence of the two load cases (level walking and stair climbing) and the different frames modelled on the converged material properties is discussed in Section 7.2. Finally, Section 7.3 draws the conclusions on the selection of the load cases and frames for modelling of bone adaptation and whether the behaviour of structural anisotropy of bone can be reproduced at a continuum level.

7.1 Shear Modulus and Directionality

Non-orthogonal intersections of trabeculae have been put suggested as the mechanism by which bone may resist the stresses in regions where shear prevails (Pidaparti and Turner 1997; Skedros and Baucom 2007). These are particularly evident in regions such as the proximal femur, where complex loading is predominant, as a result of the transfer of the off-axis hip contact force from an oblique to a vertical position (Ward 1838; Bergmann et al. 1993; Pidaparti and Turner 1997; Ryan and Ketcham 2002; Ryan and Ketcham 2005; Skedros and Baucom 2007). Skedros and Baucom's mathematical analysis of the trabecular trajectories in the proximal femur proposes that non-orthogonal trabecular orientations are an adaptation response to resist the shear stresses arising from multi-axial loading (Skedros and Baucom 2007).

The orthotropic assumption implemented in this thesis has been put forward as a more physiological way of modelling bone's anisotropy in comparison with isotropy (Ashman et al. 1984). The alignment of the local orthotropic axes with the principal stress directions, in agreement with Wolff's trajectorial theory, has been shown to be optimal under simple loading (Pedersen 1989). However, under complex multiple loading, the orthotropic assumption does not allow for accurate representation of the non-orthogonal trabecular orientations observed (von Meyer 1867; Skedros and Baucom 2007; Skedros and Brand 2011).

Shear modulus adaptation was included in the iterative strain-driven algorithm proposed in this thesis (Chapter 4) in an attempt to overcome the restriction on trabecular crossing imposed by the orthotropic assumption and to model trabecular structural adaptation at a continuum level. Non-orthogonal crossing of the dominant orthotropic axes was observed in regions where multi-axial loading is expected to occur (Chapter 6). These results from the process of selection of a guiding frame to define the directionality of the largest orthotropic Young's modulus for each element (explained in Chapter 4). These regions should have higher values of shear modulus than regions where orthogonal crossing was predicted. Figure 7.1 and Figure 7.2 compare the distribution of the mean shear modulus, G_{mean}, with the predicted dominant orthotropic axes in the three main anatomical planes (coronal, transverse and sagittal) for the proximal and distal regions of the femur, respectively. The mean shear modulus, G_{mean}, was calculated as the average of the three orthotropic shear moduli (G_{12}, G_{13} and G_{23}). All the elements with G_{mean} above 10 GPa were grouped (similarly to what has already been discussed for E_{mean}) in order to highlight the areas where trabeculae are expected to be adapted to shear. The density distributions obtained were calculated using the scheme taking into both the mean Young's modulus and mean shear modulus and was described in Chapter 6.

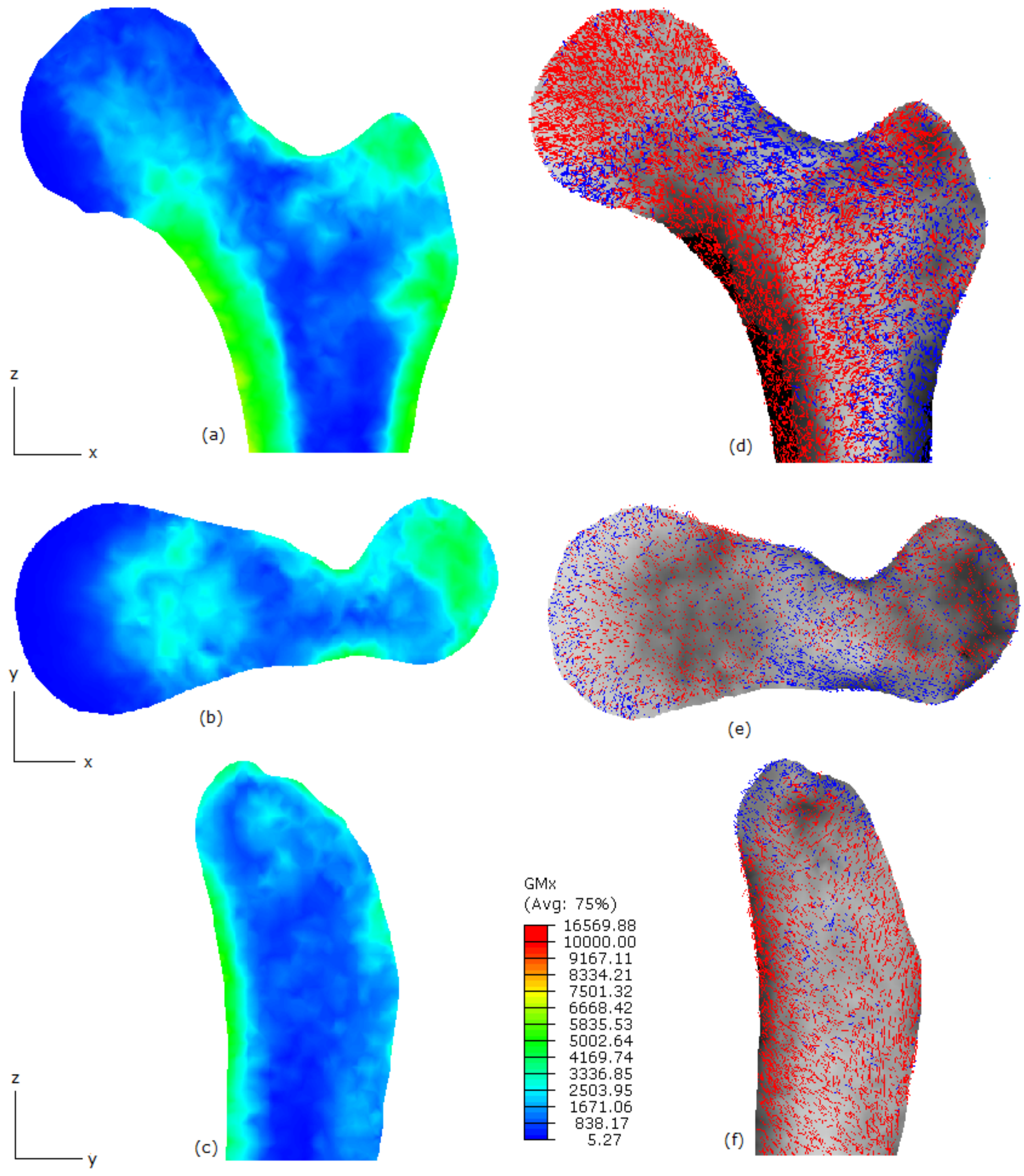

Figure 7.1 - Coronal, transverse and sagittal sections of the proximal femur representing the predicted mean shear modulus (N/mm^2) (a, b and c, respectively) and for the predicted dominant orthotropic axes (d, e and f, respectively).

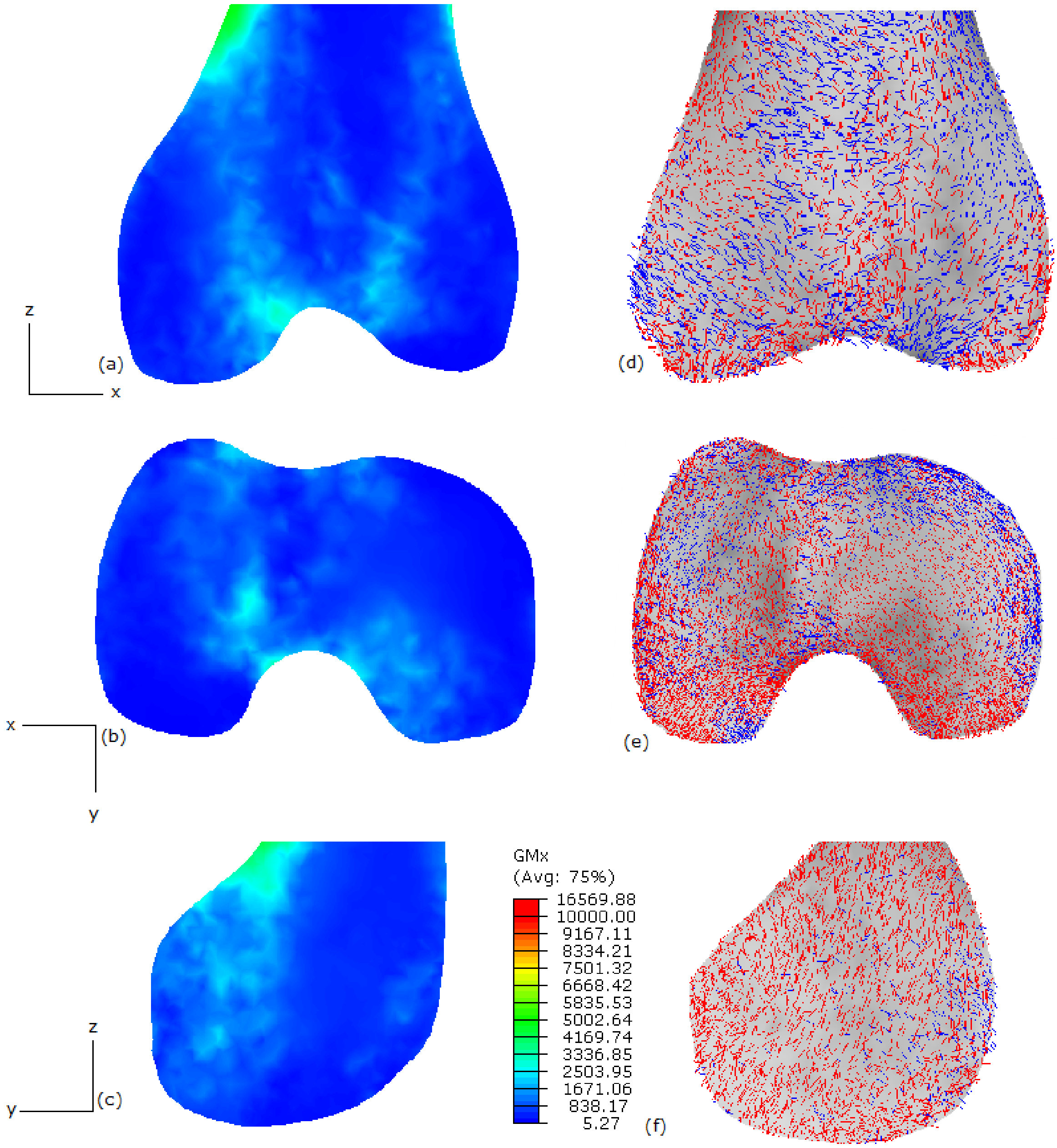

Figure 7.2 - Coronal, transverse and sagittal sections of the distal femur representing the predicted mean shear modulus (N/mm^2) (a, b and c, respectively) and for the predicted dominant orthotropic axes (d, e and f, respectively).

As it can be observed in both figures, it is clear that the regions where G_{mean} is the highest (in green) correspond to the regions where dense cortical bone is observed (in black) and predominantly in the cortical shaft. Cortical bone in the femoral shaft has been measured to be much stiffer in the longitudinal direction than in the other orthogonal directions (Rho et al. 1997; Rho et al. 1999; Taylor et al. 2002; Rudy et al. 2011; Rohrbach et al. 2012). High shear-inducing torsional moments and shear forces have also been calculated for these regions (Younge 2012).

Furthermore, the cortical shaft has been observed to have spiral alignment of its fibres (Garden 1961), an adaptation to the shear stresses present in this region (Varghese et al. 2011; Zdero et al. 2011) in response to the transfer of the oblique hip contact forces to the vertical position (Ward 1838; Ryan and Ketcham 2002; Ryan and Ketcham 2005; Skedros and Baucom 2007). Areas of low values of G_{mean} (in blue) coincide with the regions where virtually no trabeculae can be found (in white), such as the Ward's triangle and Babcock's triangle, in the proximal femur, the central epiphyseal region, in the condyles, and the intra-medullary canal along the shaft. Interestingly, the regions where trabeculae are usually observed crossing at orthogonal angles (Tobin 1955; Garden 1961; Singh et al. 1970; Takechi 1977; Skedros and Baucom 2007) correspond to regions where also low values of G_{mean} can also be found. These include the articular surface of the femoral head and the region around the lesser trochanter (Figure 7.1) and the tibio-femoral and patello-femoral contact surfaces (Figure 7.2) discussed in Chapter 6. Regions where non-orthogonal decussation angles have been measured (Chapter 6) and documented (Tobin 1955; Garden 1961; Takechi 1977; Skedros and Baucom 2007) coincide with regions where G_{mean} had values in between what was calculated for cortical bone and the regions of low density (in light blue). These include the intersection of the principal tensile group and the secondary compressive group in the superior region of the femoral mid-line, the intersection of the principal tensile and principal compressive group in the centre of the femoral head, the calcar femorale (Figure 7.1) and the regions around the intercondylar notch and between the posterior side of the condyles and their mid-line (Figure 7.2), as observed in Chapter 6.

The relationship between the calculated shear modulus and the directions of the dominant orthotropic axes is clear. Visual inspection shows that higher values of G_{mean} were predicted where these axes cross non-orthogonally. The inverse can also be observed. This indicates that the restriction on trabecular crossing imposed by the orthotropic assumption was overcome by including a shear modulus adaptation algorithm, allowing for the modelling trabecular structural adaptation at a continuum level. The next Section will assess if there is a relationship between these regions and complex loading.

7.2 Influence of the Load Cases in Bone Adaptation

Observation of the material properties distribution and their associated orientations for the Single Load Case Model (Chapter 3) indicated that inclusion of more load cases for daily activities could allow for a more accurate prediction. Chapter 4 introduced the modifications performed to the model and the remodelling algorithm in order to allow for modelling of multiple instances of frequent daily activities. The adaptation algorithm was run for the Multiple Load Case 3D Femur undergoing 80 frames of two frequent daily activities that generate high hip contact forces: level walking (frames 1-40) and stair climbing (frames 41-80). Convergence of the orthotropic material properties of the femur was achieved after the 29th iteration. For each iteration an envelope containing maximum driving stimuli was calculated by selecting the strain values for the guiding frame in each element (Chapter 4, Section 4.5.1). The guiding frame was selected as the frame where the maximum absolute value among the principal components of the maximum absolute strain tensor could be found (i.e. the frame which produced the highest absolute normal strain value). A similar method was applied to define the guiding frame for the shear modulus adaptation, with the frame producing the maximum absolute value among the shear strains being selected as the guiding frame.

The guiding frames were displayed for anterior, posterior and coronal views of the whole femur and coronal sections of its proximal and distal regions (Figure 7.3, Figure 7.4 and Figure 7.5). They were grouped into a binary representation of the two load cases modelled, level walking, in red, and stair climbing, in blue (Figure 7.3), in order to highlight the topological influence of each of the load cases in different regions of the femur for the converged Young’s moduli (Figure 7.3, top) and shear moduli (Figure 7.3, bottom). These were subsequently split into the 80 frames modelled and further emphasised by splitting the results for the 40 frames modelled for level walking (Figure 7.4 and Figure 7.5, top) and stair climbing (Figure 7.4 and Figure 7.5, bottom). This was carried out so that attention could be drawn to the influence of different frames modelled on the material properties of different areas of the complete femur.

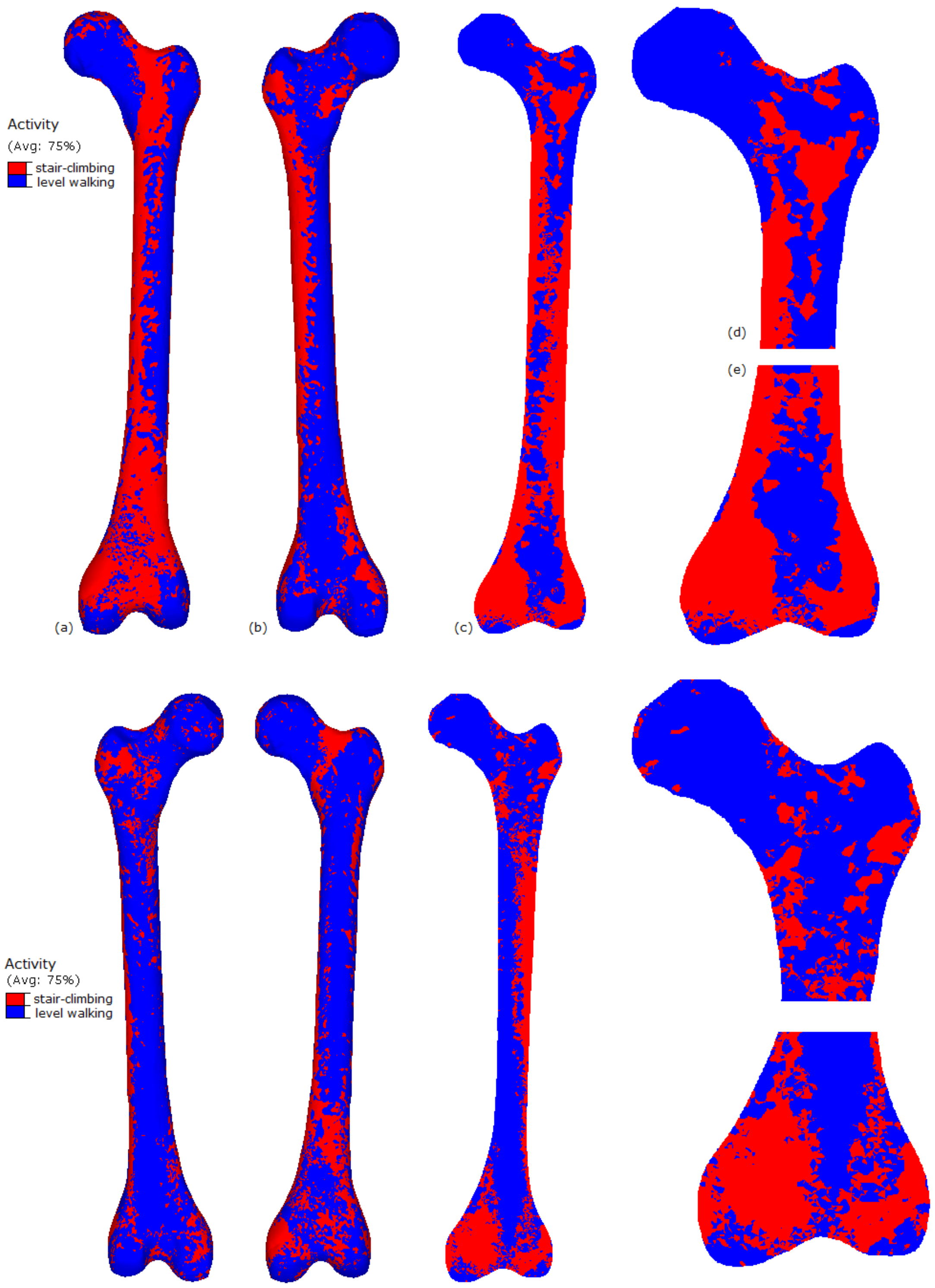

Figure 7.3 - Dominant load case: posterior (a), anterior (b) and coronal (c) views of the whole femur and coronal view of its proximal (d) and distal (e) regions. Frames 1-40 were grouped as level walking (blue) and 41-80 as stair climbing (red). The dominant load cases are shown for Young's moduli (top) and shear moduli (bottom).

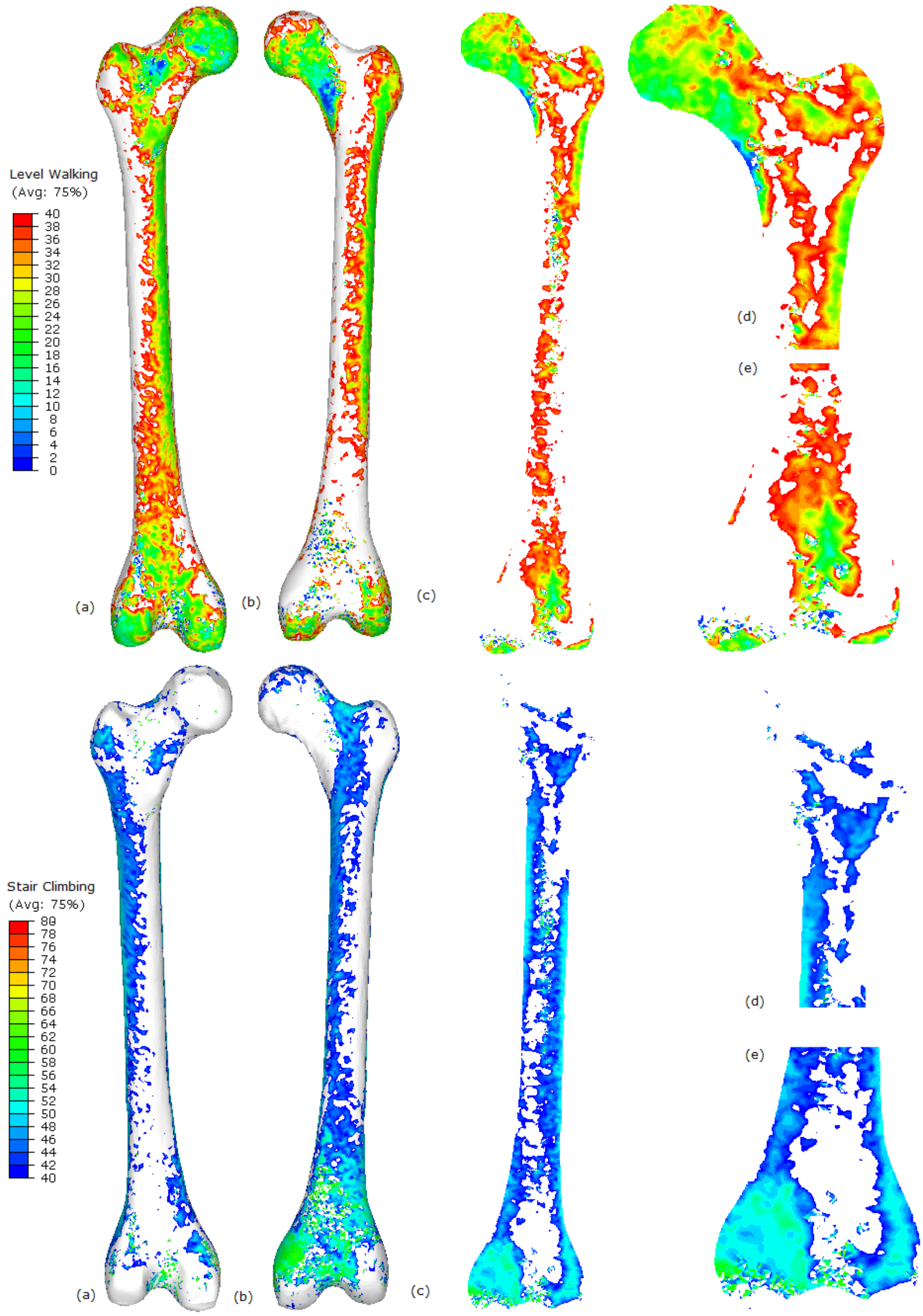

Figure 7.4 - Guiding frames for Young's moduli for level walking (top) and for stair climbing (bottom): posterior (a), anterior (b) and coronal (c) views of the whole femur and coronal views of its proximal (d) and distal (e) regions.

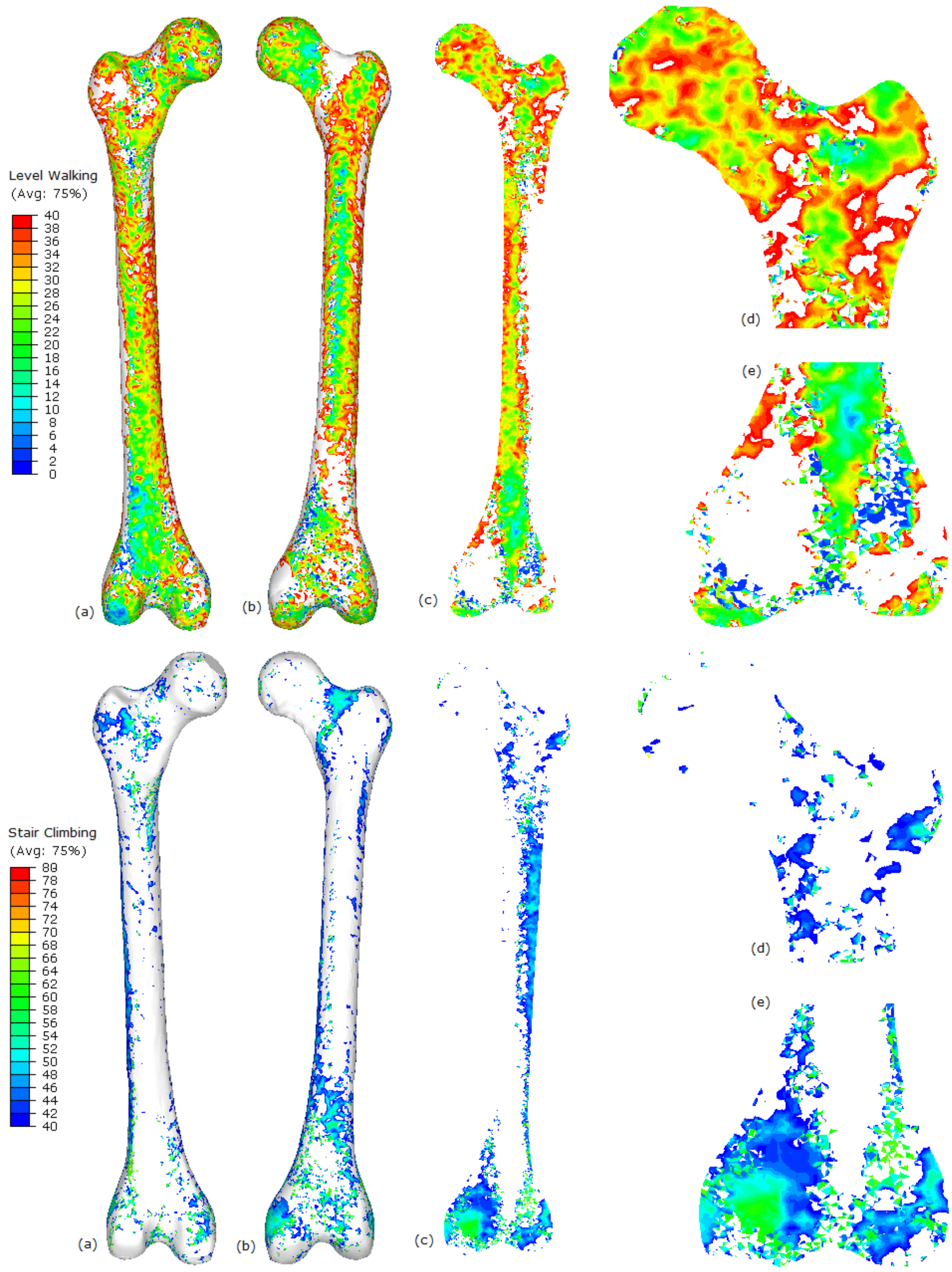

Figure 7.5 - Guiding frames for shear moduli for level walking (top) and for stair climbing (bottom): posterior (a), anterior (b) and coronal (c) views of the whole femur and coronal views of its proximal (d) and distal (e) regions.

It is interestingly highlighted in Figure 7.3 the shared contribution of both load cases modelled to the converged orthotropic material properties of the femur. Level walking (Figure 7.3, top) is shown to influence the Young's moduli adaptation in regions of the femoral head, inferior part of the femoral neck, greater trochanter, posterior-lateral aspects of the femoral shaft and posterior side of the condylar region. The stimulus produced by the stair climbing activity is shown to be dominant in the regions of the superior part of the femoral neck, lesser trochanter, medial aspect of the cortical shaft and anterior side of the distal femur. Analysis of the coronal sections of the whole femur (c), proximal region (d) and distal region (e) emphasise the contribution of both load cases in the regions where multiple load cases have been thought to be important, such as the inter-trochanteric region or the epiphyseal line in the condyles (Garden 1961; Takechi 1977; Skedros and Baucom 2007) and where adaptation of the trabecular shear modulus was observed (Section 7.1). The material properties of the femoral shaft and the femoral neck seem to be influenced by both load cases, with the line where both meet coinciding with the twisting regions of lower stiffness and density observed in Chapter 6.

When looking at the influence of both daily activities in shear modulus (Figure 7.3, bottom) it is evident that there is a shift in the influence of both activities. The stair climbing load cases seem to lose their topological dominance and level walking prevails. Since stair climbing produces higher hip and knee contact forces (Chapter 5) it is expected to be dominant in Young's modulus adaptation, which is driven by axial strains. However, shear adaptation appears to be driven mainly by the shear strains arising from level walking. This could be due to the higher internal/external rotation of the pelvis during walking (Table A.1 and Table A.2 in the Appendix). Nevertheless, the anterior aspect of the distal region and the femoral neck continue to be dominated by stair climbing. This suggests that the repetition of this activity could improve bone's resistance to axial and shear strains in these regions and mineralisation (Jämsä et al. 2006; Blain et al. 2009), reducing the chances of fracture.

The inclusion of more extreme load cases where the femur is undergoing higher flexion angles, such as standing up from a chair, is thought to influence bone mineralisation (Jämsä et al. 2006; Blain et al. 2009). Therefore, future models should attempt to model more daily activities in order to improve their predictions. Nevertheless, the contribution of both load cases to the converged material properties in vast, independent regions of the femur is clear. Thus, it is recommended that multiple load cases are considered when predicting bone adaptation by incorporating bone remodelling algorithms with finite element analysis. Several studies have only modelled bone adaptation resulting from level walking (Doblaré and Garcia 2001; Tsubota et al. 2002; McNamara and Prendergast 2007; Rossi and Wendling-Mansuy 2007; Tsubota et al. 2009), possibly missing out on the effect of other daily activities on their predicted material properties.

Figure 7.4 and Figure 7.5 show the topological influence in the converged material properties of all the 80 frames modelled for the converged Young's moduli and shear moduli, respectively. Once again, the regions of the proximal femur and the condyles where multiple load cases are thought to be influent can be seen to be dominated by multiple frames. These regions coincide with the areas where shear modulus adaptation was observed for trabecular bone in Section 7.1, hinting that the structural behaviour of trabecular bone is correctly modelled at a continuum level. Further information on the contribution of each frame can be extracted by splitting them into the two load cases they represent: level walking (Figure 7.4 and Figure 7.5, top) and stair climbing (Figure 7.4 and Figure 7.5, bottom). It is apparent from these plots that multiple frames seem to contribute towards the dominant regions of each load case and, consequently, need to be considered when attempting to model bone adaptation to its mechanical surroundings.

This is more evident in Figure 7.6, where the distribution of the percentage of elements influenced by each guiding frame for both load cases is shown for Young's moduli (top) and shear moduli (bottom). Further detail can be extracted from Figure 7.7 and Figure 7.8, which include the resultant hip contact forces (%BW) calculated by the proposed model (in blue) and measured by Bergmann's instrumented prosthesis (in red). A representation of the femur's flexion angles on the sagittal plane, are also included in the bottom in order to ease spatial visualisation.

The influence of different frames modelled in Young's moduli adaptation is unmistakably observable in Figure 7.7 (top) and Figure 7.7, with 18 frames producing the stimulus necessary to influence more than 0.5% of the elements each, and 95% of the total number of elements. Curiously, the frames representing the maximum peaks of the resultant contact force are not amongst the top 5 guiding frames across both activities. It is observed that these guiding frames correspond to combinations of high flexion angles and high hip contact forces, or an almost vertical positioning of the femur. These instances of the load cases can produce higher muscle forces, particularly in the quadriceps when high flexion occurs, which will influence greatly the distal region of the femur. Studies where bone remodelling was predicted by only modelling the peak frames of these two load cases (Fernandes et al. 1999; Boyle and Kim 2011) have also ignored the effect of these frames on the adaptation process.

The influence of the different load cases in shear adaptation can be observed in Figure 7.6 (bottom) and with more detail in Figure 7.8. It is interestingly noticed that more frames influence shear modulus adaptation than Young's modulus adaptation. However, their influence is more evenly distributed across the different frames, with no single frame being responsible for more than 13% of the converged elements. It is observable that some frames overlap in importance, influencing both adaptation processes. This is expected, since the load cases that produce higher axial strains will also generate high torsional moments (Varghese et al. 2011; Zdero et al. 2011; Younge 2012). These result from the femur's geometry that enables the load transfer from the oblique direction it is applied at the hip joint to vertical axis in the femoral shaft (Ward 1838; Tobin 1955; Garden 1961). These findings are in agreement with the hypothesis that shear modulus arises a response to complex loading, with more frames being involved in its adaptation.

The necessity to model more frames for each of the load cases considered in order to achieve physiological predictions of bone material properties was tackled in some remodelling studies by including frames where the femur undergoes high abduction or adduction angles (Miller et al. 2002; Tsubota et al. 2002; Rossi and Wendling-Mansuy 2007; Tsubota et al. 2009). However, Figure 7.7 and Figure 7.8 also highlight that the minimum sampling rate of the load cycle set with the Nyquist-Shannon sampling theorem (Shannon 1949) needs to be considered in order to reliable capture its effect in bone adaptation.

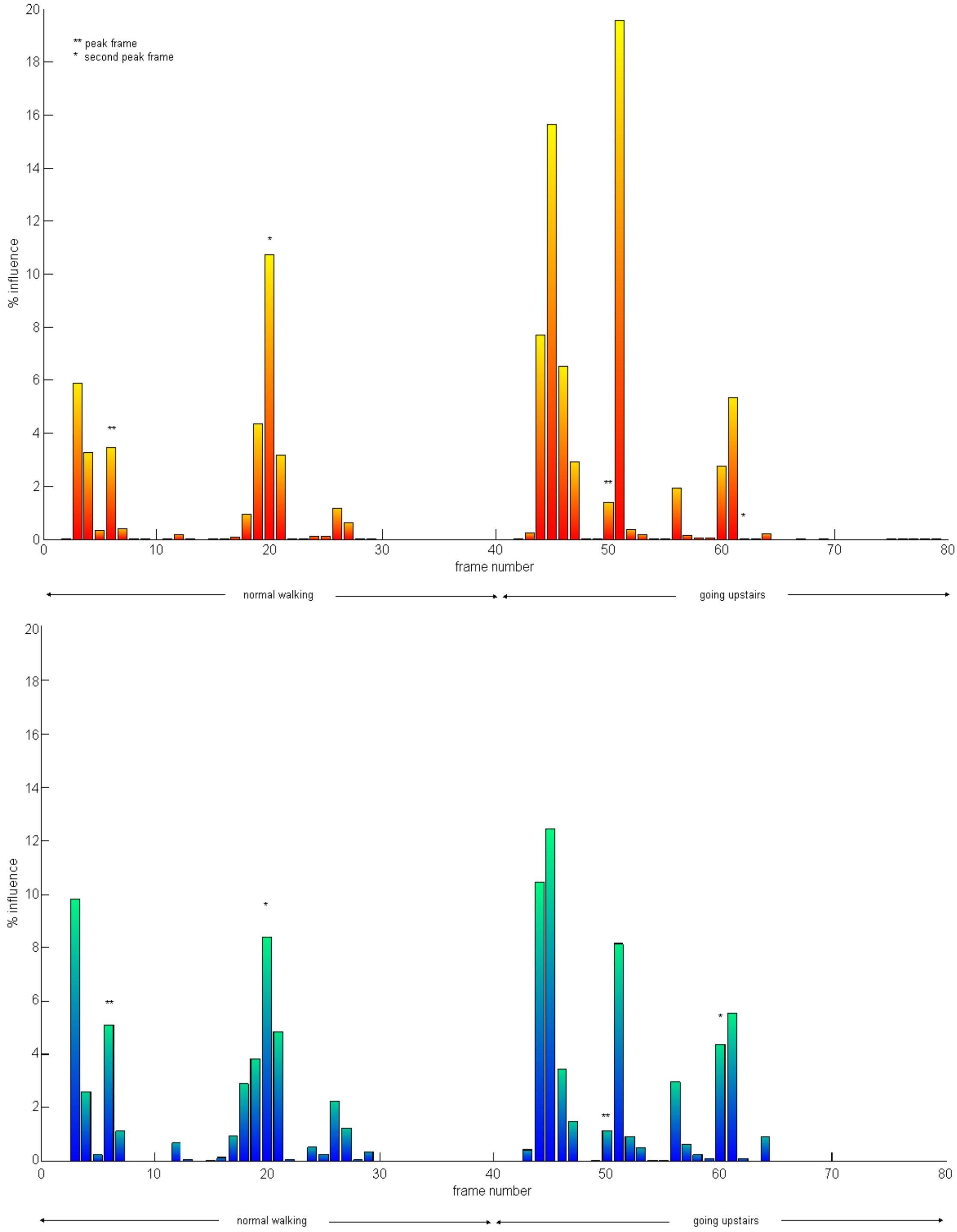

Figure 7.6 - Distribution of the percentage of elements influenced by each guiding frame for both load cases (frames 1-40 for level walking and 41-80 for stair climbing) for Young's moduli (top) and shear moduli (bottom). The frames where the first peak (**) and second peak (*) occur in the HIP 98 package are highlighted.

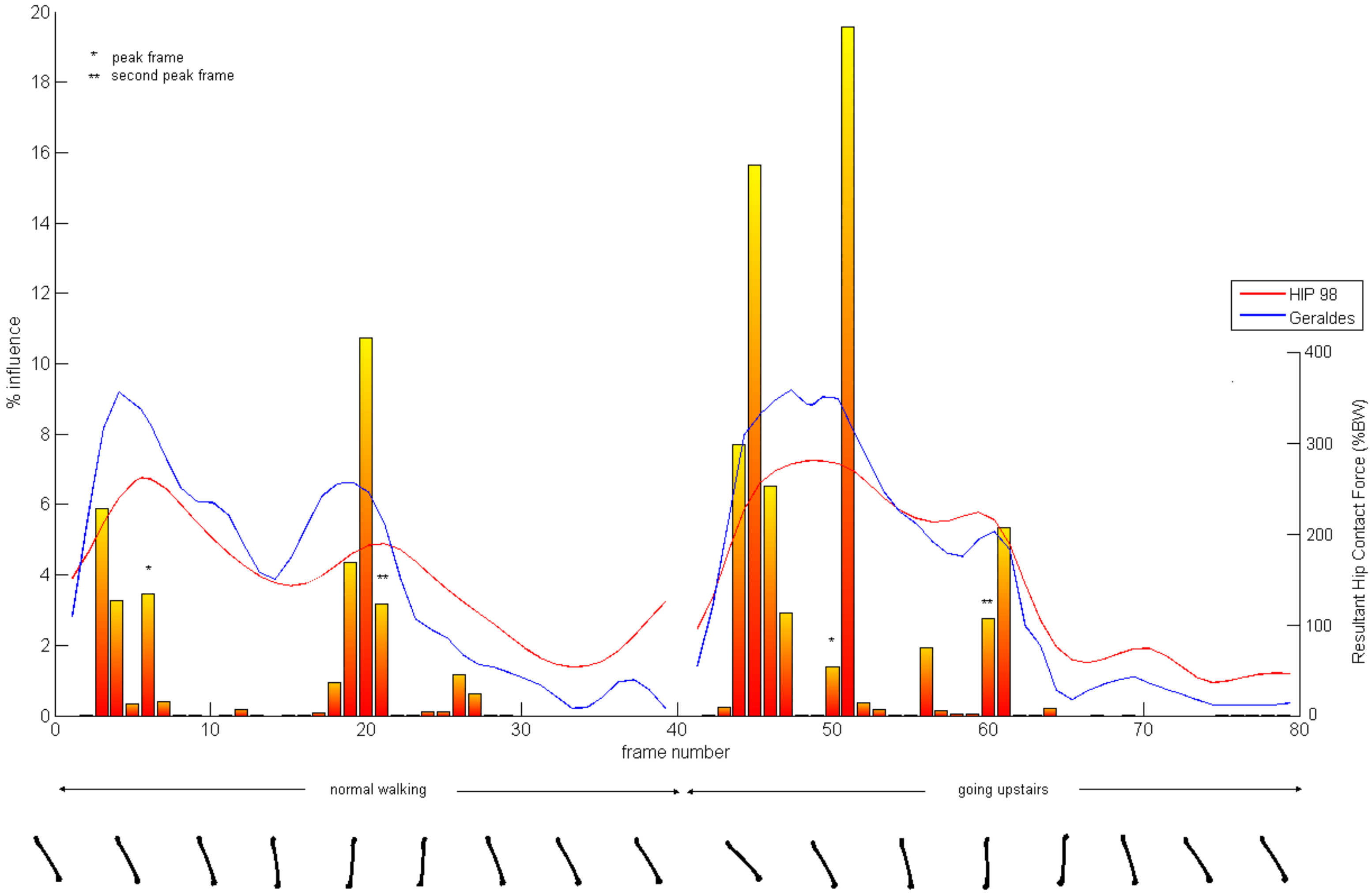

Figure 7.7 - Distribution of the percentage of elements influenced by each guiding frame (frames 1-40 for level walking and 41-80 for stair climbing) in Young's moduli adaptation. The frames where the first peak (**) and second peak (*) occur in the HIP 98 are highlighted. The resultant hip contact forces (%BW) calculated by the proposed model (Geraldes, in blue) and measured by instrumented prosthesis (HIP 98, in red) are super-imposed. The spatial positions of the femur, highlighting its flexion angle on the sagittal plane are included in the bottom.

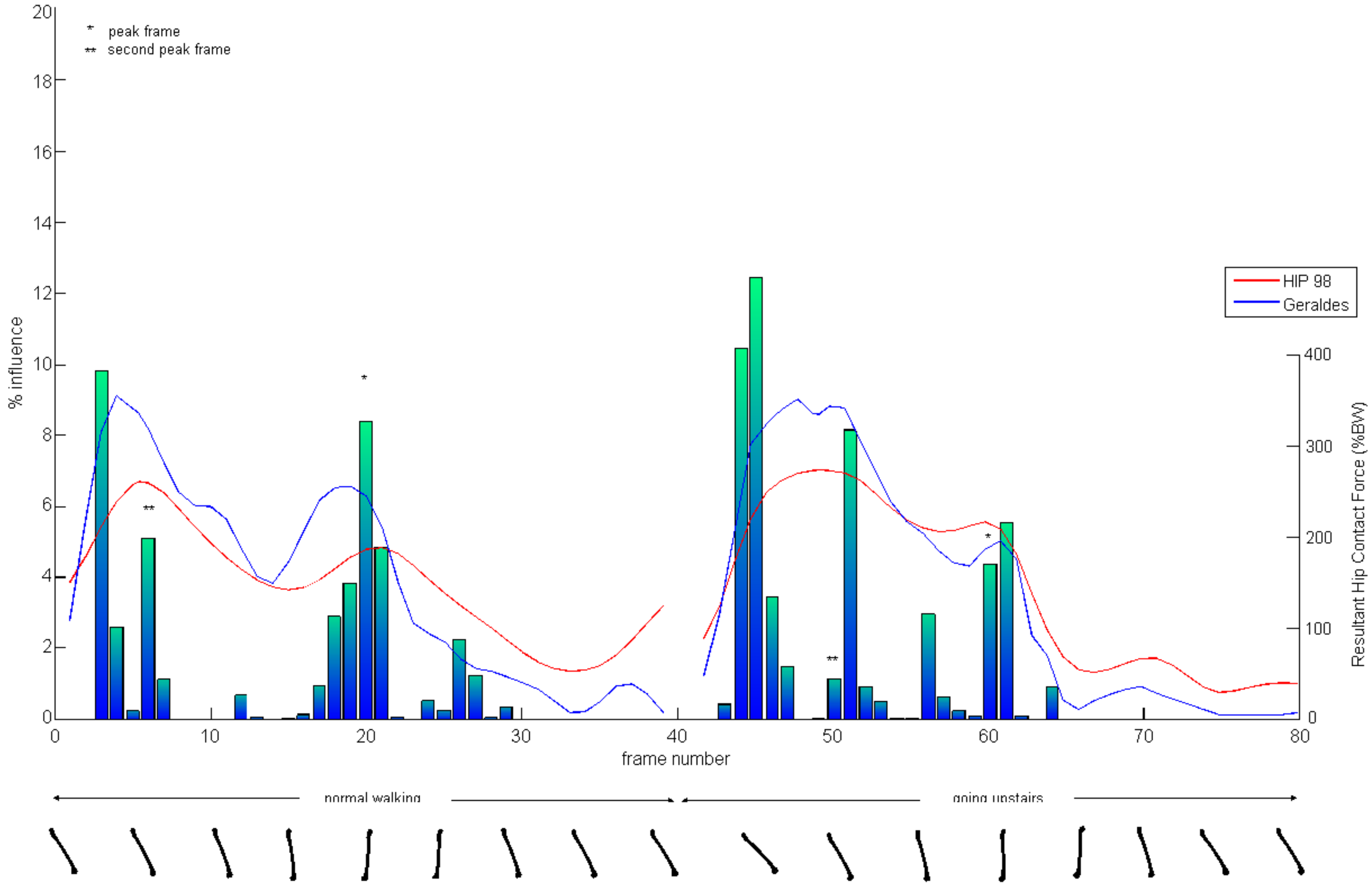

Figure 7.8 - Distribution of the percentage of elements influenced by each guiding frame (frames 1-40 for level walking and 41-80 for stair climbing) in shear modulus adaptation. The frames where the first peak (**) and second peak (*) occur in the HIP 98 are highlighted. The resultant hip contact forces (%BW) calculated by the proposed model (Geraldes, in blue) and measured by instrumented prosthesis (HIP 98, in red) are super-imposed. The spatial positions of the femur, highlighting its flexion angle on the sagittal plane are included in the bottom.

7.3 Conclusions

It has been suggested that trabeculae intersect non-orthogonally in order resist the shear stresses in regions where complex multi-axial is predominant, such as the proximal femur (Pidaparti and Turner 1997; Skedros and Baucom 2007). Notwithstanding being a more physiological way of modelling bone's anisotropy, the orthotropic assumption implemented in this thesis does not allow for accurate representation of the non-orthogonal trabecular crossings observed (Tobin 1955; Garden 1961; Skedros and Baucom 2007). In an attempt to overcome this imposed restriction and model the behaviour of femur's structural properties at a continuum level, shear modulus adaptation was included in the algorithm proposed. The converged material properties distributions were compared with literature and imaging data. Regions where non-orthogonal crossing was expected coincided with higher values of predicted shear modulus. The reverse was also observed. This relationship between the calculated average shear modulus and the directions of the dominant orthotropic axes is depicted in Figure 7.1 and Figure 7.2, hinting that the restriction on trabecular crossing imposed by the orthotropic symmetry was overcome by modelling shear modulus adaptation to shear strains. The average shear modulus was also shown to be higher in areas where complex loading occurs, in agreement with Skedro's trajectorial hypothesis (Skedros and Baucom 2007).

The guiding frames of the adaptation process were calculated for each element. Figure 7.3 to Figure 7.5 show the topological influence of the different frames in Young's modulus and shear modulus adaptation. The contribution of both load cases to the converged material properties is clear. Multiple frames were also observed to contribute towards the dominant regions of each load case (Figure 7.6 to Figure 7.8). This shows that bone remodelling studies where only one load case was considered (Doblaré and Garcia 2001; Miller et al. 2002; Tsubota et al. 2009), or the minimum sampling rate required to reliably capture the remodelling signal was not respected (Fernandes et al. 1999; Boyle and Kim 2011), have ignored the effect of these frames in bone adaptation. Thus, it is recommended that multiple activities and different instances of each load case are considered when attempting to model bone's adaptation to its mechanical surroundings.

Chapter 8

Conclusions

This thesis introduced a novel iterative 3D remodelling algorithm that successfully predicts the femur's material properties distribution and directionality of its internal structures at a continuum level. The algorithm was applied to a unique finite element (FE) model of the femur in which muscles and ligaments were explicitly represented using structural elements and physiologically-based boundary conditions were applied: the Multiple Load Case 3D Femur Model. Multiple load cases representing different instances of level walking and stair climbing were considered and their influence in the functional adaptation of the femur was assessed.

Throughout this report, conclusions on the different steps of the work have been laid out. This Chapter synthesises this study's achievements with the development of the FE model in subsection 8.1.1 and with the orthotropic bone remodelling algorithm in subsection 8.1.2. Subsection 8.1.3 summarises the conclusions made relative to the influence of the different load cases in bone adaptation. Recommendations for the improvement of the work presented are drawn in Section 8.2 and its potential applications identified in Section 8.3.

8.1 Conclusions

8.1.1 Finite Element Modelling

In order to achieve physiologically meaningful material property distributions and orientations, the chosen driving stimulus of the bone adaptation process needs to be derived from an accurate representation of the mechanical environment the femur is subjected to *in vivo*. Chapter 5 analysed the stress and strain distributions, the joint contact and reaction forces and the muscle and ligament forces produced by the Multiple Load Case 3D Femur Model.

Both combined von Mises and combined principal strains distribution patterns for the converged model agree qualitatively and quantitatively with similar numerical models (Polgar et al. 2003; Speirs et al. 2007; Phillips 2009). The joint contact forces also matched *in vivo* measurements (Bergmann et al. 1993; Bergmann et al. 2001; D'Lima et al. 2006; Kutzner et al. 2010). These findings suggest that this model is capable of producing a physiological and reliable driving signal for the remodelling process. Regardless of setting the target values for the remodelling plateau of the adaptation algorithm, there were still regions where the absolute values for the femoral principal strains fall outside this range. This suggests that the remodelling plateau is an optimum attractor state that bone attempts to optimise itself to, but not necessarily reach, resulting in a permanent state of bone remodelling.

Qualitative and quantitative comparison of the forces produced at the hip and knee joints calculated by the Multiple Load Case 3D Femur Model showed that both the level walking and stair climbing load cases show reasonable agreement with the values measured *in vivo* (Bergmann et al. 1993; Bergmann et al. 2001; D'Lima et al. 2006; Kutzner et al. 2010) and calculated using musculo-skeletal models (Heller et al. 2001; Heller et al. 2005; Modenese et al. 2011; Modenese 2012; Modenese and Phillips 2012) or static equilibrium analysis (Phillips 2009). It can be concluded that this model is capable of producing a physiological loading environment at the hip and knee joint, a key stepping stone in the attempt to produce a physiologically meaningful driving stimulus for the adaptation process of bone.

The resulting muscle force profiles for both walking and stair climbing were considered to be coherent with the muscle forces calculated by validated musculo-skeletal models (Heller et al. 2001; Modenese et al. 2011; Modenese 2012) and equilibration type models (Phillips 2009). Furthermore, the activation patterns of some muscles were in agreement with measured EMG profiles for the level walking load case (Wootten et al. 1990).

The model was considered to produce acceptable representations of *in vivo* muscle loading during walking and stair climbing. Despite the finite element method's limitation in not being able to model muscle synergism, the highly discretised muscle definition proposed is considered to be an alternative to musculo-skeletal modelling. The proposed method offers the advantage of stretching each of the spring elements within a certain muscle by different amounts, whereas musculo-skeletal models using muscle actuators do not currently allow for such high levels of discretisation.

8.1.2 Bone Adaptation Algorithm

Chapter 6 assessed if the adaptation process was accurately modelled by the orthotropic adaptation algorithm proposed. In order to evaluate whether the orthotropic assumption can reproduce the femur's structural anisotropy at a continuum level, Young's moduli, shear moduli and density distributions were analysed and compared with what has been observed *in vivo* and documented in literature. The directionality generated at the continuum level was compared with μCT slices along the three main anatomical planes for the proximal and distal femur regions of the same specimen. The values of the orthotropic Young's and shear moduli were found to be within what has been measured in literature (Rho et al. 1997; Rho et al. 1999; Taylor et al. 2002; Rudy et al. 2011; Rohrbach et al. 2012), with their distributions also matching what would be expected (Carter and Hayes 1977; Bitsakos et al. 2005). Interestingly, higher shear moduli occurred in regions where trabeculae have been found not to cross at orthogonal angles. The cumulative and topological density distributions predicted by the model seem to be in reasonable agreement with data extracted from a CT scan. The inclusion of multiple cases greatly improved the material properties and directionality predictions, particularly in the distal regions. The predicted directionality of the femur's internal structures was validated by comparison with μCT data of the proximal and distal regions of the same specimen, as well as published studies of the trabecular features of these regions (Ward 1838; von Meyer 1867; Tobin 1955; Garden 1961; Singh et al. 1970; Takechi 1977; Skedros and Baucom 2007).

It is tentatively concluded that this model can reliably produce bone's structural anisotropy at a continuum level, with physiological material properties and directionality predicted for the three main anatomical planes of the whole femur simultaneously. The orthotropic assumption can then be said to be more advantageous in comparison with the isotropic material symmetry assumption not only because is it a more accurate representation of bone's elastic symmetry, but also because it can give information about the directional stiffness in any of the three orthotropic directions, whilst still reproducing results achieved by the isotropic assumption. This is a step forward in the current way bone adaptation is achieved.

8.1.3 Influence of Load Cases in Bone Adaptation

Chapter 7 looked at the influence of the different instances of the two load cases modelled in the bone adaptation process and assessed the validity of the hypothesis that trabeculae cross at non-orthogonal angles in order to resist the shear stresses arising from complex multi-axial loading.

Shear modulus adaptation was included in the algorithm proposed in this thesis in an attempt to overcome the orthogonal restriction in trabecular crossing imposed by the orthotropic material symmetry assumption. The mean shear moduli distribution highlighted a relationship between the calculated shear modulus and the directions of the areas that experience complex loading. This suggests that the restriction on trabecular crossing imposed by orthotropy can be overcome by modelling shear modulus adaptation to shear strains, allowing for the representation of trabeculae structural adaptation at a continuum level. The dominant orthotropic axes were also show to cross at non-orthogonal angles in these same regions.

The guiding frames of the adaptation process of Young's and shear moduli were calculated for each element. It was clear that multiple load cases must be used to predict bone adaptation. Multiple frames were also observed to contribute towards the dominant regions of each load case. Furthermore, a distinct difference in the frames that dominate Young's moduli and shear moduli adaptation was also observed. Thus, it is recommended that multiple activities and different frames of each load case need to be considered when attempting to model bone’s adaptation to its mechanical surroundings. Studies where this is not respected might not be achieving the most physiological bone adaptation.

8.2 Limitations and Recommendations

Throughout this thesis, many recommendations on the ways to improve the modelling of the femur and its adaptation were laid down. These are summarised in this Section.

The geometry of the finite element model of the femur was not representative of the geometry of the subject from which kinetic and kinematic data were extracted, nor the specimen used to obtain the CT and μCT scans. This may explain some of differences between the calculated hip contact and muscle forces. It can also give a justification for some of the differences observed in the density distributions and trabecular directionality predicted. The modelling of the adaptation process using the geometry for the specimen as the basis for the finite element model will allow for more accurate assessment of how physiological the algorithm's predictions are. The displacement restrictions implemented at the medial condyle node introduced artificial constraints to movement in the distal part of the equilibrated finite element model, possibly resulting in underestimation of muscle forces and, therefore, the patello-femoral and tibio-femoral contact forces. The modelling of surface contact at the hip and knee joints could produce a more physiological behaviour of the model.

The definition of certain muscles as straight paths of action instead of their anatomical wrapping configuration can produce different contact force profiles. It is therefore suggested that more physiological modelling of the muscles paths, particularly for the gluteal muscles, will improve the predictions of the driving stimulus for the bone adaptation. The compressive and stabilising effect of the musculature surrounding the femur is also not considered when modelling the muscles as bundles of connector elements. A possible way of overcoming this problem could be the introduction of 3D finite element models of the muscles in question, with geometries extracted using medical imaging. In an attempt to overcome the restrictions on muscle synergism, the finite element mesh could model the muscle forces as point loads extracted from a static optimisation or other musculo-skeletal model with a similar number of muscle actuators. This integration of both modelling techniques could result in a powerful subject-specific diagnosis tool with possibilities of extension to the whole lower limb and body models.

It has been suggested in different parts of this thesis that the modelling of more extreme activities where higher flexion angles, quadriceps muscle activations and patello-femoral forces are involved could further improve the directionality of the structures predicted, as well as the stiffness and density calculated. In particular, stair descent and sit to stand are expected to improve the orthotropic material distributions observed. Activities involving more extreme loading, such as running, should also be considered.

Finally, a more comprehensive validation of the heterogeneous orthotropic model of the femur produced could be achieved by quantitatively comparing the dominant orthotropic axes with the dominant orientation for similar volumes of interest. Comparison with results extracted from the micro CT images was attempted but it was not reported in this thesis. The anisotropy function in the BoneJ plugin (Doube et al. 2010) for ImageJ (Rasband 1997-2012), a software package for image analysis, was used to extract the anisotropy for certain volumes of interest (VOI). BoneJ determines the material anisotropy tensor by calculating the number of interceptions between foreground and background in a binarised trabecular volume (mean intercept length - MIL) (Harrigan and Mann 1984; Odgaard 1997). An ellipsoid representing the anisotropy of the fabric within the VOI is then fit to the calculated fabric tensor by performing an eigen decomposition, which returns the three ellipsoid axes (Doube et al. 2010). These axes representing the VOI's anisotropy were compared with the observed trabecular groups for micro CT slices of the coronal plane of the proximal femur. No conclusive relation between the anisotropy obtained with the MIL method and the clear directionality documented in literature (Tobin 1955; Garden 1961; Singh et al. 1970; Skedros and Baucom 2007) was found. It was therefore concluded that insufficient comparable structural information could be obtained with the mean intercept length method used in ImageJ or Quant3D (Ketcham 2005), another software package to analyse trabecular bone architecture. It would be, therefore, of great interest to develop a method where stiffness directionality could be extracted from CT or μCT images in a manner representing the trajectory concept explored and exploited in the continuum model.

8.3 Applications

The final product of the work described in this thesis is a physiological orthotropic heterogeneous model of the femur, with directional information about its internal structures. The production and public release of these models can influence research areas where bone local structure and mechanical properties are of key importance.

Fracture mechanics can benefit from their application, since they can allow a more accurate assessment of directionally dependent strain fields and therefore more information on crack initiation and propagation can be obtained. Consequently, the development of impact mitigation devices for high-risk activities, elderly patients and in research areas like vehicle impact or blast biomechanics would also benefit from the proposed method. Integration with musculo-skeletal models could produce a powerful, time efficient tool for patient-specific diagnosis and prediction of bone adaptation. Recommendations on which physical activities may influence bone health could be inferred, potentially allowing for prevention of fractures resulting from bone deterioration induced by sedentary lifestyles. Finally, notwithstanding having been used to produce models of the naturally adapted femoral structures, nothing indicates that the proposed algorithm wouldn't work in predictions of bone remodelling or bone growth. This can have an impact in the study of bone-implant interfaces and improvement of the surgical tools and techniques that are currently used, namely in fracture reduction and total hip and knee replacements. These models can also potentially be applied to study the influence of bone degradation caused by osteoporosis in the biomechanics of the human body. Furthermore, the adaptation process could also be extended to shape optimisation by modelling bone growth at the surface, in an attempt to further increase the understanding of the function and geometry of bones.

This method could potentially be an invaluable tool in achieving a more thorough understanding of bone's structural material properties, thus improving the knowledge we have of its mechanical behaviour and contributing to the developing field of Biomechanics. It is hoped that the work described in this thesis is seen as a step in this direction.

Appendix

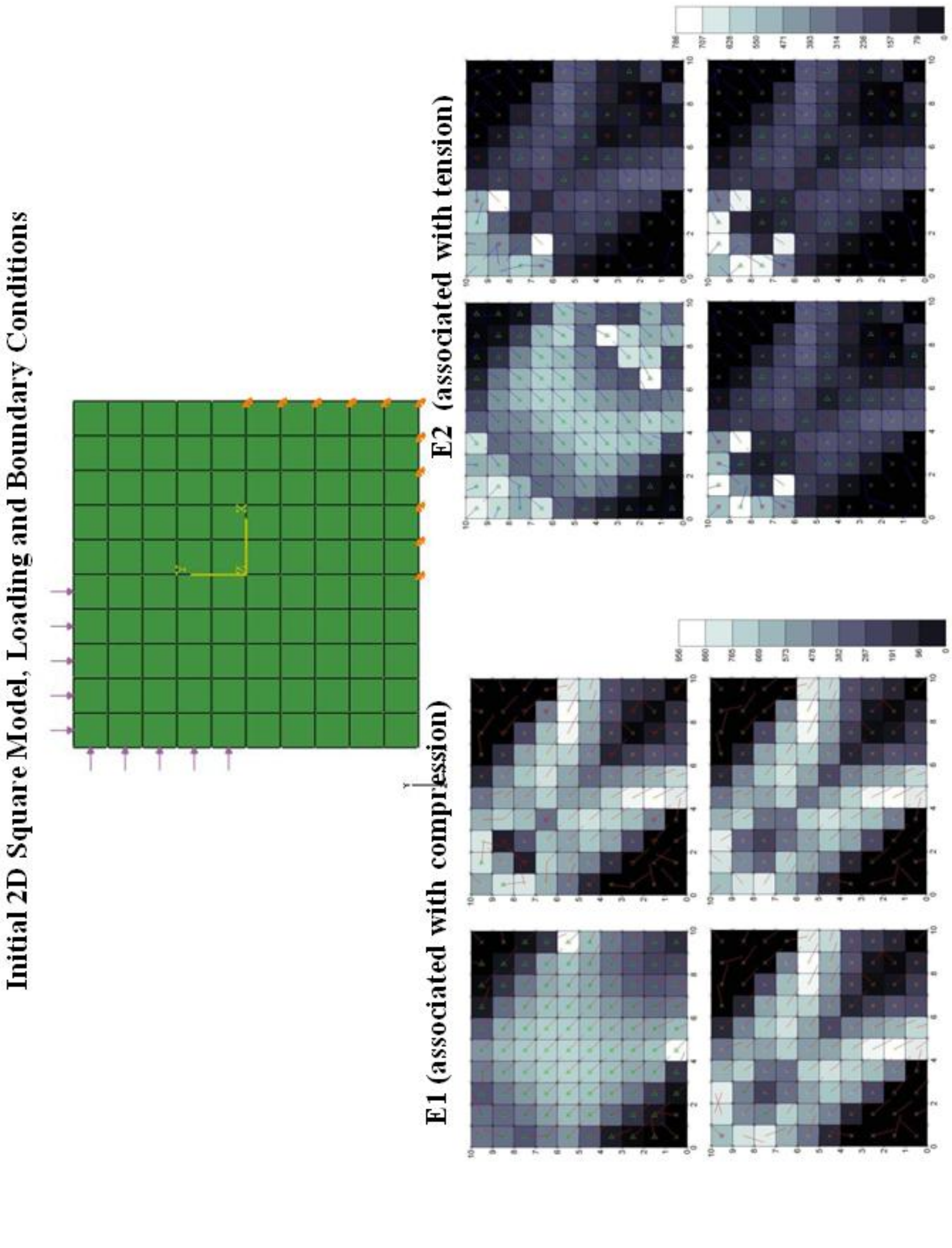

Figure A. 1 - The algorithm was tested for E_1 and E_2 at iterations 1, 5, 10 and 20 for a 2D square model, producing expected material properties distributions and orientations.

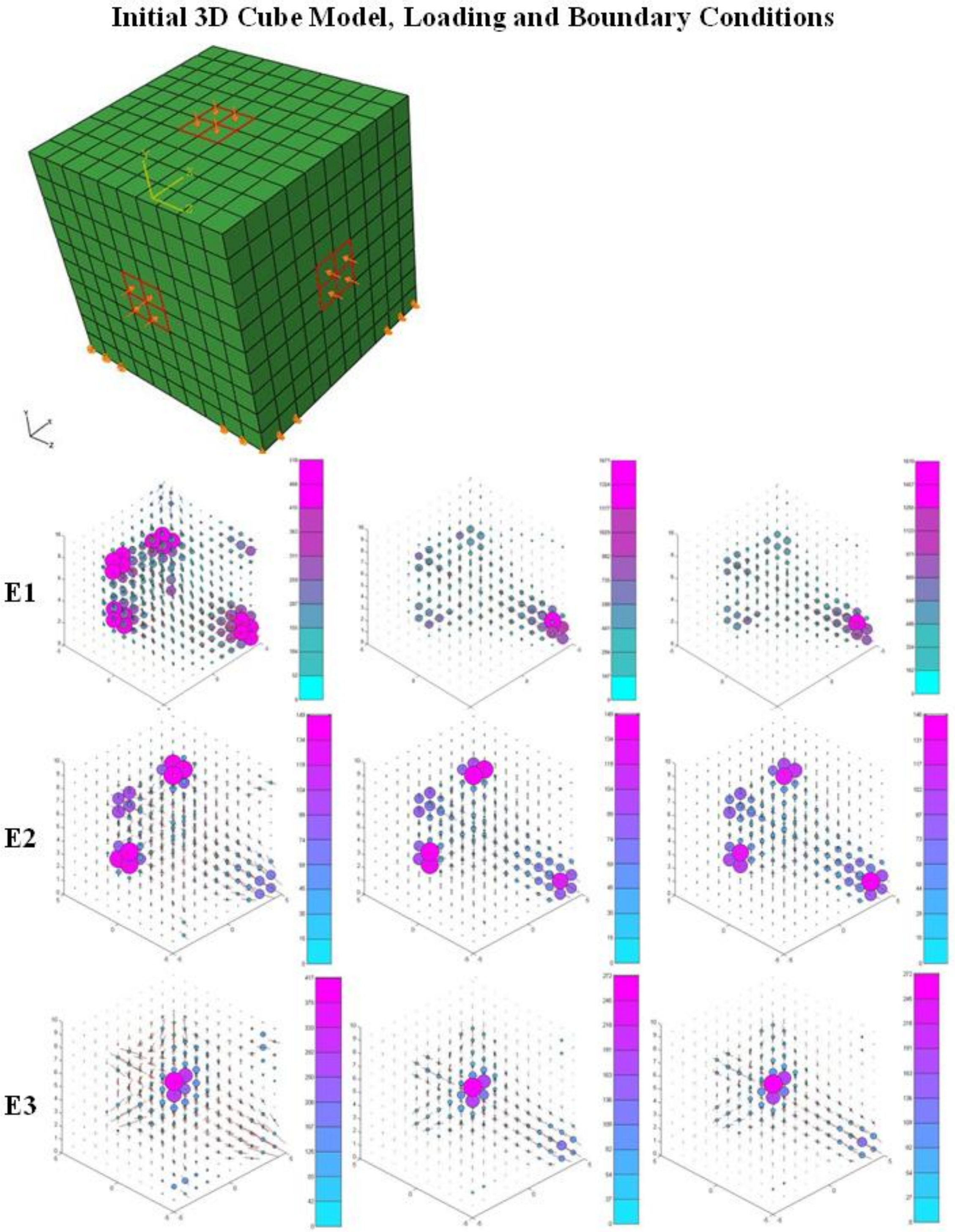

Figure A. 2 - The algorithm was tested for E_1, E_2 and E_3 at iterations 1, 5 and 20 for a 3D cube model, producing expected material properties distributions and orientations.

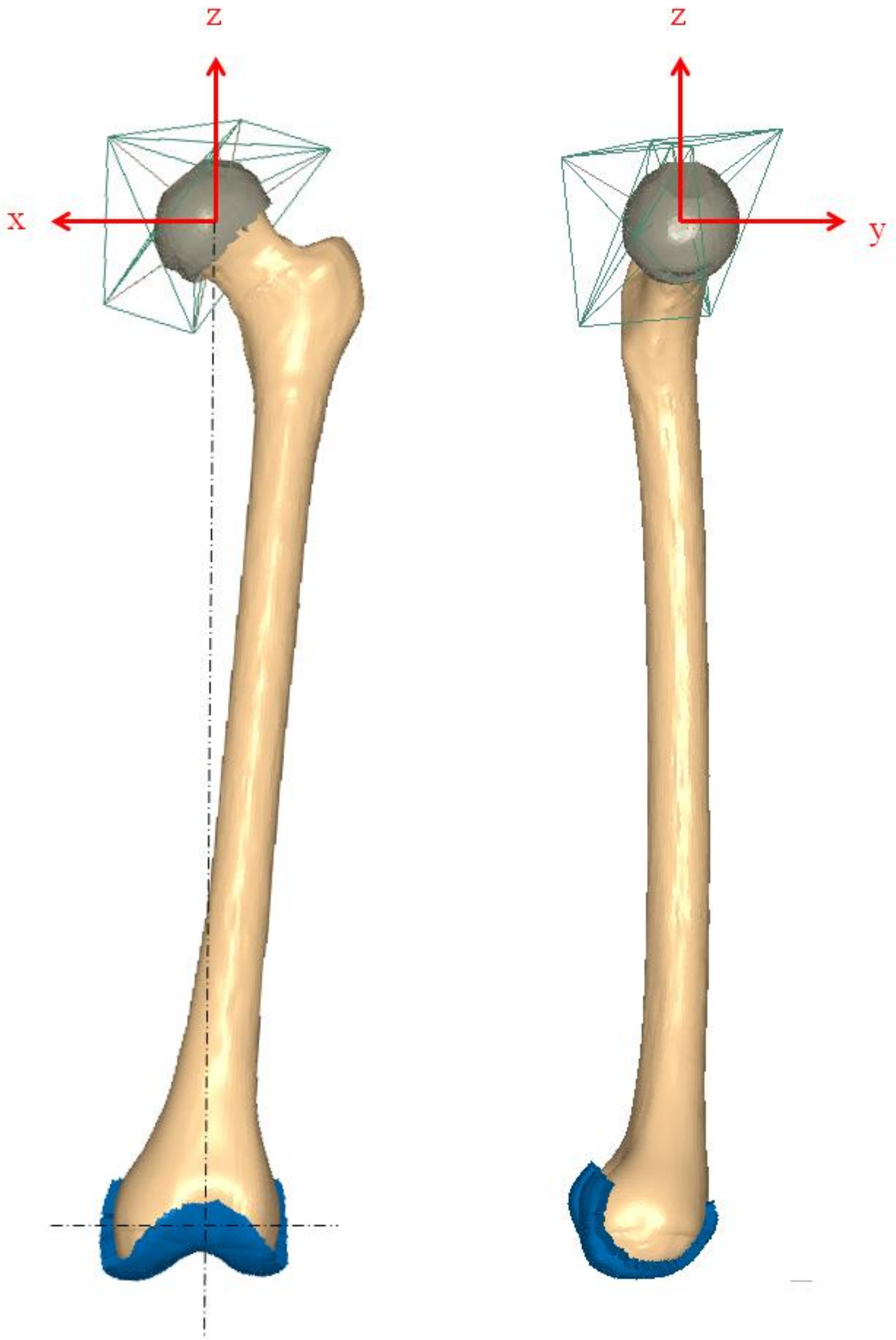

Figure A.3 - Diagram representing the global coordinate systems used for the neutral position.

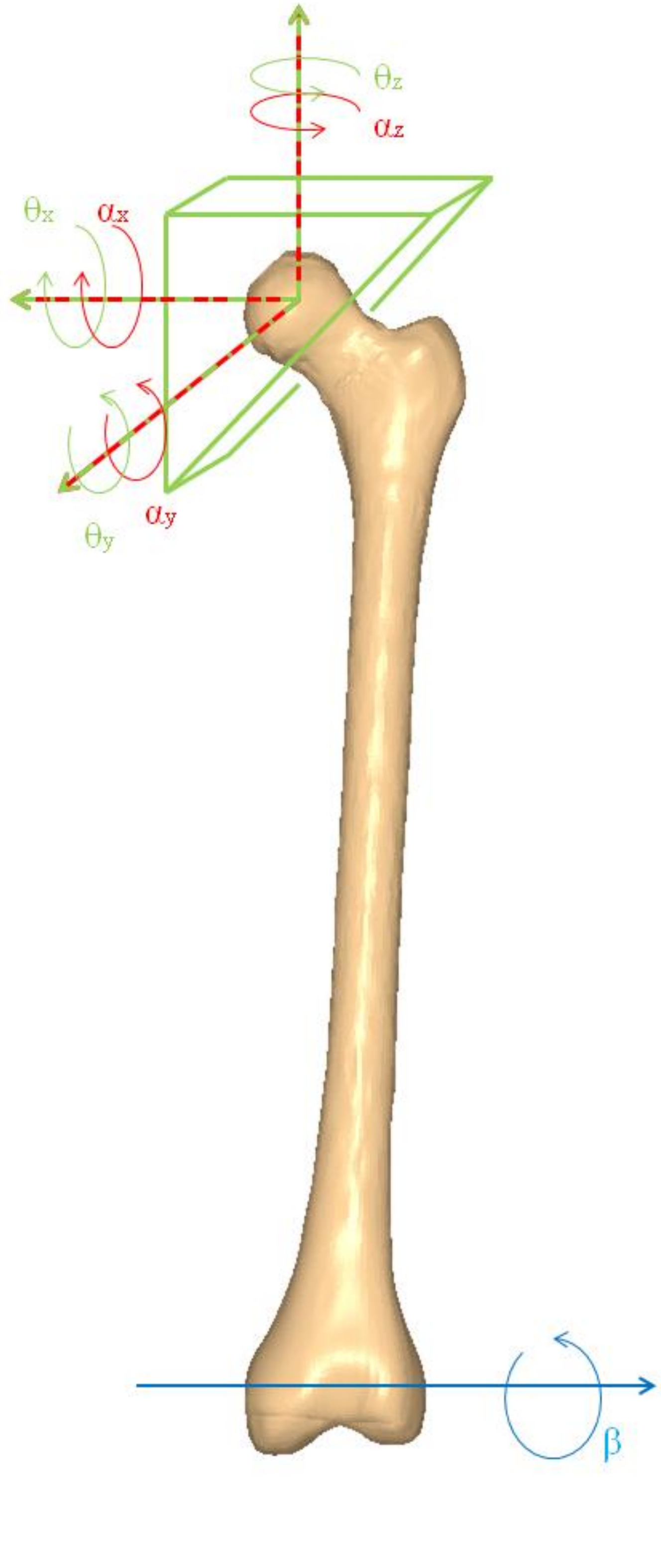

Figure A.4 - Diagram representing the local coordinate systems used for each segment for the neutral position.

Table A.1 - Angle components of the pelvis, femur and tibia segment angles for the level walking load case. The frame number corresponds to Bergmann's sampling of the level walking trial HSRWN4.

Model nr.	**Frame nr.**	**θ_x pelvis**	**θ_y pelvis**	**θ_z pelvis**	**α_x femur**	**α_y femur**	**α_z femur**	**β tibia**
1	5	-40.24	-4.83	-6.21	26.10	-0.46	0.29	-11.88
2	10	-40.01	-3.60	-6.72	25.40	-0.51	0.03	-11.32
3	15	-39.56	-2.13	-7.33	24.46	-0.48	-0.21	-11.49
4	20	-39.14	-0.51	-8.10	23.35	-0.37	-0.45	-12.29
5	25	-38.45	1.12	-8.86	22.07	-0.30	-0.59	-13.50
6	27	-38.11	1.75	-9.14	21.53	-0.30	-0.65	-14.05
7	30	-37.75	2.65	-9.60	20.65	-0.30	-0.68	-14.88
8	35	-37.19	3.95	-10.30	19.06	-0.43	-0.77	-16.18
9	40	-36.76	4.97	-10.90	17.27	-0.68	-0.81	-17.12
10	45	-36.49	5.68	-11.50	15.25	-1.02	-0.83	-17.58
11	50	-36.41	6.09	-12.08	13.03	-1.44	-0.85	-17.63
12	55	-36.52	6.25	-12.71	10.59	-1.92	-0.85	-17.19
13	60	-36.75	6.19	-13.36	7.99	-2.47	-0.82	-16.41
14	65	-37.05	5.85	-13.88	5.24	-3.06	-0.73	-15.45
15	70	-37.31	5.34	-14.31	2.41	-3.69	-0.69	-14.43
16	75	-37.57	4.67	-14.63	-0.40	-4.28	-0.53	-13.56
17	80	-37.74	3.82	-14.83	-3.11	-4.82	-0.41	-13.07
18	85	-37.86	2.87	-14.97	-5.63	-5.25	-0.18	-13.03
19	90	-37.82	1.86	-15.02	-7.82	-5.52	0.15	-13.68
20	95	-37.88	0.79	-15.10	-9.57	-5.61	0.46	-15.16
21	100	-38.00	-0.26	-15.13	-10.74	-5.48	0.76	-17.61
22	105	-38.15	-1.35	-15.13	-11.32	-5.12	0.97	-20.97
23	110	-38.42	-2.40	-14.99	-11.21	-4.55	0.98	-25.20
24	115	-38.68	-3.37	-14.75	-10.41	-3.78	0.92	-30.13
25	120	-39.01	-4.29	-14.39	-8.93	-2.83	0.79	-35.47
26	125	-39.32	-5.02	-13.89	-6.73	-1.73	0.62	-40.83
27	130	-39.53	-5.57	-13.26	-3.95	-0.59	0.39	-45.81
28	135	-39.74	-5.99	-12.50	-0.72	0.52	0.10	-50.04
29	140	-39.76	-6.22	-11.64	2.83	1.51	-0.19	-53.19
30	145	-39.71	-6.42	-10.67	6.51	2.33	-0.45	-55.00
31	150	-39.39	-6.50	-9.59	10.18	2.91	-0.65	-55.24
32	155	-39.23	-6.48	-8.32	13.72	3.22	-0.68	-53.70
33	160	-39.05	-6.40	-6.95	16.95	3.27	-0.57	-50.52
34	165	-38.77	-6.28	-5.43	19.76	3.06	-0.10	-45.91
35	170	-38.55	-6.14	-3.94	22.05	2.70	0.85	-40.22
36	175	-38.20	-5.99	-2.59	23.77	2.25	2.40	-33.95
37	180	-37.91	-5.76	-1.40	24.94	1.74	4.40	-27.69
38	185	-37.68	-5.51	-0.48	25.59	1.20	6.45	-22.01
39	190	-37.40	-5.17	0.14	25.81	0.69	8.29	-17.09
40	195	-37.26	-4.79	0.48	25.70	0.23	9.53	-13.14

Table A.2 - Angle components of the pelvis, femur and tibia segment angles for the stair climbing load case. The frame number corresponds to Bergmann's sampling of stair climbing trial HSRSU6.

Model nr.	Frame nr.	θ_x pelvis	θ_y pelvis	θ_z pelvis	α_x femur	α_y femur	α_z femur	β tibia
41	5	-4.57	10.34	1.43	50.67	2.35	12.04	-62.65
42	10	-4.17	10.09	0.61	47.98	2.22	10.02	-60.28
43	15	-4.17	9.74	-0.48	44.89	2.24	8.22	-57.98
44	20	-4.69	9.14	-1.75	41.50	2.28	6.57	-55.43
45	25	-5.58	8.22	-3.10	37.91	2.26	5.08	-52.46
46	30	-6.79	7.03	-4.45	34.23	2.13	3.78	-49.05
47	35	-8.12	5.65	-5.78	30.57	1.92	2.67	-45.36
48	40	-9.52	4.22	-7.07	27.02	1.61	1.77	-41.57
49	42	-9.98	3.59	-7.57	25.64	1.48	1.46	-40.12
50	45	-10.70	2.69	-8.38	23.62	1.29	1.05	-37.98
51	50	-11.66	1.06	-9.61	20.38	0.91	0.51	-34.78
52	55	-12.40	-0.76	-10.74	17.30	0.50	0.14	-32.11
53	60	-12.89	-2.78	-11.70	14.31	0.09	-0.01	-29.96
54	65	-13.15	-4.89	-12.53	11.39	-0.31	0.07	-28.23
55	70	-13.28	-6.96	-13.20	8.49	-0.70	0.39	-26.79
56	75	-13.18	-8.71	-13.71	5.65	-1.11	0.88	-25.50
57	80	-13.13	-10.03	-14.15	2.86	-1.54	1.57	-24.21
58	85	-13.04	-10.81	-14.34	0.22	-2.02	2.37	-22.85
59	90	-13.10	-11.14	-14.39	-2.32	-2.53	3.21	-21.26
60	95	-13.37	-11.32	-14.12	-4.69	-2.99	4.15	-19.59
61	100	-13.88	-11.66	-13.63	-6.88	-3.33	5.26	-17.98
62	105	-14.60	-12.27	-12.87	-8.73	-3.43	6.53	-16.83
63	110	-15.49	-13.06	-11.94	-9.95	-3.27	7.72	-16.68
64	115	-16.24	-13.68	-10.90	-10.28	-2.79	8.73	-17.98
65	120	-16.88	-13.89	-9.93	-9.51	-2.03	9.25	-21.13
66	125	-17.15	-13.48	-9.11	-7.58	-1.11	9.15	-26.25
67	130	-17.05	-12.43	-8.41	-4.52	-0.13	8.68	-33.06
68	135	-16.51	-10.78	-7.80	-0.54	0.83	8.21	-40.92
69	140	-15.67	-8.79	-7.32	4.05	1.74	8.01	-48.84
70	145	-14.52	-6.74	-6.85	8.94	2.58	8.17	-55.80
71	150	-13.20	-4.90	-6.33	13.79	3.33	8.62	-60.80
72	155	-11.88	-3.46	-5.73	18.35	3.91	9.14	-63.10
73	160	-10.63	-2.48	-4.90	22.38	4.20	9.57	-62.35
74	165	-9.55	-1.89	-3.99	25.65	4.18	9.83	-58.63
75	170	-8.56	-1.60	-3.07	28.01	3.87	9.92	-52.51
76	175	-7.75	-1.57	-2.20	29.40	3.35	9.88	-44.89
77	180	-7.03	-1.78	-1.60	29.81	2.76	9.67	-36.69
78	185	-6.43	-2.21	-1.35	29.33	2.22	9.25	-28.73
79	190	-5.84	-2.74	-1.60	28.10	1.85	8.46	-21.56
80	195	-5.39	-3.38	-2.31	26.30	1.67	7.25	-15.52

Table A.3 - Abaqus rotation axes (r_1, r_2, r_3), in mm, and angles (φ) for the pelvis and the femur for the HSRNW4 trial.

Model nr.	**Pelvis r_1**	**Pelvis r_2**	**Pelvis r_3**	**Pelvis φ**	**Femur r_1**	**Femur r_2**	**Femur r_3**	**Femur φ**
1	0.105	0.167	0.980	40.711	1.000	-0.015	0.015	26.110
2	0.128	0.143	0.981	40.489	1.000	-0.020	0.006	25.403
3	0.157	0.114	0.981	40.129	1.000	-0.021	-0.004	24.464
4	0.191	0.082	0.978	39.900	1.000	-0.019	-0.016	23.352
5	0.225	0.048	0.973	39.516	1.000	-0.018	-0.024	22.081
6	0.238	0.035	0.971	39.325	0.999	-0.019	-0.027	21.544
7	0.258	0.016	0.966	39.209	0.999	-0.020	-0.030	20.658
8	0.287	-0.012	0.958	39.077	0.999	-0.029	-0.036	19.077
9	0.310	-0.033	0.950	39.041	0.998	-0.046	-0.041	17.296
10	0.330	-0.046	0.943	39.144	0.996	-0.073	-0.045	15.300
11	0.345	-0.052	0.937	39.357	0.992	-0.116	-0.052	13.127
12	0.359	-0.050	0.932	39.721	0.981	-0.185	-0.062	10.785
13	0.370	-0.042	0.928	40.164	0.951	-0.301	-0.077	8.380
14	0.377	-0.028	0.926	40.545	0.856	-0.508	-0.097	6.092
15	0.380	-0.011	0.925	40.827	0.537	-0.832	-0.138	4.452
16	0.381	0.008	0.925	41.030	-0.098	-0.987	-0.126	4.335
17	0.378	0.030	0.925	41.075	-0.543	-0.835	-0.093	5.758
18	0.374	0.054	0.926	41.061	-0.731	-0.680	-0.057	7.702
19	0.369	0.078	0.926	40.861	-0.816	-0.577	-0.024	9.564
20	0.363	0.104	0.926	40.786	-0.861	-0.509	-0.001	11.084
21	0.355	0.129	0.926	40.764	-0.888	-0.459	0.020	12.044
22	0.346	0.155	0.925	40.795	-0.907	-0.419	0.037	12.417
23	0.333	0.179	0.926	40.909	-0.923	-0.383	0.044	12.100
24	0.318	0.200	0.927	41.026	-0.936	-0.347	0.052	11.082
25	0.300	0.218	0.929	41.190	-0.950	-0.307	0.061	9.380
26	0.281	0.231	0.931	41.323	-0.965	-0.253	0.074	6.970
27	0.261	0.239	0.935	41.350	-0.985	-0.149	0.091	4.012
28	0.240	0.243	0.940	41.371	-0.808	0.578	0.117	0.894
29	0.218	0.242	0.945	41.200	0.881	0.468	-0.071	3.213
30	0.196	0.240	0.951	40.963	0.940	0.332	-0.084	6.935
31	0.172	0.235	0.957	40.470	0.960	0.268	-0.085	10.627
32	0.144	0.226	0.963	40.109	0.972	0.221	-0.075	14.132
33	0.113	0.214	0.970	39.758	0.981	0.183	-0.060	17.288
34	0.079	0.200	0.977	39.323	0.988	0.150	-0.031	20.000
35	0.044	0.185	0.982	39.000	0.992	0.127	0.015	22.211
36	0.013	0.172	0.985	38.596	0.990	0.113	0.079	23.946
37	-0.015	0.157	0.987	38.283	0.982	0.106	0.156	25.309
38	-0.035	0.144	0.989	38.043	0.968	0.100	0.230	26.339
39	-0.048	0.131	0.990	37.746	0.951	0.094	0.296	27.049
40	-0.054	0.119	0.991	37.582	0.936	0.086	0.341	27.364

Table A.4 - Abaqus rotation axes (r_1, r_2, r_3), in mm, and angles (φ) for the pelvis and the femur for the HSRSU6 trial.

Model nr.	**Pelvis r_1**	**Pelvis r_2**	**Pelvis r_3**	**Pelvis φ**	**Femur r_1**	**Femur r_2**	**Femur r_3**	**Femur φ**
1	-0.089	-0.916	0.391	11.340	0.970	0.145	0.197	51.795
2	-0.022	-0.926	0.376	10.909	0.976	0.129	0.174	48.815
3	0.079	-0.915	0.396	10.617	0.981	0.117	0.152	45.488
4	0.202	-0.865	0.459	10.483	0.986	0.109	0.130	41.927
5	0.332	-0.766	0.550	10.521	0.989	0.101	0.109	38.203
6	0.445	-0.620	0.646	10.905	0.992	0.093	0.088	34.423
7	0.529	-0.448	0.720	11.655	0.994	0.084	0.068	30.698
8	0.579	-0.283	0.764	12.772	0.996	0.074	0.050	27.098
9	0.596	-0.221	0.772	13.203	0.997	0.069	0.043	25.706
10	0.615	-0.135	0.777	14.001	0.998	0.063	0.032	23.665
11	0.637	-0.005	0.771	15.206	0.999	0.048	0.017	20.402
12	0.649	0.117	0.752	16.353	1.000	0.030	0.004	17.309
13	0.651	0.234	0.722	17.405	1.000	0.006	-0.001	14.312
14	0.647	0.341	0.682	18.406	1.000	-0.026	0.009	11.391
15	0.635	0.434	0.639	19.402	0.996	-0.078	0.052	8.526
16	0.624	0.505	0.596	20.213	0.970	-0.182	0.161	5.829
17	0.616	0.551	0.563	20.953	0.795	-0.415	0.443	3.625
18	0.610	0.578	0.543	21.335	0.083	-0.646	0.759	3.126
19	0.604	0.588	0.538	21.543	-0.482	-0.556	0.677	4.668
20	0.587	0.594	0.549	21.610	-0.666	-0.460	0.587	6.865
21	0.556	0.606	0.569	21.767	-0.734	-0.397	0.551	9.161
22	0.507	0.624	0.594	22.062	-0.756	-0.348	0.555	11.268
23	0.446	0.645	0.621	22.541	-0.756	-0.306	0.578	12.834
24	0.386	0.658	0.647	22.914	-0.739	-0.262	0.621	13.600
25	0.336	0.658	0.673	23.087	-0.702	-0.210	0.681	13.298
26	0.306	0.645	0.700	22.794	-0.629	-0.144	0.764	11.870
27	0.294	0.617	0.730	21.977	-0.460	-0.048	0.886	9.780
28	0.300	0.573	0.763	20.596	-0.072	0.096	0.993	8.273
29	0.320	0.514	0.796	18.917	0.432	0.223	0.874	9.085
30	0.349	0.443	0.826	17.062	0.714	0.262	0.649	12.242
31	0.377	0.369	0.849	15.198	0.825	0.266	0.499	16.376
32	0.397	0.300	0.868	13.482	0.875	0.259	0.410	20.566
33	0.393	0.247	0.886	11.868	0.902	0.247	0.354	24.350
34	0.365	0.212	0.906	10.458	0.920	0.230	0.318	27.419
35	0.320	0.199	0.926	9.194	0.932	0.210	0.296	29.613
36	0.255	0.210	0.944	8.175	0.940	0.188	0.285	30.887
37	0.201	0.253	0.946	7.403	0.945	0.167	0.280	31.204
38	0.178	0.330	0.927	6.907	0.949	0.148	0.277	30.626
39	0.221	0.426	0.877	6.609	0.954	0.133	0.268	29.244
40	0.320	0.519	0.793	6.713	0.961	0.122	0.248	27.214

Table A.5 - Different components for the each model's hip inter-segmental forces (N) and moments (N/mm) in the global coordinate system for the level walking load case (HSRWN4) and corresponding stage of the load cycle (%).

Model nr.	Frame nr.	% Walking	F_x	F_y	F_z	M_x	M_y	M_z
1	5	2.5	4	-36	-45	-63473	714	1628
2	10	5.0	-22	-6	-338	-115473	-14474	4368
3	15	7.5	-52	55	-681	-144037	-24626	6351
4	20	10.0	-29	83	-841	-139717	4090	1810
5	25	12.4	14	89	-806	-102575	41712	-4452
6	27	13.4	25	90	-785	-87978	51562	-6116
7	30	14.9	24	87	-783	-75495	52210	-6299
8	35	17.4	4	74	-787	-63595	38228	-4624
9	40	19.9	-5	62	-772	-50300	31669	-4449
10	45	22.4	3	49	-741	-38213	38155	-5613
11	50	24.9	15	35	-696	-29842	46820	-6134
12	55	27.4	20	24	-638	-21957	48661	-5503
13	60	29.9	15	19	-579	-12589	42800	-4628
14	65	32.3	11	18	-536	-3605	36714	-3984
15	70	34.8	12	17	-520	4409	34912	-3669
16	75	37.3	15	14	-534	12253	35705	-3727
17	80	39.8	20	10	-570	21438	38835	-3820
18	85	42.3	23	2	-622	32054	41835	-3874
19	90	44.8	21	-12	-679	43589	39975	-4594
20	95	47.3	14	-33	-724	52581	34107	-5906
21	100	49.8	10	-60	-724	54293	29049	-6372
22	105	52.2	6	-83	-651	46696	20843	-5693
23	110	54.7	-3	-77	-485	38270	4999	-3813
24	115	57.2	-10	-29	-256	39243	-8150	-903
25	120	59.7	-7	35	-44	46741	-9554	974
26	125	62.2	-2	65	79	44766	-5762	1262
27	130	64.7	1	60	131	33166	-2715	1097
28	135	67.2	2	46	137	25684	-1618	733
29	140	69.7	2	31	127	22527	-1122	600
30	145	72.1	3	18	117	19789	-440	443
31	150	74.6	4	9	109	17235	188	338
32	155	77.1	4	1	105	14621	513	408
33	160	79.6	4	-8	107	10103	574	555
34	165	82.1	4	-19	111	3128	982	458
35	170	84.6	5	-34	114	-6871	2054	-7
36	175	87.1	6	-51	112	-18338	2994	-584
37	180	89.6	5	-63	108	-28123	2302	-795
38	185	92.0	1	-65	102	-30418	-157	-589
39	190	94.5	-2	-56	103	-24482	-2632	-254
40	195	97.0	-2	-36	111	-9329	-2862	52

Table A.6 - Different components for the each model's hip inter-segmental forces (N) and moments (N/mm) in the global coordinate system for the stair climbing load case (HSRSU6) and corresponding stage of the load cycle (%).

Model nr.	Frame nr.	% Stair climbing	F_x	F_y	F_z	M_x	M_y	M_z
41	5	2.5	3	-19	-28	-25905	-1419	2930
42	10	5.0	-5	3	-167	-47328	-6654	5426
43	15	7.5	6	22	-330	-71792	3349	1335
44	20	10.0	9	36	-512	-98343	7184	496
45	25	12.4	25	56	-588	-93994	18690	-2504
46	30	14.9	30	55	-652	-94784	23421	-3744
47	35	17.4	24	44	-716	-97294	23642	-4296
48	40	19.9	28	38	-707	-87024	29308	-6314
49	42	20.9	32	37	-705	-83259	34027	-7727
50	45	22.4	37	34	-719	-80751	40919	-9875
51	50	24.9	41	20	-705	-74944	48441	-11786
52	55	27.4	34	16	-665	-60624	46398	-10344
53	60	29.9	28	11	-645	-47771	43807	-8755
54	65	32.3	27	6	-612	-35805	40922	-7377
55	70	34.8	32	5	-617	-26109	41206	-6296
56	75	37.3	38	0	-635	-19686	42592	-5990
57	80	39.8	37	-11	-660	-13708	39363	-5895
58	85	42.3	33	-23	-706	-9710	35565	-5473
59	90	44.8	35	-33	-754	-4387	36839	-4749
60	95	47.3	41	-43	-790	1685	40961	-3671
61	100	49.8	43	-56	-791	4474	40822	-2640
62	105	52.2	35	-60	-723	7795	30366	-1778
63	110	54.7	5	-43	-494	7773	618	-2555
64	115	57.2	-8	-3	-126	3964	-13359	-1724
65	120	59.7	0	29	96	4271	-7146	-248
66	125	62.2	6	40	142	8327	-1205	288
67	130	64.7	6	41	139	11780	-430	458
68	135	67.2	4	37	132	13934	-452	608
69	140	69.7	0	28	122	14214	-635	654
70	145	72.1	-3	16	109	13433	-716	553
71	150	74.6	-4	5	96	11524	-685	388
72	155	77.1	-4	-3	88	9739	-219	178
73	160	79.6	-2	-9	86	8015	533	-57
74	165	82.1	0	-14	89	5748	823	-135
75	170	84.6	0	-21	95	2148	206	-103
76	175	87.1	-1	-28	98	-1828	-824	30
77	180	89.6	-2	-33	101	-4705	-1530	123
78	185	92.0	-2	-34	104	-4980	-1631	175
79	190	94.5	1	-31	112	-4459	-1316	343
80	195	97.0	2	-23	118	1998	-920	432

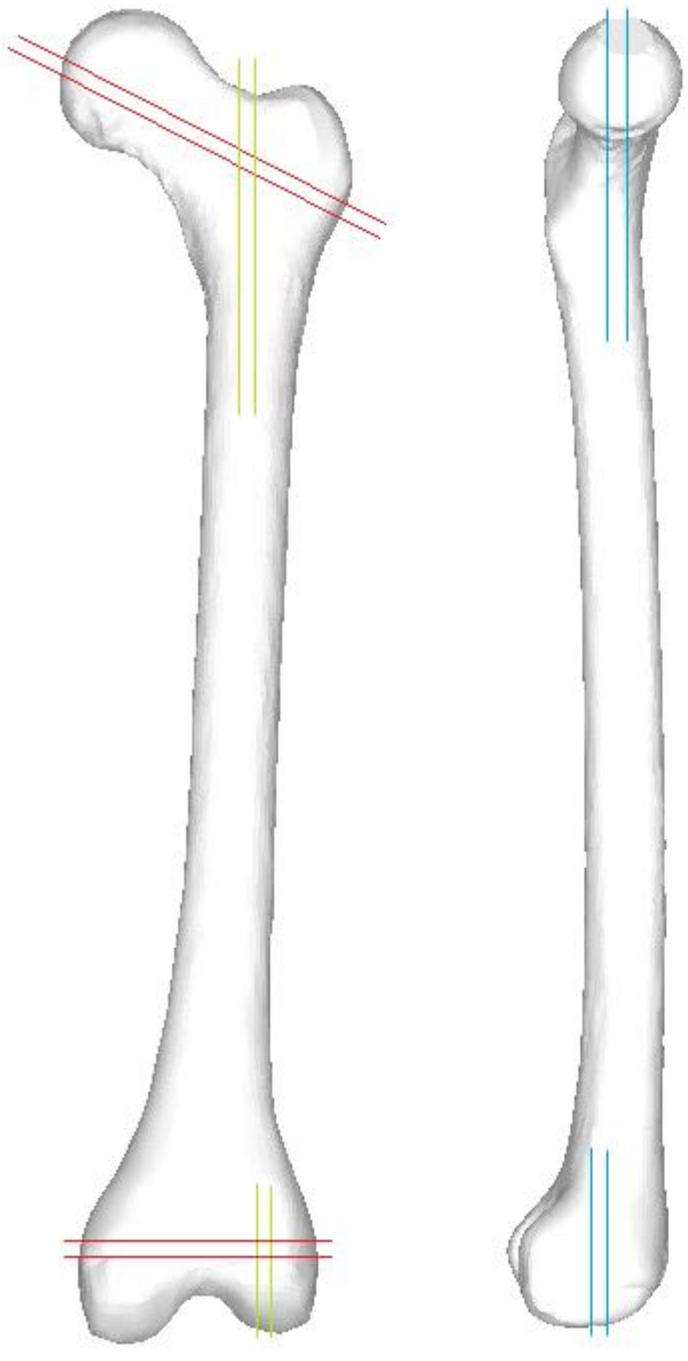

Figure A.5 - Schematic representation of the section cuts used for both femoral regions: coronal (blue), transverse (red) and sagittal (green).

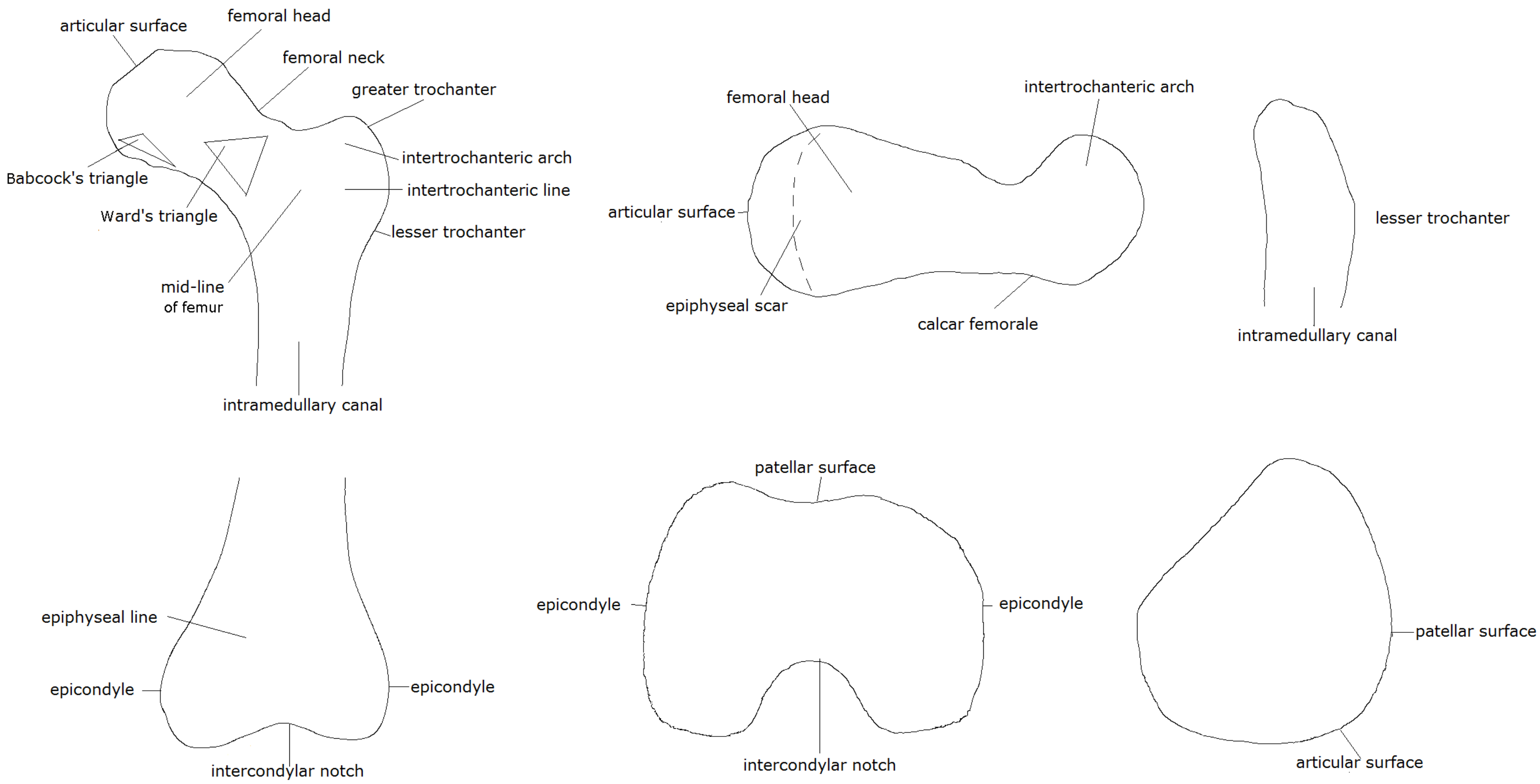

Figure A.6 - Main anatomical features for the cross sections used.

References

Aamodt, A., J. Lund-Larsen, J. Eine, E. Andersen, P. Benum and O. S. Husby (1997). "In Vivo Measurements Show Tensile Axial Strain in the Proximal Lateral Aspect of the Human Femur." Journal of Orthopaedic Research **15**(6): 927-931.

Ahmed, A. M., D. L. Burke and A. Hyder (1987). "Force Analysis of the Patellar Mechanism." Journal of Orthopaedic Research **5**(1): 69-85.

Anderson, A., C. Peters, B. Tuttle and J. Weiss (2005). "Subject-Specific Finite Element Model of the Pelvis: Development, Validation and Sensitiviy Studies." Journal of Biomechanical Engineering **127**: 364-373.

Anderson, D. E., M. L. Madigan and M. A. Nussbaum (2007). "Maximum Voluntary Joint Torque as a Function of Joint Angle and Angular Velocity: Model Development and Application to the Lower Limb." Journal of Biomechanics **40**(14): 3105-3113.

Ashman, R., S. Cowin, W. van Buskirk and J. Rice (1984). "A Continuous Wave Technique for the Measurement of the Elastic Properties of Cortical Bone." Journal of Biomechanics **17**: 349-361.

Austman, R. L., J. S. Milner, D. W. Holdsworth and C. E. Dunning (2008). "The Effect of the Density–Modulus Relationship Selected to Apply Material Properties in a Finite Element Model of Long Bone." Journal of Biomechanics **41**(15): 3171-3176.

Baca, V., Z. Horak, P. Mikulenka and V. Dzupa (2008). "Comparison of an Inhomogeneous Orthotropic and Isotropic Material Models Used for Fe Analyses." Medical Engineering and Physics **30**: 924-930.

Bagge, M. (2000). "A Model of Bone Adaptation as an Optimization Process." Journal of Biomechanics **33**: 1349-1357.

Barak, M. M., D. E. Lieberman and J.-J. Hublin (2011). "A Wolff in Sheep's Clothing: Trabecular Bone Adaptation in Response to Changes in Joint Loading Orientation." Bone **49**(6): 1141-1151.

Beaupré, G., T. Orr and D. Carter (1990a). "An Approach for Time-Dependent Bone Modelling and Remodelling - Theoretical Development." Journal of Orthopaedic Research **8**: 651-661.

Beaupré, G., T. Orr and D. Carter (1990b). "An Approach for Time-Dependent Bone Modelling and Remodelling - Application: A Preliminary Remodelling Situation." Journal of Orthopaedic Research **8**: 662-670.

Behrens, B., I. Nolte, P. Wefstead, C. Stukenborg-Colsman and A. Bouguecha (2009). "Numerical Investigations on the Strain-Adaptive Bone Remodelling in the Periprosthetic Femur: Influence of the Boundary Conditions." Biomedical Engineering Online **8**(28-34): 28.

Bergmann, G., G. Deuretzbacher, M. O. Heller, F. Graichen, A. Rohlmann, J. Strauss and G. N. Duda (2001). "Hip Contact Forces and Gait Patterns from Routine Activities." Journal of Biomechanics **34**: 859-871.

Bergmann, G., F. Graichen and A. Rohlmann (1993). "Hip Joint Loading During Walking and Running, Measured in Two Patients." Journal of Biomechanics **26**(8): 969-990.

Bergmann, G., F. Graichen and A. Rohlmann (2004). "Hip Joint Contact Forces During Stumbling." Langenbeck's Archives of Surgery **389**(1): 53-59.

Berry, D., D. Lewallen, A. Hanssen and M. Cabanela (1999). "Pelvic Discontinuity in Revision Total Hip Arthoplasty." Journal of Bone and Joint Surgery **81-A**(12): 1692-1702.

Besier, T. F., M. Fredericson, G. E. Gold, G. S. Beaupré and S. L. Delp (2009). "Knee Muscle Forces During Walking and Running in Patellofemoral Pain Patients and Pain-Free Controls." Journal of Biomechanics **42**(7): 898-905.

Bitsakos, C., J. Kerner, I. Fisher and A. A. Amis (2005). "The Effect of Muscle Loading on the Simulation of Bone Remodelling in the Proximal Femur." Journal of Biomechanics **38**: 133-139.

Blain, H., A. Jaussent, E. Thomas, J.-P. Micallef, A. Dupuy, P. Bernard, D. Mariano-Goulart, J. Cristol, C. Sultan, M. Rossi and M.-C. Picot (2009). "Low Sit-to-Stand Performance Is Associated with Low Femoral Neck Bone Mineral Density in Healthy Women." Calcified Tissue International **84**(4): 266-275.

Bonewald, L. F. (2002). "Osteocytes: A Proposed Multifunctional Bone Cell." Journal of Musculoskeletal and Neuronal Interactions **2**(3): 239-241.

Bourgery, J. B. M. and N. H. Jacob (1832). Traite Complet De L'anatomie De L'homme. Paris, France, Delaunay.

Boutroy, S., N. Vilayphiou, J.-P. Roux, P. D. Delmas, H. Blain, R. D. Chapurlat and P. Chavassieux (2011). "Comparison of 2d and 3d Bone Microarchitecture Evaluation at the Femoral Neck, among Postmenopausal Women with Hip Fracture or Hip Osteoarthritis." Bone **49**(5): 1055-1061.

Boyle, C. and I. Y. Kim (2011). "Three-Dimensional Micro-Level Computational Study of Wolff's Law Via Trabecular Bone Remodeling in the Human Proximal Femur Using Design Space Topology Optimization." Journal of Biomechanics **44**(5): 935-942.

Burger, E. and J. Klein-Nulend (1999). "Mechanotransduction in Bone - Role of the Lacuno-Canicular Network." Journal of the Federation of American Societies for Experimental Biology **13**: s101-s112.

Burkhart, J. M. and J. Jowsey (1967). "Parathyroid and Thyroid Hormones in the Development of Immobilization Osteoporosis." Endocrinology **81**(5): 1053-1062.

Butler, D. L. (1989). "Anterior Cruciate Ligament: Its Normal Response and Replacement." Journal of Orthopaedic Research **7**(6): 910-921.

Callaghan, J. P., A. E. Patla and S. M. McGill (1999). "Low Back Three-Dimensional Joint Forces, Kinematics, and Kinetics During Walking." Clinical Biomechanics **14**(3): 203-216.

Carter, D., G. Beaupré, N. Giori and J. Helms (1998). "Mechanobiology of Skeletal Regeneration." Clinical Orthopaedics and Related Research **355s**: 41-55.

Carter, D. and W. Hayes (1977). "The Compressive Behaviour of Bone as a Two-Phase Porous Structure." Journal of Bone and Joint Surgery **59**(7): 954-962.

Carter, D. R., T. E. Orr and D. P. Fyhrie (1989). "Relationships between Loading History and Femoral Cancellous Bone Architecture." Journal of Biomechanics **22**(3): 231-244.

Ciarelli, T. E., D. P. Fyhrie, M. B. Schaffler and S. A. Goldstein (2000). "Variations in Three-Dimensional Cancellous Bone Architecture of the Proximal Femur in Female Hip Fractures and in Controls." Journal of Bone and Mineral Research **15**(1): 32-40.

Clarke, S. G., A. T. M. Phillips and A. M. J. Bull (2011). "Evaluating a Suitable Level of Model Complexity for Finite Element Analysis of the Intact Acetabulum." Computer Methods in Biomechanics and Biomedical Engineering: 1-8.

Clarke, S. G., A. T. M. Phillips, A. M. J. Bull and J. P. Cobb (2012). "A Hierarchy of Computationally Derived Surgical and Patient Influences on Metal on Metal Press-Fit Acetabular Cup Failure." Journal of Biomechanics **45**(9): 1698-1704.

Coelho, P. G., P. R. Fernandes, H. C. Rodrigues, J. B. Cardoso and J. M. Guedes (2009). "Numerical Modeling of Bone Tissue Adaptation—a Hierarchical Approach for Bone Apparent Density and Trabecular Structure." Journal of Biomechanics **42**(7): 830-837.

Collet, P., D. Uebelhart, L. Vico, L. Moro, D. Hartmann, M. Roth and C. Alexandre (1997). "Effects of 1- and 6-Month Spaceflight on Bone Mass and Biochemistry in Two Humans." Bone **20**(6): 547-551.

Coughlin, T. R. and G. L. Niebur (2012). "Fluid Shear Stress in Trabecular Bone Marrow Due to Low-Magnitude High-Frequency Vibration." Journal of Biomechanics **45**(13): 2222-2229.

Cowin, S. C. (1986). "Wolff's Law of Trabecular Architecture at Remodelling Equilibrium." Journal of Biomechanical Engineering **108**(1): 83-88.

Cowin, S. C. (2001). Bone Mechanics Handbook. Boca Raton, FL, USA, CRC Press.

Cowin, S. C. and M. Mehrabadi (1989). "Identification of the Elastic Symmetry of Bone and Other Materials." Journal of Biomechanics **22**(6/7): 503-515.

Cowin, S. C. and W. van Buskirk (1986). "Technical Note: Thermodynamic Restrictions on the Elastic Constants of Bone." Journal of Biomechanics **19**: 85-88.

Cristofolini, L., M. Viceconti, A. Toni and A. Giunti (1995). "Influence of Thigh Muscles on the Axial Strains in a Proximal Femur During Early Stance in Gait." Journal of Biomechanics **28**(5): 617-624.

Crowninshield, R. D. and R. A. Brand (1981). "A Physiologically Based Criterion of Muscle Force Prediction in Locomotion." Journal of Biomechanics **14**(11): 793-801.

Culmann, K. (1865). Die Graphische Statik. Zurich, Switzerland, Verlag Von Meyer & Zeller.

Cuppone, M., B. Seedhiom, E. Berry and A. Ostell (2004). "The Longitudinal Young's Modulus of Cortical Bone in the Midshaft of Human Femur and Its Correlation with CT Scanning Data." Calcified Tissue International **74**: 302-309.

Currey, J. (1984). "Can Strains Give Adequate Information for Adaptive Bone Remodelling?" Calcified Tissue International **36**: s118-s122.

Currey, J. (2003). "The Many Adaptations of Bone." Journal of Biomechanics **36**: 1487-1495.

D'Lima, D. D., S. Patil, N. Steklov, J. E. Slamin and J. C. W. Colwell (2006). "Tibial Forces Measured in Vivo after Total Knee Arthroplasty." The Journal of Arthroplasty **21**(2): 255-262.

D'Lima, D. D., N. Steklov, B. J. Fregly, S. A. Banks and C. W. Colwell (2008). "In Vivo Contact Stresses During Activities of Daily Living after Knee Arthroplasty." Journal of Orthopaedic Research **26**(12): 1549-1555.

Daffner, R. H. and H. Pavlov (1992). "Stress Fractures: Current Concepts." American Journal of Roentgenology **159**: 245-252.

Dalstra, M. and R. Huiskes (1995). "Load Transfer across the Pelvic Bone." Journal of Biomechanics **28**(6): 715-724.

Dalstra, M., R. Huiskes, A. Odgaard and L. van Erning (1993). "Mechanical and Textural Properties of Pelvic Trabecular Bone." Journal of Biomechanics **26**(4/5): 523-535.

Dalstra, M., R. Huiskes and L. van Erning (1995). "Development and Validation of a Three-Dimensional Finite Element Model of the Pelvic Bone." Journal of Biomechanical Engineering **117**(3): 272-278.

Delp, S. L. (1990). Surgery Simulation: A Computer-Graphics System to Analyze and Design Musculoskeletal Reconstructions of the Lower Limb, Stanford University. **PhD**.

Delp, S. L., F. C. Anderson, A. S. Arnold, P. Loan, A. Habib, C. T. John, E. Guendelman and D. G. Thelen (2007). "Opensim: Open-Source Software to Create and Analyze Dynamic Simulations of Movement." Biomedical Engineering, IEEE Transactions on Biomedical Engineering **54**(11): 1940-1950.

Doblaré, M. and J. M. Garcia (2001). "Application of an Anisotropic Bone-Remodelling Model Based on a Damage-Repair Theory to the Analysis of the Proximal Femur before and after Total Hip Replacement." Journal of Biomechanics **34**: 1157-1170.

Dostal, W. F. and J. G. Andrews (1981). "A Three-Dimensional Biomechanical Model of Hip Musculature." Journal of Biomechanics **14**(11): 803-812.

Doube, M., M. M. Kłosowski, I. Arganda-Carreras, F. P. Cordelières, R. P. Dougherty, J. S. Jackson, B. Schmid, J. R. Hutchinson and S. J. Shefelbine (2010). "Bonej: Free and Extensible Bone Image Analysis in ImageJ." Bone **47**(6): 1076-1079.

Duda, G. N. (1996). Influence of Muscle Forces on the Internal Loading in the Femur During Gait. Hamburg, Arbeitsbereich Biomechanik Tu Hamburg. **PhD**.

Duda, G. N., M. O. Heller, J. Albinger, O. Schulz, E. Schneider and L. Claes (1998). "Influence of Muscle Forces on Femoral Strain Distribution." Journal of Biomechanics **31**: 841-846.

Ehrlich, P. and L. Lanyon (2002). "Mechanical Strain and Bone Cell Function: A Review." Osteoporosis International **13**: 688-700.

Erdemir, A., T. M. Guess, J. Halloran, S. C. Tadepalli and T. M. Morrison (2012). "Considerations for Reporting Finite Element Analysis Studies in Biomechanics." Journal of Biomechanics **45**(4): 625-633.

Fehling, P. C., L. Alekel, J. Clasey, A. Rector and R. J. Stillman (1995). "A Comparison of Bone Mineral Densities among Female Athletes in Impact Loading and Active Loading Sports." Bone **17**(3): 205-210.

Fernandes, P., H. Rodrigues and C. Jacobs (1999). "A Model of Bone Adaptation Using a Global Optimisation Criterion Based on the Trajectorial Theory of Wolff." Computer Methods in Biomechanics and Biomedical Engineering **2**: 125-148.

Folgado, J., P. R. Fernandes, J. M. Guedes and H. C. Rodrigues (2004). "Evaluation of Osteoporotic Bone Quality by a Computational Model for Bone Remodeling." Computers and Structures **82**(17–19): 1381-1388.

Ford, C. and T. Keaveny (1996). "The Dependence of Shear Failure Properties of Trabecular Bone on Apparent Density and Trabecular Orientation." Journal of Biomechanics **29**(10): 1309-1317.

Friederich, J. A. and R. A. Brand (1990). "Muscle Fiber Architecture in the Human Lower Limb." Journal of Biomechanics **23**(1): 91-95.

Fritton, S. P. and S. Weinbaum (2009). "Fluid and Solute Transport in Bone: Flow-Induced Mechanotransduction." Annual Review of Fluid Mechanics **41**(1): 347-374.

Frost, H. M. (1964). The Laws of Bone Structure. Springfield, Illinois, US, C.C. Thomas.

Frost, H. M. (1987). "Bone 'Mass' and the 'Mechanostat': A Proposal." The Anatomical Record **219**: 1-9.

Frost, H. M. (2003). "Bone's Mechanostat: A 2003 Update." The Anatomical Record Part A: Discoveries in Molecular, Cellular, and Evolutionary Biology **275A**(2): 1081-1101.

Galilei, G. (1638). Discorsi E Dimostrazioni Matematiche: Intorno a Due Nuoue Scienze Attenenti Alla Mecanica I Movimenti Locali. Leida, Italy.

Garden, R. S. (1961). "The Structure and Function of the Proximal End of the Femur." Journal of Bone and Joint Surgery: British Volume **43-B**(3): 576-589.

Gardner, M., A. Chong, A. Pollock and P. Wooley (2010). "Mechanical Evaluation of Large-Size Fourth-Generation Composite Femur and Tibia Models." Annals of Biomedical Engineering **38**(3): 613-620.

Geraldes, D. M. and A. T. M. Phillips (2010). A Novel 3D Strain-Adaptive Continuum Orthotropic Bone Remodelling Algorithm: Prediction of Bone Architecture in the Femur. 6th World Congress of Biomechanics (Wcb 2010). August 1-6, 2010 Singapore. C. T. Lim and J. C. H. Goh, Springer Berlin Heidelberg. **31:** 772-775.

Goldacre, M. J., S. E. Roberts and D. Yeates (2002). "Mortality after Admission to Hospital with Fractured Neck of Femur: Database Study." British Medical Journal **325**(7369): 868-869.

Goulet, R., S. Goldstein and M. Ciarelli (1994). "The Relationship between the Structural and Orthogonal Compressive Properties of Trabecular Bone." Journal of Biomechanics **27**: 375-389.

Hambli, R. (2011). "Numerical Procedure for Multiscale Bone Adaptation Prediction Based on Neural Networks and Finite Element Simulation." Finite Elements in Analysis and Design **47**(7): 835-842.

Hambli, R., A. Bettamer and S. Allaoui (2012). "Finite Element Prediction of Proximal Femur Fracture Pattern Based on Orthotropic Behaviour Law Coupled to Quasi-Brittle Damage." Medical Engineering and Physics **34**(2): 202-210.

Han, Y., S. C. Cowin, M. B. Schaffler and S. Weinbaum (2004). "Mechanotransduction and Strain Amplification in Osteocyte Cell Processes." Proceedings of the National Academy of Science of the United States of America **101**(47): 16689-16694.

Harrigan, T. P. and R. W. Mann (1984). "Characterization of Microstructural Anisotropy in Orthotropic Materials Using a Second Rank Tensor." Journal of Materials Science **19**(3): 761-767.

Hayes, W. and B. Snyder (1981). "Towards a Quantitative Formulation of Wolff's Law in Trabecular Bone." Mechanical Properties of Bone: 43-68.

Helgason, B., E. Perilli, E. Schileo, F. Taddei, S. Brynjolfsson and M. Viceconti (2008). "Mathematical Relationships between Bone Density and Mechanical Properties: A Literature Review." Clinical Biomechanics **23**: 135-146.

Heller, M. O., G. Bergmann, G. Deuretzbacher, L. Durselen, M. Pohl, L. Claes, N. P. Haas and G. N. Duda (2001). "Musculo-Skeletal Loading Conditions at the Hip During Walking and Stair Climbing." Journal of Biomechanics **34**: 883-893.

Heller, M. O., G. Bergmann, J.-P. Kassi, L. Claes, N. P. Haas and G. N. Duda (2005). "Determination of Muscle Loading at the Hip Joint for Use in Pre-Clinical Testing." Journal of Biomechanics **38**: 1155-1163.

Hellmich, C., C. Kober and B. Erdmann (2008). "Micromechanics-Based Conversion of Ct Data into Anisotropic Elasticity Tensors, Applied to Fe Simulations of a Mandible." Annals of Biomedical Engineering **36**(1): 108-122.

Hert, J., M. Liskova and J. Landa (1971). "Reaction of Bone to Mechanical Stimuli: Continuous and Intermittent Loading of Tibia in Rabbit." Folia Morphologica **19**(3): 290-300.

Ho, Y. S. (2012). Continuum Modelling of the Femur and Prediction of Osteoporotic Fracture Risk Regions. London, Imperial College London. **MEng**.

Hodge, W. A., R. S. Fijan, K. L. Carlson, R. G. Burgess, W. H. Harris and R. W. Mann (1986). "Contact Pressures in the Human Hip Joint Measured in Vivo." Proceedings of the National Academy of Sciences **83**(9): 2879-2883.

Hodgskinson, R. and J. Currey (1992). "Young's Modulus, Density and Material Properties of Cancellous Bone over a Large Density Range." Journal of Materials Science: Materials in Medicine **3**: 377-381.

Homminga, J., B. R. McCreadie, H. Weinans and R. Huiskes (2003). "The Dependence of the Elastic Properties of Osteoporotic Cancellous Bone on Volume Fraction and Fabric." Journal of Biomechanics **36**(10): 1461-1467.

Honda, A., Y. Umemura and S. Nagasawa (2001). "Effect of High-Impact and Low-Repetition Training on Bones in Ovariectomized Rats." Journal of Bone and Mineral Research **16**(9): 1688-1693.

Huiskes, R., R. Ruimerman, G. H. van Lenthe and J. Janssen (2000). "Effects of Mechanical Forces on Maintenance and Adaptation of Form in Trabecular Bone." Nature **405**: 704-706.

Huiskes, R., H. Weinans, H. Grootenboer, M. Dalstra, B. Fudala and T. Sloof (1987). "Adaptative Bone-Remodelling Theory Applied to Prosthetic-Design Analysis." Journal of Biomechanics **20**(11/12): 1135-1150.

Humphry, G. M. (1856). A Treatise on the Human Skeleton Cambridge, UK, Macmillan and co.

Jämsä, T., A. Vainionpää, R. Korpelainen, E. Vihriälä and J. Leppäluoto (2006). "Effect of Daily Physical Activity on Proximal Femur." Clinical Biomechanics **21**(1): 1-7.

Jang, I., I. Kim and B. Kwak (2009). "Analogy of Strain Energy Density Based Bone-Remodeling Algorithm and Structural Topology Optimisation." Journal of Biomechanical Engineering **131**: 7.

Jang, I. G. and I. Y. Kim (2010). "Application of Design Space Optimization to Bone Remodeling Simulation of Trabecular Architecture in Human Proximal Femur for Higher Computational Efficiency." Finite Elements in Analysis and Design **46**(4): 311-319.

Jansen, M. (1920). On Bone Formation: Its Relation to Tension and Pressure. Manchester, UK, Manchester University Press.

Johal, P., A. Williams, P. Wragg, D. Hunt and W. Gedroyc (2005). "Tibio-Femoral Movement in the Living Knee. A Study of Weight Bearing and Non-Weight Bearing Knee Kinematics Using 'Interventional' MRI." Journal of Biomechanics **38**(2): 269-276.

Judex, S. and R. F. Zernicke (2000). "High-Impact Exercise and Growing Bone: Relation between High Strain Rates and Enhanced Bone Formation." Journal of Applied Physiology **88**(6): 2183-2191.

Juszczyk, M. M., L. Cristofolini and M. Viceconti (2011). "The Human Proximal Femur Behaves Linearly Elastic up to Failure under Physiological Loading Conditions." Journal of Biomechanics **44**(12): 2259-2266.

Kabel, J., B. van Rietbergen, A. Odgaard and R. Huiskes (1999). "Constitutive Relationships of Fabric, Density, and Elastic Properties in Cancellous Bone Architecture." Bone **25**(4): 481-486.

Kaneko, T. S., J. S. Bell, M. R. Pejcic, J. Tehranzadeh and J. H. Keyak (2004). "Mechanical Properties, Density and Quantitative CT Scan Data of Trabecular Bone with and without Metastases." Journal of Biomechanics **37**(4): 523-530.

Kanis, J. A. (1994). "Assessment of Fracture Risk and Its Application to Screening for Postmenopausal Osteoporosis: Synopsis of a WHO Report." Osteoporosis International **4**(6): 368-381.

Ketcham, R. A. (2005). "Computational Methods for Quantitative Analysis of Three-Dimensional Features in Geological Specimens." Geosphere **1**(1): 32-41.

Keyak, J. H. (2001). "Improved Prediction of Proximal Femoral Fracture Load Using Nonlinear Finite Element Models." Medical Engineering and Physics **23**(3): 165-173.

Keyak, J. H., J. M. Meagher, H. B. Skinner and C. D. Mote Jr (1990). "Automated Three-Dimensional Finite Element Modelling of Bone: A New Method." Journal of Biomedical Engineering **12**(5): 389-397.

Kleemann, R. U., M. O. Heller, U. Stoeckle, W. R. Taylor and G. N. Duda (2003). "Tha Loading Arising from Increased Femoral Anteversion and Offset May Lead to Critical Cement Stresses." Journal of Orthopaedic Research **21**(5): 767-774.

Klein Horsman, M. D., H. F. J. M. Koopman, F. C. T. van der Helm, L. P. Prosé and H. E. J. Veeger (2007). "Morphological Muscle and Joint Parameters for Musculoskeletal Modelling of the Lower Extremity." Clinical Biomechanics **22**(2): 239-247.

Klenerman, L. and R. W. Marcuson (1970). "Intracapsular Fractures of the Neck of the Femur " Journal of Bone and Joint Surgery: British Edition **52-B**: 514-517.

Kluess, D., R. Souffrant, W. Mittelmeier, A. Wree, K. Schmitz and R. Bader (2009). "A Convenient Approach for Finite-Element-Analyses of Orthopaedic Implants in Bone Contact: Modelling and Experimental Validation." Computer Methods and Programs in Biomedicine **95**: 23-30.

Koch, J. C. (1917). "The Laws of Bone Architecture." American Journal of Anatomy **21**(2): 177-298.

Kopperdahl, D. and T. Keaveny (1998). "Yield Strain Behavior of Trabecular Bone." Journal of Biomechanics **31**: 601-608.

Krahl, H., U. Michaelis, H.-G. Pieper, G. Quack and M. Montag (1994). "Stimulation of Bone through Sports - a Radiologic Investigation of the Upper Extremities in Professional Tennis Players." The American Journal of Sports Medicine **22**(6): 751-757.

Kutzner, I., B. Heinlein, F. Graichen, A. Bender, A. Rohlmann, A. Halder, A. Beier and G. Bergmann (2010). "Loading of the Knee Joint During Activities of Daily Living Measured in Vivo in Five Subjects." Journal of Biomechanics **43**(11): 2164-2173.

Kyle, R. F., M. E. Cabanela, T. A. Russell, M. F. Swiontkowski, R. A. Winquist, J. D. Zuckerman, A. H. Schmidt and K. J. Koval (1994). "Fractures of the Proximal Part of the Femur." Journal of Bone and Joint Surgery **76**(A): 924–950.

Lanyon, L. E. and C. T. Rubin (1984). "Static vs. Dynamic Loads as an Influence on Bone Remodelling." Journal of Biomechanics **17**(12): 897-905.

Lempriére, B. M. (1968). "Poisson's Ratio in Orthotropic Materials." American Institute of Aeronautics and Astronautics Journal **6**(11): 2226-2227.

Lenaerts, G., F. De Groote, B. Demeulenaere, M. Mulier, G. Van der Perre, A. Spaepen and I. Jonkers (2008). "Subject-Specific Hip Geometry Affects Predicted Hip Joint Contact Forces During Gait." Journal of Biomechanics **41**(6): 1243-1252.

Lengsfeld, M., J. Kaminsky, B. Merz and R. P. Franke (1996). "Sensitivity of Femoral Strain Pattern Analyses to Resultant and Muscle Forces at the Hip Joint." Medical Engineering and Physics **18**(1): 70-78.

Lengsfeld, M., J. Schmitt, P. Alter, J. Kaminsky and R. Leppek (1998). "Comparison of Geometry-Based and CT Voxel-Based Finite Element Modelling and Experimental Validation." Medical Engineering and Physics **20**(7): 515-522.

Li, G., J. Gil, A. Kanamori and S. L. Y. Woo (1999). "A Validated Three-Dimensional Computational Model of a Human Knee Joint." Journal of Biomechanical Engineering **121**(6): 657-662.

Li, G., R. Papannagari, K. W. Nha, L. E. DeFrate, T. J. Gill and H. E. Rubash (2007). "The Coupled Motion of the Femur and Patella During in Vivo Weightbearing Knee Flexion." Journal of Biomechanical Engineering **129**(6): 937-943.

Loder, J. C. v. (1803). Tabulae Anatomicae Quas Ad Illustrandam Humani Corporis Fabricam.

Love, A. E. H. (1927). A Treatise on the Mathematical Theory of Elasticity, Cambridge University Press.

Martinet, O., J. Cordey, Y. Harder, A. Maier, M. Buhler and G. E. Barraud (2000). "The Epidemiology of Fractures of the Distal Femur." Injury **31**(1003): 62-94.

McNamara, L. M. and P. J. Prendergast (2007). "Bone Remodelling Algorithms Incorporating Both Strain and Microdamage Stimuli." Journal of Biomechanics **40**: 1381-1391.

Merican, A. M. and A. A. Amis (2009). "Iliotibial Band Tension Affects Patellofemoral and Tibiofemoral Kinematics." Journal of Biomechanics **42**(10): 1539-1546.

Merican, A. M., S. Sanghavi, F. Iranpour and A. A. Amis (2009). "The Structural Properties of the Lateral Retinaculum and Capsular Complex of the Knee." Journal of Biomechanics **42**(14): 2323-2329.

Mesfar, W. and A. Shirazi-Adl (2006). "Biomechanics of Changes in ACL and PCL Material Properties or Prestrains in Flexion under Muscle Force-Implications in Ligament Reconstruction." Computer Methods in Biomechanics and Biomedical Engineering **9**(4): 201-209.

Miller, R. K., D. W. Murray, H. S. Gill, J. J. O'Connor and J. W. Goodfellow (1997). "In Vitro Patellofemoral Joint Force Determined by a Non-Invasive Technique." Clinical Biomechanics **12**(1): 1-7.

Miller, Z., M. Fuchs and M. Arcan (2002). "Trabecular Bone Adaptation with an Orthotropic Material Model." Journal of Biomechanics **35**: 247-256.

Miller, Z. and M. B. Fuchs (2005). "Effect of Trabecular Curvature on the Stiffness of Trabecular Bone." Journal of Biomechanics **38**(9): 1855-1864.

Modenese, L. (2012). Hip Contact Force Prediction Using a Musculoskeletal Model of the Lower Limb. London, Imperial College London. **PhD**.

Modenese, L. and A. M. Phillips (2012). "Prediction of Hip Contact Forces and Muscle Activations During Walking at Different Speeds." Multibody System Dynamics **28**(1-2): 157-168.

Modenese, L., A. T. M. Phillips and A. M. J. Bull (2011). "An Open Source Lower Limb Model: Hip Joint Validation." Journal of Biomechanics **44**(12): 2185-2193.

Morgan, E. F., H. H. Bayraktar and T. M. Keaveny (2003). "Trabecular Bone Modulus–Density Relationships Depend on Anatomic Site." Journal of Biomechanics **36**(7): 897-904.

Morlock, M., E. Schneider, A. Bluhm, M. Vollmer, G. Bergmann, V. Muller and M. Honl (2001). "Duration and Frequency of Every Day Activities in Total Hip Patients." Journal of Biomechanics **34**: 873-881.

Mullender, M. G. and R. Huiskes (1995). "Proposal for the Regulatory Mechanism of Wolff's Law." Journal of Orthopaedic Research **13**: 503-512.

Mullender, M. G. and R. Huiskes (1997). "Osteocytes and Bone Lining Cells: Which Are the Best Candidates for Mechano-Sensors in Cancellous Bone?" Bone **20**(6): 527-532.

National Center for Health Statistics (2009). Number of All-Listed Procedures from Discharges from Short-Stay Hospitals by Procedure, Category and Age: United States 2009.

National Joint Registry (2011). National Joint Registry for England and Wales - 8th Annual Report.

Nazarian, A., J. Muller, D. Zurakowski, R. Muller and B. D. Snyder (2007). "Densitometric, Morphometric and Mechanical Distributions in the Human Proximal Femur." Journal of Biomechanics **40**: 2573-2579.

Nieves, J., J. Bilezikian, J. Lane, T. Einhorn, Y. Wang, M. Steinbuch and F. Cosman (2010). "Fragility Fractures of the Hip and Femur: Incidence and Patient Characteristics." Osteoporosis International **21**(3): 399-408.

Odgaard, A. (1997). "Three-Dimensional Methods for Quantification of Cancellous Bone Architecture." Bone **20**(4): 315-328.

Pedersen, D. R., R. A. Brand and D. T. Davy (1997). "Pelvic Muscle and Acetabular Contact Forces During Gait." Journal of Biomechanics **30**(9): 959-965.

Pedersen, P. (1989). "On Optimal Orientation of Orthotropic Materials." Structural Optimisation **1**: 101-107.

Peng, L., J. Bai, X. Zeng, Z. Yongxin and V. Baca (2006). "Comparison of Isotropic and Orthotropic Material Property Assignments on Femoral Finite Element Models under Two Loading Conditions." Medical Engineering and Physics **28**: 227-233.

Perry, J. (1992). Gait Analysis: Normal and Pathological Function. Thorofare, New Jersey, SLACK Incorporated.

Phillips, A. T. M. (2005). Numerical Modelling of the Pelvis and Acetabular Construct Following Hip Arthroplasty. Edinburgh, University of Edinburgh. **PhD:** 264.

Phillips, A. T. M. (2009). "The Femur as a Musculo-Skeletal Construct: A Free Boundary Condition Modelling Approach." Medical Engineering and Physics **31**: 673-680.

Phillips, A. T. M. (2012). "Structural Optimisation in Assessing the Biomechanics of the Femur." Proceedings of the Institution of Civil Engineers: Engineering and Computational Mechanics **165**: 147 -154.

Phillips, A. T. M., P. Pankaj, C. R. Howie, A. S. Usmani and A. H. Simpson (2007). "Finite Element Modelling of the Pelvis: Inclusion of Muscular and Ligamentous Boundary Conditions." Medical Engineering and Physics **29**: 739-748.

Pidaparti, R. and C. Turner (1997). "Cancelous Bone Architecture: Advantages of Nonorthogonal Trabecular Alignment under Multidirectional Joint Loading." Journal of Biomechanics **30**(9): 979-987.

Polgar, K., H. S. Gill, M. Viceconti, D. W. Murray and J. J. O'Connor (2003). "Strain Distribution within the Human Femur Due to Physiological and Simplified Loading: Finite Element Analysis Using the Muscle Standardized Femur Model." Proceedings of the Institution of Mechanical Engineers Part H: Journal of Engineering in Medicine: 173-189.

Pulkkinen, P., J. Partanen, P. Jalovaara and T. Jämsä (2004). "Combination of Bone Mineral Density and Upper Femur Geometry Improves the Prediction of Hip Fracture." Osteoporosis International **15**(4): 274-280.

Ramos, A. and J. A. Simões (2006). "Tetrahedral Versus Hexahedral Finite Elements in Numerical Modelling of the Proximal Femur." Medical Engineering and Physics **28**: 916-924.

Rasband, W. S. (1997-2012). Imagej. Bethesda,Maryland, USA, U. S. National Institutes of Health**:** http://imagej.nih.gov/ij/.

Reilly, D. T. and M. Martens (1972). "Experimental Analysis of the Quadriceps Muscle Force and Patello-Femoral Joint Reaction Force for Various Activities." Acta Orthopaedica **43**(2): 126-137.

Rho, J. Y., M. E. Roy II, T. Y. Tsui and G. M. Pharr (1999). "Elastic Properties of Microstructural Components of Human Bone Tissue as Measured by Nanoidentation." Journal of Biomedical Materials Research **45**(1): 48-54.

Rho, J. Y., T. Y. Tsui and G. M. Pharr (1997). "Elastic Properties of Human Cortical and Trabecular Lamellar Bone Measured by Nanoidentation." Biomaterials **18**: 1325-1330.

Rodgers, J. and A. Nicewander (1988). "Thirteen Ways to Look at the Correlation Coefficient." The American Statistician **42**(1): 59-66.

Rohrbach, D., S. Lakshmanan, F. Peyrin, M. Langer, A. Gerisch, Q. Grimal, P. Laugier and K. Raum (2012). "Spatial Distribution of Tissue Level Properties in a Human Femoral Cortical Bone." Journal of Biomechanics **45**(13): 2264-2270.

Rossi, J.-M. and S. Wendling-Mansuy (2007). "A Topology Optimization Based Model of Bone Adaptation." Computer Methods in Biomechanics and Biomedical Engineering **10**(6): 419 - 427.

Rubin, C. T. and L. E. Lanyon (1985). "Regulation of Bone Mass by Mechanical Strain Magnitude." Calcified Tissue International **37**(4): 411-417.

Rubin, C. T. and L. E. Lanyon (1987). "Osteoregulatory Nature of Mechanical Stimuli: Function as a Determinant for Adaptive Remodeling in Bone." Journal of Orthopaedic Research **5**(2): 300-310.

Rudy, D. J., J. M. Deuerling, A. A. Espinoza Orías and R. K. Roeder (2011). "Anatomic Variation in the Elastic Inhomogeneity and Anisotropy of Human Femoral Cortical Bone Tissue Is Consistent across Multiple Donors." Journal of Biomechanics **44**(9): 1817-1820.

Ryan, T. M. and R. Ketcham (2002). "Femoral Head Trabecular Bone Structure in Two Omomyid Primates." Journal of Human Evolution **43**(2): 241-263.

Ryan, T. M. and R. A. Ketcham (2005). "Angular Orientation of Trabecular Bone in the Femoral Head and Its Relationship to Hip Joint Loads in Leaping Primates." Journal of Morphology **265**(3): 249-263.

Salminen, S., H. Pihlajamaki, V. Avikainen, A. Kyro and O. Bostman (1997). "Specific Features Associated with Femoral Shaft Fractures Caused by Low-Energy Trauma." The Journal of Trauma and Acute Care Surgery **43**(1): 117-122.

Scannell, P. T. and P. J. Prendergast (2009). "Cortical and Interfacial Bone Changes around a Non-Cemented Hip Implant: Simulations Using a Combined Strain/Damage Remodelling Algorithm." Medical Engineering and Physics **31**: 477-488.

Shannon, C. E. (1949). "Communication in the Presence of Noise." Proceedings of the Institute of Radio Engineers **37**(1): 10-21.

Shefelbine, S., P. Augat, L. Claes and U. Simon (2005). "Trabecular Bone Fracture Healing Simulation with Finite Element Analysis and Fuzzy Logic." Journal of Biomechanics **38**: 2440-2450.

Shim, V., R. Pitto, R. Stricher, P. Hunter and I. Anderson (2007). "The Use of Sparse CT Datasets for Auto-Generating Accurate FE Models of the Femur and Pelvis." Journal of Biomechanics **40**: 26-35.

Simões, J. A., M. A. Vaz, S. Blatcher and M. Taylor (2000). "Influence of Head Constraint and Muscle Forces on the Strain Distribution within the Intact Femur." Medical Engineering and Physics **22**: 453-459.

Singh, M., A. R. Nagrath and P. S. Maini (1970). "Changes in Trabecular Pattern of the Upper End of the Femur as an Index of Osteoporosis." Journal of Bone and Joint Surgery **52**: 457-467.

Skedros, J. and S. Baucom (2007). "Mathematical Analysis of Trabecula 'Trajectories' in Apparent Trajectorial Structures: The Unfortunate Historical Emphasis on the Human Proximal Femur." Journal of Theoretical Biology **244**: 15-45.

Skedros, J. and R. Brand (2011). "Biographical Sketch: Georg Hermann Von Meyer (1815–1892)." Clinical Orthopaedics and Related Research **469**(11): 3072-3076.

Skerry, T. M. (2006). "One Mechanostat or Many? Modifications of the Site-Specific Response of Bone to Mechanical Loading by Nature and Nurture." Journal of musculoskeletal & neuronal interactions **6**(2): 122-127.

Skerry, T. M. (2008). "The Response of Bone to Mechanical Loading and Disuse: Fundamental Principles and Influences on Osteoblast/Osteocyte Homeostasis." Archives of Biochemistry and Biophysics **473**(2): 117-123.

Speirs, A. D., M. O. Heller, G. N. Duda and W. R. Taylor (2007). "Physiologically Based Boundary Conditions in Finite Element Modelling." Journal of Biomechanics **40**: 2318-2323.

Stäubli, H. U., L. Schatzmann, P. Brunner, L. Rincón and L. P. Nolte (1996). "Quadriceps Tendon and Patellar Ligament: Cryosectional Anatomy and Structural Properties in Young Adults." Knee Surgery, Sports Traumatology, Arthroscopy **4**(2): 100-110.

Streubel, P., W. Ricci, A. Wong and M. Gardner (2011). "Mortality after Distal Femur Fractures in Elderly Patients." Clinical Orthopaedics and Related Research **469**(4): 1188-1196.

Sverdlova, N. S. and U. Witzel (2010). "Principles of Determination and Verification of Muscle Forces in the Human Musculoskeletal System: Muscle Forces to Minimise Bending Stress." Journal of Biomechanics **43**(3): 387-396.

Szivek, J. A., J. B. Benjamin and P. L. Anderson (2000). "An Experimental Method for the Application of Lateral Muscle Loading and Its Effect on Femoral Strain Distributions." Medical Engineering and Physics **22**: 109-116.

Tabor, Z. and E. Rokita (2007). "Quantifying Anisotropy of Trabecular Bone from Gray-Level Images." Bone **40**(4): 966-972.

Taggart, H. and T. R. O. Beringer (1984). "Relevance of Osteoporosis in Women with Fracture of the Femoral Neck." British Medical Journal **288**(6425): 1233-1233.

Takechi, H. (1977). "Trabecular Architecture of the Knee Joint." Acta Orthopaedica **48**(6): 673-681.

Taylor, M. E., K. E. Tanner, M. A. R. Freeman and A. L. Yettram (1996). "Stress and Strain Distribution within the Intact Femur: Compression or Bending?" Medical Engineering and Physics **18**(2): 122-131.

Taylor, W., E. Roland, H. Ploeg, D. Hertig, R. Klabunde, M. Warner, M. Hobatho, L. Rakotomanana and S. Clift (2002). "Determination of Orthotropic Bone Elastic Constants Using FEA and Modal Analysis." Journal of Biomechanics **35**: 767-773.

Tobin, W. J. (1955). "The Internal Architecture of the Femur and Its Clinical Significance: The Upper End." Journal of Bone and Joint Surgery **37**(1): 57-88.

Tomaszewski, P., N. Verdonschot, S. Bulstra and G. Verkerke (2010). "A Comparative Finite-Element Analysis of Bone Failure and Load Transfer of Osseointegrated Prostheses Fixations." Annals of Biomedical Engineering **38**(7): 2418-2427.

Tsubota, K., T. Adachi and Y. Tomita (2002). "Functional Adaptation of Cancellous Bone in Human Proximal Femur Predicted by Trabecular Surface Remodeling Simulation toward Uniform Stress State." Journal of Biomechanics **35**: 1541-1551.

Tsubota, K., Y. Suzuki, T. Yamada, M. Hojo, A. Makinouchi and T. Adachi (2009). "Computer Simulation of Trabecular Remodeling in Human Proximal Femur Using Large-Scale Voxel Fe Models: Approach to Understanding Wolff's Law." Journal of Biomechanics **42**: 1088-1094.

Turner, C., V. Anne and R. Pidaparti (1997). "A Uniform Strain Criterion for Trabecular Bone Adaptation: Do Continuum-Level Strain Gradients Drive Adaptation?" Journal of Biomechanics **30**(6): 555-563.

Turner, C., J. Rho, Y. Takano, T. Tsui and G. Pharr (1999). "The Elastic Properties of Trabecular and Cortical Bone Tissues Are Similar: Results from Two Microscopic Measurement Techniques." Journal of Biomechanics **32**: 437-441.

Tursa, J. (2007). angleaxis.m http://cs.gmu.edu/~kosecka/cs485/code/angleaxis.m.

van Campen, A., F. De Groote, L. Bosmans, L. Scheys, I. Jonkers and J. De Schutter (2011). "Functional Knee Axis Based on Isokinetic Dynamometry Data: Comparison of Two Methods, Mri Validation, and Effect on Knee Joint Kinematics." Journal of Biomechanics **44**(15): 2595-2600.

van Rietbergen, B., A. Odgaard, J. Kabel and R. Huiskes (1998). "Relationships between Bone Morphology and Bone Elastic Properties Can Be Accurately Quantified Using High-Resolution Computer Reconstructions." Journal of Orthopaedic Research **16**: 23-31.

van Rietbergen, B., H. Weinans, R. Huiskes and A. Odgaard (1995). "A New Method to Determine Trabecular Bone Elastic Properties and Loading Using Micromechanical Finite Element Models." Journal of Biomechanics **28**(1): 69-81.

Varghese, B., D. Short, R. Penmetsa, T. Goswami and T. Hangartner (2011). "Computed-Tomography-Based Finite-Element Models of Long Bones Can Accurately Capture Strain Response to Bending and Torsion." Journal of Biomechanics **44**(7): 1374-1379.

Viceconti, M., M. Ansaloni, M. Baleani and A. Toni (2003a). "The Muscle Standardized Femur: A Step Forward in the Replication of Numerical Studies in Biomechanics." Proceedings of the Institution of Mechanical Engineers, Part H: Journal of Engineering in Medicine **217**(2): 105-110.

Viceconti, M., M. Ansaloni, M. Baleani and A. Toni (2003b). "The Muscle Standardised Femur." Journal of Biomechanics **36**(1): 145-146.

Vogel, J. M. and M. W. Whittle (1976). "Bone Mineral Changes: The Second Manned Skylab Mission." Aviation, Space and Environmental Medicine **47**(4): 396-400.

von Meyer, G. H. (1867). "Die Architektur Der Spongiosa." Archiv für Anatomie Physiologie und wissenschaftliche Medicin **34**: 615-628.

Wang, Z. and A. Mondry (2005). "Volume-Based Non-Continuum Modeling of Bone Functional Adaptation." Theoretical Biology and Medical Modelling **2**(1): 6.

Ward, F. O. (1838). Outlines of Human Osteology, Renshaw.

Weinans, H., R. Huiskes and H. J. Grootenboer (1992). "The Behaviour of Adaptive Bone-Remodeling Simulation Models." Journal of Biomechanics **25**(12): 1425-1441.

WHO (1994). Assessment of Fracture Risk and Its Application to Screening for Postmenopausal Osteoporosis. Report of a Who Study Group, World Health Organisation Techical Report Series.

Wickiewicz, T. L., R. R. Roy, P. L. Powell and V. R. Edgerton (1983). "Muscle Architecture of the Human Lower Limb." Clinical Orthopaedics and Related Research **179**: 275-283.

Winter, D. A., H. G. Sidwall and D. A. Hobson (1974). "Measurement and Reduction of Noise in Kinematics of Locomotion." Journal of Biomechanics **7**(2): 157-159.

Wirtz, D., T. Pandorf, F. Portheine, K. Radermacher, N. Schiffers, A. Prescher, D. Weichert and F. Niethard (2003). "Concept and Development of an Orthotropic FE Model of the Proximal Femur." Journal of Biomechanics **36**: 289-293.

Wirtz, D., N. Schiffers, T. Pandorf, K. Radermacher, D. Weichert and R. Forst (2000). "Critical Evaluation of Known Bone Material Properties to Realize Anisotropic FE-Simulation on the Proximal Femur." Journal of Biomechanics **33**: 1325-1330.

Wolff, J. (1892). The Law of Bone Remodelling (Translated by Maquet, P. And Furlong, R.). Berlin, Heidelberg, New York, London, Tokyo, Springer-Verlag.

Wootten, M. E., M. P. Kadaba and G. V. B. Cochran (1990). "Dynamic Electromyography. Ii. Normal Patterns During Gait." Journal of Orthopaedic Research **8**(2): 259-265.

Wu, G., S. Siegler, P. Allard, C. Kirtley, A. Leardini, D. Rosenbaum, M. Whittle, D. D. D'Lima, L. Cristofolini, H. Witte, O. Schmid and I. Stokes (2002). "ISB Recommendation on Definitions of Joint Coordinate System of Various Joints for the Reporting of Human Joint Motion—Part I: Ankle, Hip and Spine." Journal of Biomechanics **35**(4): 543-548.

Yang, G., J. Kabel, B. van Rietbergen, A. Odgaard, R. Huiskes and S. Cowin (1999). "The Anisotropic Hooke's Law for Cancellous Bone and Wood." Journal of Elasticity **53**: 125-146.

Younge, A. (2012). Computational and Experimental Modelling of the Femur. London, Imperial College. **PhD**.

Zajac, F. E. (1989). Muscle and Tendon: Properties, Models, Scaling, and Application to Biomechanics and Motor Control. Crc Critical Reviews in Biomedical Engineering, CRC Press (Boca Raton). **17**.

Zdero, R., A. J. McConnell, C. Peskun, K. A. Syed and E. H. Schemitsch (2011). "Biomechanical Measurements of Torsion-Tension Coupling in Human Cadaveric Femurs." Journal of Biomechanical Engineering **133**(1): 014501.